Measurement of particle interaction properties for the incorporation into Discrete Element Methods

By Rajiv Chandramohan

MSc Dissertation 2005
University of Cape Town

Supervisor: Dr M S Powell

"The important thing is not to stop questioning"

Albert Einstein: 1879-1955, German-born American Physicist

To my grandfather, Pappa

a great man with a great soul.

Statement of originality

I declare that the work presented in this thesis is, to the best of my knowledge and belief, original, except as acknowledged in the text, and that the material has not been submitted, either in whole or in part, for a degree at this or any other university. I know the meaning of plagiarism and declare that all the work in the document, except for that which is properly acknowledged, is my own

Rajiv Chandramohan

Signed: 

Date: 16/9/2005

Acknowledgments

In completion of this thesis I would like to thank the following people for their support:

Firstly, I would to thank the lord for his guidance. To my parents and my sisters, Kasthu and Gaya, for their loving support. To Nina, for your care and enthusiasm.

To my supervisor, Dr Malcolm Powell, for his inspiration and leadership. Malcolm, I thank you for your patience and motivation and believing in my abilities, I thank you for your never ending provision of great ideas. To Dr Robert Sarracino, thank you for your constant encouragement and world of knowledge. To my mentors, Andrew and Indresen, thank you for your unconditional support. To my colleagues, in the Comminution group; Andre, Aubrey, Jason, Musa, Reuben, Sonny, Percy and Mdu, thank you for all your help. To the Mineral Processing Research Unit (MPRU) Executive Committee, for giving me the opportunity to travel Australia to extend my research. To Dr Rob Morrison, Dr Nenad Djordjevic and the technical staff of the Julius Kruttschnitt Mineral Research Unit (JKMRC), thank you for your expert advice and collaboration while I was in Australia. A special thank you for the following researchers for the interesting discussions: Dr Paul Cleary of the CSIRO - Centre for Mathematical and Information Sciences (CMIS); Dr Emmy Manlapig, project leader of the AMIRA P9 projects; Dr Graham Brooker, CRC mining - Australian Centre for Field Robotics (ACFR); Dr Shivakumar Karekal, CRC mining - University of Queensland; Dr Hugh Blackburn, CSIRO - Centre for Manufacturing and Infrastructure Technology (CMIT); Dr Phil Schwartz, CSIRO Minerals. To the MPRU staff, thank you for your support. To my friends, Neville and Steve, the guys from the Blast Impact Research, helping me to understand those collisions. Mr Julian Mayer, the wizard of electronics; thank you for your assistance. To all the Mechanical Engineering workshop technicians, for their precise manufacture of the drop tester! Finally, to all the industrial sponsors, thank you for giving me the opportunity to promote my work.

Since the inception of this project two years ago, there have been many difficulties along the way. I am very grateful to all the people mentioned above, who supported and provided me with good advice in times of trouble. The outcome of this project will hopefully embark on a new method of experimental testing and validation of the Discrete Element Models for application mass media flow in the various comminution circuits.

Thank you to all.

Contents

Chapter 10

List of Figures

Chapter 2

Chapter 4

Chapter 5

Chapter 6

Chapter 7

Chapter 8

Chapter 10

List of Tables

Chapter 5

Chapter 6

Chapter 7

Chapter 10

Nomenclature

α	Angle between $\boldsymbol{u}$ and $\boldsymbol{t}$
α_{ang}	Offset angle
α_i	Local angle of incidence of the contact area
$\alpha_{n,s}$	Fraction of critical damping in the normal and shear directions
ΔAng	Offset angle of impact plots in the X-direction
β	Coefficient of rotational / tangential restitution
$\Delta\beta$	Error in Coefficient of tangential restitution
C_c	The critical damping constant
$C_{n,s}$	The damping constant
$C_{1,2}$	Translational velocities of particle 1 and 2
$d_{n,s}$	Total over closure at the contact point
$D_{1,2}$	Diameters of particle 1 and 2
$e_{n,t}$	Coefficient of normal and tangential restitution
e	Coefficient of normal restitution
e_r	Error due to specular reflection
e_a	Error due to angular offset
Δe	Error in Coefficient of normal restitution
$F_{n,s}$	Normal and shear forces
G	shear modulus
$\boldsymbol{H}$	Angular momentum for sphere
i	Angle of incidence
I	Moment of inertia

I_{off} Absolute error in the offset

I_y Absolute error in the pre collision measurements in the Y plane

$I'_{x,y}$ Absolute error in the post collision measurements in the X and Y plane

$\boldsymbol{J}$ Impulse at the point of contact

K Angle of Repose

$K_{n,s}$ Stiffness of the normal and shear contact spring

K_r Radius of gyration

L Measured relative distance

ΔL Error in the measured relative distance

$\Delta L_{off} = \Delta x_{off}$ Error in the measured offset distance

m Reduced mass of the particle

$m_{1,2}$ Masses of particle 1 and 2

Δm Measured mass error for each particle

$\boldsymbol{n}$ Normal unit vector perpendicular to the contact point

N Normal loading

r Angle of reflection

r_a Angle of apparent reflection

$r_{1,2}$ Radii of particle 1 and 2

sf Scale factor

Δsf Error in the scale factor

ΔS Specular reflection offset error for shiny material

$\boldsymbol{t}$ Unit tangent vector about the contact point

μ Coefficient of friction at the contact interface

$\Delta\mu$ Error in Coefficient of friction

$\boldsymbol{u}$ Relative velocity at the contact point

v The relative velocity

ν Poisson ratio

γ Angle of incidence between $\boldsymbol{u}$ and $\boldsymbol{n}$

$\boldsymbol{\omega}_{1,2}$ Angular velocities of particle 1 and 2

x_{off} Offset distance

χ Non dimensional radius of gyration

ψ_1 Non-dimensional angle of incidence

ψ_2 Non-dimensional angle of reflection

ϑ Angle between $\boldsymbol{J}$ and $\boldsymbol{n}$

Synopsis

The principle aim of this research project is to measure parameters which are pertinent for numerical simulations in discontinuous media. One such numerical tool, the Discrete Element Method (DEM), is a promising technique for predicting the dynamics of charge motion within a mill.

Particle interactions in DEM are calculated by contact force and force displacement laws at each particle contact. These contact events are characterized by parameters that are often fitted or estimated due to the lack of accurate experimental measurements. The aim of this project is to experimentally measure the necessary interaction properties required for the DEM analysis and to test the DEM models against the measured experimental results.

An in-flight binary collisions drop tester is constructed to measure the material interaction properties of two spheres. The collision event is captured photographically and pre- and post- relative velocities are measured. The binary collisions of the particles are carefully controlled by relay timing circuits and they are captured on digitized images using a SLR digital camera. The particles are illuminated using digital strobes controlled by a signal generator. The heights of the colliding particles are adjusted to vary the drop velocities prior to collision. The measured relative velocities are applied in rigid body theory of binary impact to extract the required material interaction properties.

The parameters measured from the binary collision include coefficients of tangential and normal restitution and friction. The analysis presented here draws on the work of Maw *et al* [29] and Foerster *et al* [35], which is an extension of the Hertz theory of impact to the oblique impact of the elastic bodies with circular contacts.

Initial numerical simulations using the viscous damping model is performed in Particle Flow Code (PFC) and a comparison between experimental and numerical results presented.

The results show that the numerical simulation predicts well for collisions that involve sticking or direct impact and for collisions that involve sliding the viscous damping model does not predict the region well. It was concluded that the frictional sliding assumed by the model is inadequate.

An experimental technique has been developed to rigorously test models in the DEM, and this technique can be used to refine the DEM contact models for a variety of materials. This should significantly improve the accuracy of the DEM predictions applied to tumbling systems, and enhance the capability of this technique to simulating grinding mills.

Chapter 1

Introduction

1.1 Background

Grinding is an essential step of mineral processing. It accounts for a large proportion of any processing plant's capital expenditure and operating cost and requires considerable mechanical energy. It is known that grinding mills are not particularly energy efficient and about 25 – 55% of total concentrator plant power is utilised for grinding and up to 70% for harder ore, Napier Munn *et al* [1] Considering the decrease in the availability of high grade minerals and the resulting motivation to lower overheads in the mineral liberation process, there is interest in investigating better means to improve grinding efficiency.

Comminution has been the subject of research for over a century. Historically, the main driving force in research has been in developing semi empirical models of grinding output and power consumption for mill design. With the advent of low cost, high performance computers, the Discrete Element Method (DEM) has the potential to make a significant contribution to understanding the fundamentals of the grinding mechanism and power consumption of mills.

Existing semi-empirical modelling methods used to design mills are based on data obtained from pilot and full scale mills. They have successfully been used in design and scale up but suffer the limitations of any empirical model; in that they are unreliable beyond the range over which they are developed. They depend primarily on operator trials of existing equipment. A limitation of these methods is that they provide very little insight into the mechanics of charge motion and the fundamentals of rock breakage within the mill. In contrast, DEM allows modelling of the individual collisions, which when applied to the entire system over time, results in the prediction of the overall charge behaviour in mills. This holds tremendous possibilities for improved modelling of

grinding action in mills. DEM analysis provides a host of useful information, such as impact energy distribution, wall stresses, force transmission paths, etc. To understand qualitative and quantitative aspects of the grinding mill operation, we must first understand the dynamics of charge motion, and the depth of simulation theory that is pertinent for modelling mills.

In this thesis the fundamental physical material interaction properties such as density, coefficient of friction and coefficient of restitution that govern the laws of the interacting particles are investigated. For a successful implementation of DEM to solve mill problems, rigorous experimental work should be conducted to establish the values of the material interaction properties used in the model, and to test the DEM predictions with the parameters used.

1.2 Thesis Outline

The outline of this thesis focuses on the following topics:

- ***Chapter 2: The Literature Review***
    - This section examines the areas of research which motivated this thesis project. From the earliest studies in charge motion in mills to recent developments in the field of Discrete Element Analysis, the review focuses on the need to understand the inter-particle interactions that will be utilised to improve numerical models.

- ***Chapter 3: Hypothesis***
    - The hypothesis and objectives are given, and a description of the type and area of work this thesis will undertake to address the objectives.

- ***Chapter 4: The design***
    - This section of the thesis focuses on the developments in the experimental design. This will cover areas in instrumentation, camera control and design concepts.

- ***Chapter 5: Experimental Procedure***
    - This section focuses on the procedure for running the experiment to extract the pertinent results. The influence of error propagation and image processing are covered in this section.

- ***Chapter 6: Results and Discussions***
    - The results obtained for the material interaction properties of the tested materials are presented in this chapter. The influence of error on the data and its effect on the overall results are also examined.

- ***Chapter 7: Discrete Element Method Comparisons and Testing***
    - Various Models in the Discrete Element Method are tested and compared with experimental data.

- ***Chapter 8: Conclusions and Recommendations***
    - Finally the thesis draws conclusions from the results and tests conducted on the Discrete Element Models.

Chapter 2

Literature

The development of the theory pertinent to this thesis is presented through a review of the literature. The literature reviewed in this chapter will focus on the following sections: Discrete Element Method as an application to analyse the motion of the charge; an overview of the charge motion studies; detailed look into the DEM theory; and the effect of and measurement of particle interaction properties for incorporating into the Discrete Element Method.

2.1 Discrete Element Method

"The Discrete Element Method (DEM) is a numerical technique which models a system as a collection of bonded or unbonded particles. It involves following the motion of distinct general shaped rigid bodies or particles that are subjected to interactions between neighbouring particles and the environment. Engineering problems that exhibit such large scale discontinuous behaviour cannot be easily solved with a conventional continuum based procedure such as the Finite Element Method (FEM). Meshless methods, such as DEM, are more naturally suited to modelling the motion of brittle and granular solids than continuum-based methods such as conventional FE and FD methods. The discrete element procedure is used to determine the dynamic interaction of the bodies and has successfully reproduced complex non-linear interaction phenomena".
– http://egweb.mines.edu/dem/

DEM simulation has found widespread application since it was first proposed by Cundall and Strack [2]. They applied DEM to model soil particles under dynamic loading conditions. Later this method was applied to simple flow studies in rapid granular flow by Campbell [3], Barker [4] and Walton [5]. The first industrial application of DEM in the simulation of mineral processing was by Mishra and Rajamani [6]. Inoue and Okaya

[7] studied the grinding mechanism of centrifugal mills using DEM simulation. They investigated charge motion in a centrifugal mill at various operating conditions. In their model they were able to predict energy dissipation classified for various interactions, i.e. particle on particle and particle on surface interactions. This categorization enables one to examine the wear rate of grinding component and mill liners. Since then studies on ball mills and in particular using DEM simulations have proliferated. Mishra and Rajamani [8], Cleary [9], Dong and Moys [10] have focused on traditional ball mills and have done an appreciable amount of work in this area.

The simplest particles in DEM are rigid, circular discs, for a 2D model, and rigid spheres, for a 3D model. The behaviour of particles at contact points is modelled using the soft contact approach, whereby the individual particles are allowed to overlap one another, and interparticle forces are characterized by the repeated implementation of a contact force law at each contact within the system and a force displacement law for each particle within the system during every time-step within the analysis duration. This process, as utilized in a particular DEM code, Particle Flow Code (PFC) is depicted schematically in **Figure 2-1**. An extensive overview of the DEM is presented in the Particle Flow Code (PFC) manual [11].

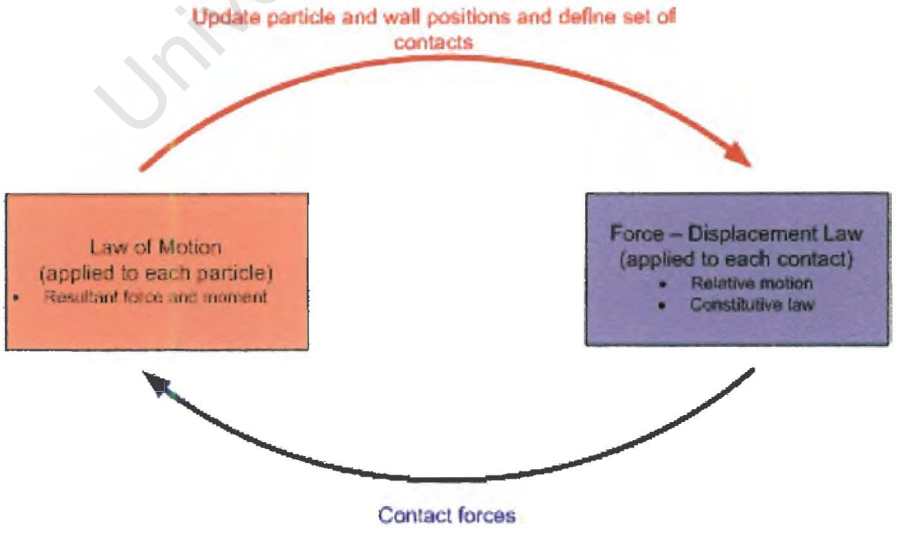

Figure 2-1 – The calculation cycle for the DEM.

Due to the computational expense of DEM, material modelling is best served by utilizing a simplified contact model to describe the interaction between particles. Contact force laws are modelled using a linear spring and dashpot; **Figure 2-2** illustrates the schematic of the model after McBride [12]. This has in the past few years become a commonly used model. The numerical springs simulate the normal and shear contact forces at the contact area. The dashpots dissipate energy for both normal and tangential motion. The magnitude of these contact forces are a function of the numerical spring stiffness and the amount of over-closure at the contact point. Frictional forces are modelled according to the Mohr-Coulomb law using the numerical spring.

The Mohr Coulomb law is based on sliding friction; here the law is applicable when the material experiences shear stress. The Mohr-Coulomb law does not provide any prediction of how the granular material deforms and flows, it rather describes the onset of yielding. The Plastic Potential theory provides the required constitutive equations for describing the deformation of a granular material under frictional motion

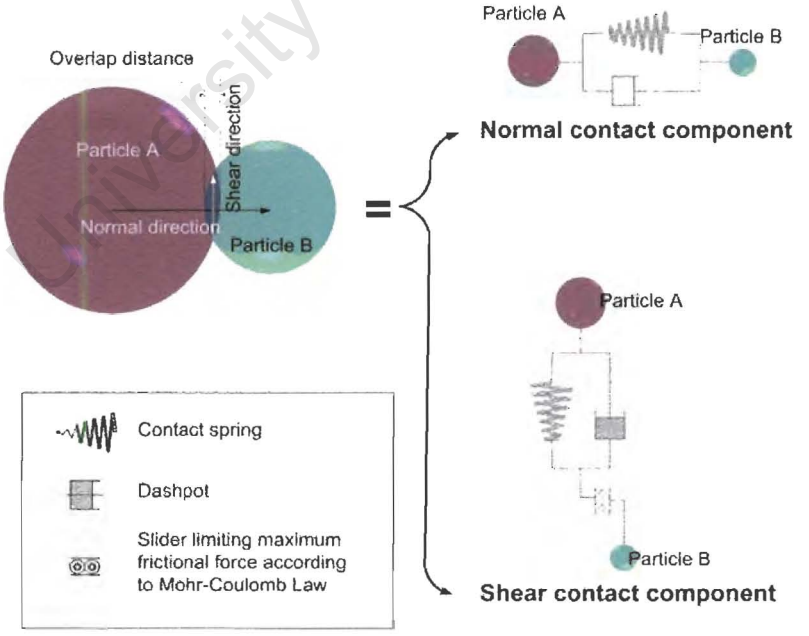

Figure 2-2 – Schematic of the linear spring and dash pot model, McBride [12]

The events at the contact area are denoted by:

$$F_n = K_n d_n - C_n v_n \qquad \textbf{Equation 2-1}$$

$$F_s = F_s^0 + K_s \Delta d_s - C_s v_s + \omega r \qquad \textbf{Equation 2-2}$$

$$F_s = F_n \mu \qquad \textbf{Equation 2-3}$$

Where, F_n and F_s are the normal and shear forces, K_n and K_s are the stiffness of the normal and shear contact spring, d_n relates the total over closure at the contact point to the normal force, μ describes the coefficient of friction at the contact interface, v the relative contact velocity, and C the damping constant. The damping coefficients $C_{n,s}$ are calculated as a fraction of the critical damping constant for a simple mass-spring system as follows:

$$C_{n,s} = \alpha_{n,s} C_c \qquad \textbf{Equation 2-4}$$

and,

$$C_c = 2m\varpi = 2m\sqrt{\frac{K_{n,s}}{m}} \qquad \textbf{Equation 2-5}$$

Therefore, α is the fraction of critical damping (α=0 would mean an undamped system and α=1 would mean a critically damped system), C_c the critical damping constant, m the reduced mass of the contacting pair, and ϖ the angular frequency of the (C_n damped) spring-mass system.

Simplifying the solution by neglecting the gravity term the fraction of critical damping can be related to coefficients of restitution, which is the ratio of velocities pre- and post impact. Therefore $e_{n,t}$ (normal and tangential restitution) using the relationship referenced by Mishra and Rajamani [6] as follows:

$$C_{n,s} = \frac{-2\ln(e_{n,t})\sqrt{K_{n,s}m}}{\sqrt{\ln(e_{n,t})^2 + \pi^2}} \qquad \textbf{Equation 2-6}$$

These restitution values in the critical damping coefficients are often estimated or fitted. Therefore, there is a strong motivation to determine particle interaction parameters that govern the interparticle contact in DEM.

2.2 Charge Motion Dynamics

The application of DEM is widespread, from understating soil mechanics to flow of media in mills; it has been applied to suit various problems in industry. The work presented in this section looks at the history of charge motion studies of rotary tumbling mills and the numerical research that followed.

The earliest study into charge motion dynamics dates back to 1905 when White [13] investigated the motion of the particles in the periphery of the mill which are projected onto the impact point when the gravitational and centrifugal forces are balanced. He assumed that the particles are not subjected to slip when being lifted up in contact with the mill shell or a layer of balls. This led to over prediction, when compared with experimental results, of the equilibrium point at which the balls are projected into flight. Thus excessive cataracting onto the mill shell was predicted. Later Davis [14] formulated a mathematical model for the behaviour of a single particle in a mill and validated the theory with an experimental mill. The compared results showed discrepancy between the observed trajectories of the particles in the experimental mill and the simplified theory. This was however, concluded as accidental and probably caused by low charge filling.

Following the work of Davis and White, Gow *et al* [15] and Fahrenwald and Lee [16] looked at including friction to predict the trajectory of the catarating particles and compared them with ball trajectories in short length laboratory mills. This setup had problems as the cataracting balls interacted with the end walls in the mill, which resulted

in abnormal trajectories. Following this work, McIvor [17] looked at the trajectory of a single particle in the mill and formulated a mathematical model. His model included the effects of various lifter profiles and the coefficient of friction of a single interacting particle which is subjected to free fall. His model is illustrated in **Figure 2-3.** The illustration describes the projection a single particle as a function of the rotational velocity and the lifter angle.

Therefore the projection angle is:

$$\hat{\varphi}_{proj} = \hat{\theta}_{fric} - \hat{\beta} + \arcsin\left[\frac{\omega_0^2 R}{g}\cos\left(\hat{\theta}_{fric} - \hat{\beta}\right)\right] \qquad \textbf{Equation 2-7}$$

where $\hat{\theta}_{fric} = \arctan\mu$

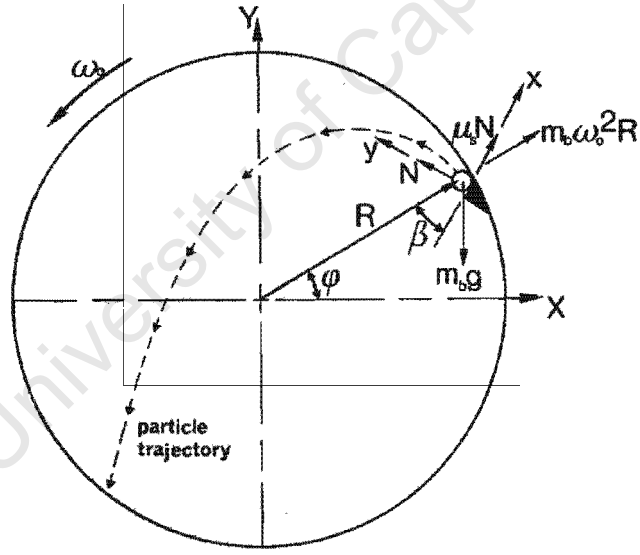

Figure 2-3 – Trajectory of a single particle

The first investigation into *en masse* (whole body / group) behaviour of multiple particles was investigated by Vermeulen and Howat [18]. They looked at surge phenomena in rod mills and their effects on liner wear; they discovered that the fluctuation on charge slippage was due to the oscillating behaviour of the catarating and cascading charge. This effect causes wear between the liner and the periphery of the charge and is driven by the

changes in *en masse* pressure. Following this work Vermeulen and Howat [19] investigated the effect of lifter bars on the *en masse* charge in an experimental mill and concluded that the slip occurs on the inter-facial surface layers.

Tracking the particles in the mills to validate and understand the motion of charge has been a subject of interest. Powell and Nurick [20, 21, 22] devised a novel experiment to track particles in a tumbling mill. In the first part of their work they extended McIvor's theory of the projection of a single particle. They then included an explicit integration of the lifter profile and concluded that the particle is still in contact with the mill shell, even though it has reached the equilibrium point, and that it continues to stay in contact with the shell until it slides off the lifter under gravitational acceleration. Following this work they were able to redefine the various regions of the mill to appropriate terminology.

The terminologies Powell and Nurick [20] developed as result of their experimental work describe the various regions of mill, as illustrated in **Figure 2-4**. The equilibrium surface separates the ascending charge from the descending charge. The Centre of Circulation (CoC) is defined as the point about which all charge in the mill circulates. The shoulder and toe are loosely defined as the points at which charge enters into projectile motion or cascades down the face of the charge, and the point at which the cataracting or cascading charge impacts with the charge or the shell in the lower region of the mill.

The Centre of Mass (CoM) is defined as the point at which the total mass of the charge concentrates at a point. The CoM and CoC do not necessarily lie on the same point, in fact they only coincide when the charge in the mill centrifuges. The angle of repose K as illustrated in **Figure 2-4** is the angle subtended between the charge (CoC) and the vertical at the centre of the mill.

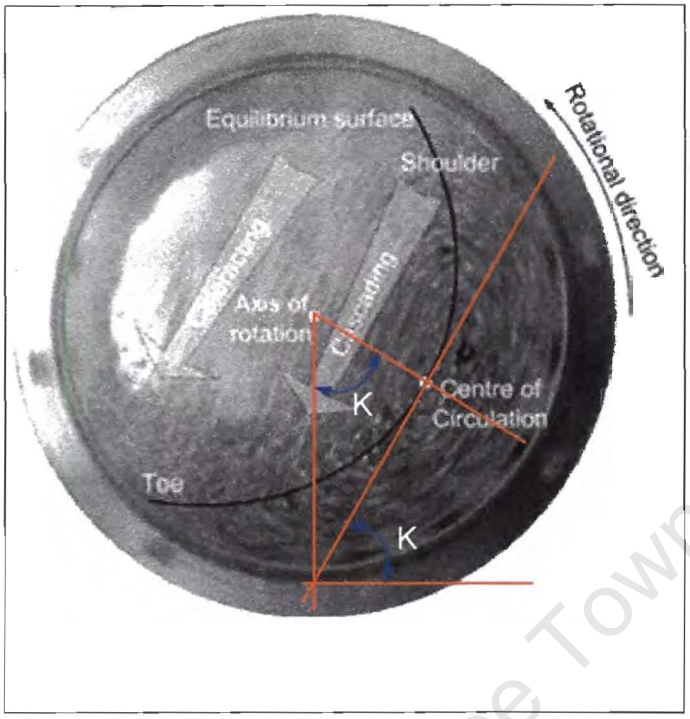

Figure 2-4 – Mill Motion terminology

In the second part of their work, Powell and Nurick [21] tracked particles using an X ray machine. They used a Perspex mill with plastic media and tracked denser particles. Following this work, Govender [23] later employed this technique in his PhD studies to reconstruct the 3 dimensional trajectory data. This novel approach based on Powell's technique employs two X-ray sources to track an individual particle in two planes. The individual images are captured at 50 frames per second and then reconstructed using complex image processing algorithms. The end product is the tracking history of the individual particle for various lifter types, mill speed and mill filling conditions. This tracking history data is pertinent to validating DEM simulations. Comparisons between experimental and DEM trajectory data conducted by Govender *et al* [24] have shown there were good predictions in the overall *en masse* motion but poor predictions in the shoulder and toe regions. This is attributed to the estimations made of the material interaction properties of the simulated particle.

The work conducted in this thesis will provide measured material interaction properties of the tested material which can be used in Govender's particle tracking experiments. The

properties will be used in the contact models in DEM to simulate the experimental measurements made by Govender, and thus better test the DEM simulations.

2.3 Contact Mechanics - The evolution of the collision model

This section of the chapter investigates the kinematics of the collision model. It focuses on the evolution of the theory from classical rigid body analysis to more complex analysis taking into account inelasticity and tangential compliance.

The interaction of particles investigated in the field of rapid granular flow is the basis for understanding the theory of particle interaction. Here, the rigid particles are subjected to successions of collisions. These collisions create random fluctuations in particle velocity, which are responsible for transfer of momentum and impulse. This is directly applicable to charge flow in a tumbling mill.

The description of the observed interaction of two bodies is generally defined by three coefficients. The coefficients, restitution t, n and friction, define the property of the interacting bodies. The Text book definition of the restitution is the measure of elasticity of the collision between two objects and calculated by the ratio of velocities before and after the collision. Friction is defined as the resistive force that prevents two objects from sliding freely against each other and the coefficient of friction is the ratio of tangential force to normal loading during a sliding process.

The observation of a simple of two body interaction can be described with the classical approach to the theory of rigid body analysis which was originally postulated by Wren, Wallis and Newton between 1670 and 1686 [25]. This is based on the conservation of linear momentum and angular momentum. To understand the underlying premise of rigid body impact, Walton [26] assumed the following:

- The contact area of the colliding bodies remains small in comparison with the cross sectional surface area.
- The contact period is brief, and the displacement negligible therefore the contact event can be described as instantaneous.

A stereo-mechanical impact (classical theory of impact) of two bodies can be described by the following deformation history as given in **Figure 2-5**.

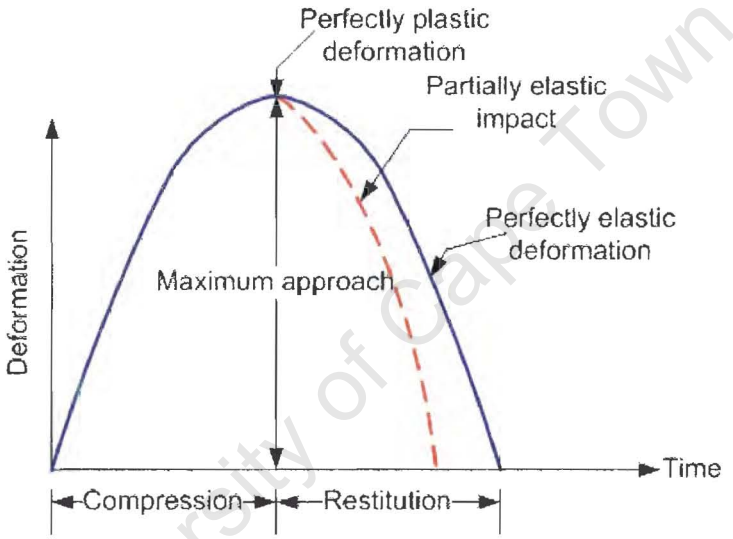

Figure 2-5 - Assumed deformation history – Goldsmith [27]

Goldsmith [27] envisaged that impact consisted of two sub-intervals: compression and restitution. The approach period (compression) extends from the instant of the contact to maximum deformation; this is when kinetic energy is transformed into internal energy of deformation. Restitution follows compression for the period until the instant of separation.

In 1882, Hertz [28] first looked at the possible influence of elastic deformation when studying Newton's optical interference fringes in the gap between two glass lenses. He formulated a theory that is still today used to explain deformation in solid bodies. Interference fringes are an optical effect, which may for example result form narrow gaps

between two optically more dense surfaces. The fringes do not have any effect on the size of the contact area. This is purely mechanical effect. **Figure 2-6** illustrates Hertz's conditions.

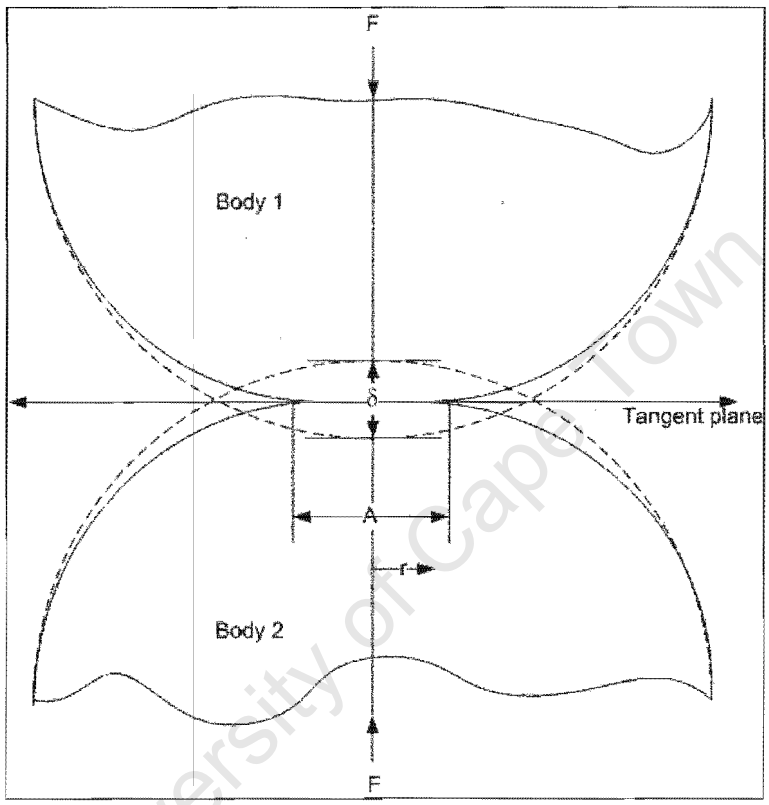

Figure 2-6 – Hertz's theory of contact

Interacting bodies 1 & 2 (in this case spheres) have respective radiuses R_1 & R_2. The non-conforming bodies are compressed by force F in the normal direction. Hertz showed that the contact region spreads to radius *a* or annulus radius of the contact area (where, A = 2*a*) and an elliptical pressure distribution is generated:

$$p(r) = p_0\left(1 - r^2/a^2\right)^{1/2} \qquad \textbf{Equation 2-8}$$

Where *r* is the radial coordinate originating at the centre and p_0 is the pressure at the centre of the contact area.

Maw *et al* [29] argued that although Hertz's contact theory predicts the stress and displacement fields for the duration of the impact, it is quasi static, in the sense that it neglects loss of energy in transmitted waves. They demonstrated that Hertz's theory fails to correctly predict the elastic deformations for oblique impacts and assumes that the contacting surfaces are frictionless. An example of such a case is the projection of the rubber "super ball" with backspin onto a horizontal surface. The ball rebounds backwards contrary to predictions made by Hertz's theory.

The effect of friction was noted by Maw *et al* [29] for the observed oblique collisions where some of the work done in deflecting the bodies is stored as elastic strain energy in the tangential direction. Maw *et al* refer to Mindlin [30] who showed that for the static case of two spheres pressed together under normal loading force, when subjected to tangential loading. They experience slip at the contact area. As the tangential loading increases the contact area reduces until the tangential loading overcomes static friction and the two bodies begin to slip.

Mindlin derived an expression for the tangential compliance vs. displacement for spheres with an elastic Hertzian normal stress distribution in their contact regions, the force is:

$$F = \mu N\left[1-\left(1-\frac{16Ga}{3(2-\nu)\mu N}\delta s\right)^{3/2}\right] \qquad \textbf{Equation 2-9}$$

Where G is the shear modulus, ν is the Poisson ratio, N the normal loading, μ the coefficient of friction, δs the tangential displacement and a is the Hertzian contact radius represented by $a=\left(E^{*}NR\right)^{1/3}$, and $E^{*}=\frac{3}{2}\left(\frac{1-\nu^{2}}{E}\right)$ where E is the Young's Modulus, and, $\delta s=\frac{3(2-\nu)\mu N}{16Ga}$ governs the impact sliding limit up to when the entire contact experiences slip, and the tangential force is just equal to the Coulombic friction μN.

Walton [5] noted that Mindlin's theory does not adequately comply for colliding spheres experiencing rotation, either about their contact normal or when rolling coupled with the tangential sliding.

Taking a closer look at the point of the oblique interaction of the colliding balls, Maw *et al* [29] show that the collisions either exhibit rolling or sliding at direct and oblique impacts. They define these conditions in the following manner:

"When two bodies collide, sliding will generally occur at the start of the contact and then proceed to stick when an opposing frictional force overcomes to reduce sliding velocity. When the sliding velocity reduces to zero, rolling is achieved to end the impact." – Maw *et al* [29]

In developing their theories of impact for oblique collisions, Maw *et al* [29] made the following assumptions:

- The ratio of contact area to the area of the colliding body is small.
- The theory is an extension of Hertz's theory of impact and is quasi-static.
- The coefficients of static and kinetic friction are equal.
- The impacting bodies are elastic.
- Tangential traction is regarded as axisymmetric, where the impact region is surrounded by the slip region. (If the slip region is surrounded by stick region then it would be non-axisymmetric, but Maw *et al* note that for this condition the contributing error is small).

Maw *et al* [29] investigated this theory using circular pucks sliding on a cushion of air and derived the following non dimensional parameters which can be applied to all materials.

The first is;

$$\chi = \frac{(1-\nu)\left(1+(1/K)^2\right)}{2-\nu} \qquad \textbf{Equation 2-10}$$

Where χ is the non dimensional radius of gyration, and ν the Poisson ratio which is the ratio of transverse contraction strain to longitudinal extension strain in the direction of stretching force, and K radius of gyration denoted by, $K = \sqrt{I/MR^2}$ (I is the moment of inertia and M and R are respectively the mass and radius of the impacting body). The second parameter is the non-dimensional angle, which is related to the normal and tangential velocities about the contact point. Therefore the non dimensional angle or parameter is proportional to the ratio of local angle of incidence and the angle of friction.

$$\psi = \frac{2(1-\nu)}{\mu(2-\nu)} \tan\alpha \qquad \textbf{Equation 2-11}$$

Where μ is the coefficient of friction and $\tan\alpha$ is the local angle of incidence of the contact area. ψ_1 is defined as the non-dimensional angle of incidence and ψ_2 is the non-dimensional angle of reflection. Kharaz *et al* [31] describes Maw *et al* analysis in the following manner **Figure 2-7**:

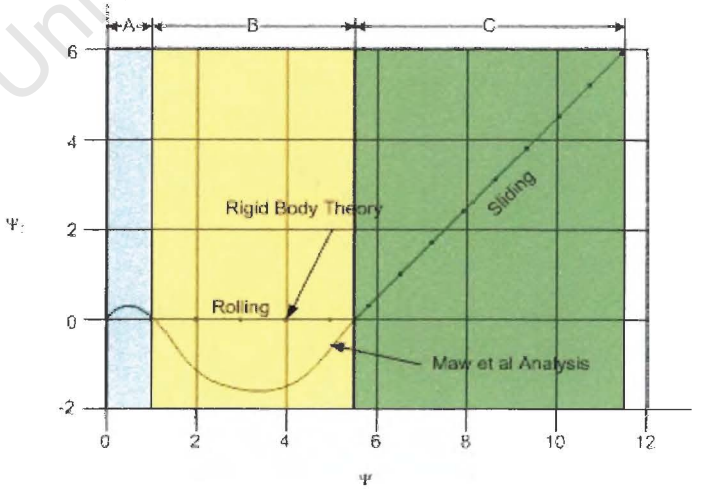

Figure 2-7 – Maw *et al* [29] numerical analysis - ref. Kharaz *et al* [31]

In **Figure 2-7**, the plot of the Maw *et al* [29] analysis (line) is compared with the rigid body model (points). Regions A, B and C depend on the angle of incidence which remains in the defined area and are described as:

- ***Region A***: For $\psi_1 \leq 1$, initial contact begins with a condition of stick as the contact area grows. Then as the contact load decreases the tangential elastic strain energy causes an annulus of micro slip that spreads inward until the whole contact area slides (gross slip).
- ***Region B***: For $1 < \psi_1 < 4\chi - 1$, the intermediate angle of incidence. The impact commences at gross slip then proceeds rapidly to stick at some point during the impact cycle and thereafter returns to gross slip. This gives the regions of stick – slip during collision. Kharaz *et al* [31] refer to the negative angle as a clear indication of the effect the tangential compliance.
- ***Region C***: For $\psi_1 \geq 4\chi - 1$, is defined as the region of gross slip occurring throughout the remainder of impact.

Kharaz *et al* referred to the work of Johnson [32] and Thornton and Yin [33] in which they showed the need to consider the tangential compliance over the contact area. Stronge [34] included an approximation for the effects of the tangential compliance for rigid bodies. He noted that at impact the tangential compliance significantly alters the friction, thus affecting the rebound velocity. However, this is not so for very large incidence angles, where there is continuous sliding in the initial direction.

For oblique impacts the largest tangential force generated by frictional resistance occurs during compression, and this frictional force has no effect on the coefficient of restitution.

Walton [5] extended Maw's analysis and derived a more realistic definition for the inelastic, frictional collision:

- The coefficient of restitution e, in the normal direction. (where $0 \leq e \leq 1$)

- Coefficient of rotational restitution β, for contacts that are not continuously sliding during the collision. (where $-1 \leq \beta \leq 1$, for $\beta = -1$ being perfectly smooth and $\beta = 1$ being perfectly rough and $\beta = 0$ correspond to the rolling contact)
- Coefficient of friction μ, for collisions that are sliding or grazing.

Therefore using the Walton's model, Foerster *et al* [35] derive the following calculations for sphere on sphere collisions, according to the diagram of **Figure 2-8**:

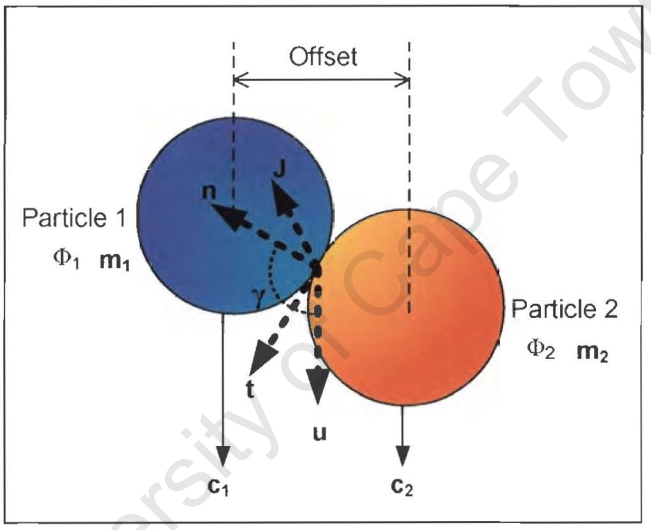

Figure 2-8 – in-flight collisions of two spheres

Notation:

$\boldsymbol{n}$ = normal unit vector perpendicular to the contact point (vector)

$\boldsymbol{u}$ = relative velocity at the contact point (vector)

$\boldsymbol{J}$ = impulse at the point of contact (vector)

$\boldsymbol{t}$ = unit tangent vector about the contact point (vector)

γ = angle of incidence between u and n

$\boldsymbol{C}_1$ and $\mathbf{C}_2$ = translational velocities (vector)

$\boldsymbol{\omega}_1$ and $\boldsymbol{\omega}_2$ = angular velocities (vector)

post collision velocities are denoted by primes

D_1 and D_2 = corresponding diameters of the two balls (scalar)

m_1 and m_2 = masses of each ball (scalar)

I_1 *and* I_2 = Moment of inertia about the centre of a homogeneous sphere

For individual offsets (centre to centre) of the colliding ball (particle 1), the relative velocities of the pre- and post- collisions are calculated for both particles. Foerster *et al* [35] derive pre- and post- velocity components in the following calculations:

The total collisional impulse $\boldsymbol{J}$, this represents the integral of force over the total collisional time.

$$m_1\left(\boldsymbol{C}_1^{'}-\boldsymbol{C}_1\right)=-m_2\left(\boldsymbol{C}_2^{'}-\boldsymbol{C}_2\right)=\boldsymbol{J} \qquad \textbf{Equation 2-12}$$

The post angular velocities can be inferred from the impulse, pre- collision velocities. (In this case $\boldsymbol{\omega}_1$ and $\boldsymbol{\omega}_2 = 0$, no spin prior to collision for the pre-collision angular velocities)

$$\left(\frac{2I_1}{D_1}\right)\left(\boldsymbol{\omega}_1^{'}-\boldsymbol{\omega}_1\right)=\left(\frac{2I_2}{D_2}\right)\left(\boldsymbol{\omega}_2^{'}-\boldsymbol{\omega}_2\right)=-\boldsymbol{n}\times\boldsymbol{J} \qquad \textbf{Equation 2-13}$$

Where $I_{sphere}=\frac{mD^2}{10}$ for homogenous spheres

Pre- Relative velocity about the contact point is defined as.

$$\boldsymbol{u}=\left(\boldsymbol{C}_1-\boldsymbol{C}_2\right)-\left[\left(\frac{D_1}{2}\boldsymbol{\omega}_1+\frac{D_2}{2}\boldsymbol{\omega}_2\right)\times\boldsymbol{n}\right]=\boldsymbol{C}_1-\boldsymbol{C}_2 \qquad \textbf{Equation 2-14}$$

And post- relative velocity about the contact point is:

$$\boldsymbol{u}^{'}=\boldsymbol{u}_1^{'}-\boldsymbol{u}_2^{'} \qquad \textbf{Equation 2-15}$$

This can be simplified as:

$$\boldsymbol{u}' = \left(\boldsymbol{C}_1' - \boldsymbol{C}_2'\right) - \left[\left(D_1\boldsymbol{\omega}_1' + D_2\boldsymbol{\omega}_2'\right) \times \frac{\boldsymbol{n}}{2}\right] \qquad \textbf{Equation 2-16}$$

where,

$$\boldsymbol{u}_1' = \boldsymbol{C}_1' - \left(\frac{D_1}{2}\boldsymbol{n}\right) \times \boldsymbol{\omega}_1' \qquad \textbf{Equation 2-17}$$

$$\boldsymbol{u}_2' = \boldsymbol{C}_2' - \left(\frac{D_2}{2}\boldsymbol{n}\right) \times \boldsymbol{\omega}_2' \qquad \textbf{Equation 2-18}$$

The angular velocity terms in **Equations 2-17** and **Equations 2-18** above may be expressed as pre- and post- collisional translational velocities using the conservation of angular momentum. The angular momentum for a sphere about a contact point on its surface ***H*** is illustrated in **Figure 2-9.**

$$\boldsymbol{H} = I\boldsymbol{\omega} + \boldsymbol{r} \times m\boldsymbol{v} \qquad \textbf{Equation 2-19}$$

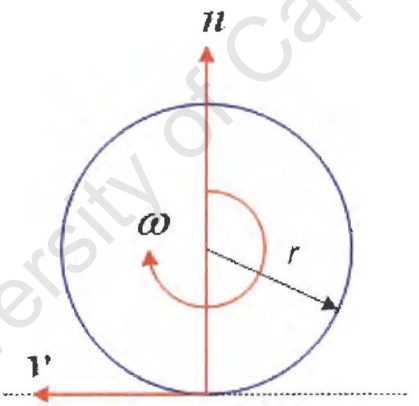

Figure 2-9 – Angular momentum for sphere

Therefore, the conservation of angular momentum for the two particle collision system may be written as:

$$I_{sphere}\boldsymbol{\omega}_1 + \frac{D_1}{2}\boldsymbol{n} \times m_1\boldsymbol{C}_1 = I_{sphere}\boldsymbol{\omega}_1' + \frac{D_1}{2}\boldsymbol{n} \times m_1\boldsymbol{C}_1' \qquad \textbf{Equation 2-20}$$

$$I_{sphere}\boldsymbol{\omega}_2 + \frac{D_2}{2}\boldsymbol{n} \times m_2\boldsymbol{C}_2 = I_{sphere}\boldsymbol{\omega}_2' + \frac{D_2}{2}\boldsymbol{n} \times m_2\boldsymbol{C}_2' \qquad \textbf{Equation 2-21}$$

Given that pre- collision angular velocities are zero and impulse $\boldsymbol{J}$ which is equated in **Equation 2-12**, the conservation of angular momentum can be simplified to:

$$\left(D_1\boldsymbol{\omega}_1^{'}+D_2\boldsymbol{\omega}_2^{'}\right)=-\frac{1}{2}\left(\frac{D_1^2}{I_{sphere}}+\frac{D_2^2}{I_{sphere}}\right)\boldsymbol{n}\times\boldsymbol{J} \qquad \textbf{Equation 2-22}$$

Substituting into **Equation 2-16,** the relative post- collisional velocities:

$$\boldsymbol{u}^{'}=\left(\boldsymbol{C}_1^{'}-\boldsymbol{C}_2^{'}\right)-\frac{1}{4}\left(\frac{D_1^2}{I_{sphere}}+\frac{D_2^2}{I_{sphere}}\right)\left[\left(\boldsymbol{n}\cdot\boldsymbol{J}\right)\boldsymbol{n}-\boldsymbol{J}\right] \qquad \textbf{Equation 2-23}$$

Therefore the relative post- collisional velocity is, where $m^{*}=\frac{1}{m_1^{-1}+m_2^{-1}}$ the reduced mass about the contact point:

$$\boldsymbol{u}^{'}=\left(\boldsymbol{C}_1^{'}-\boldsymbol{C}_2^{'}\right)+\left[\frac{5}{2}m^{*}\boldsymbol{J}\right]-\left[\frac{5}{2}m^{*}\left(\boldsymbol{n}\cdot\boldsymbol{J}\right)\boldsymbol{n}\right] \qquad \textbf{Equation 2-24}$$

Simplifying, Relative post- collisional velocity can be related as:

$$\boldsymbol{u}^{'}=\boldsymbol{u}+\left[\left(\frac{7}{2m^{*}}\right)\boldsymbol{J}\right]-\left[\left(\frac{5}{2m^{*}}\right)\boldsymbol{n}\left(\boldsymbol{J}\cdot\boldsymbol{n}\right)\right] \qquad \textbf{Equation 2-25}$$

The normal coefficient of restitution e is defined as:

$$e=-\frac{\boldsymbol{n}\cdot\boldsymbol{u}^{'}}{\boldsymbol{n}\cdot\boldsymbol{u}} \qquad \textbf{Equation 2-26}$$

Where $0\leq e\leq 1$

For collisions that involve sliding, the tangential and the normal components of the impulse are related by the coefficient of friction μ.

$$\mu = \frac{|\boldsymbol{n} \times \boldsymbol{J}|}{(\boldsymbol{n} \cdot \boldsymbol{J})} \qquad \textbf{Equation 2-27}$$

Where $\mu \geq 0$

The angle of incidence between u and n characterizes the impact geometry,

$$\cot \gamma \equiv \frac{\boldsymbol{u} \cdot \boldsymbol{n}}{|\boldsymbol{u} \times \boldsymbol{n}|} \qquad \textbf{Equation 2-28}$$

Impacts occur when $\boldsymbol{u} \cdot \boldsymbol{n} \leq 0$, therefore this angle lies between $\pi / 2 \leq \gamma \leq \pi$.

$$\boldsymbol{n} \times \boldsymbol{u}' = -\beta(\boldsymbol{n} \times \boldsymbol{u}) \qquad \textbf{Equation 2-29}$$

Where β is the coefficient of tangential restitution, as defined by Foerster *et al* [35], about the contact point. The range for the tangential restitution is $0 \leq \beta \leq 1$.. When γ exceeds the limiting angle γ_0, sliding no longer exists.

$$\gamma_0 = \pi - \arctan \frac{7(1+e)\mu}{2(1+\beta)} \qquad \textbf{Equation 2-30}$$

Using Maw *et al* [29] analysis, a plot of non dimensional angle of incidence Ψ_1 vs. non dimensional angle of reflection Ψ_2 of the contact point is plotted.

$$\psi_1 \equiv -\frac{(\boldsymbol{u} \cdot \boldsymbol{t})}{(\boldsymbol{u} \cdot \boldsymbol{n})} \qquad \textbf{Equation 2-31}$$

and

$$\psi_2 \equiv -\frac{\left(\boldsymbol{u}^{'} \cdot \boldsymbol{t}\right)}{\left(\boldsymbol{u} \cdot \boldsymbol{n}\right)} \qquad \textbf{Equation 2-32}$$

In the plot of Ψ_1 vs. Ψ_2, two slopes help distinguish the sticking and sliding regions.

For sticking conditions:

$$\psi_2 = -\beta\psi_1 \qquad \textbf{Equation 2-33}$$

and for sliding:

$$\psi_2 = \psi_1 - \left[\left(\frac{7}{2}(1+e)\mu\right)\mathrm{sgn}\left(\boldsymbol{u} \cdot \boldsymbol{t}\right)\right] \qquad \textbf{Equation 2-34}$$

From a plot of Ψ_1 vs. Ψ_2, the slope of **Equation 2 - 32** and the intercept of **Equation 2-33**, yield values for β, e and μ.

For collisions that involve particle on surface, the calculations follow the same as above but the second particle velocity is treated as zero having infinite mass and radius.

It is concluded that the theory Maw *et al* [29] using non–dimensional analysis of collision and the derivations derived by Foerster *et al* [35] is the most appropriate available relationship for calculating the material impact parameters required for DEM modelling.

2.4 Experimental Investigation

This section looks at the experimental techniques used to formulate the rigid body theory. From the Hertzian contact model to the investigation of the in-flight collisions of the two spheres, the section reviews in detail the procedures that evaluate the theory.

To define the kinematics of rigid body theory experimental investigations are conducted. Looking at the classic theory of impact to define the coefficients of restitution and friction simple experiments determine the material interaction properties.

For a ball bouncing on a table, normal restitution is defined as:

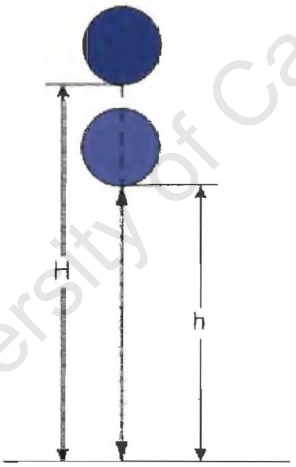

Figure 2-10 – Bouncing ball experiment

$$e = \sqrt{\frac{h}{H}} \qquad \textbf{Equation 2-35}$$

Where, H is the initial drop height and h is the maximum height after collision. For the collisions of two balls,

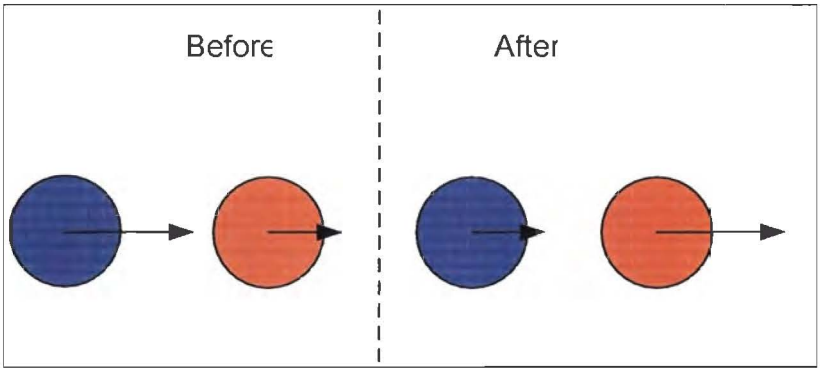

Figure 2-11 – Billiard ball collision

$$e_n = \frac{v_{after}^{blue} - v_{after}^{red}}{v_{before}^{red} - v_{before}^{blue}}$$ **Equation 2-36**

This only applies for collisions that are head-on and e_n is the normal coefficient of restitution.

For friction, a mass sliding on an inclined plane provides the Friction, illustrated in **Figure 2-12.**

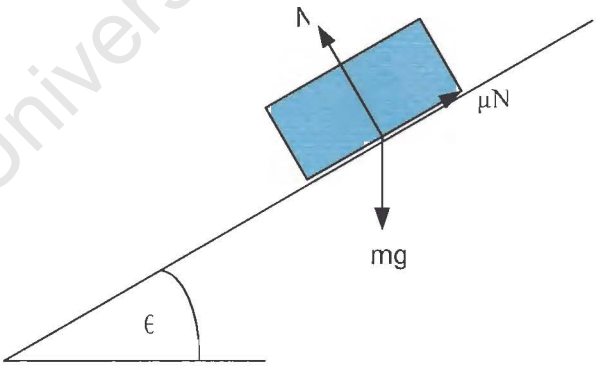

Figure 2-12 - Mass sliding on the surface

$$\mu = \frac{Force_{frictional}}{Force_{normal}}$$ **Equation 2-37**

Looking at a simple example of the oblique interaction of the billiard balls, the collision of the two balls can be described in an idealised case that follows the Newtonian Laws. This analogy however does not take into consideration the local elastic deformation and spin.

2.4.1 Experiments to measure particle interaction

In this section three pertinent experiments are summarised. Key experimental techniques and procedures of these experiments are noted.

2.4.1.1 Maw *et al [29]* Experimental set-up

Maw's experimental setup was based on the observations of sliding pucks on a cushion of air. A summary of their experiments follows:

- Disk shaped puck was sliced off a sphere; therefore the contacting surfaces between two pucks were not flat, but a point.
- The pucks were levitated on a jets of air maintained at equilibrium pressure. This provided a virtually frictionless surface.
- A heavy launching device, a pendulum was used to launch the pucks and maintain repeatability.
- The experiments were conducted in a darkroom, and the impacts of the pucks on a similar static material were photographically recorded under stroboscopic lighting, **Figure 2-13**.
- The surfaces of the pucks were sprayed matt black and reflective tape was placed on them so as to highlight the position and thereby measure the relative velocities pre- and post- collision.
- Maw *et al* pay considerable attention to the selection of their materials. For their experiment, Maw uses three different materials to test the theory. It was

noted by them that the selection and the forging of material considerably affected their results, especially with the rubber puck.

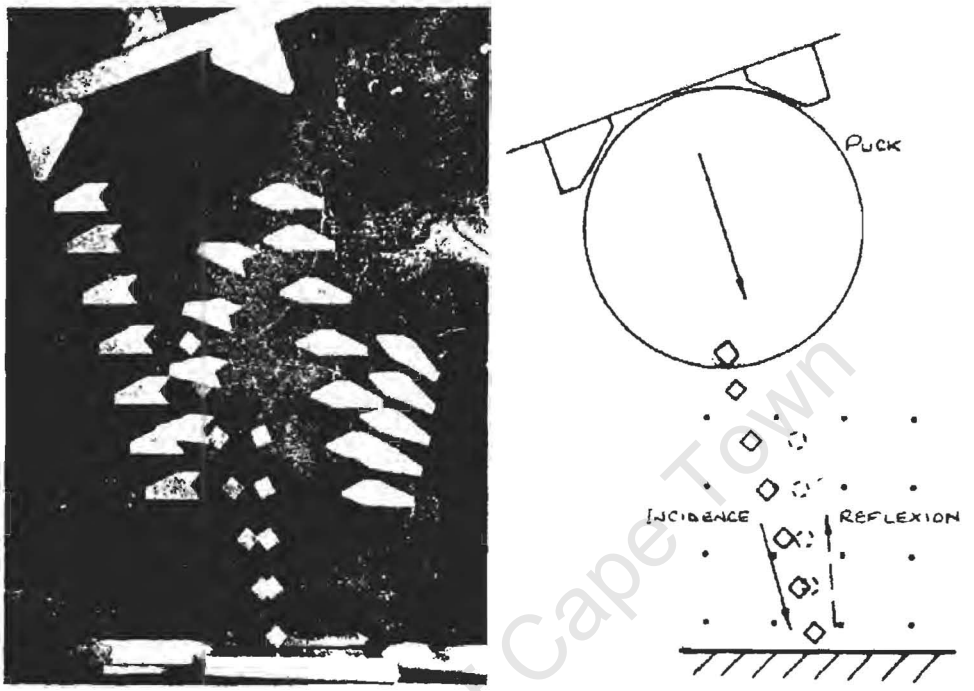

Figure 2-13 – Photographic and schematic image of the colliding puck

2.4.1.2 Kharaz *et al* [31] Experimental set-up

Kharaz et al reported a detailed experimental setup for the rebound behaviour of spheres. They used glass spheres striking an aluminium anvil to analyse the rebound behaviour. The authors reported using Ning's [36] scalar analysis of the rigid body model rather than the vector model proposed by Walton [5]. Their experimental setup is as follows:

- The particles are held in a vacuum nozzle above the anvil, so as to release the particle without initial spin before collision.
- Optical-fibre triggering device was used to switch-on the strobe and camera when the particle is in range of the field of view of the camera.

- The mechanical structure, camera, the optical trigger and the strobe are mounted on optical benches so as to maintain their alignment. (Lasers are used to align the benches)
- The strobe used in the experiment is used to illuminate the impact event very close to the image axis. A uniform beam was maintained using electronic control and the strobe is triggered only for those flashes which are required in the image.
- The collision event was captured using a digital camera with a resolution of 768 × 484 pixels. The camera was set to single frame mode and the exposure time was set to 200 milliseconds.
- The captured images are processed using commercial software, Global Lab Image. Circles are superimposed over the particle images to identify the centre of area.
- A calibration map was utilised to obtain stationary images of the particles and an overall positional accuracy of ± 0.1 pixels for a particle and ± 0.05° for the orientation of the anvil was noted.

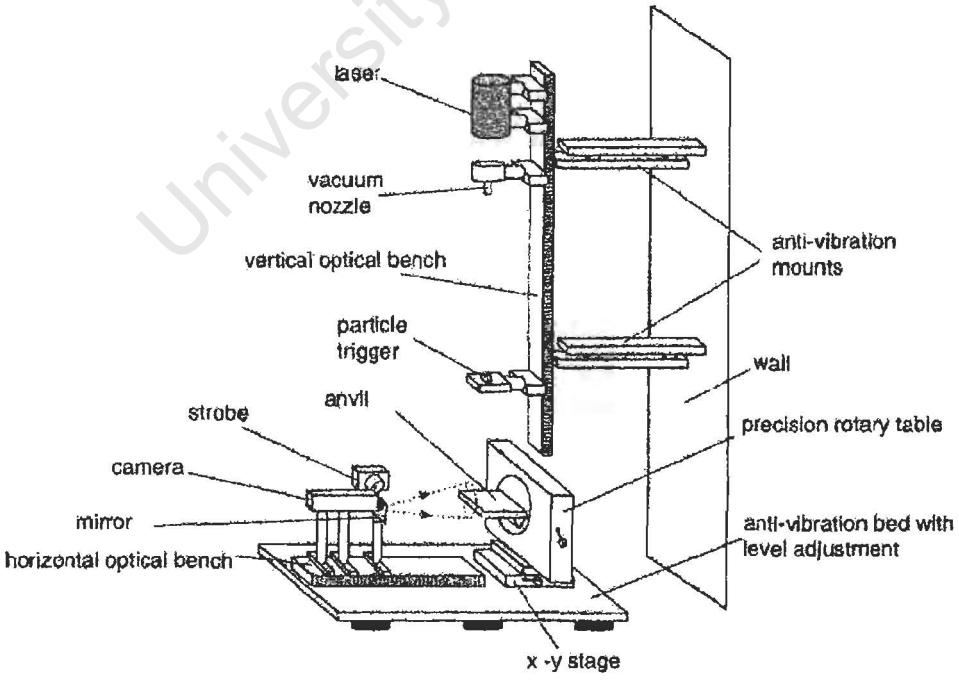

Figure 2-14 – Schematic of Kharaz et al experimental setup

Kharaz *et al* motivated the importance of high stability of the experimental rig and the precise control of the strobe pulses that allows virtually identical images of the repeated drop tests. Their setup is illustrated in **Figure 2-14**.

2.4.1.3 Foerster *et al* [35] Experimental set-up

For the collision of two spheres Foerster *et al* [35] investigated a study of the in-flight binary collision of two spheres. Foerster's experimental setup is based on Walton's [4] model. Their experimental setup is as follows, and an illustration of Foerster's experimental setup is shown in **Figure 2-15**.

- The main features of the experiment consist of two sections: the drop valve and the rapid retracting mechanism each at 539mm and 279mm from the landing stage respectively.
- The investigated spheres are released without spin prior to collision, to allow for the solution to be tractable when using rigid body analysis.
- The spheres ranging in size from 3-6mm diameter, they are suspended by orifices with a 380 micrometers diameter. The surface finish of the orifice is milled in-order to maintain consistency of the drop.
- The release of the spheres are controlled by pneumatic solenoids
- The temporal reproducibility of the release mechanism is checked by recording the impacts on the landing stage.
- Acetate spheres are imprinted with small black dots to establish if the spheres fall with no spin prior to collision.
- Electronic timing circuits coordinate the successive release of both particles, retraction of release mechanism, and triggering of the camera.
- Response times of the release mechanism and opening of the shutter of the camera are calculated so that the particles collide near the centre of the camera's field of view.

- The field of view is made high enough to capture at least two images of spheres before and after collision.
- The field of view is illuminated by two strobes positioned at 45° to either side of the camera, and they are triggered simultaneously at 200Hz using a function generator.
- To check if the particles collide in the "collision plane" which is perpendicular to the field of view of the camera, the impacts on the landing stage are recorded using a carbon paper. The camera is then repositioned to the new collisional plane.
- The materials tested by Foerster *et al* [35] include soda lime glass and cellulose acetate spheres. They also tested particle on wall effects and calculated the corresponding material interaction properties. The results they got are within the ranges $0.29ms^{-1}$ and $1.2ms^{-1}$ for relative normal impact velocities and $0.06ms^{-1}$ and $0.86ms^{-1}$ for relative tangential velocities.
- To calculate the material interaction values of the normal and tangential coefficient of restitution and friction from the measured data, firstly the authors removed outliers from the data which are not within the acceptable range then they used the standard t – test to calculate the deviations. The calculated values have acceptable standard deviation values.
- Because of the complexity of the binary collision experiment, the authors mention that scatter in the data is unavoidable and the only way to make sense of the data is to remove outliers which are not within the acceptable range.

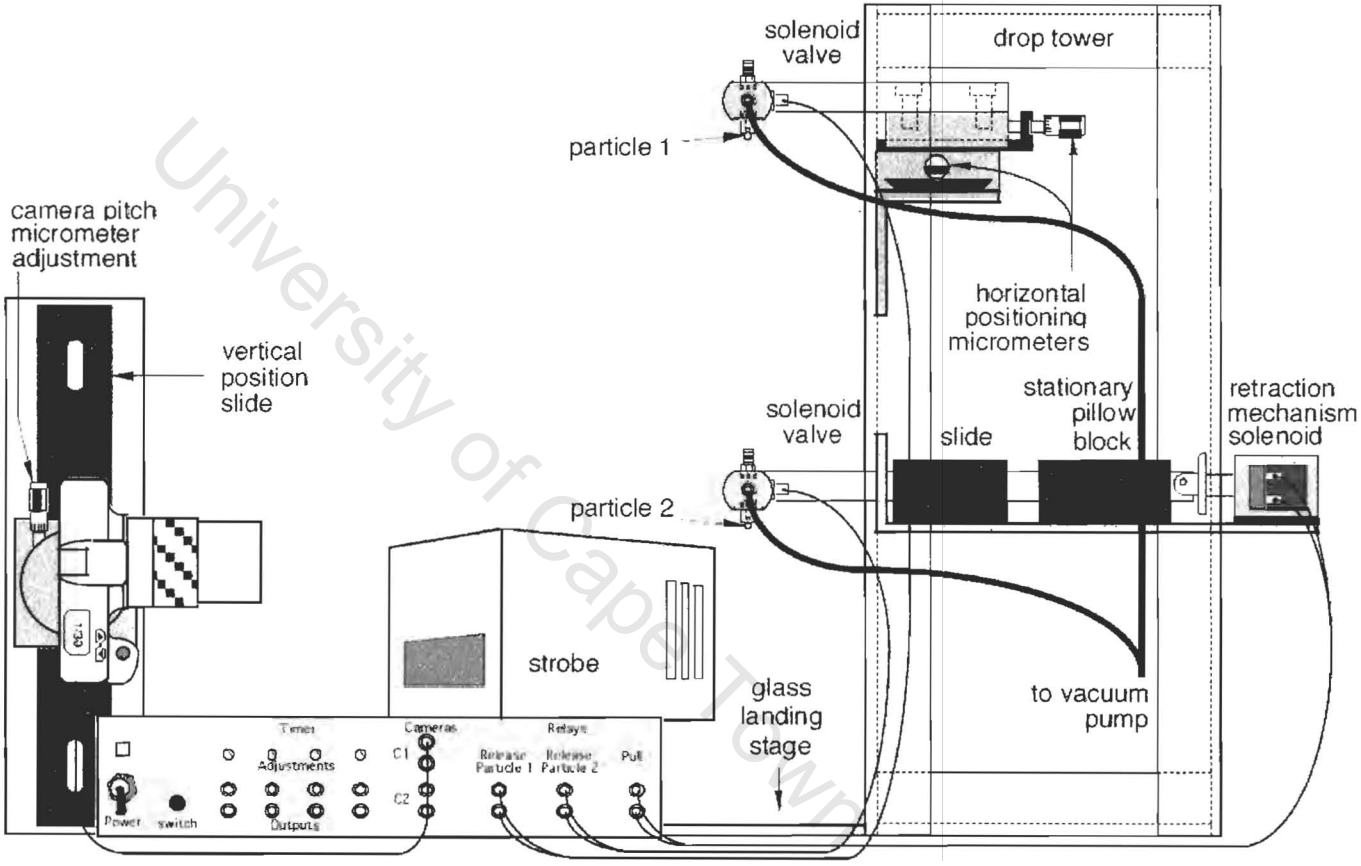

Figure 2-15 – Binary collision experimental setup, Foerster *et al* [35]

2.4.2 Application to this study

The experimental techniques presented in **Section 2.4.1** have defined procedures to measure the material interaction properties. For the application of this work, the experimental procedures of Foerster *et al* [35] and Kharaz *et al* [31] will be used. These experimental techniques have demonstrated a useful methodology to capture and measure the colliding spherical materials photographically. Foerster *et al* [35] technique, of two particle collision experiments is most appropriate to this application of study. To capture the collision of the two particles, Foerster *et al* [35] used a digital camera set at open frame mode. The collision event was illuminated using stroboscopic light in a dark room. The sequence of drops of the colliding particles was carefully controlled by electronic timing circuitry. These contributions made by Foerster *et al* [35] will be used to define the experimental design and construction of the two particle collision experiment.

2.5 Discussion

The literature presented here encompasses a new form of analysis of the rigid body theory for the application of Numerical simulations. The numerical tool such as the Discrete Element Method used to simulate charge motion in mills provides suitable approximations for *en masse* behaviour. Understanding the charge the motion in mills has been a subject of interest for comminuters all over the world. The trend, in comminution research is shifting towards energy efficient devices. Therefore, DEM has tremendous application in this area. In DEM, the individual collisions are described by contact force laws and force displacement laws, McBride [12]. If DEM is going to be used as a practical tool to model charge movement in AG and SAG mills, suitable contact models should be developed

Commercial DEM codes such as Particle Flow Code (PFC) distributed by Itasca use the viscous damping model. This model requires three material properties to define the

interaction between particles: coefficient of normal restitution, coefficient of shear or tangential restitution, and friction.

The technique developed by Maw *et al* [29] and later used by Foerster *et al* [35] and Kharaz *et al* [31] in their experiments have shown that it is possible to measure key material interaction properties. They have also shown that it is possible to distinguish regions of interactions such as sticking and sliding impacts.

The work presented in this thesis incorporates combination of experimental techniques of Foerster *el al* [35] and Kharaz *et al* [31] with modifications to measure material interaction properties and apply them in DEM codes to test its applicability.

Chapter 3

Hypothesis

To derive an adequate hypothesis the motivation behind this project is clarified. The aim of this project is to set up a suitable experiment to measure material interaction properties which can then be utilised in DEM.

3.1 Hypothesis Statement

From the discussions presented in the literature review, the following hypothesis was developed.

The so called material properties attributed to the parameters used in DEM are not solely properties of the materials but rather material interaction properties that are also dependent on the conditions of the impact.

Applying measured material interaction properties in DEM rather than fitting or estimating them, in the contact models that govern the inter-particle contact – force laws, can contribute to the overall reliability and accuracy in predicting the motion of grinding media in rotary mills.

This is because in DEM fitting a number of parameters to give the best correlation with one simulation does not imply that they are correct. Simulations with new conditions are likely to give incorrect predictions and these parameters therefore don't represent the overall system.

3.2 Objectives

The objectives are designed to address the hypothesis. The list of the high-level objectives is given here:

- Establish an experiment that measures the material interaction properties such as coefficients of normal and tangential restitution, and friction.
- Apply these properties to the various numerical models in DEM that define the contact properties for simulation.
- Test the DEM predictions against the experimental data.

It is proposed that the technique developed by Forester *et al* [35] is the most appropriate experimental procedure for the application of grinding media modelling, as the majority of the interactions within mill exhibit inter-particle collisions. To measure these inter-particle interactions, binary collisions of two particles in free-fall can provide an unambiguous measure of the material interaction properties.

The specific tasks of the work that are required in order to address the objectives are:

- Duplicate the experiment of Foerster *et al* [35] and make refinements.
- Ensure that accurate, reproducible data can be obtained.
- Establish whether the material interaction properties are dependent upon the impact conditions of the particles – such as velocity.
- The drop heights of the experiment must be varied in order to acquire a range of impact velocities.
- To check the general applicability of the technique, a range of materials should be tested, and the values tested in DEM predictions.
- The material interaction values that are obtained should be used in a DEM code to test the predictions of different contact models used in the DEM. This will be done by comparing DEM predictions against the experimental binary collision data.

Chapter 4

The Design

This chapter examines the design of the two particle in-flight collision experiment conducted for this project. The basic design duplicates that of the Foerster *et al* [35], *although, as will be seen, several modifications are introduced to correct some of the errors inherent in their experiment.*

4.1 Design Specification

The experimental procedure and setup have clear requirements, based on the original experimental setup by Foerster *et al* [35] and Kharaz *et al* [31], as listed below:

- The primary objective is to provide mid-air collisions of two particles, where particle 1 is dropped first then particle 2 is released from a quick release mechanism to allow a mid-air collision.
- The experiment is designed to carry out a binary collision of similar and dissimilar materials. The materials to be tested range from plastic, steel, ceramic, and smoothed stones, which are materials used in the laboratory validation experiment mills.
- The types of collisions should range from direct to sliding impacts. Therefore adjusting the impact offset is important in the experiment.
- The principle feature of colliding two particles is that they should be dropped without any prior spin to collision.
- The experimental rig should vary the drop height and incorporate particle collisions on various material surfaces.
- The colliding particles are to be captured as photographic images for analysis of their relative velocities.

4.2 The Design

The in-flight drop tester comprises two sections: the Centering block and the rapid release mechanism. These sections are supported by a solid steel structure which is mounted on the wall. The structure is designed to allow variations in the drop height of the colliding particles. Each section suspends a particle mounted on an unbeveled orifice of 1.5 mm diameter which is subjected to partial vacuum. The pneumatic system, supplied by Festo, comprises a piston, two way valves, solenoids and vacuum nozzles. The rapid release of the partial vacuum allows the particles to be released without spin.

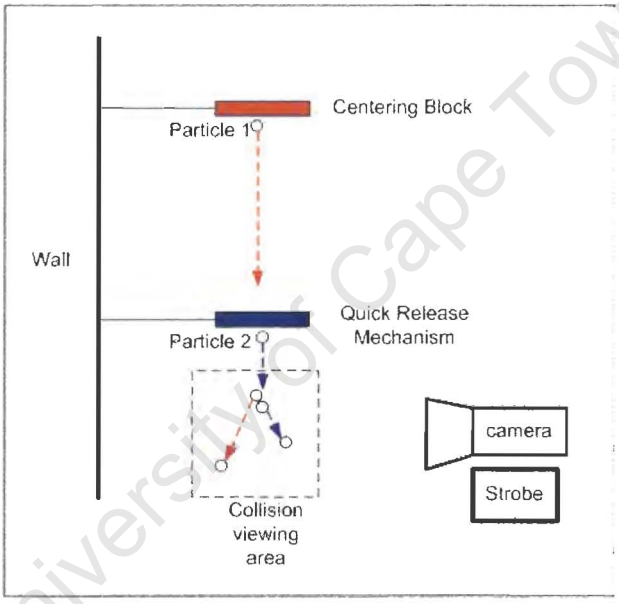

Figure 4-1 – Experimental Setup

A Schematic of the basic operation and specification of the experiment is illustrated in **Figure 4-1**. Based on the design specifications, the experiment can be broken down into the following sections, Centering block, Release Mechanism, height support mountings, camera support, and pneumatics

4.2.1 The Centering Block

The basic operation of the Centering block as illustrated in **Figure 4-2** is to locate the X and Y positions of the colliding particle. Particle 1 is suspended in the nozzle hole by vacuum. The micrometers adjust the minute increments of offsets. The initial design incorporated two manually adjusted micrometers, but trial runs of the experiment have shown that finer adjustment to 0.005 mm is required to acquire a good set of results; therefore one of the manually operated micrometers was replaced with a digital micrometer with a maximum offset distance of 50mm.

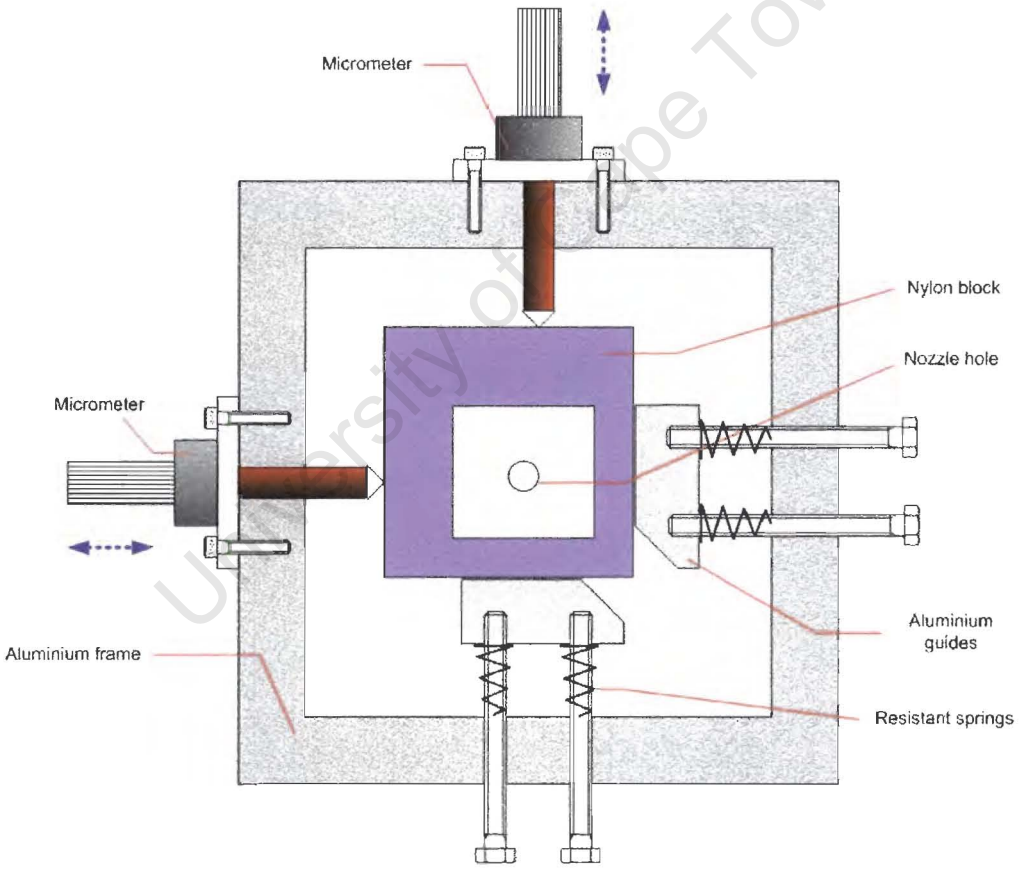

Figure 4-2 – Schematic of the Centering block

4.2.2 The Release Mechanism

The basic operation of the quick release mechanism as illustrated in **Figure 4-3** is to release particle 2 and retract before particle 1 has reached it. Particle 2 is suspended in the nozzle hole by vacuum. The piston shown in the figure acts as the retraction mechanism. The pneumatically operated piston was chosen as the ideal mechanism because the whole experimental operation can be controlled by pneumatic solenoids for very rapid action.

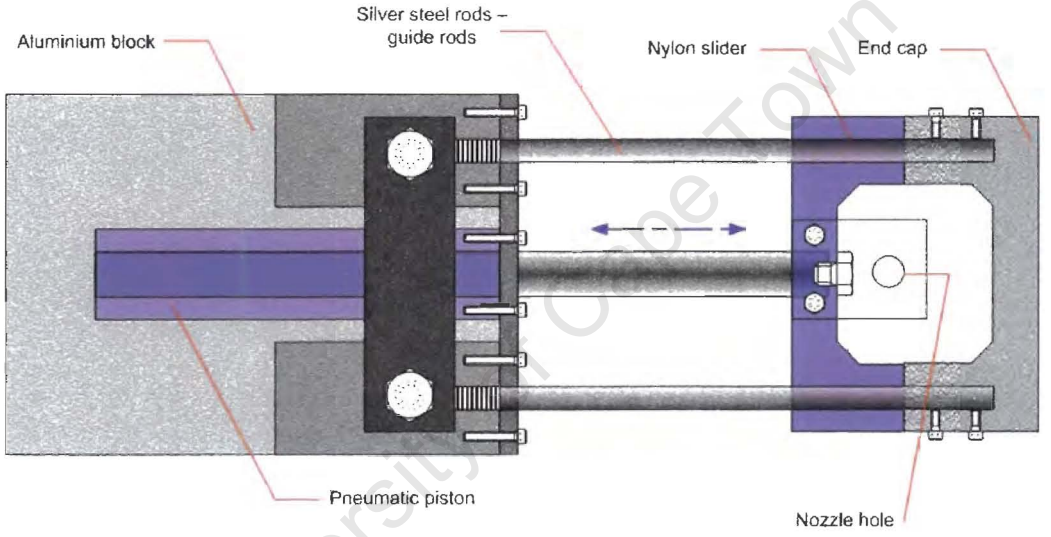

Figure 4-3 – Schematic of Quick Release Mechanism

4.2.3 Height Support and Mountings

One of the specifications of the experiment is to change the drop heights of the incident ball (particle 1). Initial trial runs were conducted to assess the type of structure required to support the Centering block and release mechanism. **Figure 4-4** illustrates the L-Bar which supports the two sections. The L-Bar supports were constructed from steel and bolted onto the wall using Rawl bolts.

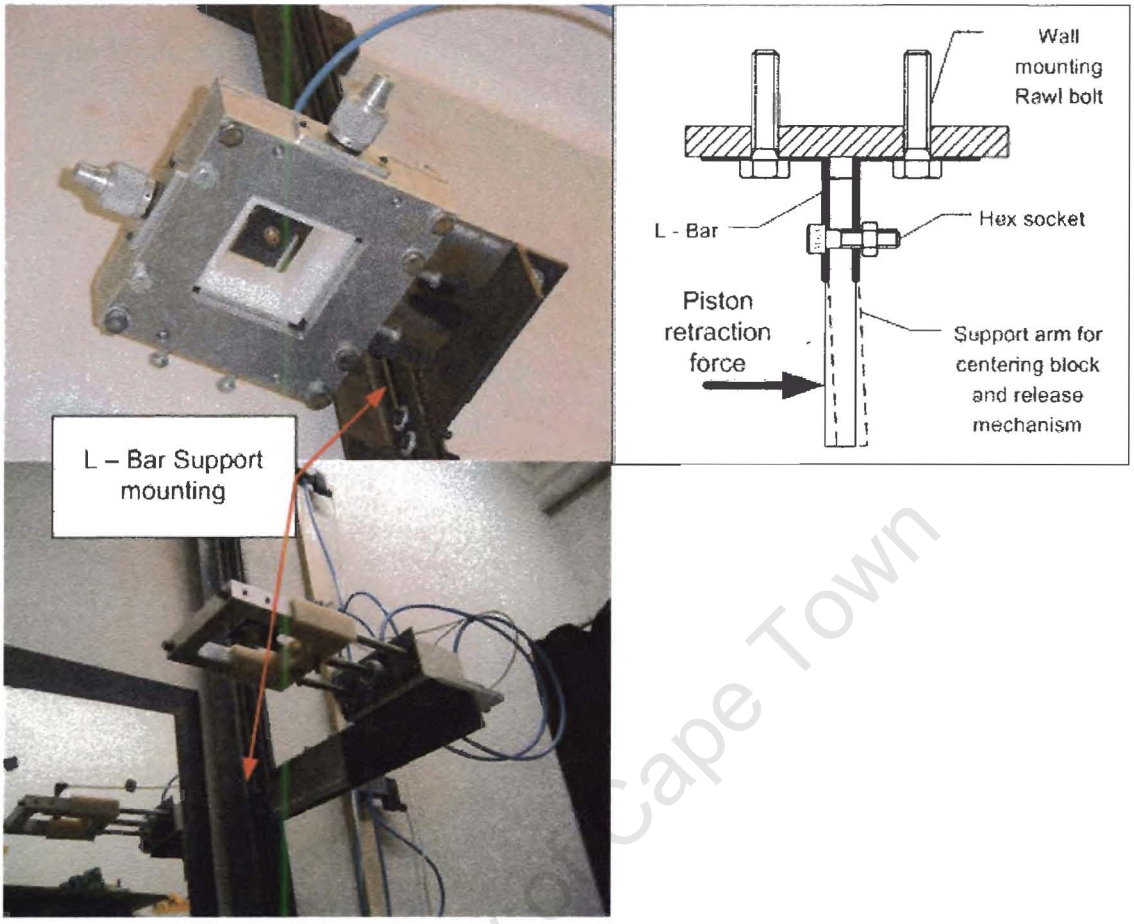

Figure 4-4 – Preliminary design of wall mount support, Centering block (top) and release mechanism (bottom), L – bar mounting (right)

This L-Bar design was later rejected because there were significant errors in the collisional data. It was noticed that the L-Bars were subjected to torsion by the retracting piston. This force twisted the L-Bar supports as shown in **Figure 4-4**.

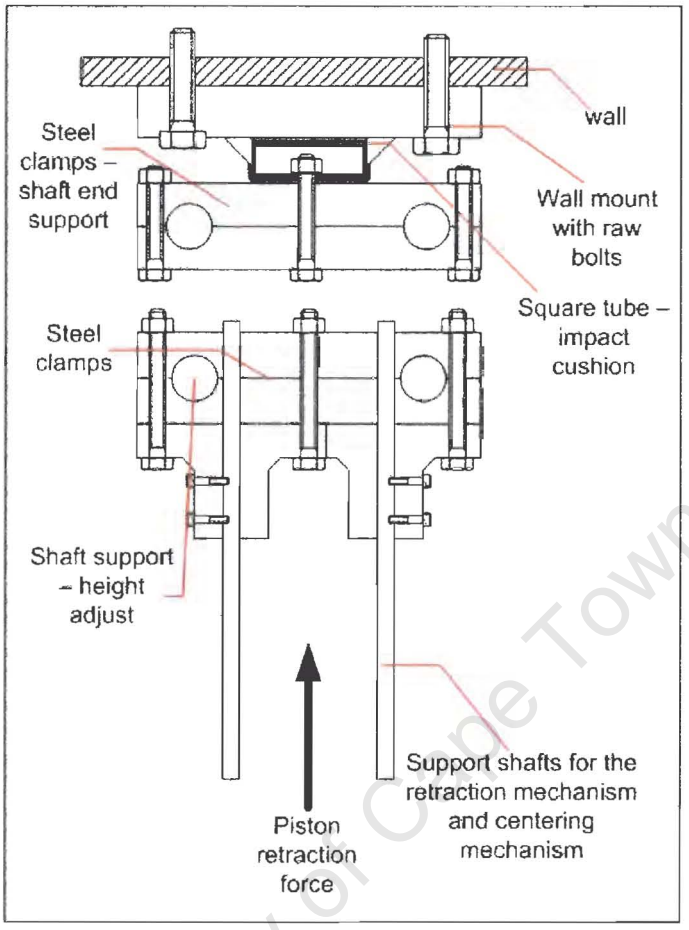

Figure 4-5 – Improved support mounting

In the Foerster *et al* [35] experiment anti-vibration mountings were incorporated in the design. Following their lead, an improved design for the support was devised as shown in **Figure 4-5**. This new design overcomes issues pertaining to retraction force and vibrations along whole support mountings. To resolve any unwanted vibrations, the whole support is made from solid steel and the square tubing, shown in yellow in **Figure 4-7**, welded to the wall mountings to absorb any stray vibrations carried along the steel shafts. The new design is illustrated in **Figure 4-6**.

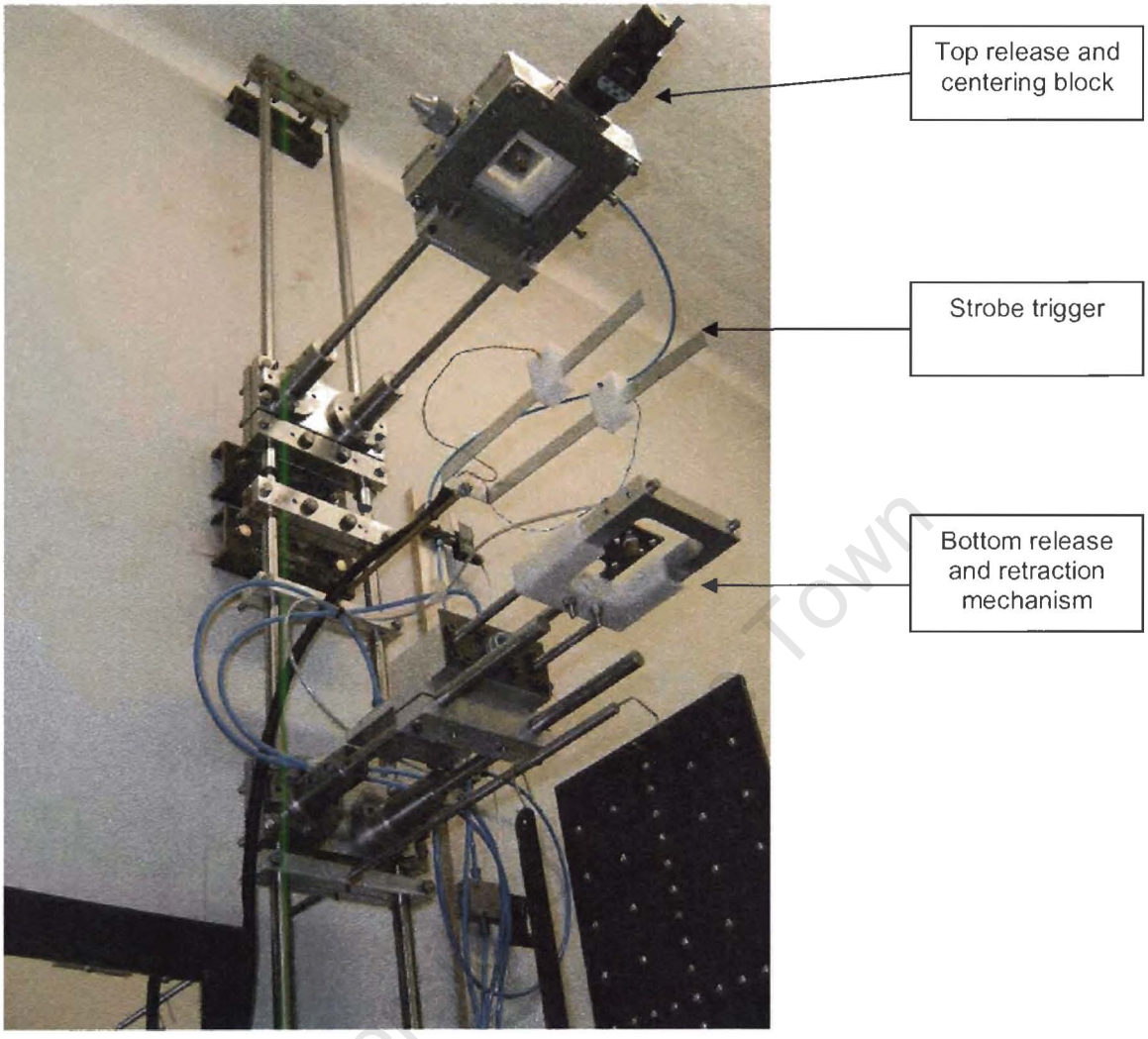

Figure 4-6 – Improved wall mount design with Centering block and release mechanism.

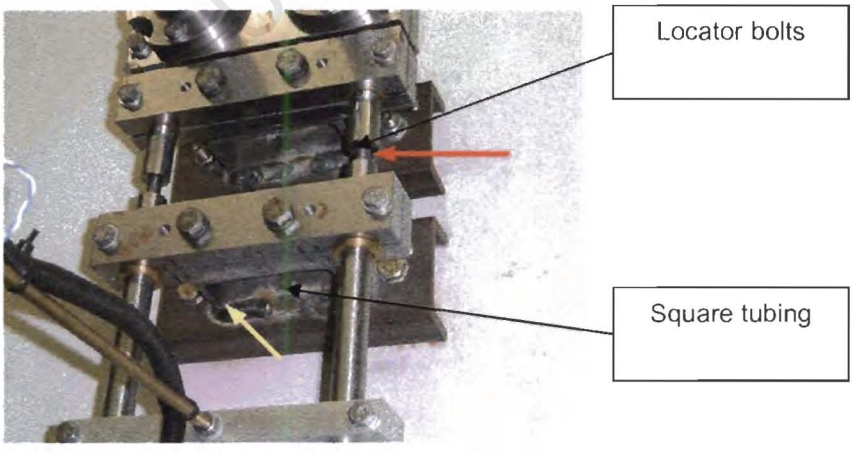

Figure 4-7 – Shaft End supports with locator bolts and square tubing

The full setup of the experiment as illustrated in **Figure 4-6** shows the Centering block and release mechanism mounted on two separated pairs of steel tracks. The advantage of this design is that the heights of the two sections can be adjusted independently and any stray vibrations caused by the release mechanism are damped by the locator bolts as highlighted in **Figure 4-7**.

4.2.4 Camera support

The support illustrated in **Figure 4-8** was made from salvaged photographic copying equipment. The copying equipment was modified and mounted on the wall as shown in the figure. Additional camera mountings were added to enable flexibility of the movement of the camera.

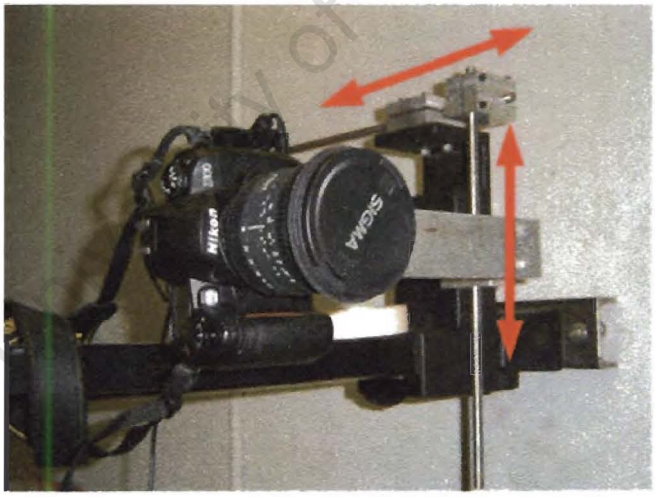

Figure 4-8 - camera support

The position of the camera relative to the in-flight tester is shown in **Figure 4-9**. The camera mounting is positioned 540mm from the particle collision plane.

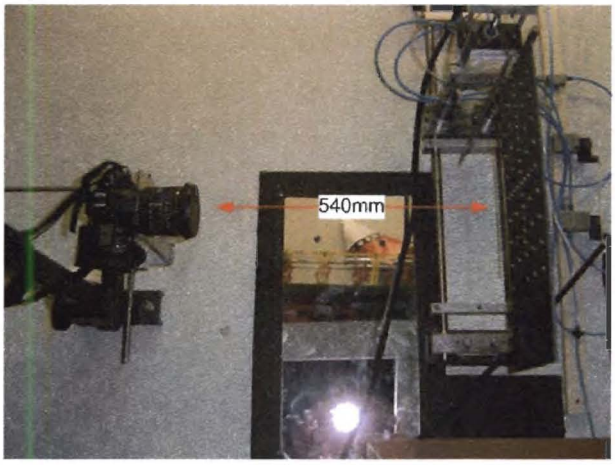

Figure 4-9 - camera support position

4.2.5 Pneumatic design

The choice of pneumatics to suit the problem was carefully considered. One of the main requirements is to ensure that the particles are released with no initial spin. To achieve this a partial vacuum is maintained through the nozzles which suspend the tested materials. Foerster *et al* [35] mention that the advantage of using vacuum to suspend the particles is in the lack of instabilities in releasing the particles without prior spin. If, instead, electromagnetic devices were used to suspend and release the particle, (a device such as electromagnetic solenoids) the effects of magnetism can alter the collision, i.e. the ferrous particle may become magnetic and spin can be introduced by the electromagnets upon release of the particle.

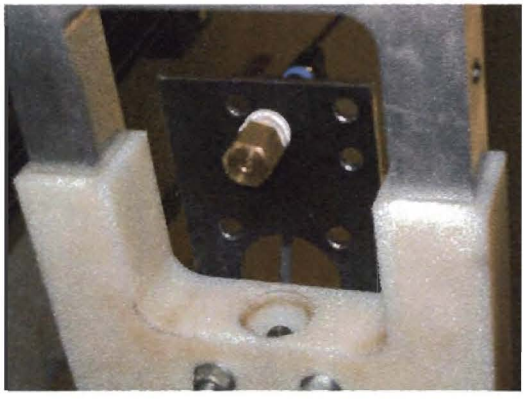

Figure 4-10 – Bottom view of the brass vacuum nozzle

Figure 4-10 illustrates the design chosen for the vacuum nozzle. This is based on the Foerster *et al* [35] experiment which incorporated a brass unbeveled orifice. The orifice is machined to suit to the size of the particle. For 5 – 10mm diameter particles, a 1.5mm diameter orifice is drilled and for 10 – 25mm diameter particles a 3mm orifice is drilled. The final setup of the pneumatic system is illustrated in **Figure 4-11**. The types of the pneumatics used are: 4/3 valve, 3/2 valves, venturies and solenoids. The solenoids trigger the valves with a 24V DC supply.

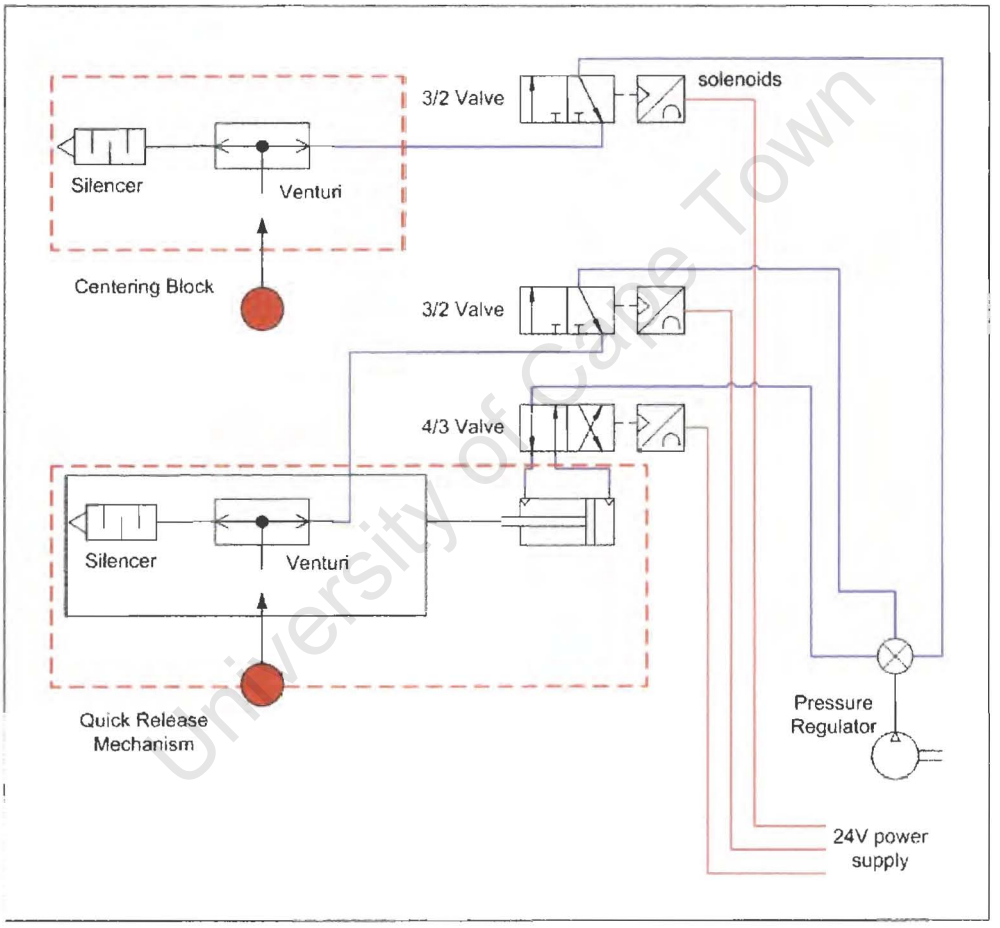

Figure 4-11 – Schematic of the pneumatic setup

4.3 Design Discussion

Design and construction of the drop tester based on the specifications defined by Foerster *et al* [35] and Kharaz *et al* [31] has been achieved. Modifications have been made to the rig to accommodate a variable height setting. Because this type of experiment requires precision drop and collision of two particles in free- fall, every effort has been made to maintain its accuracy and rigidity. The pneumatic controls ensure relative accuracy in the drop times and flexibility in testing a variety of ferrous and non ferrous materials. The design and construction of the experimental rig ensures adequate repeatability of drop tests.

Critical component in the design of the experiment:

- Support structures: Ensuring rigidity and stability.
- Alignment: Ensuring nozzle to nozzle and in-plane alignment.
- Pneumatics: Ensuring reliable control and flexibility in testing a variety of materials.
- Computer control: Controlled timing drops for a variety of denser materials.
- Photography and image processing.

Chapter 5

Experimental Procedure

This chapter discusses the experimental setup and procedure for conducting the in-flight collision tests. Sections covered include; photographic techniques, image processing, and analysis and error analysis.

The experimental procedure incorporates techniques from both Foerster *et al* [35] and Kharaz *et al* [31]. **Figure 5-3** illustrates a break down of the tasks and the dependency between each other. The experimental procedure can be grouped into three sub stages:

- Mechanical setup
- Electronic or electrical setup
- Image capture setup

5.1 Mechanical setup

This is a critical stage in the experimental procedure and setup. The accuracy of the experiment is determined by the repeatability tests. Kharaz *et al* [31] reported that the draw back of the in-flight collision experiment is the consistency of the tests. Since the colliding spheres impact on a very small area (contact patch); the probability of the collision landing on the same contact patch is limited by how consistently the spheres are released.

Pre- test conditions were applied in the experimental procedure of the mechanical design to test the consistency of the collisions. They were, repeated drop tests on the landing stage, where carbon paper placed over a sheet of paper records the impact point indentations. To check if the collisions were planar, binary collisions were conducted at random centre to centre offset distances.

Figure 5-3 illustrates the overall flow of the experimental procedure. The green shaded region describes the mechanical procedure of the experiment. This includes the pneumatics and the support structures. The feed back loops amongst decision boxes indicate the checks for consistency and repeatability.

5.2 Summary of the flowchart in the mechanical assembly and procedure

1. Before switching on the air supply for the pneumatics, the alignments of the nozzle holes from the Centering block to the release mechanism must be checked. This is checked by using a weighted plumb line. For initial alignment this methodology is fairly accurate, **Figure 5-1** illustrates the brass nozzles through which initial alignment is assessed using a plumb line. All the digital and mechanical micrometer readings are zeroed.

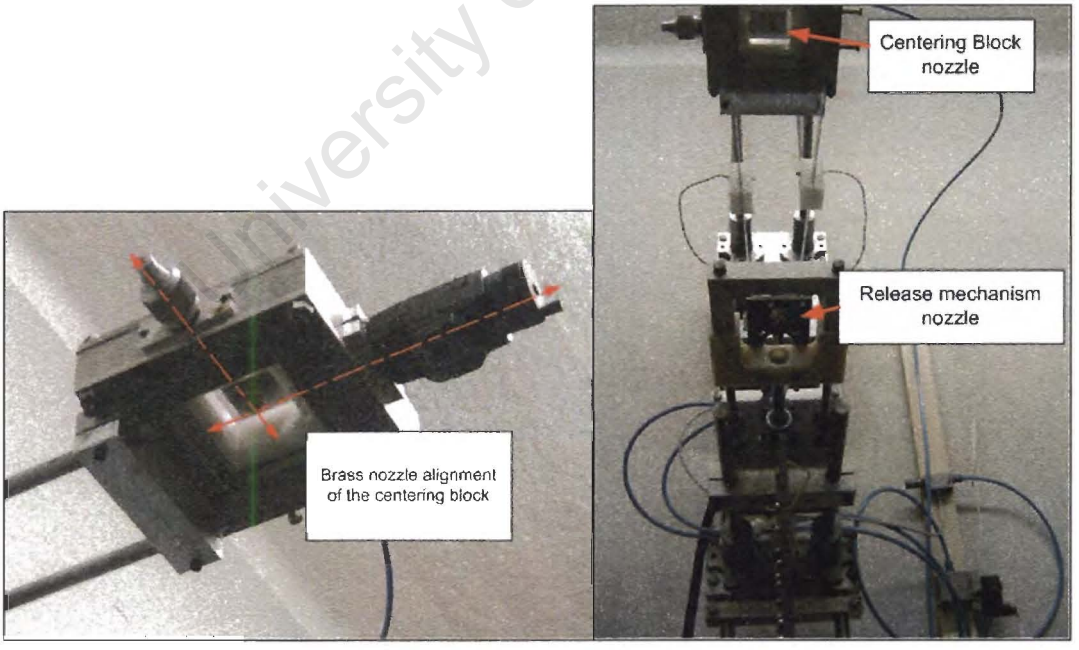

Figure 5-1 – Brass nozzle for the Centering block and Nozzle alignment

2. Carbon paper and recording paper are placed on the landing stage grid and the alignment is ensured to be perpendicular to the camera. Since the structures supporting the camera and the in-flight drop tester are rigid and mounted on the wall, the perpendicular alignment to camera, and "collision plane" (the plane in which particles collide for various offsets) is at 90 ± 2 degrees. This accuracy can be checked later by the initial trial drops. Illustration of the landing stage is shown in **Figure 5-2**.

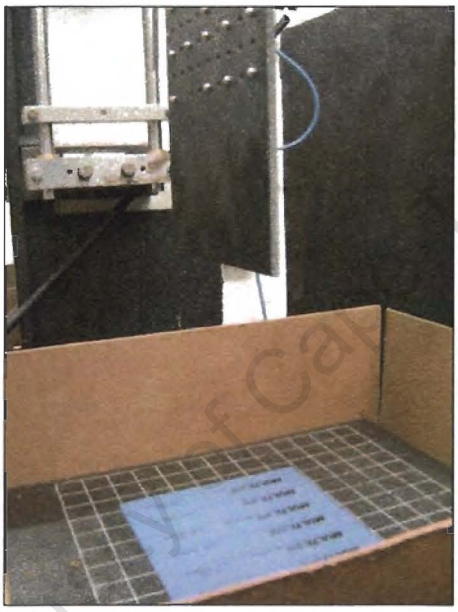

Figure 5-2 – landing stage (carbon paper on grid)

3. For initial trial runs a single Strobotak Strobe is used for the illumination. The strobe is mounted firmly onto a tripod.

4. The air supply to the pneumatics are switched on and checked for leaks in the system.

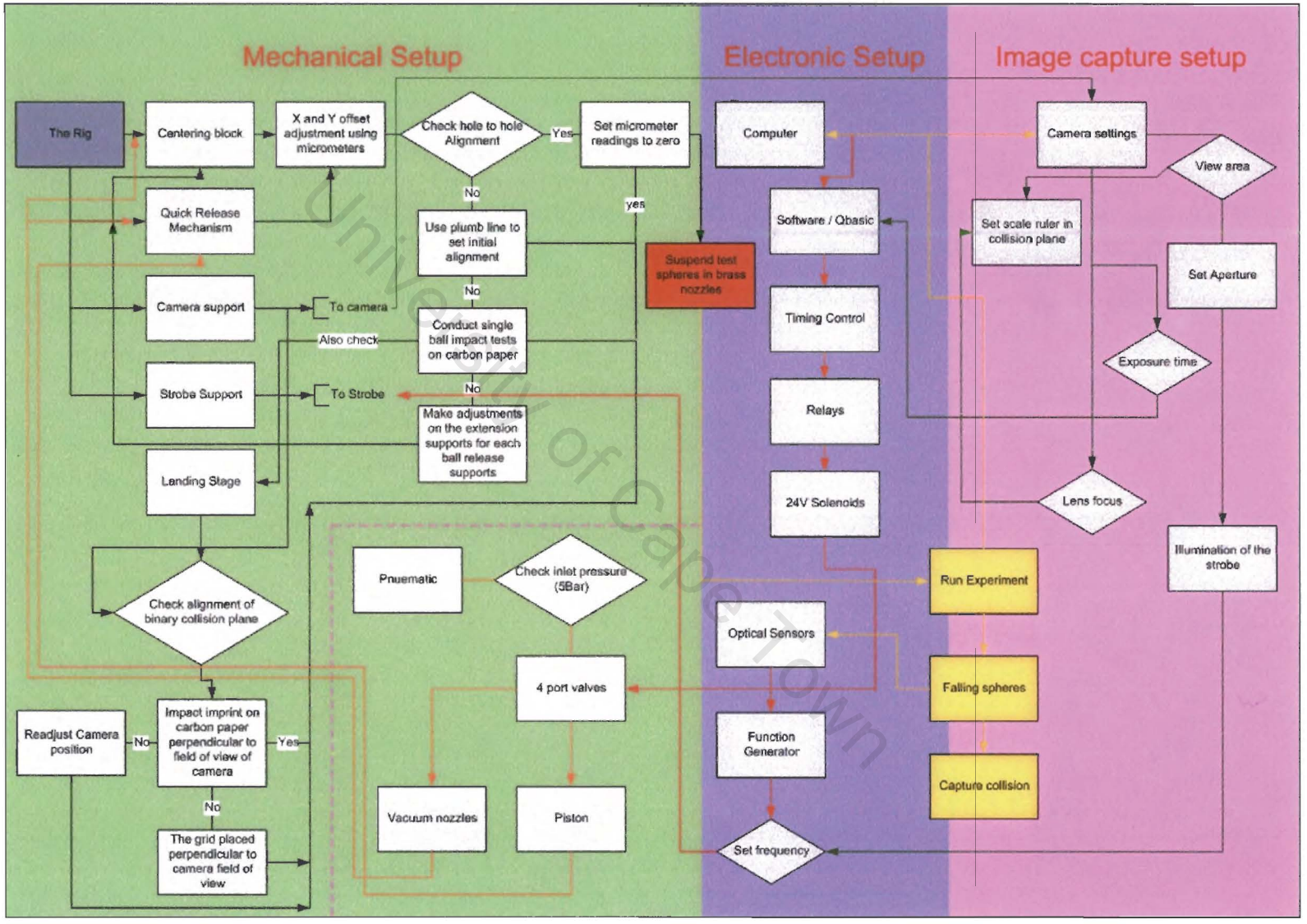

Figure 5-3 – Experimental Procedure flow chart

5.3 The Electronic setup

The operations of the pneumatic valves are controlled by 24 Volt DC solenoids. Foerster *et al* [35] mention the importance of the DC (direct current) in the experimental design as opposed to AC (alternating current) to avoid uncertainties in the activation time of the valves.

The pneumatic system is controlled by relays whose electronic timings are operated by software programmed in QBasic. The timing for the software is a function of the processor speed. A Pentium 2, 350MHZ computer with 716 time steps per second is adequate for the experiment. Appropriate times are entered in the software so that the particles collide within the field of view of the camera. The time step sequence for the software is illustrated in **Figure 5-4**. The whole event, from triggering the camera to reset, takes place in 3 seconds.

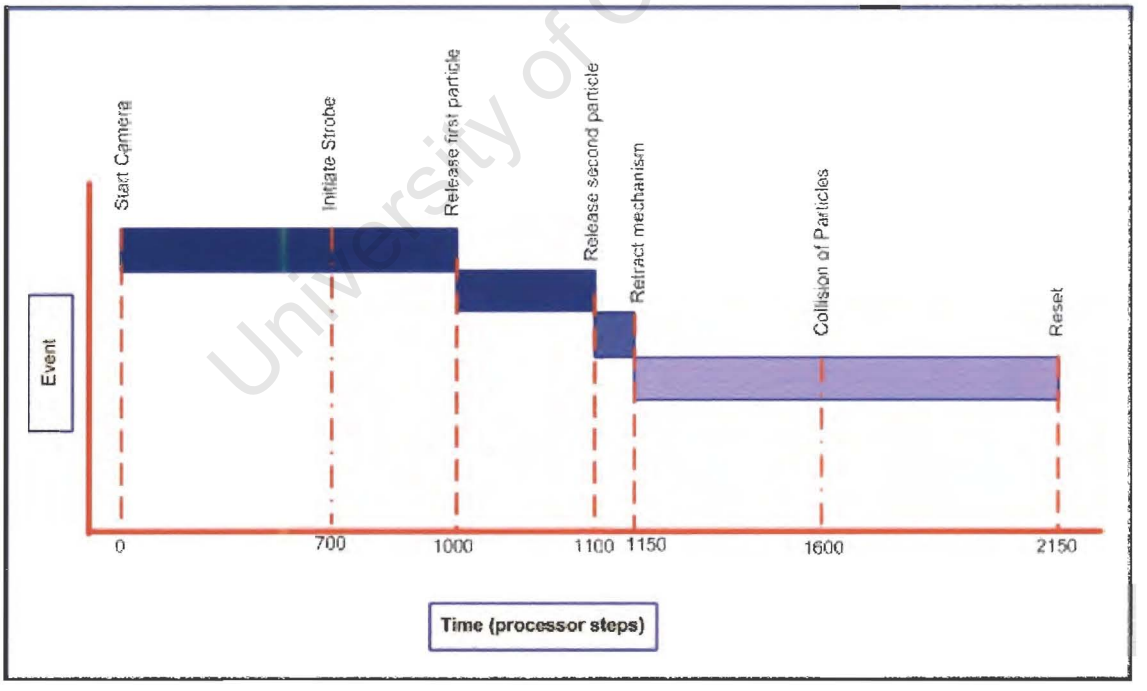

Figure 5-4 – Overall time steps for the experiment

The type of operating system (OS) used to run the interface is very important in the experimental design, as complicated operating systems (such as the windows interface) can hinder the time steps in the operation of the solenoids. The preferable and basic type of OS is DOS or Disk Operating System. DOS utilizes very little memory (RAM) and interfacing to the ports (parallel and serial) is often easier. Often in software, programmers implement redundant codes as a failsafe. These extra lines of codes slow down the operations of the software, therefore it is critical in the current experimental design to maintain simplicity in all possible ways.

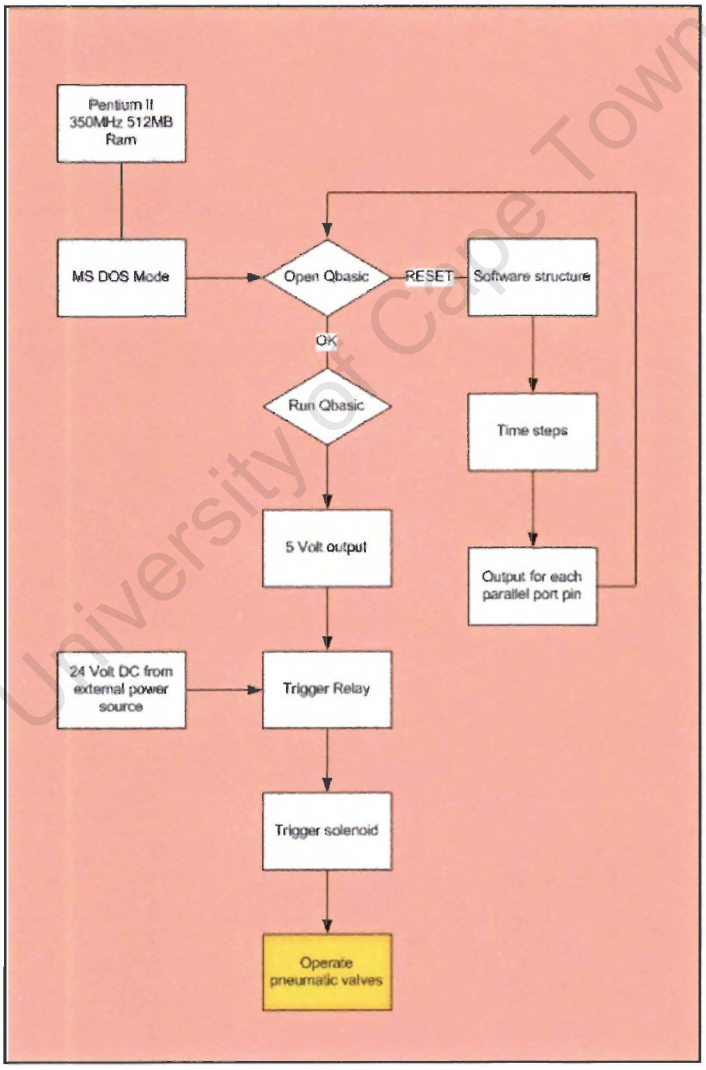

Figure 5-5 – Computer control structure

The basic feature of the computer control is illustrated in **Figure 5-5**. The relays are triggered by a 5V signal from the computer (relay input voltage). The relay triggers the external power source that provides the required voltage to operate the solenoids.

5.4 Summary of the flowchart in the Electronic procedure:

1. The computer is restarted in the MSDOS mode and the software in Qbasic is opened.

2. The 24V power is supplied to the relays and strobe, and the software is engaged to check if the relays are working and triggering the solenoids.

3. Alignment tests and drop time sequential tests are run to ensure that the particles are colliding. To do this the trigger times for the relays are adjusted accordingly. As shown in the **Figure 5-6**, a few lines from the QBasic programme, the red region controls the release of the first particle from the Centering block; the blue region controls the release of the second particle, and the Yellow region controls the retraction time of the quick release mechanism.

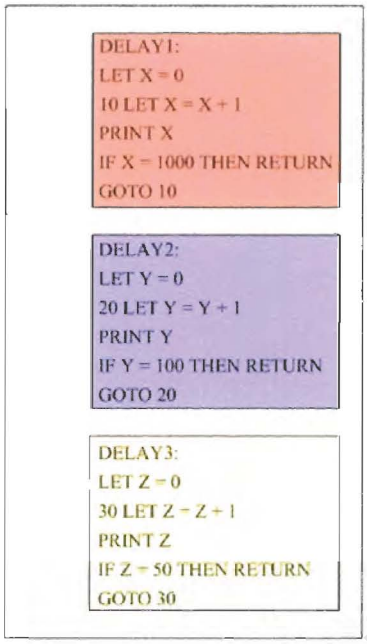

Figure 5-6 – QBasic relay control code

4. When the drop height of the first particle is changed, which is the Centering block height relative to the release mechanism, the times are readjusted in the blue region, which is the release of the second particle.

5. The triggering of the strobe is controlled by the optical trigger. Preliminary tests have shown that the image quality is greatly affected by continuously recording the drop sequence. This effect of the "strobe noise" is mentioned in the experimental work conducted by Kharaz *et al* [31] and they overcame the problem by triggering the strobe when the colliding particles are in the field of view of the camera.

5.5 Image processing

In this section we review the image enhancement and scaling techniques used in image processing.

Digitised images are captured using a digital SLR camera (Nikon D100) fitted with a 17 to 35 mm wide angle zoom lens. The maximum resolution of the camera is 6.1Mega Pixels, but for current experiment the resolution was reduced to 3.3 Mega Pixel. The resolution was reduced because the capacity of the 6.1 Mega Pixel image is approximately 3 Megabytes and 3.3 Mega pixel images take up approximately half that amount. The smaller image size is desirable as the storage capacity of the camera is limited, thus having a smaller resolution enables one to capture and store more images. Secondly, reduced picture resolution is easier to edit and manipulate, whilst still maintaining an adequate quality for image processing.

Figure 5-7 illustrates the various stages in the image processing. The use of a normal digital camera (i.e. not SLR) will not suffice for this type of experiment because control in fixing the focal length is not possible in the dark. Initial tests were conducted with Canon S50 5.1 Mega pixel digital camera. The Canon has similar features to the Nikon, such as aperture and exposure settings, but fixing the manual focal length is impossible. The camera automatically refocuses onto the black screen in the background, which results in blurred images for the colliding balls.

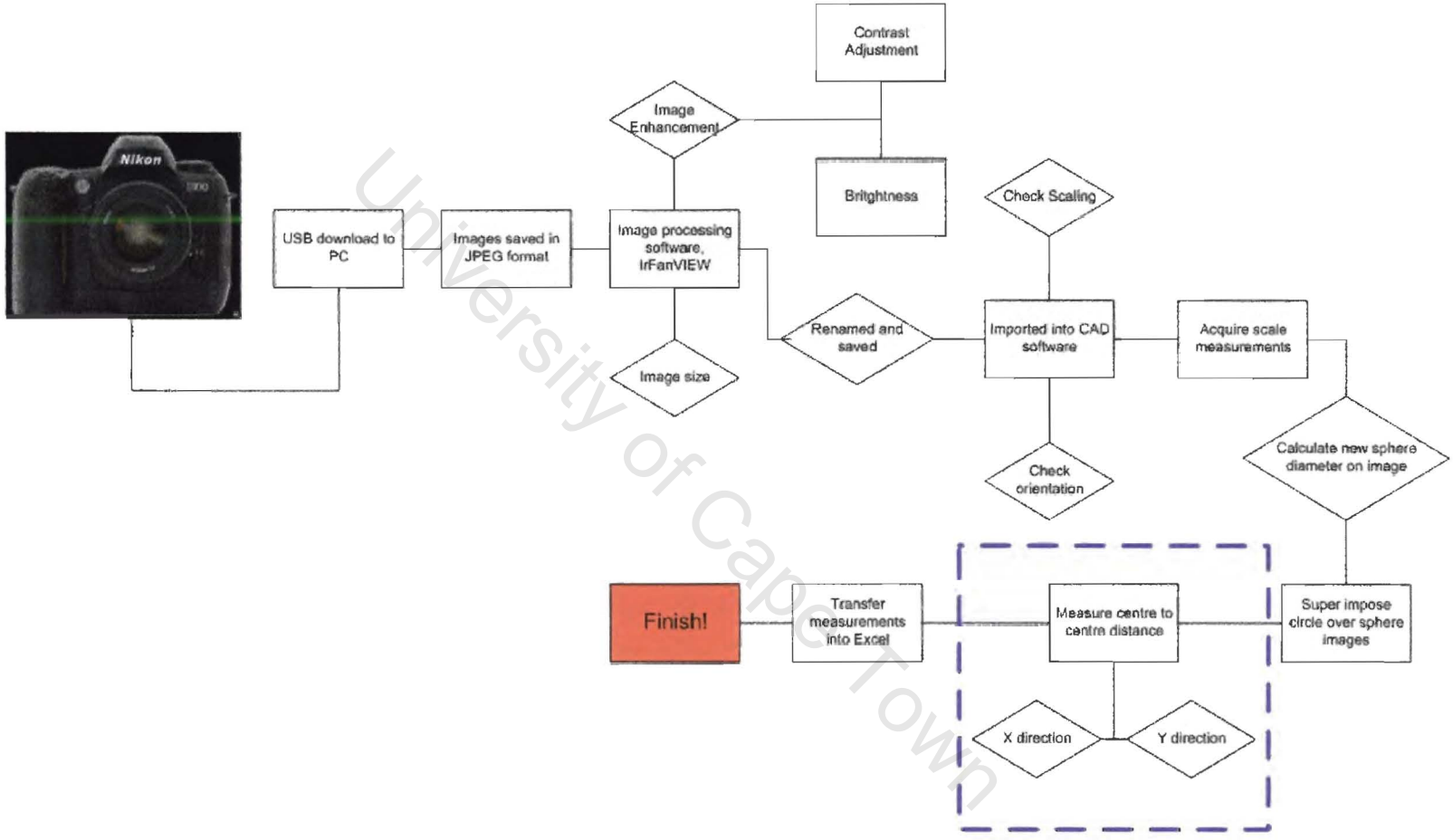

Figure 5-7 – Flow chart of image processing

5.5.1 Strobe Positions

Illumination of the colliding balls is a critical factor in acquiring clear images. Illumination of the colliding balls is governed by the strobe position with respect to the position of the camera. **Figure 5-8 – Figure 5-12** illustrate possible scenarios for the strobe orientations.

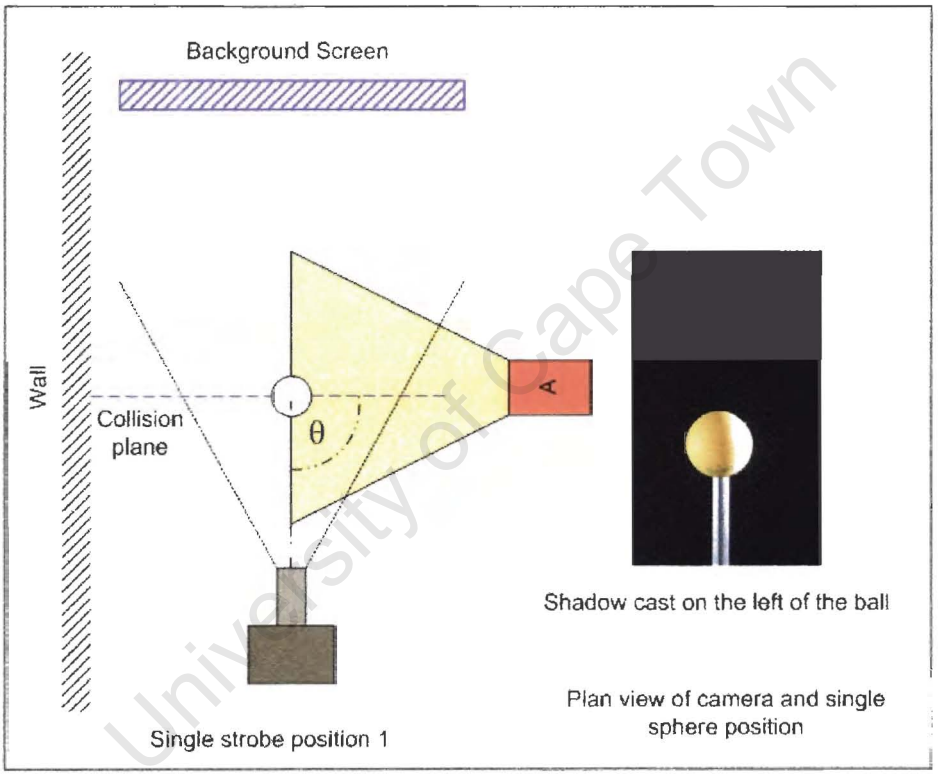

Figure 5-8 – Single strobe @ 90°

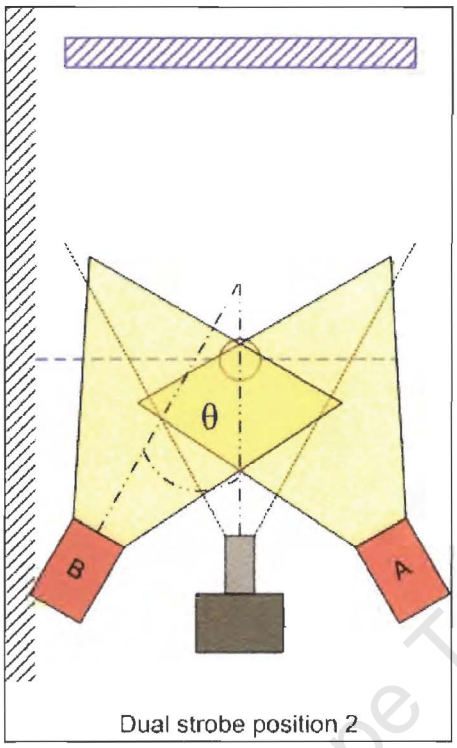

Figure 5-9 – Dual strobe @ $\pm 45^{\circ}$

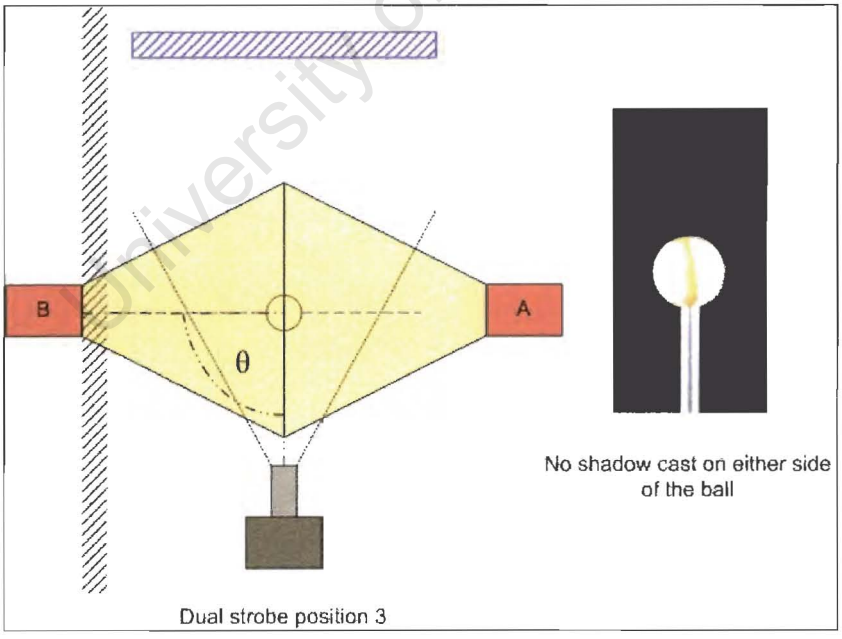

Figure 5-10 – Dual strobe @ $\pm 90^{\circ}$

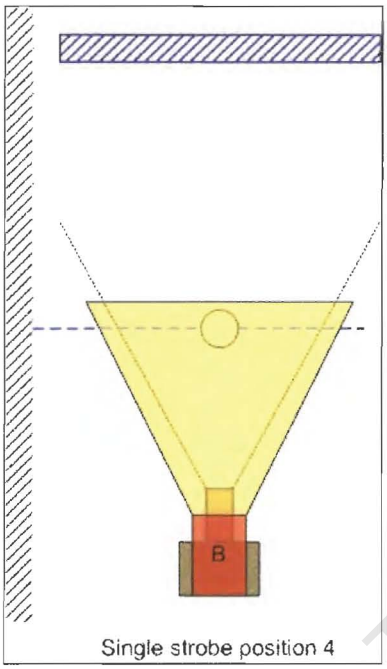

Figure 5-11 – Single strobe @ 0°

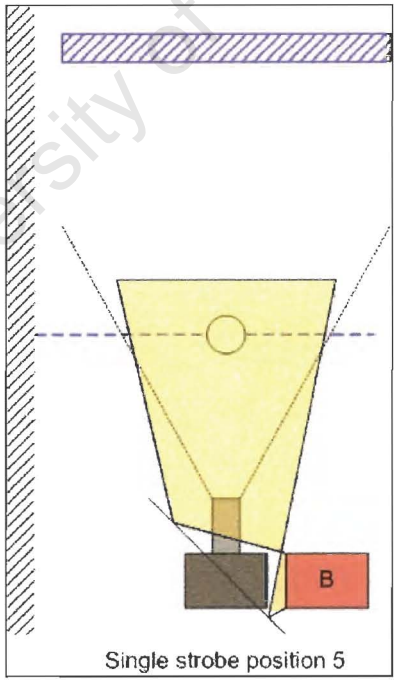

Figure 5-12 – Single strobe reflection

The effective positions of the strobe illumination were tested for the given plan view of the camera position with respect to the plane of collision. Foerster *et al* [35] described in their experimentation using the dual strobe $\pm 45^{\circ}$ setup as illustrated in **Figure 5-9**. The Strobe setup $\pm 90^{\circ}$ as illustrated in **Figure 5-10** was also tested, but instead of using strobe B, a mirror was placed facing strobe A. Essentially; the mirror replaced the illumination from strobe B. Using mirrors to reflect illumination is a useful technique as the space constraints in the experimental design can be overcome.

The Strobe position setup illustrated in **Figure 5-12** was used by Kharaz *et al* [31] for their experimentation. They incorporated a mirror placed under the camera at 45° to the field of view; the strobe positioned perpendicular to the camera reflects the light off the mirror onto the colliding particle. For the current in flight collision experiments, the single strobe 0° position setup as illustrated in **Figure 5-11** was chosen as the ideal choice because:

- No comprise was made on the strobe size, therefore illumination was much brighter and direct on colliding spheres.
- Easier to calculate specular reflection / phongs positions.

The setup that was utilised is illustrated in **Figure 5-13**.

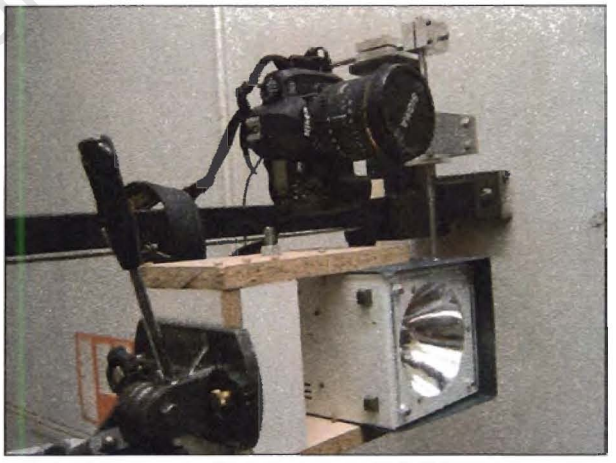

Figure 5-13 – Final Position of the strobe

5.5.2 Specular Reflections

The effects of specular reflections: specular reflection or phongs are the reflections of the light source on the surface of the steel balls or on any shiny surface. There may be more than one specular reflection depending on the number of light source points (i.e. strobes). The surface property of the steel ball makes it difficult to pick out the full shape of the sphere, thus making it difficult to locate the ball position using image processing. In the initial experiments two strobes were used, as per **Figure 5-9**. For the steel ball bearings the second strobe was removed so as to leave only one specular reflection to track. The image from the dual strobe $\pm 45^{\circ}$ setup on the steel ball is compared with the image from a single 0° strobe in **Figure 5-14**.

Since it is difficult to distinguish the full shape of the steel ball in the images, specular reflections were used as reference locations to the centres of the spheres. Specular reflection is viewpoint dependent. Light striking a specular surface, by Snell's Law, will be reflected at an angle which mirrors the incident light angle, so the viewing angle is very important. Specular reflection forms tight, bright highlights, making the surface appear glossy.

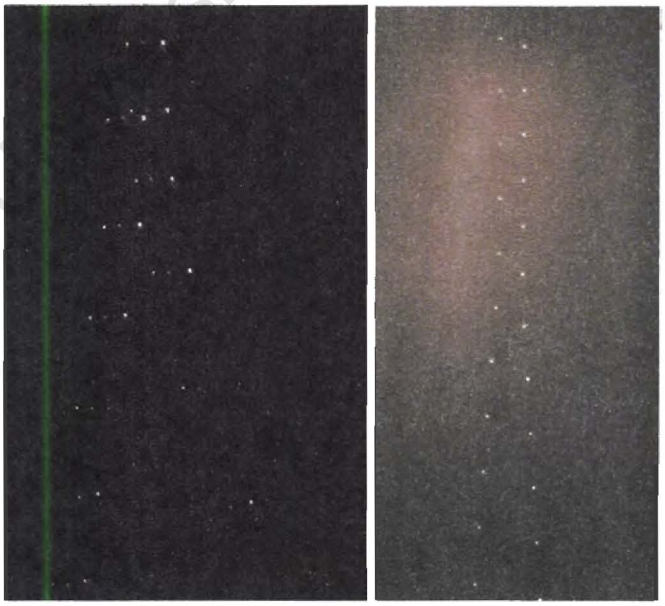

Figure 5-14 – Effect to two strobes and single strobe on the image

Lorenz *et al* [37] first mention the effects of the specular reflection in their experiment. They overcome the problem by coating a portion of the steel ball bearing with a fluorescent dye. Therefore the steel balls only come into contact on the non-coated side. The choice the non-reflective coating is particularly important, as modern dyes are solvent based chemicals; therefore they leave a thick residue when dry. This however can cause the steel balls to spin due to an unbalanced coefficient of drag.

A calibration frame with indented ball bearings was used to determine the specular reflection errors, illustrated in **Figure 5-15**. The distances between each ball bearing were measured using a coordinate measuring machine with accuracies of ± 0.003mm.

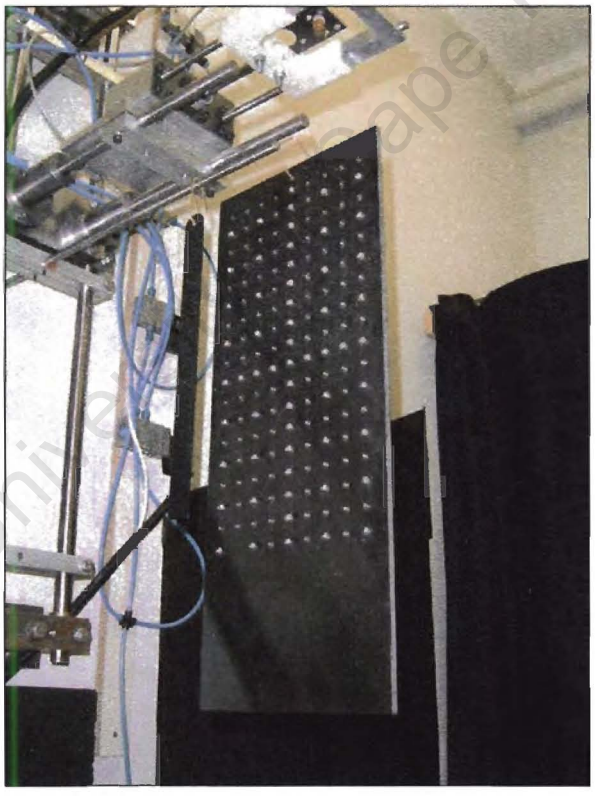

Figure 5-15 – Calibration frame

The offset distances were calculated for the control frame using a CAD package. The images were imported into ACAD ver.2002; linear measurements were taken of the ruler and the spaces between each centroid.

The positions of these reflections are dependent on the position of the camera with respect to the light source and the position of the camera with respect to the plane of collision. Accordingly, to minimise deviation, the following key features were incorporated into the image analysis:

- The light source was moved closer to the camera; the strobe was placed below the camera with centre to centre distance of 194 ± 2 mm, thus reducing the angle of incidence and reflection. This was also a key feature in Kharaz *et al* [31] experimental setup, where a mirror was placed below the camera lens to project light from the strobe which was placed on the side of the camera.

- The optimum location of the camera is 578 ± 2 mm from the plane of collision. The angles of incidence and reflection are reduced by the camera distance from the collision plane. The position of the camera was tested at various perpendicular lengths without compromising the image quality and size. The 35mm wide angle lens of the camera was a limiting factor for the camera position. The optimum positions of the camera and strobe are illustrated in **Figure 5-16** and the effect it has on the specular reflection is shown in **Figure 5-17**.

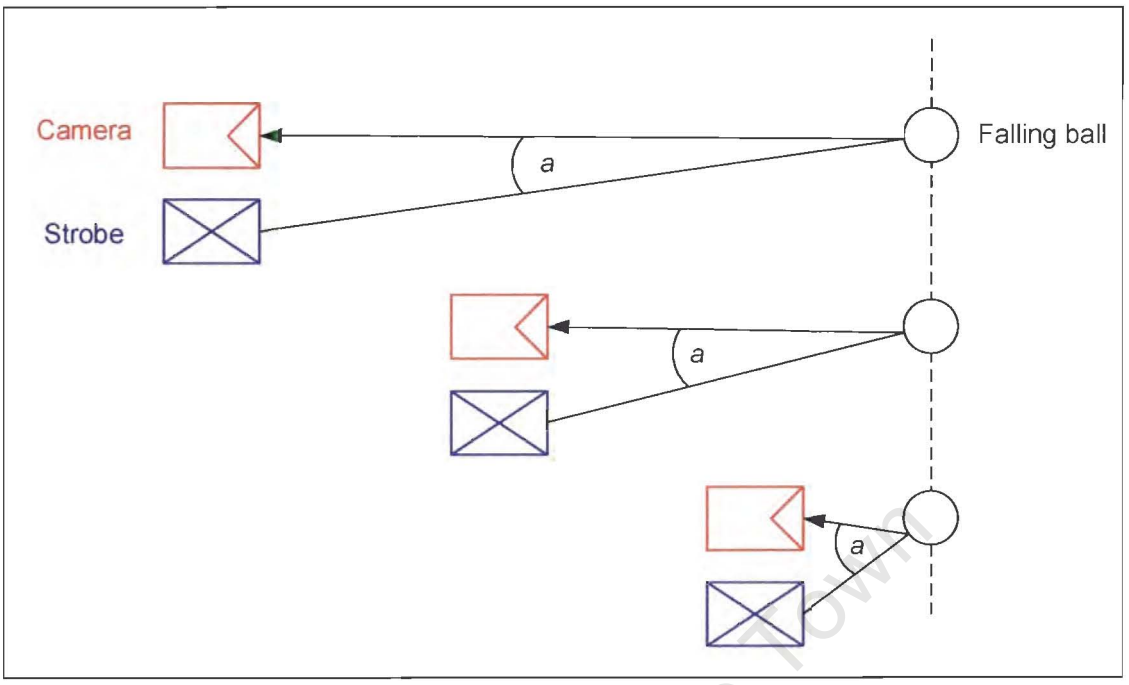

Figure 5-16 – Camera & strobe distances from the collision plane (side view)

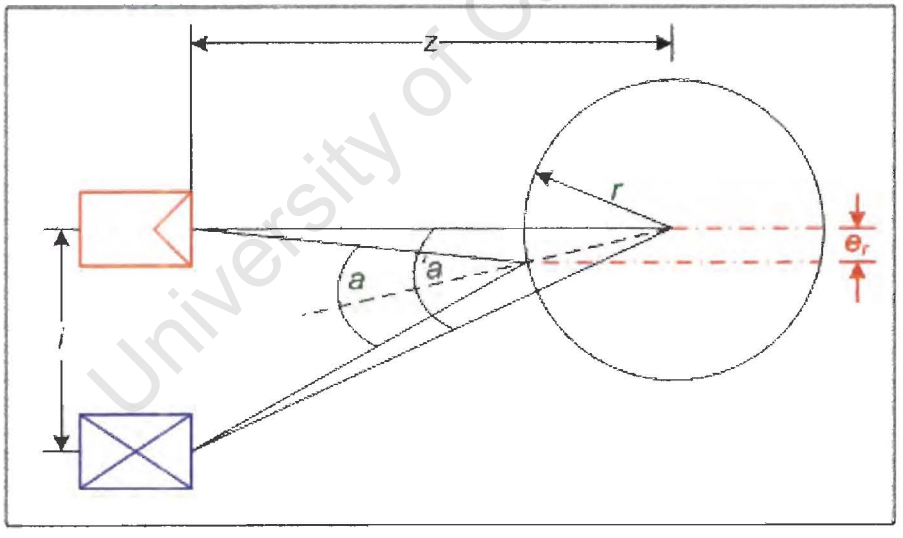

Figure 5-17 – Specular reflection relative position (in-line with camera field of view)

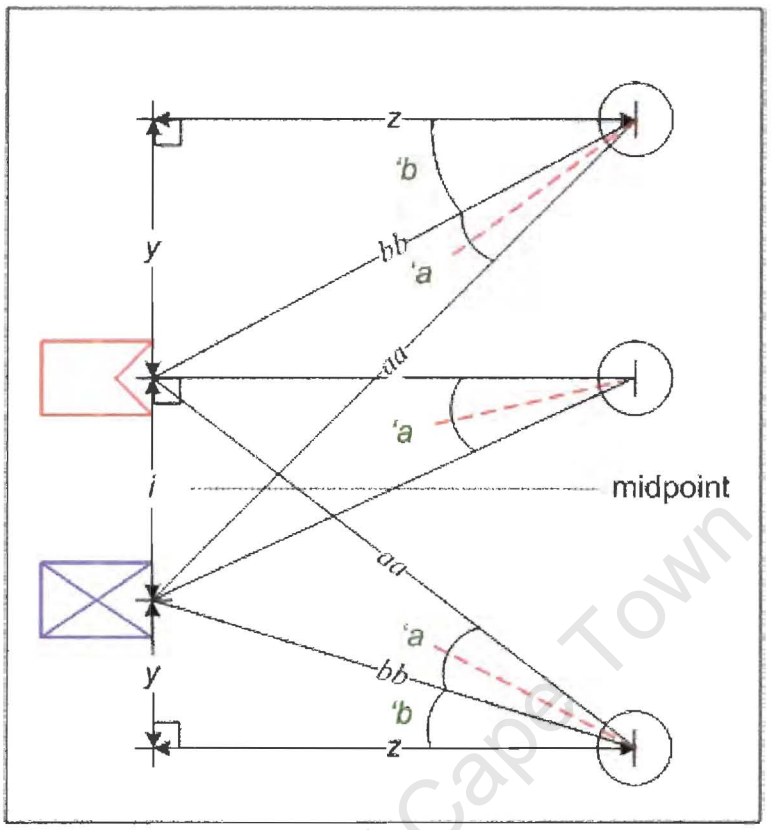

Figure 5-18 – Specular reflection for multiple positions

The positions of camera and strobe are used to calculate the relative specular reflection position about the centroid of the ball. This is illustrated schematically in **Figure 5-17** and **Figure 5-18.**

Angles a and $'a$ in **Figure 5-17** represent the angles of reflection for a sphere of radius r and at the centroid respectively, where $'\hat{a} < \hat{a}$. The terms i and z represent the distance between camera and strobe and the distance to collision plane respectively. The strobe is vertically below the camera.

Calculating the effect on the angle $'a$ for height y as shown in **Figure 5-18:**

$$bb^2 = z^2 + y^2$$

$$aa^2 = z^2 + (i + y)^2$$

Therefore,

$$\cos\ '\hat{a} = \frac{bb^2 + aa^2 - i^2}{2(bb)(aa)} \qquad \textbf{Equation 5-1}$$

$$\tan\ '\hat{b} = \frac{y}{z} \qquad \textbf{Equation 5-2}$$

But angle of incidence and reflection are equal, (laws of reflection of light), therefore e_r the distance between surface specular reflection and centroid for a given radius as illustrated in **Figure 5-17**:

$$e_r = \sin\left('\hat{b} + \frac{'\hat{a}}{2}\right) \times r \qquad \textbf{Equation 5-3}$$

From **Equation 5-3,** e_r becomes smaller when the r is small. Alternatively, e_r becomes smaller when sin $'\hat{a}$ approaches a small value. This can be achieved by reducing i (i.e. strobe and camera lie on top of each other) or make z, the distance from camera to collision plane very large. The value e_r is viewing area specific; therefore the offset errors are smaller closer to the camera focus area and greater at the edges of the images.

Specular reflection errors are calculated from the calibration frame. Because the balls are fixed on the calibration frame, this gives a good estimate of how much the error is inferred by the reflections. **Figure 5-19** illustrates the calibration frame relative ball positions. The relative grid distances between the 6mm diameter balls on the frame is 10mm, therefore initial calculations are calculated for these positions and then estimated for the captured images of binary particle collisions for varying diameter and measured relative y pre- and post- colliding ball image positions.

Figure 5-20 illustrates the calculated distances for the specular reflection errors. This illustration is a side view of the calibration frame. From the diagram the influence of the $Y_{measured}$ on the Y_{actual} are calculated.

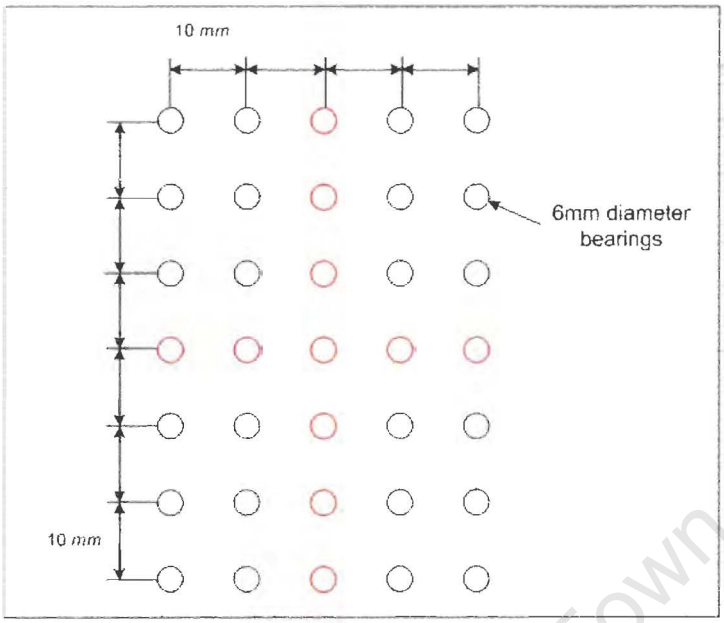

Figure 5-19 – Calibration frame ball bearing relative positions

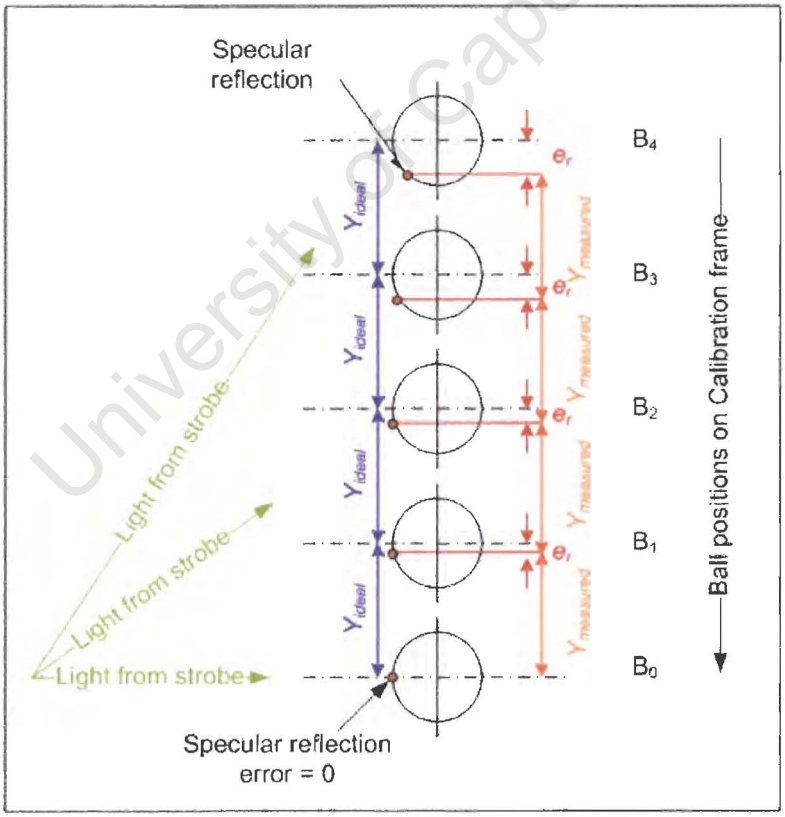

Figure 5-20 – Measuring the specular reflection relative distances between the ball images on Calibration frame

Calculated the relative errors are tabulated in **Table 5-1.** The influence of 4 different relative distances on the calibration frame was tested, namely: 10mm, 20mm, 30mm and 40mm. The following procedure was undertaken to calculate the relative distance error:

- The centre to centre distances on the calibration frame were estimated for B_0, B_1, and B_2. Therefore Y_{actual} is known.
- Influence of specular reflection error is added to Y_{actual} for $B_{0\text{-}1}$ and $B_{0\text{-}2}$.
- Because we require the relative distance between B_1 and B_2, the relative reflection distances between the ball images are calculated.
- Percentage error is determined by the ratios Y_{actual} and $Y_{measured}$.

Rel $y = y_{b2} - y_{b1}$	Diameter	$E_{y1} = y_{b1} - e_{r(b1)}$	$E_{y2} = y_{b2} - e_{r(b2)}$	$E_{y2} - E_{y1}$	% Error
10.00	6.00	4.49	14.44	9.95	0.48
15.00	6.00	4.49	19.42	14.93	0.48
20.00	6.00	4.49	24.40	19.90	0.48
25.00	6.00	4.49	29.37	24.88	0.48
10.00	6.30	4.47	14.42	9.95	0.51
15.00	6.30	4.47	19.39	14.92	0.51
20.00	6.30	4.47	24.37	19.90	0.50
25.00	6.30	4.47	29.34	24.87	0.50
10.00	8.15	4.31	14.24	9.93	0.66
15.00	8.15	4.31	19.21	14.90	0.65
20.00	8.15	4.31	24.18	19.87	0.65
25.00	8.15	4.31	29.15	24.84	0.65

Table 5-1 – Specular reflection relative height error (Between two subsequent images, B_1 and B_2 for yb_1 = 5mm)

Rel $y = y_{b2} - y_{b1}$	Diameter	$E_{y1} = y_{b1} - e_{r(b1)}$	$E_{y2} = y_{b2} - e_{r(b2)}$	$E_{y2} - E_{y1}$	% Error
5.00	6.00	9.47	14.44	4.98	0.48
10.00	6.00	9.47	19.42	9.95	0.48
15.00	6.00	9.47	24.40	14.93	0.48
20.00	6.00	9.47	29.37	19.90	0.48
5.00	6.30	9.44	14.42	4.97	0.51
10.00	6.30	9.44	19.39	9.95	0.50
15.00	6.30	9.44	24.37	14.92	0.50
20.00	6.30	9.44	29.34	19.90	0.50
5.00	8.15	9.28	14.24	4.97	0.65
10.00	8.15	9.28	19.21	9.93	0.65
15.00	8.15	9.28	24.18	14.90	0.65
20.00	8.15	9.28	29.15	19.87	0.65

Table 5-2 – Specular reflection relative height error (Between two subsequent images, B_1 and B_2 for $yb_1 = 10mm$)

As shown in **Table 5-1** and **Table 5-2**, for relative Y distances of 5, 10, 15, 20, 25 *mm* the maximum specular reflection error is less than 1%, indicating that the error contribution by the reflections for the measured relative distances range of 15 – 20mm for 8.15mm diameter steel and 6.3mm diameter ceramic ball bearings will not be greatly affected and are well within range.

5.5.3 Image Enhancement

Once the images are captured in the digital camera, they are imported into image processing software to enhance the quality and visibility, so as to identify the colliding balls. The Raw image captured by the camera as illustrated in **Figure 5-21** is processed by the following techniques and checked for quality. Since the images are imported into CAD for scaling, the raw images are only enhanced by the brightness and contrast.

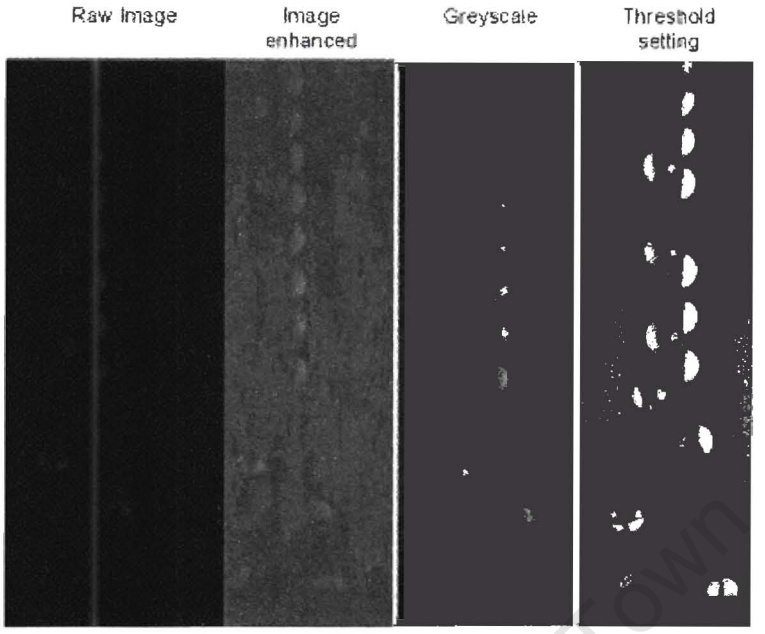

Figure 5-21– Image enhancement techniques

The imported images in CAD are scaled and the relative contact velocities pre- and post- of the colliding particles are measured using the dimensional tool.

5.6 Summarising the flowchart in the Image processing procedure:

1. Camera and strobe are placed perpendicular to the collision plane. The strobe positioned below the camera.
2. The captured images are downloaded from the camera to the computer and processed.
3. The images are pre-processed in the **IrFanView** software. The brightness and contrast of the images are adjusted and they are renamed.
4. The enhanced images are copied and then pasted into **ACAD ver 2002** software for post processing.
5. Lines are drawn over the desired scaled ruler length (100mm length) and the relative reflection points of the colliding particles. An experimental procedure convention is adhered to whereby the impacting particle is always positioned on

the left-hand side to the particle which is being released by the release mechanism. The dimension tool in ACAD software is used to measure apparent image distances in the X and Y velocity components. Where X is the horizontal axis and Y the vertical. The set of measurements from each processed image are logged in **EXCEL**.

5.7 Error Propagation

"It is common and well established practice that the first time an experiment is performed the results bear little resemblance to the "truth" being sought. As more data points are obtained with successive refinements of the technique and method, the overall results gradually approach to some confident description of events." – Philip R Bevington, Data Reduction and Error Analysis for the Physical Sciences. (McGraw-Hill 1969)

The source of error in experiments is a major contributing factor to consistent data analysis. For the in-flight collision of spherical particles, alignment and repetition of the drop test is critical in the experimental design.

Obtaining precise measurements even of simple impact configurations is not easy, as reported by Kharaz *et al* [31]. In all previous experimental work, a significant degree of random variation in collision geometry combined with measurement errors have led to a wide scatter of the individual data points that are presented, Foerster *et al* [35], Maw *et al* [29]. This is particularly a problem for a particle–particle experiment, in which precise control of impact conditions is very difficult, as reported by Kharaz *et al* [31].

An aim of the present work was to improve both the reproducibility of impact experiments and the precision of measurement so that scatter could be reduced. Sphere-on sphere collisions were used to maintain tight control over the impact geometry and

material properties, and critical attention was paid to all aspects of the experimental set-up.

The impact of the spheres occurs at a small contact area. Therefore consistency of impacting on the same contact area will greatly be affected if one does not have a clear understanding of what contributes to the sources of "misalignments" in the experimental procedure.

In order to have a clear understanding of these propagations of possible errors in the experimental procedures, the contributing errors can be separated into four sections, which are: construction of the experiment; experimental setup; image acquisition; and image processing. These contributing errors in each of these sections are broken down further into its elements and their tolerances calculated. The combinations of errors contribute globally to the accuracy of the results gathered.

5.7.1 Construction

Designing and constructing precise experiments are not trivial tasks. Especially when the experiments require dropping two spherical particles with a minimum diameter of 5mm and they are required to collide with same offset in repeat experiments. Generally, mechanical set-up affects reproducibility rather than accuracy, except for vibration and spin, which do affect accuracy, and are determined by the construction. In mechanical manufacturing processes, tolerances are used to get an appropriate fit. Every attempt in the design and manufacturing of the components has maintained high standards in machining and fabrication. The support structure was machined to tolerance of ± 0.1mm, and the centering block and quick release mechanism to tolerance of ± 0.01mm.

5.7.2 Experimental setup

The setup determines whether the impact plane is parallel to the image plane. This contribution is illustrated in **Figure 5-22.** Because the collision is assumed to be in the plane perpendicular to the camera, it is critical to maintain consistent precision when dropping the particles.

To check if the particles collisions occur in this plane an impact plate with carbon paper is used. This is shown as a schematic in **Figure 5-23.** Any slight misalignment introduces a source of error to the final calculations, as they are assumed to be parallel.

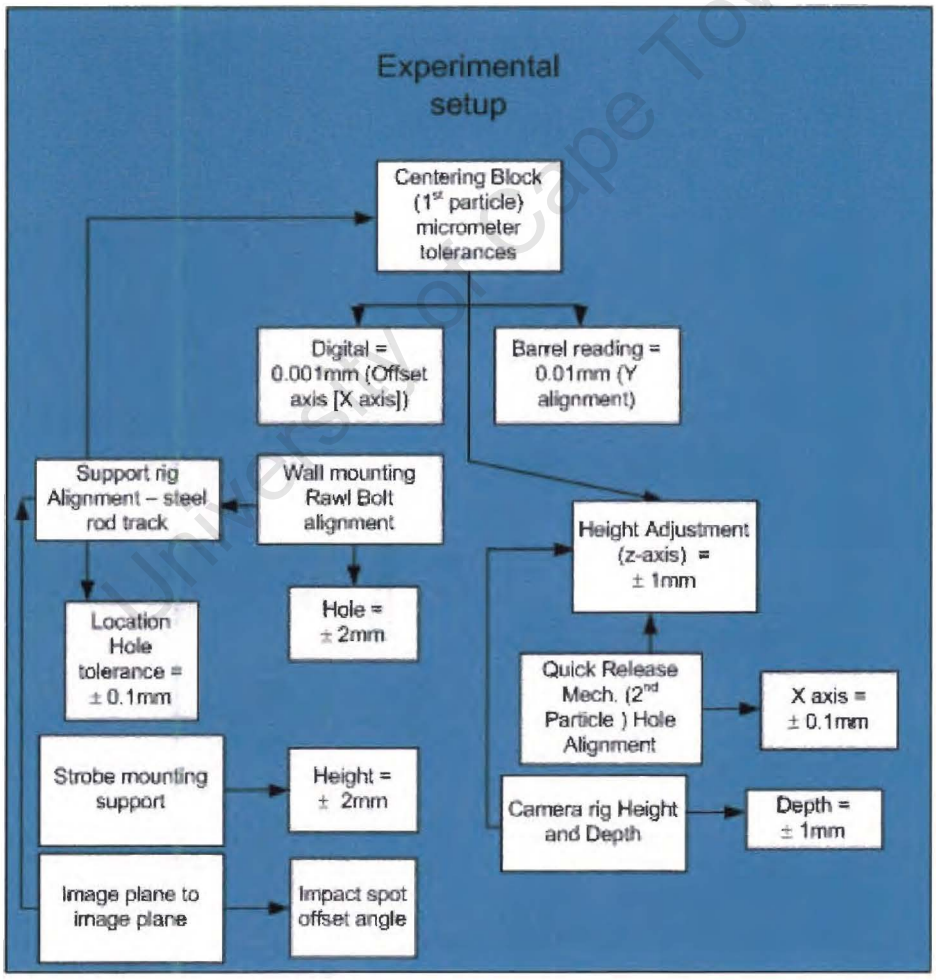

Figure 5-22 – Contribution of errors in the Experimental Setup

In **Figure 5-23**, plane 1-1 (shown as impact spots on the carbon paper) is required to get good data. Plane 2-2 has an angular offset α_{ang}. To check the contribution of angular offset on the measured data, **Figure 5-24** illustrates contribution of error on the measured angle in the collected data.

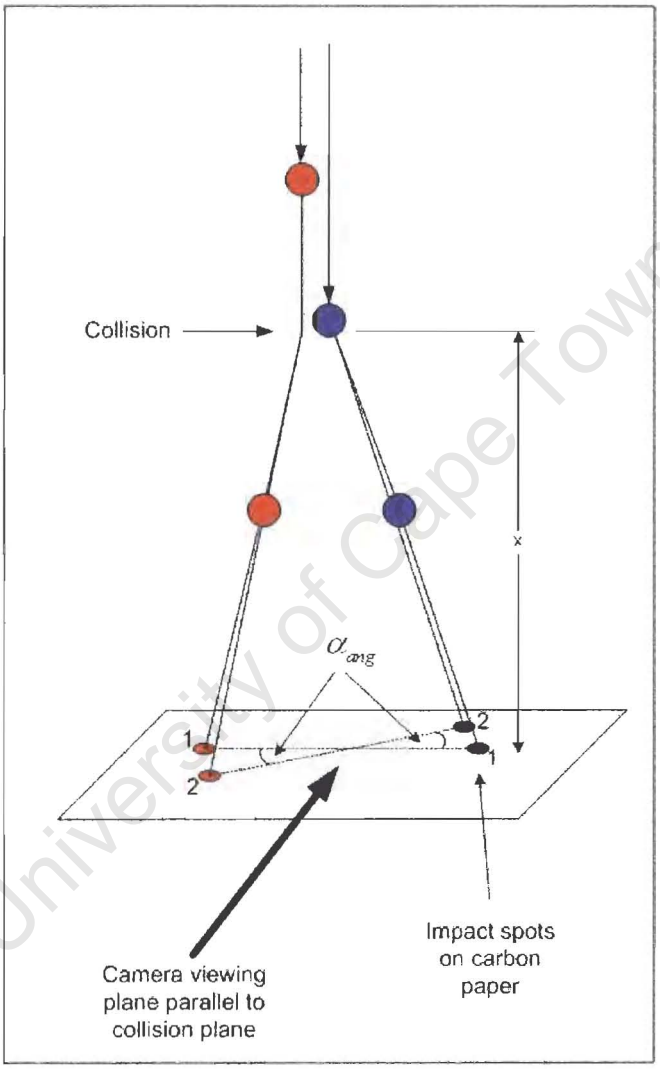

Figure 5-23 – Impact spots caused by slight misalignment

For x = unit length, the prescribed error e_a is:

$$e_a = \left(1 - \cos \alpha_{ang}\right) * 100 \qquad \textbf{Equation 5-4}$$

To make e small we must change the maximum allowable offset angle. Therefore, in the experiments tight control and alignment of the dropped particles are administered in order

to reduce the onset this angular offset error. **Table 5-3** illustrates the calculated errors for impact plots presented in **Figure 5-25** to **Figure 5-27** for steel, ceramic and Teflon. Points outside the range were excluded from the analysed data.

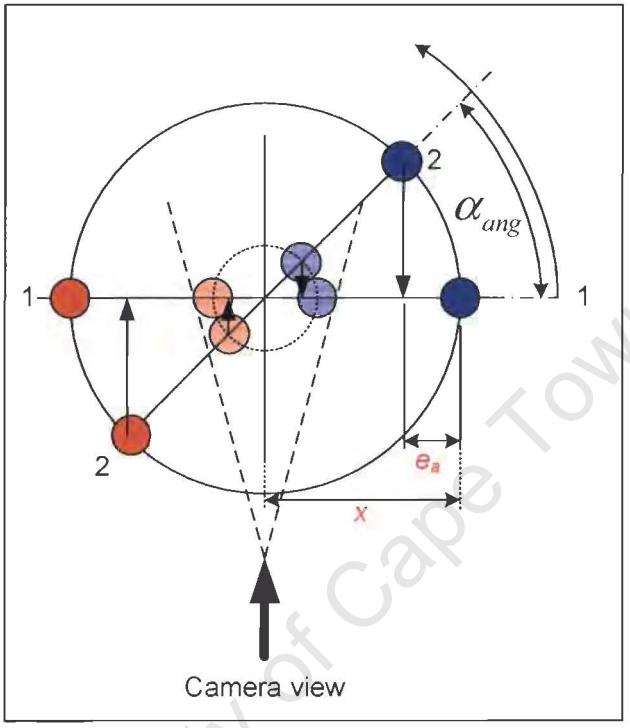

Figure 5-24 – Selecting suitable images based on impact spots

Material	Angle	Error for unit length
Steel	3°	0.14%
Ceramic	10°	1.51%
Teflon	3°	0.14%

Table 5-3 – Angular offset error

Note, that the contribution of *e* to the measured distance only affects the X – direction component of the relative distance. The Y- direction component is not affected because the twist or rotation of the colliding occurs about the Y- axis, which is vertical.

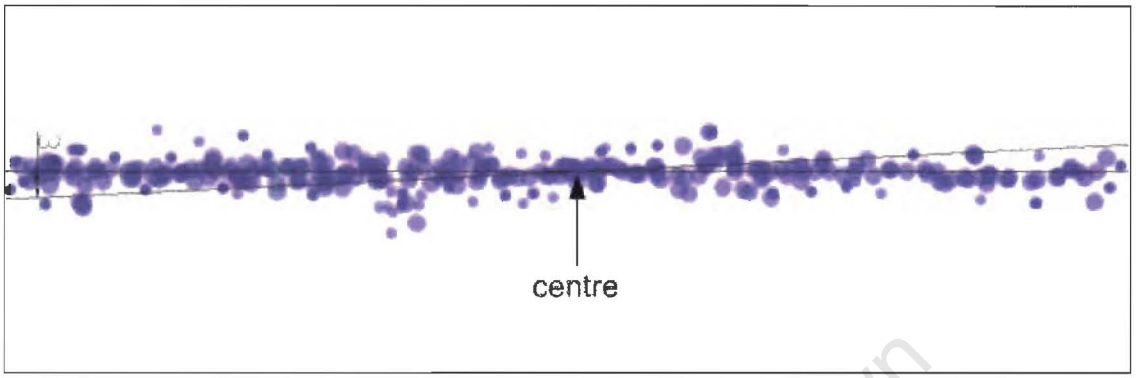

Figure 5-25 – Impact plots for steel balls

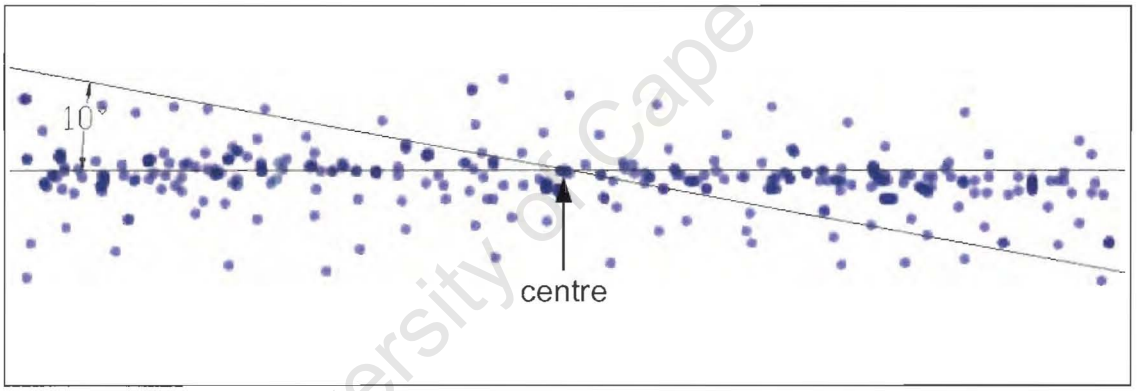

Figure 5-26 – Impact plots for ceramic balls

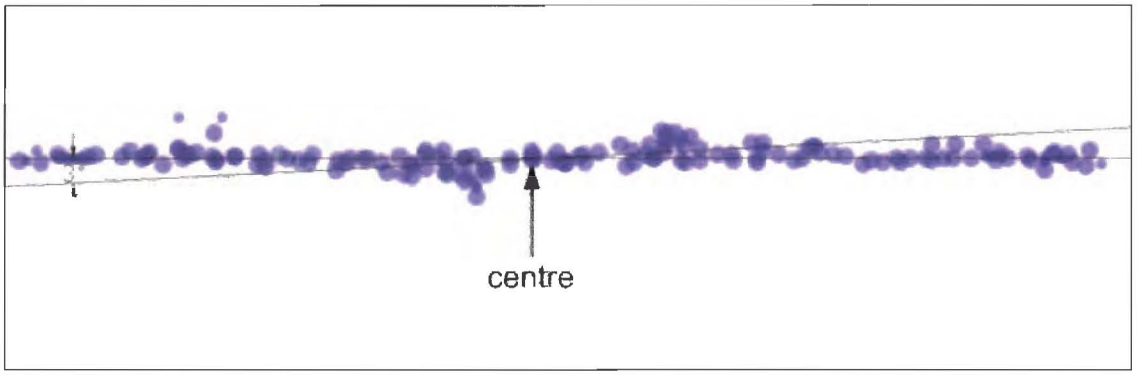

Figure 5-27 – Impact plots for Teflon balls

5.7.3 Image acquisition

In order to understand the major effects of these errors, we must first look at the type of results gathered. For this, the results obtained are a series of digitized photographic images illustrated in **Figure 5-28**. The photographic images of the colliding spheres are captured in single frame mode, i.e. exposure time of 3 seconds. During which the strobe illuminates at a given frequency, and captures a sequence of "ghost images" of the each sphere.

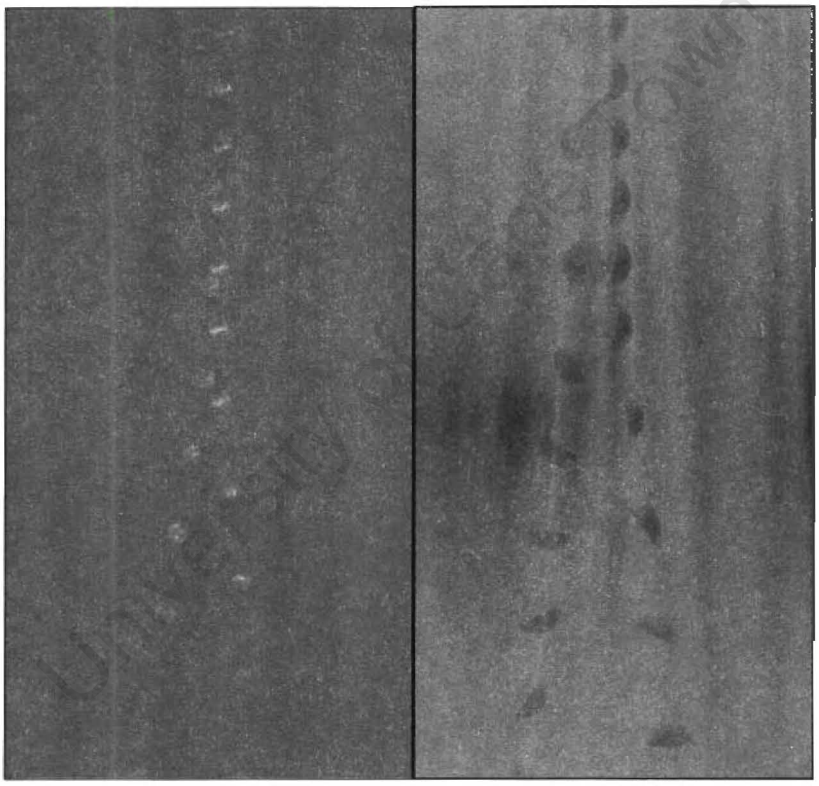

Figure 5-28 - Digitized photographic images

Figure 5-29 illustrates the source of inaccuracies in the captured images. Before acquiring suitable images, it is important to understand the sources of errors that contribute to the overall images. This analysis is a benchmark to identify any possible sources of error before capturing the required images for analysis.

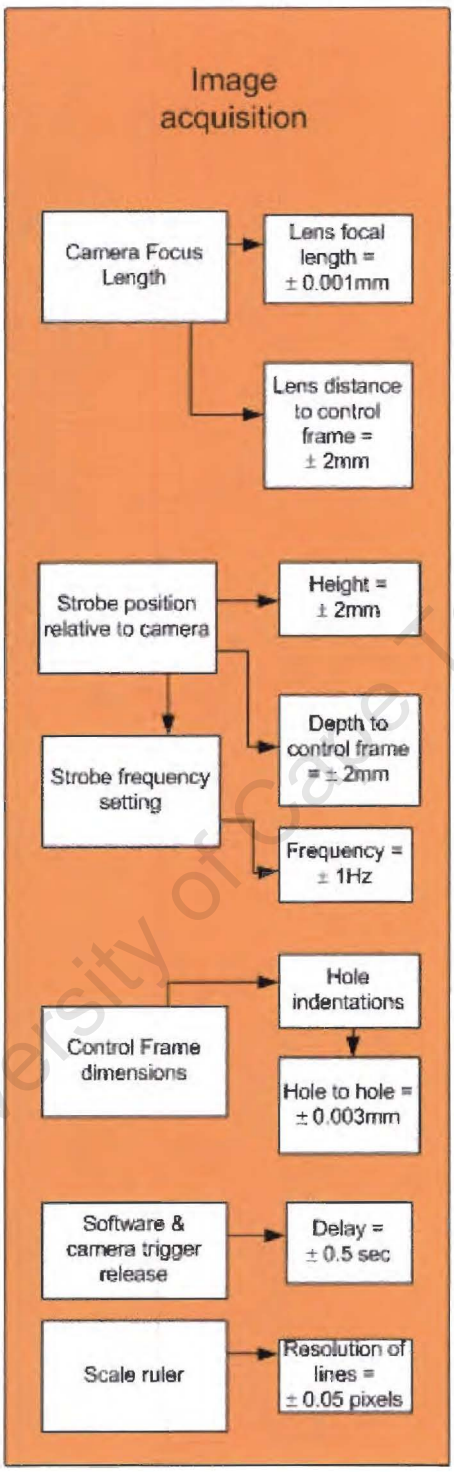

Figure 5-29 – Sources of inaccuracies in image acquisition

From the illustration presented in **Figure 5-29**, key sources of possible errors are broken down. Real sources of errors, i.e. errors which contribute to the overall measurement of

the pertinent data are constituted by the strobe frequencies and the resolution of the scale ruler. This is because the free falling balls experience no external interactions, and therefore limiting any onset of the experimental setup errors, the real sources of errors are inferred in the images captured. The strobe frequency is the only mechanical/electrical source of error on the images. The frequency of the strobe sets how far part the successive images of the colliding balls are in the photographs. The Strobotak manufactured bulb strobe and the GNS manufactured bright LED strobe contribute a frequency of error of ± 1 Hz for frequency range (200 – 1000Hz). This error is determined from the machine specifications.

The factors contributing to the quality of the image are the light source, i.e. the strobe and the image capturing device, i.e. the digital camera. Each of the pieces of equipment can be broken down into the elements which contribute to overall image quality. **Figure 5-30** illustrates the breakdown of possible sources of errors that could affect the quality of the image.

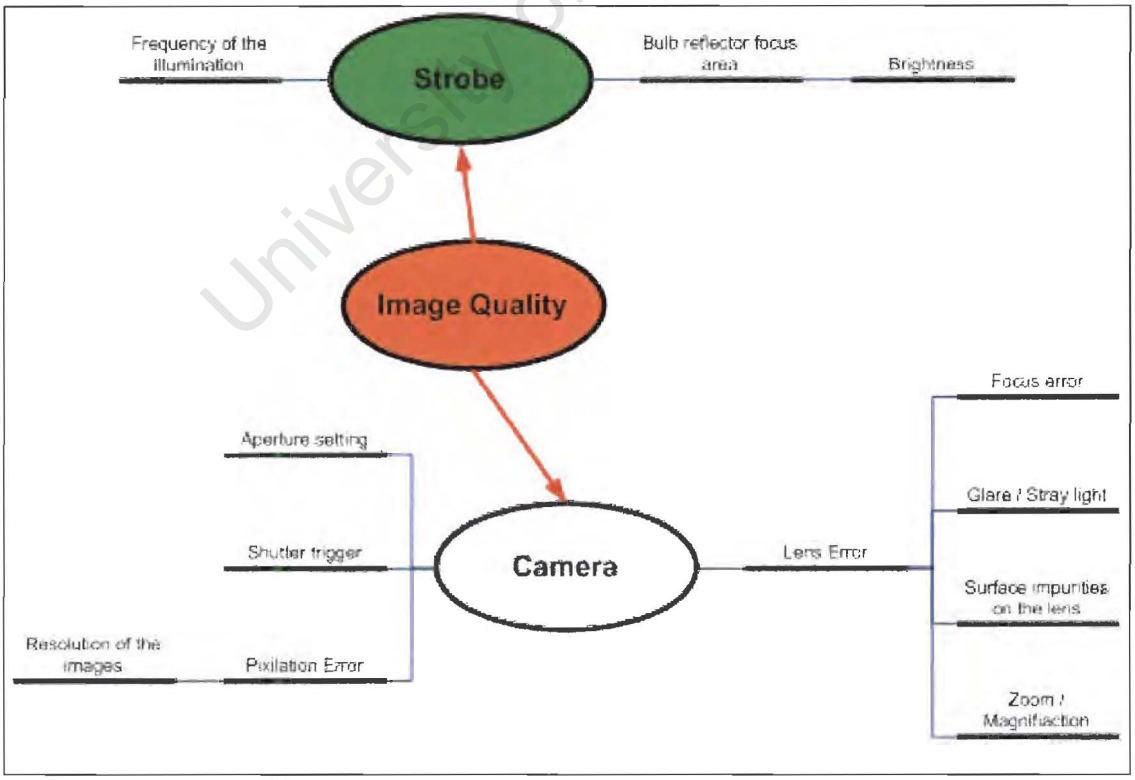

Figure 5-30 – Source of image quality errors

As shown in **Figure 5-30**, the choice of the camera and lens affects the quality of image. In experiments conducted by Maw *et al* [29], Foerster *et al* [35], and Kharaz *et al* [31], the type of camera chosen to capture the collision clearly shows the quality of the images captured. When Maw *et al* first investigated the theory of oblique impacts by colliding pucks on the flat plates; the availability in the photographic technology limited them to use manual SLR (Single Lens Reflex) cameras. The images were captured on the 35mm film and processed. This method becomes cumbersome when recording hundreds of collisions, as firstly the observer will not know if the images captured were in focus, adequate and clear to experimental specifications until the film has been processed into negatives. Secondly, each film role can hold only a limited number of pictures and having to process numerous film roles is costly. In 1994, Foerster *et al* [35] used high speed black and white film and a manual SLR camera to capture the in-flight collision of spheres. They digitized the images by scanning them using a 300dpi scanner (dots per inch). Digitizing the photographic film may have negative implications as the resolution of the image is limited to the dpi. Therefore the photographic images have to be enlarged in order to obtain good digital resolution.

With the advent of digital technology, the cameras have now been fitted with a CCD array of chips which can capture high quality images, close to the quality of their film role counterparts. Following Foerster *et al* [35] work, Lorenz *et al* [37] employed a 1.31 Mega Pixel camera to capture the collision of in-flight spheres. Kharaz *et al* [31] in their experiment employed a 0.3 Mega Pixel camera concentrating on a small area of the field of view of the collision between spheres and flat plate.

In all these attempts, although the results obtained seem reasonable, i.e. of Foerster *et al* [35] and Kharaz *et al* [31], the authors did not take into account the error caused by the lens distortions of the camera.

the lenses of optical instruments cannot be perfect and so introduce lens errors that distort the image by a variety of mechanisms associated with defects (commonly referred to as

aberrations) resulting from the spherical geometry of lens surfaces. There are three primary sources of non-ideal lens action (errors) that are observed:

- The on-axis lens errors such as chromatic and spherical aberration.
- The major off-axis errors manifested as coma, astigmatism, and field curvature.
- And a third class of aberrations, commonly seen in cameras that have zoom lens systems, is geometrical distortion, which includes both barrel distortion and pincushion distortion.

The Focal point is where light converges to a single point after passing through the lens. Focal length is the distance between the focal point and optical centre of the lens. **Figure 5-31** illustrates these terminologies.

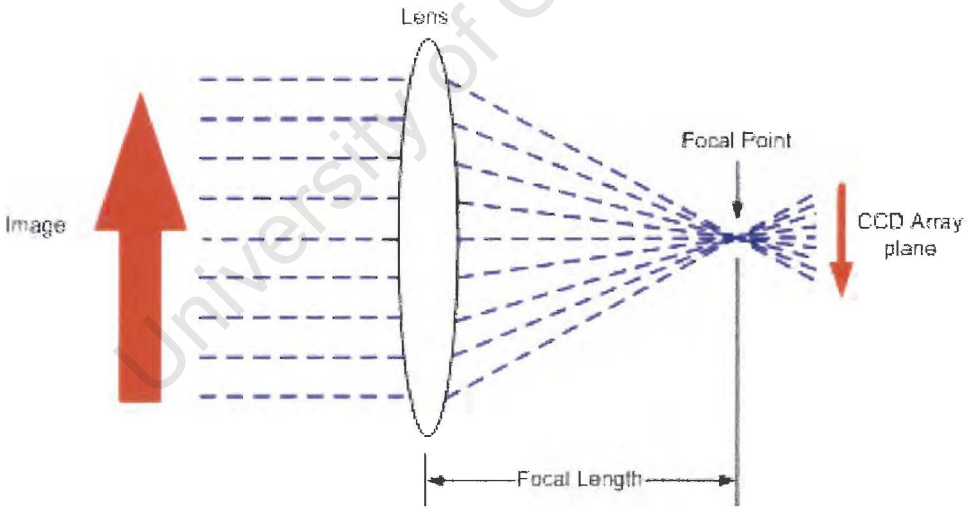

Figure 5-31 – Focal points and Focal Length

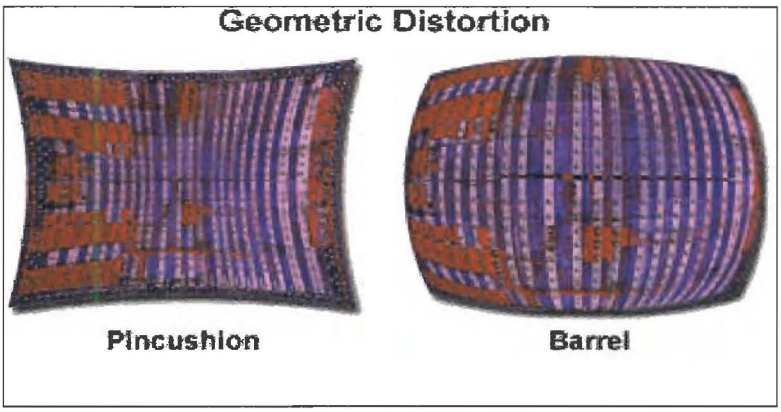

Figure 5-32 – Types of geometric distortion

Olympus microscopy resource centre have defined the geometrical distortion aberration in the following manner:

"Geometric distortion is manifested by changes in the shape of an image rather than the sharpness or colour spectrum. The two most prevalent types of geometrical distortion, positive and negative are termed pincushion and barrel, respectively." – www.olympusmicro.com

When images suffer from distortion, the true geometry of a specimen is no longer maintained in the image. This is a critical factor when measuring relative distances of the colliding spheres that can result in under or over estimated values. **Figure 5-32** illustrates exaggerated examples of significant pincushion and barrel distortion in the image of a computer microprocessor integrated circuit.

Geometric distortion can be difficult to detect, especially when the aberration is relatively slight and the image lacks periodic structures. This is most severe in images that have straight lines, such as periodic grids, squares, rectangles or other regular polygonal features that readily show the curvature present from distortion. Distortion is often found in optical designs utilizing compound lens systems (telephoto, fisheye, and zoom) containing meniscus, concave, hemispherical, and thick convex lenses.

Complex lens systems, such as the zoom design, can result in pronounced distortion, which may vary with focal length, producing pincushion distortion at long focal lengths and barrel distortion at short focal lengths.

5.7.3.1 Geometric Lens Correction

Initial grid calibration tests were conducted to check the profound effect of the geometric aberration. **Figure 5-33** illustrates the calibration grid used to check for aberrations. This image was imported into a CAD (Computer Aided Design) software package to check if the parallel lines were "truly" parallel.

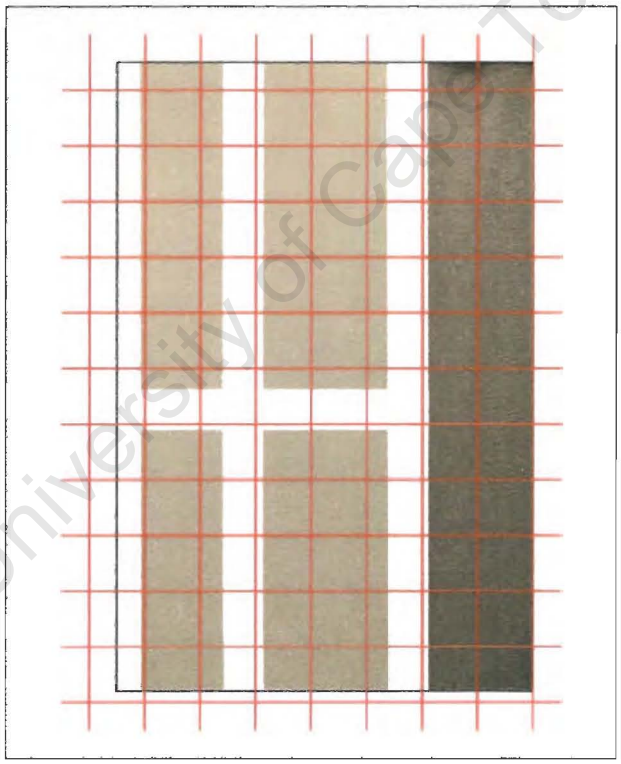

Figure 5-33 – Checking for image distortions

If the image was distorted, considerable effect of the geometric aberration will be noticed around the edges. As shown in **Figure 5-33**, the quality of the image is suitable for data analysis and collection. There are no observed geometric aberrations in the image. Since the colliding spheres are captured at the centre of the frame, there will not be any

measurable effect of the barrel and pincushion type errors; therefore the contribution to error is set to zero.

5.7.4 Image processing

This is the final stage of the rigorous assessments of the experimental procedure. Here the enhanced images are imported into ACAD for scaling and measuring the pertinent dimensions from the relative particles. **Figure 5-34** illustrates the breakdown of the possible sources of errors which may affect the dimensional outcomes.

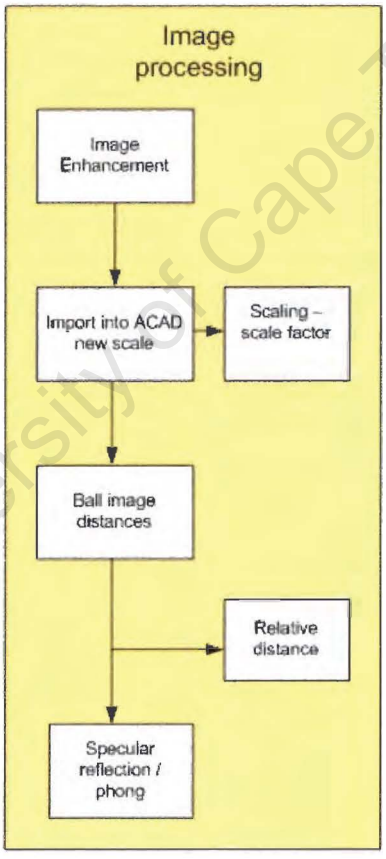

Figure 5-34 – Sources of inaccuracies in image processing

The following section calculates the sources of errors at various stages of image processing. The summed sources of errors are then propagated into the pertinent pre- and post impact relative impact velocities. The mechanical setup reliably reproduces the two

particle collision in free fall. The mechanical setup has no effect on the particles when they are in free fall and therefore cannot contribute to experimental error.

5.7.4.1 Scaling error

In the image processing, the captured images are ACAD and scaled according the relative scale factor between pixel measurement and the known actual measurement. A methodology is presented here to measure any onset errors while scaling the images.

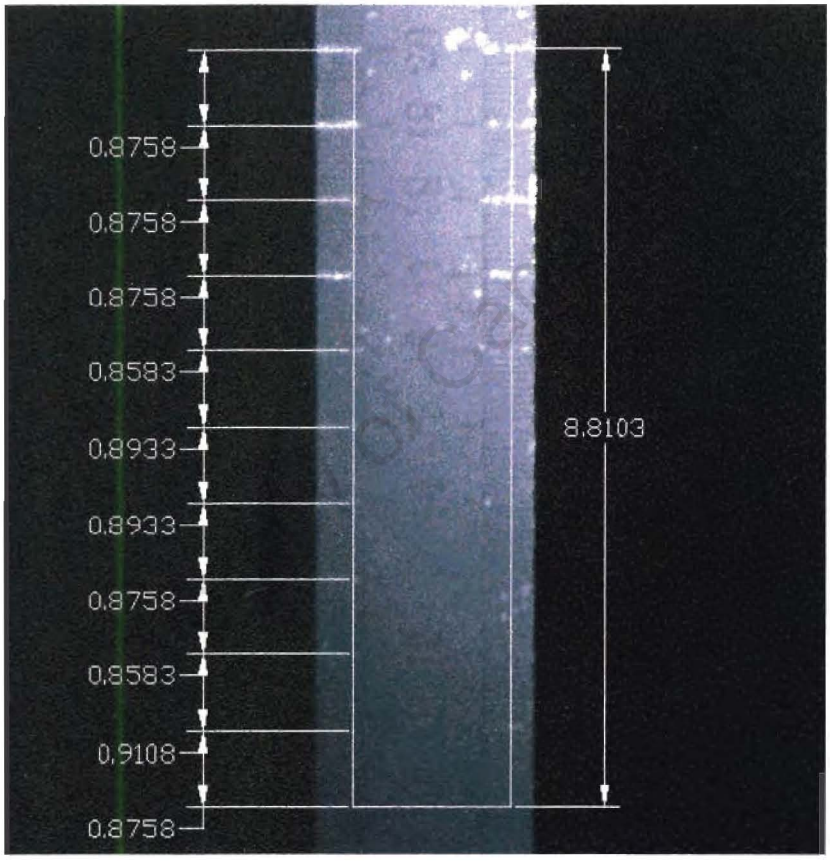

Figure 5-35 – Scale factor calibration, ACAD units of length

To calibrate the scale ruler in the image, **Figure 5-35** illustrates the scale factor calibration error. Because the imported images in CAD are rescaled automatically, all images are scaled in order to get the actual relative distances. Therefore $ActualL = sf * measuredL$.

sf, scale factor is $= \frac{8.8103}{100}$ unit / mm

And the error in the scale factor sf is:

$$\Delta sf, \text{ error in the scale factor} = \frac{\left(\sum_{n=10} unitlength10mm\right) - unitlength100mm}{100}$$

$$= \frac{|(8.793 - 8.8103)|}{100}$$

$$= 0.000173$$

The error in the scale factor is conducted on 10 separate images; giving an average calculated error of ± 0.00012 Acad unit/mm. It can be assumed that this error is propagated for all tested materials as the length of the scaled ruler does not change; only the pixel length is rescaled in the CAD software.

Therefore percentage error on the scale factor is:

$$\% \text{ Error} = \frac{\Delta sf}{sf} * 100$$

$$= \frac{0.000173}{0.088103} * 100$$

$$= 0.20\%$$

The percentage error contributed by the scale factor is less than 0.2% as assessed by multiple measurements in ACAD length units of fixed ruler intervals.

5.7.4.2 Image drift error

The error in the offset calculation is presented here. It is important to determine the effect of image processing on the estimated offsets from individual images, because the offsets are used to estimate the normal and tangent about the contact point which results in the

calculation of the normal and tangential coefficients of restitutions and friction, it is imperative to determine the effects of any onset of errors on the offsets. To estimate these errors we calculate the error in horizontal drift of the measured centroids of the tested materials.

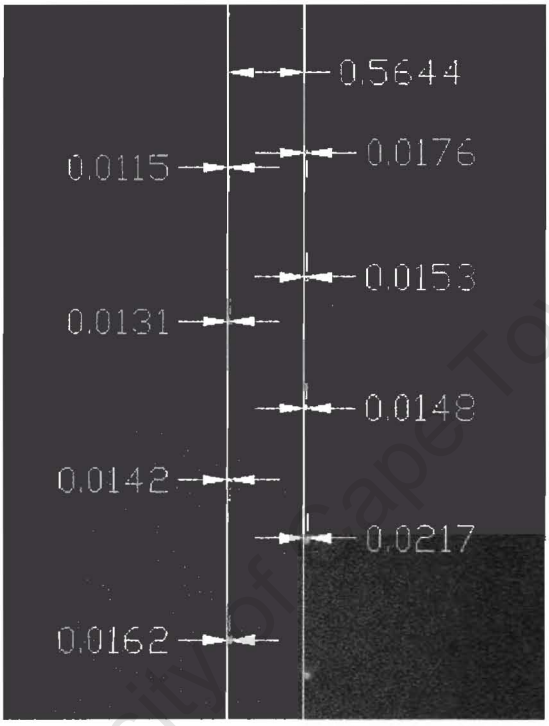

Figure 5-36 – ACAD measurement of drift for shiny materials

Figure 5-36 and **Figure 5-40,** illustrates centroid drift calculations for shiny and non shiny materials. The measurements are the distance between a vertical line and the measured centre of the ball. For the shiny materials, because of the high reflectivity, the specular reflections are used as reference points of the centres of the images. These specular reflection points are used to determine the pre- and post- relative distances before and after collision and offset distances pre- collision. Therefore it is pertinent to identify if the measured distances are affected by drift in the horizontal axis, because each collision is a product of the varying offset distance in the horizontal axis.

Two vertical lines are drawn as illustrated in **Figure 5-36** for particle 1 and 2 images using the ORTHAGONAL function in ACAD. Each specular image of particle 1 and 2

are ZOOMED in on as shown in **Figure 5-37** to identify the centroid. As shown in **Figure 5-37** the image becomes pixelled as we ZOOM in. If we regenerate the pixels, we can superimpose a circle, thus determining the centroid of the shiny particle.

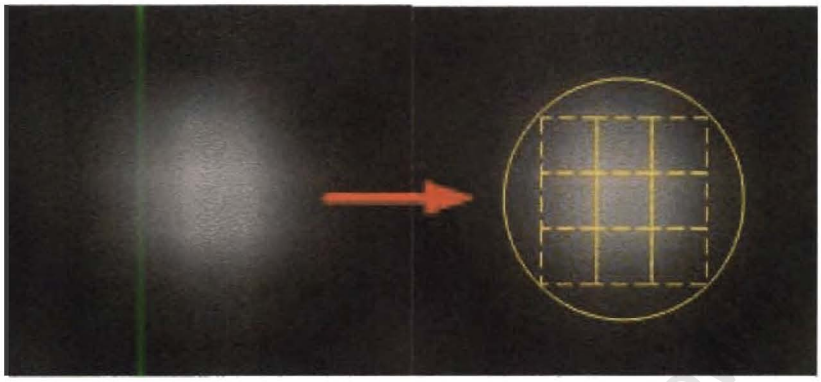

Figure 5-37 – Identifying the centroid of the specular reflection

Once the centroids of the specular reflections of particle 1 and 2 have been identified, the vertical lines are drawn cutting through the rest of the specular reflection images above and below as illustrated in **Figure 5-36**. It is assumed that the balls fall vertically and any scatter about the best fit vertical line arises from image analysis errors.

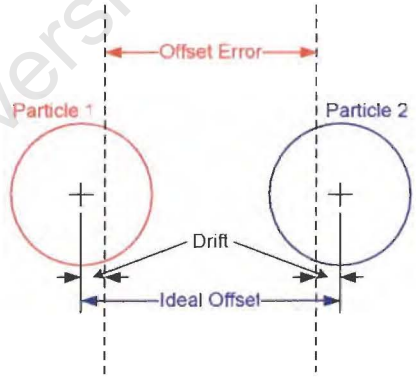

Figure 5-38 – Calculating the drift

Using the sign convention as illustrate in the schematic **Figure 5-38,** we can identify the maximum and minimum drift distances for particle 1 and 2 as given in **Table 5-4**.

Similarly we can now calculate the drift for the non-shiny materials. Because the non-shiny materials do not exhibit properties such as specular reflections, full images of the surfaces can be distinguished. The process of the identifying the full shape image depends on the scale factor; the following method is used to superimpose circles over the images:

- The scale factors of the individual images are calculated.
- Actual dimensions (diameter) of the balls are measured using a digital Vernier calliper with an accuracy of ± 0.01 mm.
- Image diameter is calculated using the scale factor and the actual diameter.
- Circles are drawn of the estimated dimensions of the balls.
- The circles are copied and pasted over the colliding ball images pre- and post collision by the user based on subjective fit as shown in **Figure 5-39**.

Figure 5-39 – Identifying the overall shape of the non shiny balls

Once the circles are fitted over the ball images in the CAD software, centroid of the circle is identified using the OBJECT SNAP function and vertical lines are drawn for both particle 1 and 2 using the ORTHAGONAL function. Similar to the reflective materials, the vertical lines passing through the ball images are drawn.

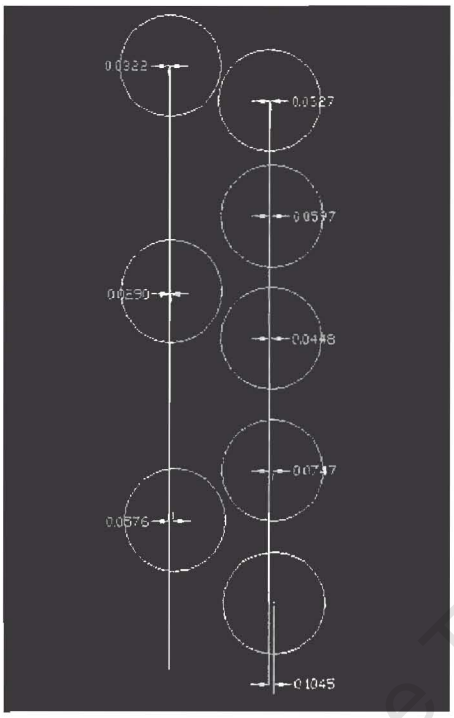

Figure 5-40 – ACAD measurement of drift for non shiny materials

Calculating and identifying the maximum and minimum drift distances for particle 1 and 2 are shown in **Figure 5-40.** The errors in the measurement of the offset are presented in **Table 5-4.**

Material	**Offset Error**			
	Offset Distance	*Drift Max*	*Drift Min*	*Sum of Drift For P_1 and P_2*
Steel Particle 1	0.5644	+0.0217	-0.0148	+0.0379
Steel Particle 2		+0.0162	-0.0115	-0.0263
Ceramic Particle 1	0.4432	+0.0189	-0.0163	+0.0335
Ceramic Particle 2		+0.0146	-0.0145	-0.0308
Teflon Particle 1	1.9654	+0.1045	-0.0327	+0.1367
Teflon Particle 2		+0.0322	-0.0290	-0.0617

Table 5-4 – Drift for Steel, Ceramic and Teflon (dimensions in ACAD length units)

The offset drift errors shown in **Table 5-4,** are offset specific. That is the relative errors will be greater for small offsets than larger offsets. Therefore to determine the percentage error for varying offset distance, **Table 5-4** is recalculated for the corresponding variable shown in **Table 5-5**.

Material	**Offset Error**				
	Offset Distance	*Drift Max*	*Drift Min*	*Ave. Drift For P_1 and P_2*	*Error*
Steel Particle 1	*XXX*	+0.0217	-0.0148	$\frac{0.0379-0.0263}{2}$	$\frac{0.0058}{(XXX+0.0058)}$
Steel Particle 2		+0.0162	-0.0115		
Ceramic Particle 1	*XXX*	+0.0189	-0.0163	$\frac{0.0335-0.0308}{2}$	$\frac{0.00135}{(XXX+0.00135)}$
Ceramic Particle 2		+0.0146	-0.0145		
Teflon Particle 1	*XXX*	+0.1045	-0.0327	$\frac{0.1367-0.0617}{2}$	$\frac{0.0375}{(XXX+0.0375)}$
Teflon Particle 2		+0.0322	-0.0290		

Table 5-5 – Drift errors for changing offset

Table 5-5 shows the change in the measured error for varying offset dimensions. It is noted that these offset dimensions are image specific; that is whenever an image is imported into ACAD for dimensioning, the user has no control over the scaling. For these particular images as illustrated in **Figure 5-36** and **Figure 5-40**, the corresponding errors are tabulated in **Table 5-6** :

Material	Offset	Error Formulae	% Error
Steel	0.5644	$\frac{0.0058}{(XXX+0.0058)}$	1%
Ceramic	0.4432	$\frac{0.00135}{(XXX+0.00135)}$	0.3%
Teflon	1.9654	$\frac{0.0375}{(XXX+0.0375)}$	1.8%

Table 5-6 – Percentage Drift error

Introducing a suitable drift error based on the measured offset value is a cumbersome task. This is because the errors are changing considerably for the measured offset distances from direct impact to completely sliding. The offset value is particularly used to determine the contact angle between the colliding balls. **Figure 5-41** illustrates the relationship for varying offset distances and contact angle. From the relationship it is noted that the contact angle is not linear with respect to the offset; indicating that for small offset distance, the change in contact angle will be less and have small %error than for large offset distance.

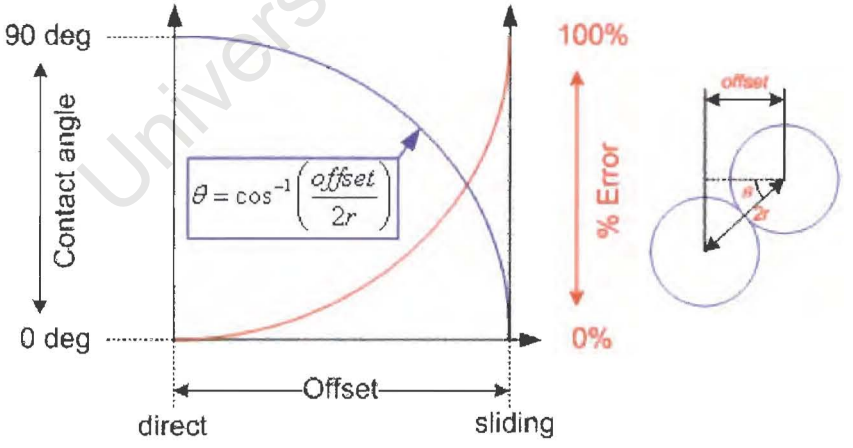

Figure 5-41 – Function of offset on contact angle and %error

Therefore the errors calculated for the offset drift as shown in **Table 5-6** cannot be used to generalise the overall experimental errors introduced for the offset. Instead, the

absolute errors will be used to define the errors about the offset. To calculate the absolute errors, the following procedure was implemented:

- Sample images were selected randomly to get a range of offset values for Steel, Ceramic and Teflon ball bearings (10 images per material).
- Vertical lines were drawn as shown in **Figure 5-36** and **Figure 5-40** to demarcate the drift in the falling ball images.
- Drift for each subsequent ball images for Particle 1 and 2 were tabulated and converted into actual measurements using the scaled ruler ratio calculation.
- Because the vertical lines drawn are best possible fit through all ball images, average drift is calculated about the line using the standard root mean squared (RMS) calculation.
- These calculated RMS values are the absolute errors for the all selected centres about the vertical line.
- Because the absolute error calculated is the drift about the vertical line, we assume that the error in vertical locations of the ball is the same as the horizontal error and then this same absolute error can be used on the likely error in the measured relative distances between successive images of the balls in the pre – and post- collision.

Material	*RMS*
Steel Particle 1	0.195
Steel Particle 2	0.188
Ceramic Particle 1	0.172
Ceramic Particle 2	0.165
Teflon Particle 1	1.161
Teflon Particle 2	1.656

Table 5-7 – Calculating the Absolute error for Steel, Ceramic and Teflon (all dimensions in mm)

As shown in **Table 5-7** the absolute errors calculated for steel, ceramic and Teflon balls change for the particle 1 and 2. It is noted that the Teflon balls contribute significant error

on drift about the vertical lines. This is resulted by the selection of the non-specular reflection ball image on the photographs.

To calculate the error in the offset, the absolute error of particle 1 and 2 are added and is tabulated in **Table 5-8**.

Material	Offset Error
Steel	± 0.383
Ceramic	± 0.338
Teflon	± 2.817

Table 5-8 – Absolute offset error (in mm)

The absolute errors for the pre- and post- collision ball images are shown in **Table 5-10** and **Table 5-9**.

Material	Post X_1 error	Post X_2 error	Post Y_1 error	Post Y_2 error
Steel	± 0.390	± 0.376	± 0.390	± 0.376
Ceramic	± 0.344	± 0.330	± 0.344	± 0.330
Teflon	± 2.322	± 3.312	± 2.322	± 3.312

Table 5-9 – Post collision absolute errors (in mm)

Material	Pre Y_1 error	Pre Y_2 error
Steel	± 0.390	± 0.376
Ceramic	± 0.344	± 0.330
Teflon	± 2.322	± 3.312

Table 5-10 – Pre collision absolute errors (in mm)

To calculate the pre- and post- collision errors, the corresponding Particle 1 and Particle 2 errors are doubled. This is because the pre- and post- collision velocities are calculated for each particle separately, therefore their corresponding errors are calculated the same.

Figure 5-42 illustrates how the corresponding absolute errors are summed for post-collision. It is noted that the X and Y error component are equal for each material type.

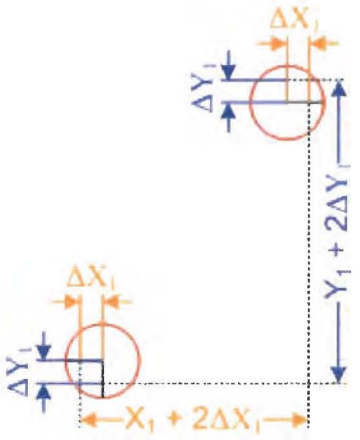

Figure 5-42 – Post collision error calculation (for particle1)

5.7.4.3 Post collisional spin error

Post- collisional spin orientations are calculated from the captured on photographic images as shown in **Figure 5-43.** Spin orientations of the Teflon balls are measured in ACAD using the ANGULAR dimension function as shown in **Figure 5-44.**

Figure 5-43 – Teflon spin orientations

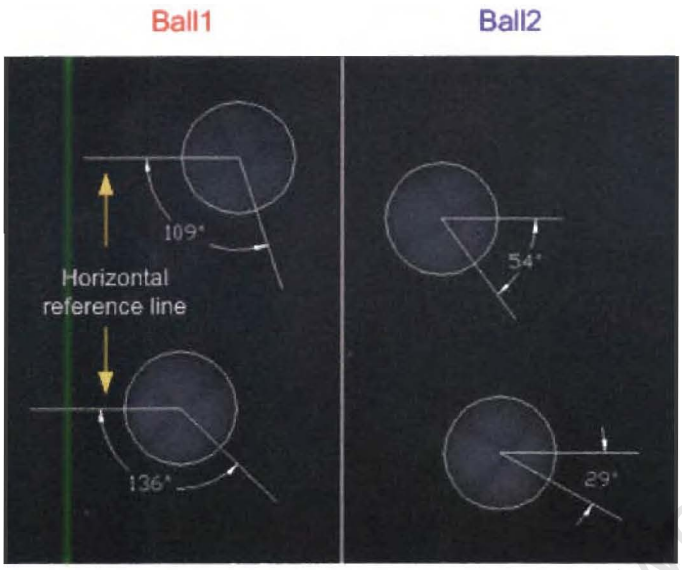

Figure 5-44 – Angular dimension in ACAD

Measuring the angles of spin in ACAD is subjective. This leads to error in fitting the best fit lines about the centroids of the Teflon balls to measure the angles. Once the circles are superimposed over the images as explained extensively earlier in this chapter, horizontal lines are drawn using the OBJECT SNAP and ORTHO functions about the centres of each subsequent image. The next step is to switch off the ORTHO function and draw lines from the centres to the demarcated line edges on the images. Because the lines are fitted by the user, errors are calculated in fitting angular lines in the images. This is illustrated in the schematic shown in **Figure 5-45.**

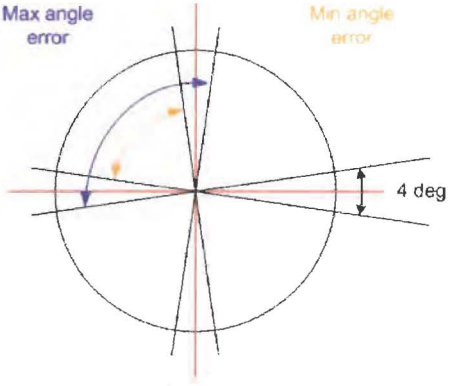

Figure 5-45 – Error in spin calculation

From repeated measures the error in estimating the angle for the total maximum minus minimum error is approximately ± 4 degrees. This is estimated from the fitted lines which have an error of ± 2 degrees about each axis as shown in **Figure 5-45.**

5.8 Propagation of Error Calculation

Summarising all the contributing errors from the various stages of the experimental procedures, the following pertinent sources of inaccuracies which can affect the overall results have been identified. Therefore, errors which significantly affect the measured relative distances of the particles are listed below and tabulated in **Table 5-11** :

- Specular reflections affecting the location of the centroid of highly polished materials.
- Angular offset angles from image plane to image plane. Those outside a selected angular range were discarded to reduce this error.
- Importing images into ACAD and scaling and dimensioning.
- Accuracy of location of the centre of the image – this was derived from the drift about the ideal vertical drop line.

Table of Errors								
Material	*Offset Drift(X) – (mm)*	*Specular Reflection($Y_{1,2}$)*	*Angular offset($X_{1,2}$)*	*Scaling and importing in ACAD(X&Y)*	*Pre collision(Y_1) – (mm)*	*Pre collision(Y_2) – (mm)*	*Post collision (X_1 & Y_1) – (mm)*	*Post collision (X_2 & Y_2) – (mm)*
Steel	± 0.383	0.7%	0.14%	0.2%	± 0.390	± 0.376	± 0.390	± 0.376
Ceramic	± 0.338	0.5%	1.51%	0.2%	± 0.344	± 0.330	± 0.344	± 0.330
Teflon	± 2.817	nil	0.14%	0.2%	± 2.322	± 3.312	± 2.322	± 3.312

Table 5-11 – Table of Errors in the appropriate X and Y directions

The calculated errors are listed below. Δm is estimated from the instrument specification, and it is $\pm 0.001g$ for the weighing scale.

- ΔS is the specular reflection offset error for shiny material. This is zero for other materials.
- ΔAng is the angular offset angle of impact plots in the X-direction.
- Δsf is the error in the scale factor.
- I_{off} is the absolute error in the offset.
- I_y, absolute error in the pre collision measurements in the Y plane
- I'_x and I'_y, absolute error in the post collision measurements in the X and Y plane
- Δm, measured mass error for each particle (assumed to be equivalent for both particles)

Therefore summing up all of the above errors which contribute to the measured relative distances L (m):

For X – direction components (pre- collision):

$$\Delta L_{off} = \left(L_{off} * \left[\Delta sf + \Delta Ang\right]\right) + \left(I_{off} + \left[I_{off} * \Delta sf\right]\right) \qquad \textbf{Equation 5-5}$$

For X – direction components (post- collision):

$$\Delta L'_x = \left(L'_x * \left[\Delta sf + \Delta Ang\right]\right) + \left(I'_x + \left[I'_x * \Delta sf\right]\right) \qquad \textbf{Equation 5-6}$$

For Y – direction components (pre- collision):

$$\Delta L_y = \left(L_y * \left[\Delta sf + \Delta S\right]\right) + \left(I_y + \left[I_y * \Delta sf\right]\right) \qquad \textbf{Equation 5-7}$$

For Y – direction components (post- collision):

$$\Delta L'_y = \left(L'_y * \left[\Delta sf + \Delta S\right]\right) + \left(I'_y + \left[I'_y * \Delta sf\right]\right) \qquad \textbf{Equation 5-8}$$

The calculated relative velocities are shown in **Table 5-12.** The derivation of these velocities will be discussed further in the **Chapter 6**.

	Pre- impact vel.	**Post- impact *y* vel.**	**Post- impact *x* vel.**
Particle 1	$v_1 = \frac{y_1 + \frac{1}{2}at^2}{t}$	$u(y)_1 = \frac{y_1' - \frac{1}{2}at^2}{t}$	$u(x)_1 = \frac{x_1'}{t}$
Particle 2	$v_2 = \frac{y_2 + \frac{1}{2}at^2}{t}$	$u(y)_2 = \frac{y_2' - \frac{1}{2}at^2}{t}$	$u(x)_2 = \frac{x_2'}{t}$

Table 5-12 – Relative velocities for Particle 1 and 2

Note: y_1 and y_2 and x_1 and x_2 are measured relative distances and are equal to L_y and L_x respectively. C_1 and C_2 are calculated pre-impact relative velocities and are equal to v_1 and v_2, C_1' and C_2' are post- impact velocities and are equal to u_1 and u_2. Now including the error in the L and t, using the propagation error analysis from **Appendix [E]** – Propagation of Errors:

Pre- velocity example:

$$C_1 = \frac{L_1 + \frac{1}{2}at^2}{t}$$

Given that a is the acdeleration due to gravity and is a constant and time t is assumed to have no source of error;

$$\left(\frac{\Delta C_1}{C_1}\right)^2 = \left(\frac{\Delta L_1}{L_1}\right)^2$$

$$\Delta C_1 = C_1\left(\frac{\Delta L_1}{L_1}\right) \qquad \textbf{Equation 5-9}$$

Post- velocity example:

$$C_1' = \frac{L_1'}{t}$$

$$\left(\frac{\Delta C_1'}{C_1'}\right)^2 = \left(\frac{\Delta L_1'}{L_1'}\right)^2$$

$$\Delta C_1' = C_1'\left(\frac{\Delta L_1'}{L_1'}\right) \qquad \textbf{Equation 5-10}$$

Now that we have established the ΔC for the relative velocities, it can be applied for both particles. Therefore particle 1 and particle 2 will have following velocity errors as illustrated in **Table 5-13**.

	Pre- Collision Vel.		Post- Collision Vel.	
Velocity Component	**Particle 1**	**Particle 2**	**Particle 1**	**Particle 2**
X	0	0	$\Delta C_{1x}'$	$\Delta C_{2x}'$
Y	ΔC_{1y}	ΔC_{2y}	$\Delta C_{1y}'$	$\Delta C_{2y}'$

Table 5-13 - Velocity error components

Note, $\Delta C_{1x}'$ and $\Delta C_{2x}'$ have the angular offset angle of impact plots incorporated in them. The propagation of error is applied to the Foerster *et al* [35] rigid body theory to calculate the total error in each of the derived material interaction parameters.

5.8.1 Error – Non Dimensional Constants

Using Maw et al's analysis, the non dimensional angle of incidence Ψ_1 vs. non dimensional angle of reflection Ψ_2 of the contact point is calculated as:

$$\psi_1 \equiv -\frac{(\boldsymbol{u}\cdot\boldsymbol{t})}{(\boldsymbol{u}\cdot\boldsymbol{n})} \qquad \textbf{Equation 5-11}$$

To evaluate the propagated error, the geometry of the collision is drawn as illustrated in **Figure 5-46.**

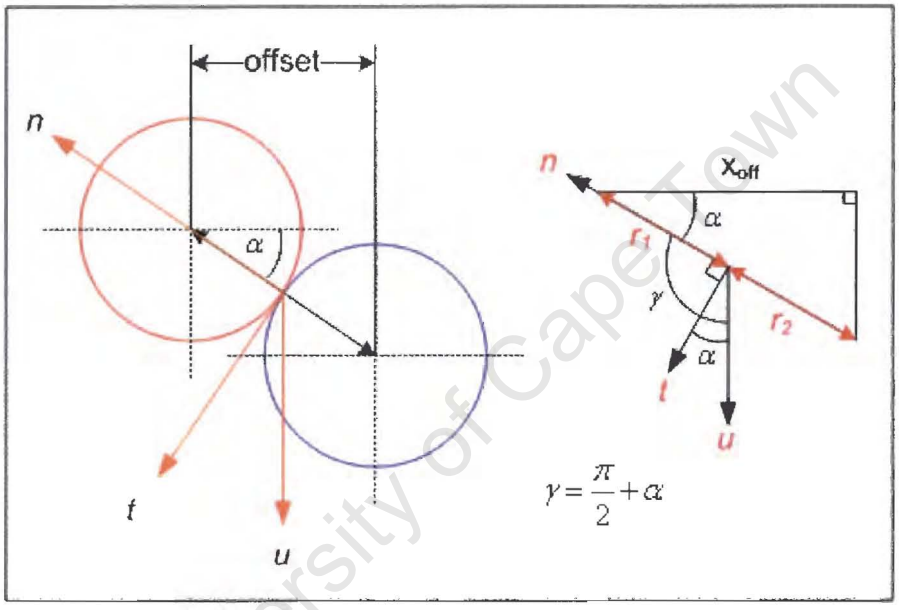

Figure 5-46 – Geometric Analysis of the collision

ψ_1 can be rewritten as:

$$\psi_1 \equiv -\frac{|\boldsymbol{u}|\cdot|\boldsymbol{t}|\cos\alpha}{|\boldsymbol{u}|\cdot|\boldsymbol{n}|\cos\left(\frac{\pi}{2}+\alpha\right)} \equiv -\frac{\cos\alpha}{\cos\left(\frac{\pi}{2}+\alpha\right)} \qquad \textbf{Equation 5-12}$$

It is noted that unit vectors $\boldsymbol{n}$ and $\boldsymbol{t}$ are equal to 1 and therefore ψ_1 is dominated by the offset distance between the two particles.

The error in the angle α, where $D = r_1 + r_2$ and $\Delta D = \Delta r_1 + \Delta r_2$

$$\cos\alpha = \frac{x_{off}}{r_1 + r_2} = \frac{x_{off}}{D} \qquad \textbf{Equation 5-13}$$

$$\Delta\cos\alpha = \cos\alpha\sqrt{\left(\frac{\Delta x_{off}}{x_{off}}\right)^2 + \left(\frac{\Delta D}{D}\right)^2} \qquad \textbf{Equation 5-14}$$

Thus,

$$\Delta\cos\alpha = \frac{x_{off}}{D}\sqrt{\left(\frac{\Delta x_{off}}{x_{off}}\right)^2 + \left(\frac{\Delta D}{D}\right)^2} \qquad \textbf{Equation 5-15}$$

The contributing error from ΔD is very small, therefore can be omitted from **Equation 5-15**. Therefore,

$$\Delta\cos\alpha = \frac{x_{off}}{D} * \frac{\Delta x_{off}}{x_{off}} = \frac{\Delta x_{off}}{D} \qquad \textbf{Equation 5-16}$$

Thus using equation 5-12, calculating the error in ψ_1:

$$\Delta\psi_1 = \psi_1\sqrt{\left(\frac{\Delta x_{off}}{D}\right)^2 + \left(\frac{\Delta x_{off}}{D}\right)^2} = \psi_1\sqrt{2}\frac{\Delta x_{off}}{D} \qquad \textbf{Equation 5-17}$$

To resolve the error the in ψ_2, where ψ_2 is given by::

$$\psi_2 \equiv -\frac{\left(\boldsymbol{u}' \cdot \boldsymbol{t}\right)}{\left(\boldsymbol{u} \cdot \boldsymbol{n}\right)} \qquad \textbf{Equation 5-18}$$

This is expanded using the relationships in Chapter 2 – literature review:

$$\psi_2 \equiv -\frac{\left(\left\{\left(\boldsymbol{C}_1^{'}-\boldsymbol{C}_2^{'}\right)+\left[\frac{5}{2}m^{*}\boldsymbol{J}\right]-\left[\frac{5}{2}m^{*}\left(\boldsymbol{n}\cdot\boldsymbol{J}\right)\boldsymbol{n}\right]\right\}\cdot\boldsymbol{t}\right)}{\left(\boldsymbol{u}\cdot\boldsymbol{n}\right)} \qquad \textbf{Equation 5-19}$$

Where, $m^{*}=\frac{1}{m_1^{-1}+m_2^{-1}}$. Resolving for pre- velocity using the impulse equations:

$$\psi_2 \equiv -\frac{\left(\left[\left(\frac{\boldsymbol{J}}{m_1}+\boldsymbol{C}_1\right)-\left(\boldsymbol{C}_2-\frac{\boldsymbol{J}}{m_2}\right)+\left(\frac{5}{2}m^{*}\boldsymbol{J}\right)\right]\cdot\boldsymbol{t}\right)}{\left(\boldsymbol{u}\cdot\boldsymbol{n}\right)} \qquad \textbf{Equation 5-20}$$

Therefore:

$$\psi_2 \equiv -\frac{\left(\boldsymbol{u}\cdot\boldsymbol{t}+\left(\frac{7}{2}m^{*}\boldsymbol{J}\cdot\boldsymbol{t}\right)\right)}{\left(\boldsymbol{u}\cdot\boldsymbol{n}\right)} \qquad \textbf{Equation 5-21}$$

$$\psi_2 \equiv -\frac{|\boldsymbol{u}||\boldsymbol{t}|\cos\alpha+\frac{7}{2}m^{*}|\boldsymbol{J}||\boldsymbol{t}|\left(\cos\vartheta+\frac{\pi}{2}\right)}{|\boldsymbol{u}||\boldsymbol{n}|\cos\gamma} \qquad \textbf{Equation 5-22}$$

The angle ϑ is calculated geometrically as shown in **Figure 5-47** and **Figure 5-48.** The impulse is given by the post impact velocity vector minus the pre-impact velocity vector.

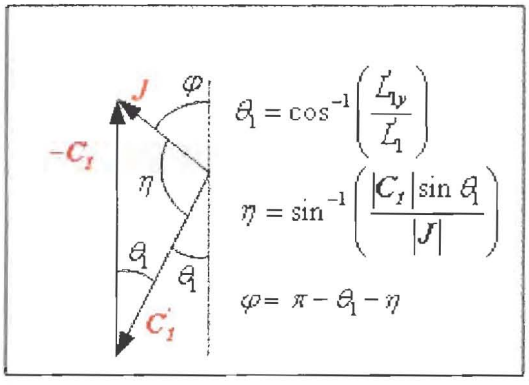

Figure 5-47 – Vector diagram of the Impulse

In Figure 5-48 the relationship of J to the normal vector, n, is derived.

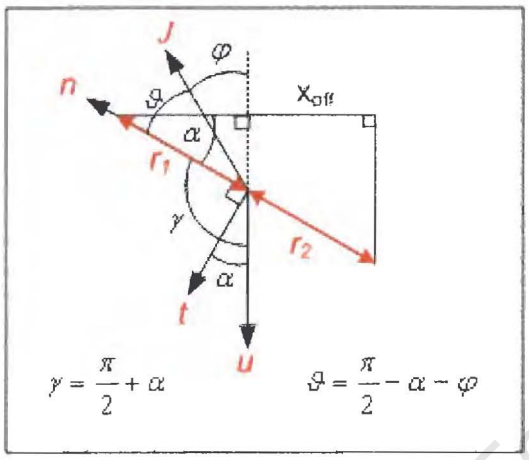

Figure 5-48 – Geometric analysis of the collision with Impulse

Thus the error the in ψ_2,

$$\Delta\psi_2 \equiv \psi_2 \sqrt{\left(\frac{\Delta x_{off}}{D}\right)^2 + \left(\frac{\Delta x_{off}}{D}\right)^2 + \left(\frac{\Delta x_{off}}{D}\right)^2 + \left(\frac{\Delta \boldsymbol{u}}{\boldsymbol{u}}\right)^2 + \left(\frac{\Delta \boldsymbol{u}}{\boldsymbol{u}}\right)^2 + \left(\frac{\Delta \boldsymbol{J}}{\boldsymbol{J}}\right)^2 + \left(\frac{\Delta\theta_1}{\theta_1}\right)^2 + \left(\frac{\Delta\eta}{\eta}\right)^2}$$

Equation 5-23

Where:

$\frac{\Delta\theta_1}{\theta_1} = \sqrt{\left(\frac{\Delta L_{1y}^{'}}{L_{1y}^{'}}\right)^2 + \left(\frac{\Delta L_1^{'}}{L_1^{'}}\right)^2} = \sqrt{\left(\frac{\Delta L_{1y}^{'}}{L_{1y}^{'}}\right)^2 + \left(\frac{\Delta L_{1y}^{'} + \Delta L_{1x}^{'}}{L_1^{'}}\right)^2}$ (First order Taylor series estimation)
$\Delta \boldsymbol{J} = \boldsymbol{J}\sqrt{\left(\frac{\Delta m_1}{m_1}\right)^2 + \left(\frac{\Delta \boldsymbol{C}_1^{'}}{\boldsymbol{C}_1^{'}}\right)^2 + \left(\frac{\Delta \boldsymbol{C}_1}{\boldsymbol{C}_1}\right)^2}$ (Note $\frac{\Delta m_1}{m_1}$ is very small, therefore negligible)
$\Delta \boldsymbol{u} = \Delta \boldsymbol{C}_1 + \Delta \boldsymbol{C}_2$

$$\frac{\Delta\eta}{\eta}=\sqrt{\left(\frac{\Delta C_1^{'}}{C}\right)^2+\left(\frac{\Delta J}{J}\right)^2+\left(\frac{\Delta\theta}{\theta}\right)^2}$$ (First order Taylor series estimation)

$$u^{'}=u+\left[\left(\frac{7}{2m^*}\right)J\right]-\left[\left(\frac{5}{2m^*}\right)n(J\cdot n)\right]$$

$$u^{'}=u+\left[\left(\frac{7}{2m^*}\right)J\right]-\left[\left(\frac{5}{2m^*}\right)n(|J||n|\cos\vartheta)\right]$$

$$\Delta u^{'}=u^{'}\sqrt{\left(\frac{\Delta u}{u}\right)^2+3\left(\frac{\Delta J}{J}\right)^2+\left(\frac{\Delta x_{off}}{D}\right)^2+\left(\frac{\Delta L_{1y}^{'}}{L_{1y}^{'}}\right)^2+\left(\frac{\Delta L_{1y}^{'}+\Delta L_{1x}^{'}}{L_1^{'}}\right)^2+\left(\frac{\Delta n}{n}\right)^2}$$

$$\Delta u^{'}=u^{'}\sqrt{\left(\frac{\Delta C_1+\Delta C_2}{u}\right)^2+3\left(\frac{\Delta C_1^{'}}{C_1^{'}}\right)^2+3\left(\frac{\Delta C_1}{C_1}\right)^2+2\left(\frac{\Delta x_{off}}{D}\right)^2+\left(\frac{\Delta L_{1y}^{'}}{L_{1y}^{'}}\right)^2+\left(\frac{\Delta L_{1y}^{'}+\Delta L_{1x}^{'}}{L_1^{'}}\right)^2}$$

Simplified:

$$\Delta\psi_2\equiv\psi_2\sqrt{3\left(\frac{\Delta x_{off}}{D}\right)^2+2\left(\frac{\Delta C_1+\Delta C_2}{u}\right)^2+3\left(\frac{\Delta C_1^{'}}{C_1^{'}}\right)^2+2\left(\frac{\Delta C_1}{C_1}\right)^2+2\left(\frac{\Delta L_{1y}^{'}}{L_{1y}^{'}}\right)^2+2\left(\frac{\Delta L_{1y}^{'}+\Delta L_{1x}^{'}}{L_1^{'}}\right)^2}$$

Equation 5-24

5.8.2 Error – Coefficient of Normal Restitution

Calculating the coefficient of normal restitution:

$$e=-\frac{n\cdot u^{'}}{n\cdot u}$$ **Equation 5-25**

$$e=-\frac{\left[\left(\frac{J}{m_1}+C_1\right)-\left(C_2-\frac{J}{m_2}\right)+\left(\frac{5}{2}m^*J\right)-\left(\frac{5}{2}m^*(n\cdot J)n\right)\right]\cdot n}{u\cdot n}$$ **Equation 5-26**

$$e=-\frac{u\cdot n+m^*J\cdot n}{u\cdot n}$$ **Equation 5-27**

$$e = -\frac{|\boldsymbol{u}||\boldsymbol{n}|\cos\gamma + m^*|\boldsymbol{J}||\boldsymbol{n}|\cos\vartheta}{|\boldsymbol{u}||\boldsymbol{n}|\cos\gamma}$$ **Equation 5-28**

And its error is:

$$\Delta e = e\sqrt{\left(\frac{\Delta x_{off}}{D}\right)^2 + \left(\frac{\Delta x_{off}}{D}\right)^2 + \left(\frac{\Delta \boldsymbol{u}}{\boldsymbol{u}}\right)^2 + \left(\frac{\Delta \boldsymbol{u}}{\boldsymbol{u}}\right)^2 + \left(\frac{\Delta \boldsymbol{J}}{\boldsymbol{J}}\right)^2 + \left(\frac{\Delta\theta_1}{\theta_1}\right)^2 + \left(\frac{\Delta\eta}{\eta}\right)^2}$$

Equation 5-29

Simplified:

$$\Delta e = e\sqrt{2\left(\frac{\Delta x_{off}}{D}\right)^2 + 2\left(\frac{\Delta \boldsymbol{C}_1 + \Delta \boldsymbol{C}_2}{\boldsymbol{u}}\right)^2 + 3\left(\frac{\Delta \boldsymbol{C}_1'}{\boldsymbol{C}_1'}\right)^2 + 2\left(\frac{\Delta \boldsymbol{C}_1}{\boldsymbol{C}_1}\right)^2 + 2\left(\frac{\Delta L_{1y}'}{L_{1y}'}\right)^2 + 2\left(\frac{\Delta L_{1y}' + \Delta L_{1x}'}{L_1'}\right)^2}$$

Equation 5-30

5.8.3 Error – Coefficient of Friction

For collisions that involve sliding, the tangential and the normal components of the impulse are related by the coefficient of friction μ.

$$\mu = \frac{|\boldsymbol{n} \times \boldsymbol{J}|}{(\boldsymbol{n} \cdot \boldsymbol{J})}$$ **Equation 5-31**

$$\mu = \frac{|\boldsymbol{n}||\boldsymbol{J}|\sin\vartheta}{|\boldsymbol{n}||\boldsymbol{J}|\cos\vartheta} = \tan\vartheta$$ **Equation 5-32**

And it error is:

$$\Delta\tan\vartheta = \tan\vartheta\sqrt{\left(\frac{\Delta \boldsymbol{J}}{\boldsymbol{J}}\right)^2 + \left(\frac{\Delta\theta_1}{\theta_1}\right)^2 + \left(\frac{\Delta\eta}{\eta}\right)^2}$$ **Equation 5-33**

Simplified:

$$\Delta \tan\vartheta = \tan\vartheta\sqrt{3\left(\frac{\Delta C_1^{'}}{C_1^{'}}\right)^2 + 2\left(\frac{\Delta C_1}{C_1}\right)^2 + 2\left(\frac{\Delta L_{1y}^{'}}{L_{1y}^{'}}\right)^2 + 2\left(\frac{\Delta L_{1y}^{'} + \Delta L_{1x}^{'}}{L_1^{'}}\right)^2}$$

Equation 5-34

5.8.4 Error – Coefficient of Tangential Restitution

Coefficient of tangential restitution is defined as:

$$\boldsymbol{n}\times\boldsymbol{u}^{'} = -\beta(\boldsymbol{n}\times\boldsymbol{u})$$ **Equation 5-35**

Also,

$$\beta = -\frac{\boldsymbol{u}^{'}\cdot\boldsymbol{t}}{\boldsymbol{u}\cdot\boldsymbol{t}}$$

$$\beta = -\frac{\left[\left(\frac{\boldsymbol{J}}{m_1} + \boldsymbol{C}_1\right) - \left(\boldsymbol{C}_2 - \frac{\boldsymbol{J}}{m_2}\right) + \left(\frac{5}{2}m^{*}\boldsymbol{J}\right) - \left(\frac{5}{2}m^{*}(\boldsymbol{n}\cdot\boldsymbol{J})\boldsymbol{n}\right)\right]\cdot\boldsymbol{t}}{\boldsymbol{u}\cdot\boldsymbol{t}}$$ **Equation 5-36**

$$\beta = -\frac{\left(\boldsymbol{u}\cdot\boldsymbol{t} + \left(\frac{7}{2}m^{*}\boldsymbol{J}\cdot\boldsymbol{t}\right)\right)}{\boldsymbol{u}\cdot\boldsymbol{t}}$$ **Equation 5-37**

$$\beta \equiv -\frac{|\boldsymbol{u}||\boldsymbol{t}|\cos\alpha + \frac{7}{2}m^{*}|\boldsymbol{J}||\boldsymbol{t}|\left(\cos\vartheta + \frac{\pi}{2}\right)}{|\boldsymbol{u}||\boldsymbol{t}|\cos\alpha}$$ **Equation 5-38**

And its error is defined as:

$$\Delta\beta = \beta\sqrt{\left(\frac{\Delta x_{off}}{D}\right)^2 + \left(\frac{\Delta x_{off}}{D}\right)^2 + \left(\frac{\Delta x_{off}}{D}\right)^2 + \left(\frac{\Delta \boldsymbol{u}}{\boldsymbol{u}}\right)^2 + \left(\frac{\Delta \boldsymbol{u}}{\boldsymbol{u}}\right)^2 + \left(\frac{\Delta \boldsymbol{J}}{\boldsymbol{J}}\right)^2 + \left(\frac{\Delta\theta_1}{\theta_1}\right)^2 + \left(\frac{\Delta\eta}{\eta}\right)^2}$$

Equation 5-39

Simplified:

$$\Delta\beta = \beta\sqrt{3\left(\frac{\Delta x_{off}}{D}\right)^2 + 2\left(\frac{\Delta \boldsymbol{C}_1 + \Delta \boldsymbol{C}_2}{\boldsymbol{u}}\right)^2 + 3\left(\frac{\Delta C_1^{'}}{C_1^{'}}\right)^2 + 2\left(\frac{\Delta C_1}{C_1}\right)^2 + 2\left(\frac{\Delta L_{1y}^{'}}{L_{1y}^{'}}\right)^2 + 2\left(\frac{\Delta L_{1y}^{'} + \Delta L_{1x}^{'}}{L_1^{'}}\right)^2}$$

Equation 5-40

It is noted that the error in β and ψ_2 are similar, indicating that the Non dimensional angle of reflection is dominated by the tangential restitution. Summarising the contribution of errors on the material properties in **Table 5-14**:

Material property	Formulae	Error Contribution
Normal restitution	$e \pm \Delta e$	Offset, Pre- and Post velocities, Post ball image positions
Tangential restitution	$\beta \pm \Delta\beta$	Offset, Pre- and Post velocities, Post ball image positions
Friction	$\mu \pm \Delta\mu$	Pre- and Post velocities, Post ball image positions

Table 5-14 – Summary of error contribution

The error analysis calculations presented here will be a good measure of consistency of the data. It was reported by previous authors that this experimental technique is difficult to reproduce. Therefore if suitable measured material interaction properties are going to be incorporated into DEM, statistical analysis of the data should be given. In the results section that follows, the measured data is checked for inconsistency before proceeding to test the models in DEM.

5.9 Discussion

The experimental procedure presented in this chapter follows a rigorous methodology to minimise sources of error. Because the collisions of two particles are captured on photographic film in a dark room, methods and techniques to capture images using stroboscopic light were utilised. For Shiny materials such as steel ball bearings, the specular reflection is unavoidable, therefore limiting the capture of the full image.

An in depth analysis was conducted to quantify any possible sources of errors, and they were:

- Specular reflections affecting the location of the centroid of highly polished materials: This was calculated using the geometry and the position of the balls prior to collision
- Angular offset angles from image plane to image plane, and selecting and discarding images within the required angles: This was calculated from the impact scatter plots on carbon paper.
- Importing images into ACAD and scaling and dimensioning: This was calculated from the ACAD images.
- Accuracy of location of the centre of the image: This was derived from the drift about the ideal vertical drop line.

Each of the listed sources of errors was calculated as percentages and will be applied in the measured relative velocities and use the Foerster *et al* [35] rigid body theory to calculate the pertinent material interaction properties and their effects when the error is propagated.

Chapter 6

Experimental Results and Discussions

Particle interactions of steel, ceramic, and Teflon ball bearings are measured. This chapter shows the methodology of the rigid body calculations and derives relevant material interaction properties. These will then be applied to testing Discrete Element Method Models.

6.1 Summary of pertinent formulae

A summary of the pertinent formulae which are used to calculated the material interaction properties are presented here. **Figure 6-1** illustrates a schematic of the unit vector ***n*** and the tangent vector ***t*** at the contact point. The unit vector ***n*** is a function of the centre to centre offset distance:

$$\boldsymbol{n} = arc\ cos\left(\frac{offset}{r_1 + r_2}\right) \qquad \textbf{Equation 6-1}$$

Note that the directions of unit vectors ***n*** and ***t*** are dependent on the angle theta as shown in **Figure 6-1** and they are orthogonal to each other.

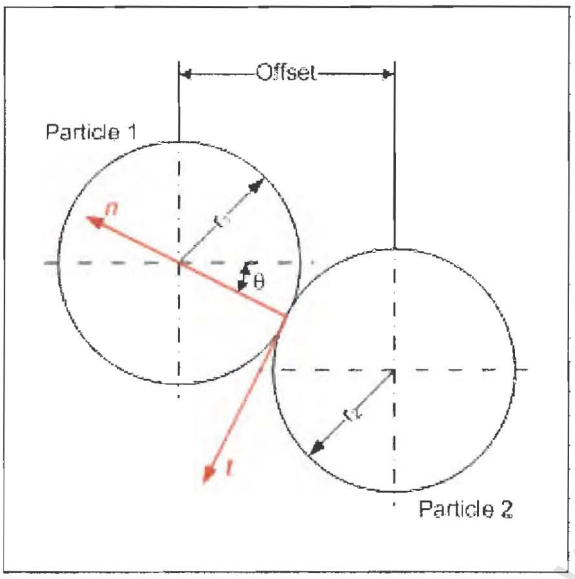

Figure 6-1– Calculating the normal and tangent at contact point

Recalling the equations from **Chapter 2** – Evolution of the contact model, calculating the total collisional impulse ***J***, this represents the integral of force over the total collisional time.

$$m_1\left(\boldsymbol{C}_1^{'}-\boldsymbol{C}_1\right)=-m_2\left(\boldsymbol{C}_2^{'}-\boldsymbol{C}_2\right)=\boldsymbol{J} \qquad \textbf{Equation 6-2}$$

Velocity has following vector components ($x \quad y \quad z$) in 3 dimensional space, where x is positive when it is pointing to the right and y is positive when it is pointing up. The z component is zero, as it is out of plane of the collision, so it is omitted. Therefore the (x, y) velocities are:

$$\boldsymbol{C}_1=\left(0,-\mathrm{v}_{n1}\right)$$

$$\boldsymbol{C}_2=\left(0,-\mathrm{v}_{n2}\right)$$

$$\boldsymbol{C}_1^{'}=\left(-\mathrm{v}_{x1},-\mathrm{v}_{y1}\right)$$

$$\boldsymbol{C}_2^{'}=\left(\mathrm{v}_{x2},-\mathrm{v}_{y2}\right)$$

The post angular velocities can be inferred from the impulse, pre- collision velocities. (In this case ω_1 and $\omega_2 = 0$, no spin prior to collision for the pre-collision angular velocities).

$$\left(\frac{2I_1}{D_1}\right)\left(\omega_1' - \omega_1\right) = \left(\frac{2I_2}{D_2}\right)\left(\omega_2' - \omega_2\right) = -\boldsymbol{n}\times\boldsymbol{J} \qquad \textbf{Equation 6-3}$$

Where $I = \frac{mD^2}{10}$ for homogenous spheres

Applying the measured pre- velocities to calculate the Pre- Relative velocity about the contact point:

$$\boldsymbol{u} = \left(\boldsymbol{C}_1 - \boldsymbol{C}_2\right) - \left[\left(\frac{D_1}{2}\boldsymbol{\omega}_1 + \frac{D_2}{2}\boldsymbol{\omega}_2\right)\times\boldsymbol{n}\right] = \boldsymbol{C}_1 - \boldsymbol{C}_2 \qquad \textbf{Equation 6-4}$$

Applying the measure post- velocities and angular spin to calculate the Post- Relative velocity about the contact point:

$$\boldsymbol{u}' = \left(\boldsymbol{C}_1' - \boldsymbol{C}_2'\right) + \left[\frac{5}{2}m^*\boldsymbol{J}\right] - \left[\frac{5}{2}m^*\left(\boldsymbol{n}\cdot\boldsymbol{J}\right)\boldsymbol{n}\right] \qquad \textbf{Equation 6-5}$$

The normal coefficient of restitution e is defined as.

$$e = -\frac{\boldsymbol{n}\cdot\boldsymbol{u}'}{\boldsymbol{n}\cdot\boldsymbol{u}} \qquad \textbf{Equation 6-6}$$

Friction μ between the two surfaces:

$$\mu = \frac{\left|\boldsymbol{n}\times\boldsymbol{J}\right|}{\left(\boldsymbol{n}\cdot\boldsymbol{J}\right)} \qquad \textbf{Equation 6-7}$$

The tangential restitution β is defined as:

$$\boldsymbol{n}\times\boldsymbol{u}' = -\beta\left(\boldsymbol{n}\times\boldsymbol{u}\right) \qquad \textbf{Equation 6-8}$$

Using Maw *et al* [29] analysis, a plot of non dimensional angle of incidence Ψ_1 vs. non dimensional angle of reflection Ψ_2 of the contact point is plotted, from which the pertinent material interaction properties are derived.

$$\psi_1 \equiv -\frac{(u \cdot t)}{(u \cdot n)}$$ **Equation 6-9**

and

$$\psi_2 \equiv -\frac{(u' \cdot t)}{(u \cdot n)}$$ **Equation 6-10**

6.2 Application of the theory - Example

The derived theory of the in-flight collision of two bodies is applied to the range of materials that were tested. To apply the theory appropriately, firstly the data has to be processed to pick out the pertinent measurement data. This is explained extensively in **Chapter 5**.

Figure 6-2 illustrates an example of a captured image; here the material tested was 8.15mm diameter steel ball bearings. **Figure 6-3** illustrates Teflon balls and their pre- and post- relative measurements in ACAD.

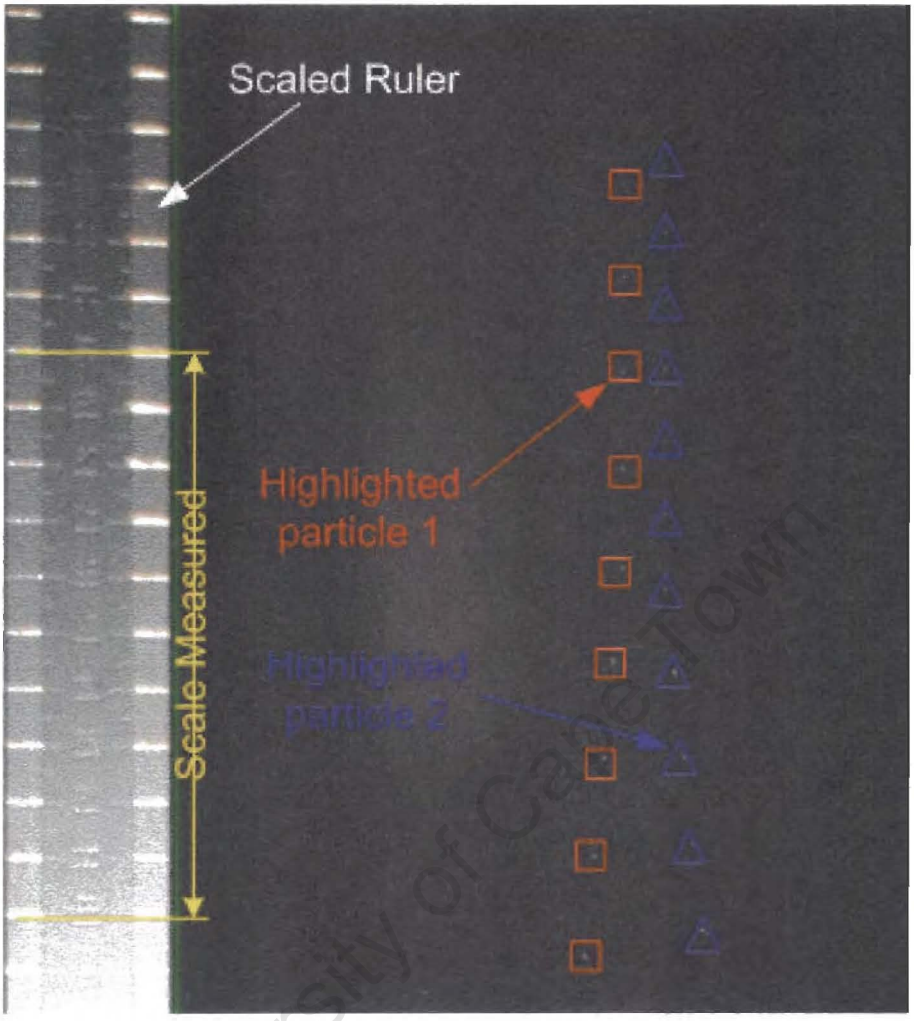

Figure 6-2 – Steel ball colliding – glancing collision

The image features the bright spots of reflection or phongs. Detailed description of the effects of specular reflection or phongs is described in **Chapter 5** – Image Processing.

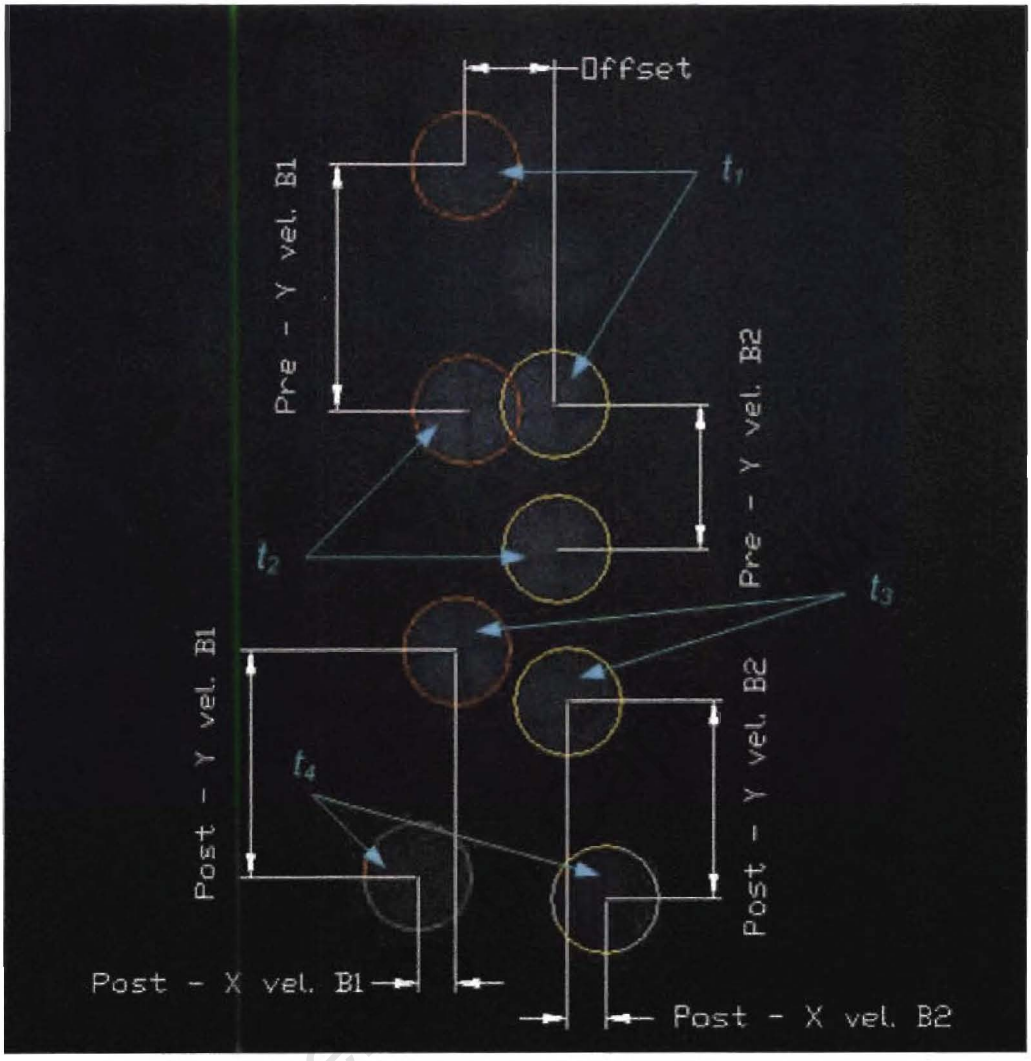

Figure 6-3 – Teflon balls with markings, and relative measurements about the contact point

The next stage in the procedure is to tally all the dimensions in EXCEL. This experimental procedure is computed for the varying offset distances. To extract a good set of data, the offset distances are incremented less than a millimetre (0.05 – 0.25mm); this increment is determined by the size of the particle.

6.2.1 Calculation Example

The methodology used to calculate the pre- and post- impact velocities are explained in this section. Centre of mass calculations are conducted to extract velocities just prior to and after impact. A step by step procedure of the calculation is presented below for one set of data.

6.2.1.1 Data collection

The binary collision of 8.15mm diameter steel ball bearings with material designation stainless steel X105 CrMo17 carbon chrome alloy, mass 2.424g, with offset increments of 0.05mm, provide the data of 140 individual collision points. **Table 6-1** presents some of this data of the measured relative distances. This is for a centering block to release mechanism drop height distance of 568 ± 1 mm and for ten separate drops for a range of offsets.

Ln is the distance between the two images directly prior to collision and *Lx* and *Ly* are the post relative distances in the X and Y directions of the 2 images directly after impact. The measured length of the scaled ruler on the image is indicated as "Scale Measured", this is illustrated in **Figure 6-2**, and its actual length is indicated as "Scale Actual." The Ratio is calculated as: Scale Actual / Scale Measured. This is varied because the CAD package automatically rescales the imported images, so the user cannot control the images to a fixed pixel scale and resolution. From this scale the actual relative distance between the image points can be determined as shown in the data set **Table 6-2.**

No.	Scale	Scale Measured		Ball 1				Ball2		
	Actual (mm)	(pixel)	Pixel/mm	*Ln*	*Lx*	*Ly*	Offset	*Ln*	*Lx*	*Ly*
1	100	81.0	1.23	22.9	0.15	18.9	0.41	14.5	0.52	19.6
2	100	83.8	1.19	24.4	0.7	16.7	0.98	15.8	1.01	24.8
3	100	89.4	1.12	25.9	0.36	18.5	0.58	17.1	0.71	26.6
4	100	89.0	1.12	23.9	0.54	18.3	0.54	16.2	0.90	26.4
5	100	92.5	1.08	26.1	0.57	18.1	0.70	16.1	0.45	23.9
6	100	90.0	1.11	25.9	0.36	17.7	0.52	16.7	0.38	22.8
7	100	91.8	1.09	25.9	0.35	18.2	0.46	16.4	0.89	23.6
8	100	93.0	1.07	27.1	0.87	19.0	0.88	17.4	1.07	27.5
9	100	92.7	1.08	26.3	0.82	18.5	0.78	17.0	0.56	22.7
10	100	217.0	0.46	63.2	1.48	43.7	1.82	40.6	2.58	62.3

Table 6-1 – Raw data points from CAD (all ACAD units)

Ball 1			Offset	Ball2		
Ln	Lx	Ly		Ln	Lx	Ly
28.21	0.19	23.35	0.51	17.89	0.64	24.24
29.15	0.83	19.95	1.17	18.87	1.20	29.62
28.95	0.40	20.63	0.65	19.13	0.79	29.75
26.81	0.61	20.58	0.61	18.19	1.01	29.66
28.25	0.62	19.60	0.76	17.45	0.49	25.80
28.82	0.40	19.65	0.58	18.50	0.42	25.33
28.23	0.38	19.79	0.50	17.85	0.97	25.75
29.16	0.94	20.46	0.95	18.66	1.15	29.59
28.41	0.88	19.92	0.84	18.29	0.60	24.47
29.17	0.68	20.17	0.84	18.73	1.19	28.75

Table 6-2 – Rescaled measured length (all dimensions in mm)

Once the actual distance are known, the relative pre- and post impact velocities can be calculated. The following section looks at the centre of mass calculations where the measured distances are used to calculate the velocities just before and after collisions.

6.2.1.2 Relative velocity calculations

It is improbable that the position of the impact is captured on film, the nearest images pre– and post– collision are used to calculate the velocities prior to and after collision as shown in **Figure 6-4.**

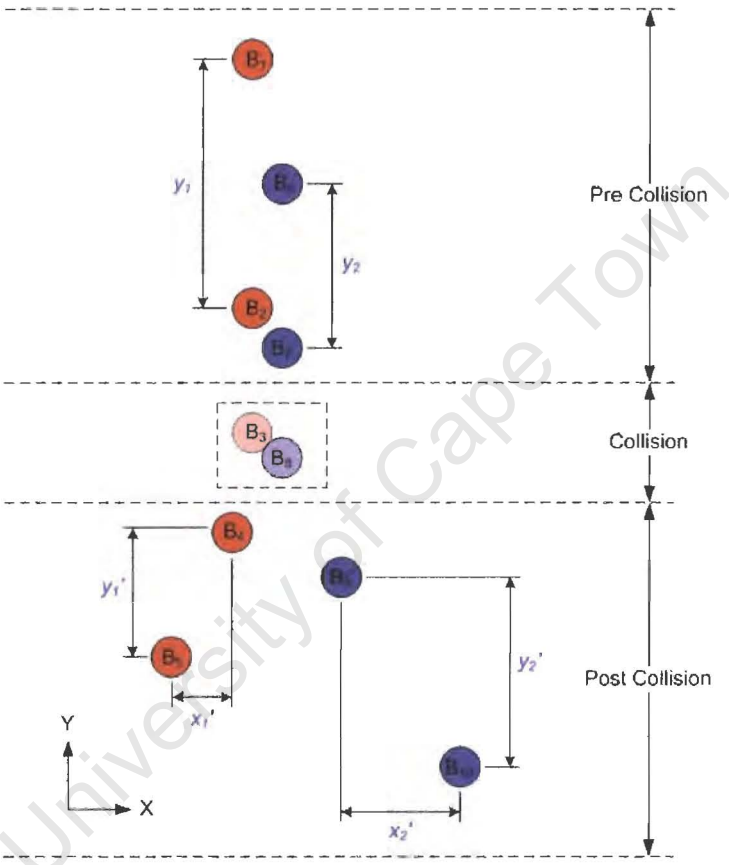

Figure 6-4– Centre of mass schematic

For the given strobe frequency, we capture subsequent images for the collision of two balls. Ball positions B_1 and B_2, B_6 and B_7 pre- impact images for ball 1 and 2 respectively, and B_4 and B_5, B_9 and B_{10} yield the post- impact images. The relative distances between these ball positions are demarcated by y_1 and y_2 for pre collision images, y_1', y_2', x_1', x_2' are post collision distances. We can determine the average pre- and post- velocities from the measured relative distances between the images and strobe time. The average velocities should not be used to calculate the material interaction

properties. This is because the measured averages velocities will not be same as the velocities of the particles at points B_2, B_7, B_4, B_9 which give the velocities just before and after the collision. Ideally the velocities should be calculated immediately prior to and after the impact, but as the point of impact is not known, the closest known velocities are used. Therefore we use relative velocity calculations to determine the velocities of these ball images.

To calculate the velocities of ball images B_2, B_7, B_4, B_9, we use the following equations:

- Deriving the ball velocity at B_2 (particle 1) pre- impact velocity:

If initial velocity u at B_1 is known and the time taken for the particle to travel to ball image B_2, then the distance traveled with the influence of gravitational acceleration a is:

$$y_1 = u_{B1}t + \frac{1}{2}at^2 \qquad \textbf{Equation 6-11}$$

Given that $t = \frac{1}{f}$, where t is the time between the images in seconds for strobe frequency f.

If the final velocity v is also given by:

$$v = u + at \qquad \textbf{Equation 6-12}$$

Then substituting **Equation 6 - 12** into **Equation 6 - 11** will yield the distance traveled by the particle for the given final velocity v_{B2} at B_2:

$$y_1 = v_{B2}t - \frac{1}{2}at^2 \qquad \textbf{Equation 6-13}$$

Therefore rearranging the **Equation 6 - 13** to calculate the velocity at B_2, given the measured distance y_1 and strobe time t:

$$v_{B2} = \frac{y_1 + \frac{1}{2}at^2}{t} \qquad \textbf{Equation 6-14}$$

Similarly we can calculate the pre- impact velocity for ball image B_7

$$v_{B7} = \frac{y_2 + \frac{1}{2}at^2}{t} \qquad \textbf{Equation 6-15}$$

- Deriving ball velocity at B_4 (particle 1) post- impact velocity:

Because the post impact velocities are a component of the y and x directional velocities, we need to resolve them individually.

Calculating the Y –component velocity for B_4 given that the distance traveled from B_4 to B_5 is y_1' within time t under the influence of gravity:

$$u_{B4}(y) = \frac{y_1' - \frac{1}{2}at^2}{t} \qquad \textbf{Equation 6-16}$$

Calculating the X –component velocity for B_4 given that the distance traveled from B_4 to B_5 is x_1' within time t with no influence of gravity:

$$u_{B4}(x) = \frac{x_1'}{t} \qquad \textbf{Equation 6-17}$$

Similarly we can calculate the post- impact Y and X velocities for ball image B_9:

$$u_{B9}(y) = \frac{y_2' - \frac{1}{2}at^2}{t}$$ **Equation 6-18**

$$u_{B9}(x) = \frac{x_2'}{t}$$ **Equation 6-19**

Therefore summarising, **Table 6-3,** illustrates the calculations for the pre- and post-impact velocities which are used to resolve velocities about the centre of mass.

	Pre- impact vel.	**Post- impact *y* vel.**	**Post- impact *x* vel.**
Particle 1	$v_{B2} = \frac{y_1 + \frac{1}{2}at^2}{t}$	$u_{B4}(y) = \frac{y_1' - \frac{1}{2}at^2}{t}$	$u_{B4}(x) = \frac{x_1'}{t}$
Particle 2	$v_{B7} = \frac{y_2 + \frac{1}{2}at^2}{t}$	$u_{B9}(y) = \frac{y_2' - \frac{1}{2}at^2}{t}$	$u_{B9}(x) = \frac{x_2'}{t}$

Table 6-3– centre of mass velocities

6.2.1.3 Data Calculations

The actual velocities of the particle can now be determined with information gathered from the strobe frequency, for this particular experiment, the frequency of the strobe is set at 150Hz. Therefore the time between each consecutive image is 1/150 second. **Table 6-4** illustrates the velocities pre- and post- impact after centre of mass calculations for the data presented in **Table 6-1** .

	Ball1			Offset	Ball2		
No.	*Vn*	*Vx*	*Vy*	(mm)	*Vn*	*Vx*	*Vy*
1	4.26	0.03	3.47	0.51	2.72	0.10	3.60
2	4.40	0.13	2.96	1.17	2.86	0.18	4.41
3	4.37	0.06	3.06	0.65	2.90	0.12	4.43
4	4.05	0.09	3.05	0.61	2.76	0.15	4.41
5	4.27	0.09	2.91	0.76	2.65	0.07	3.84
6	4.35	0.06	2.91	0.58	2.81	0.06	3.76
7	4.27	0.06	2.93	0.50	2.71	0.15	3.83
8	4.40	0.14	3.03	0.95	2.83	0.17	4.40
9	4.29	0.13	2.95	0.84	2.77	0.09	3.64
10	4.41	0.10	2.99	0.84	2.84	0.18	4.28

Table 6-4 – Actual velocities for steel ball bearings (velocities in ms^{-1})

These results are now imported into Matlab software for post processing using the Foerster *et al* [35] rigid body technique. **Appendix C**, illustrates the details of the Matlab software to derive the pertinent characteristic plot of Ψ_1 vs. Ψ_2 non dimensional angles of incidence vs. reflection, as proposed by Maw *et al* [29]. Velocity and Offset measurements from **Table 6-4** are then imported into the rigid body calculations for in-flight binary collisions to quantify the pertinent Non-dimensional, restitution and friction values. Calculated values of the relative velocities are presented in **Appendix F** – Binary impact data.

The derived materials interactions are tabulated in **Table 6-5**. The calculated material interaction properties are shown for all tested materials in **Appendix G** – Material interaction property data.

No.	Ψ_1	Ψ_2	Normal Restitution	Friction	Tangential Restitution
1	0.06	-0.04	0.03	0.03	0.58
2	0.14	-0.24	0.90	0.06	1.64
3	0.08	-0.13	0.79	0.03	1.65
4	0.07	0.16	0.56	0.02	-2.19
5	0.09	-0.06	0.69	0.03	0.61
6	0.07	-0.12	0.87	0.03	1.70
7	0.06	-0.05	0.72	0.02	0.81
8	0.12	0.03	0.76	0.01	-0.24
9	0.10	0.07	0.78	0.00	-0.72
10	0.10	-0.09	0.82	0.03	0.91

Table 6-5 – Results example for steel ball bearings

As shown in calculated data presented in **Table 6-5,** the material interaction properties of normal and tangential restitution and friction exhibit scatter. This is observed in particular in the tangential restitution values where there is significant fluctuation for different offsets. This phenomenon will be discussed further in this chapter. The observed value of the negative restitution is a result of experimental scatter.

6.2.2 Propagating the error

The corresponding errors are now calculated for the two particle experiment, as derived in **Chapter 5** – Error propagation calculation. Relative Error in the measured distances:

For X – direction components (pre- collision):

$$\Delta L_{off} = \left(L_{off} * \left[\Delta sf + \Delta Ang\right]\right) + \left(I_{off} + \left[I_{off} * \Delta sf\right]\right) \qquad \textbf{Equation 6-20}$$

For X – direction components (post- collision):

$$\Delta L'_x = \left(L'_x * \left[\Delta sf + \Delta Ang\right]\right) + \left(I'_x + \left[I'_x * \Delta sf\right]\right) \qquad \textbf{Equation 6-21}$$

For Y – direction components (pre- collision):

$$\Delta L_y = \left(L_y * \left[\Delta sf + \Delta S\right]\right) + \left(I_y + \left[I_y * \Delta sf\right]\right) \qquad \textbf{Equation 6-22}$$

For Y – direction components (post- collision):

$$\Delta L'_y = \left(L'_y * [\Delta sf + \Delta S]\right) + \left(I'_y + \left[I'_y * \Delta sf\right]\right) \qquad \textbf{Equation 6-23}$$

The individual error contributions:

Table of Errors								
Material	*Offset Drift(X) – (mm)*	*Specular Reflection($Y_{1,2}$)*	*Angular offset($X_{1,2}$)*	*Scaling and importing in ACAD(X&Y)*	*Pre collision(Y_1) – (mm)*	*Pre collision(Y_2) – (mm)*	*Post collision (X_1 & Y_1) – (mm)*	*Post collision (X_2 & Y_2) – (mm)*
Steel	± 0.383	0.7%	0.14%	0.2%	± 0.390	± 0.376	± 0.390	± 0.376
Ceramic	± 0.338	0.5%	1.51%	0.2%	± 0.344	± 0.330	± 0.344	± 0.330
Teflon	± 2.817	nil	0.14%	0.2%	± 2.322	± 3.312	± 2.322	± 3.312

Table 6-6 – Table of Errors in the appropriate X and Y directions

Now adding all the errors;

Calculating the *actual L (for shiny materials – Steel ball bearings):*

- ***For X – direction components (pre- collision):***

$$\Delta L_{off} = \left(L_{off} * [0.002 + 0.0014]\right) + \left(0.383 + [0.383 * 0.002]\right) = \left(L_{off} * 0.0034\right) + (0.3838)$$

- ***For X – direction components (post- collision P_1):***

$$\Delta L'_x = \left(L'_x * [0.002 + 0.0014]\right) + \left(0.390 + [0.390 * 0.002]\right) = \left(L'_x * 0.0034\right) + (0.3901)$$

- ***For X – direction components (post- collision P_2):***

$$\Delta L'_x = \left(L'_x * [0.002 + 0.0014]\right) + \left(0.376 + [0.376 * 0.002]\right) = \left(L'_x * 0.0034\right) + (0.3768)$$

- ***For Y – direction components (pre- collision P_1):***

$$\Delta L_y = \left(L_y * [0.002 + 0.007]\right) + \left(0.390 + [0.390 * 0.002]\right) = \left(L_y * 0.0034\right) + (0.3901)$$

- ***For Y – direction components (pre- collision P_2):***

$$\Delta L_y = \left(L_y * [0.002 + 0.007]\right) + \left(0.376 + [0.376 * 0.002]\right) = \left(L_y * 0.0034\right) + (0.3768)$$

- ***For Y – direction components (post- collision P_1):***

$$\Delta L'_y = \left(L'_y * [0.002 + 0.007]\right) + \left(0.390 + [0.390 * 0.002]\right) = \left(L'_y * 0.009\right) + (0.3901)$$

- ***For Y – direction components (post- collision P_2):***

$$\Delta L'_y = \left(L'_y * [0.002 + 0.007]\right) + \left(0.376 + [0.376 * 0.002]\right) = \left(L'_y * 0.009\right) + (0.3768)$$

Calculating the *actual L (for shiny materials – Ceramic ball bearings):*

- ***For X – direction components (pre- collision):***

$$\Delta L_{off} = \left(L_{off} * [0.002 + 0.0151]\right) + \left(0.338 + [0.338 * 0.002]\right) = \left(L_{off} * 0.0171\right) + (0.3387)$$

- ***For X – direction components (post- collision P_1):***

$$\Delta L'_x = \left(L'_x * [0.002 + 0.0151]\right) + \left(0.344 + [0.344 * 0.002]\right) = \left(L'_x * 0.0171\right) + (0.3447)$$

- ***For X – direction components (post- collision P_2):***

$$\Delta L'_x = \left(L'_x * [0.002 + 0.0151]\right) + \left(0.330 + [0.330 * 0.002]\right) = \left(L'_x * 0.0171\right) + (0.3307)$$

- ***For Y – direction components (pre- collision P_1):***

$$\Delta L_y = \left(L_y * [0.002 + 0.005]\right) + \left(0.344 + [0.344 * 0.002]\right) = \left(L_y * 0.007\right) + (0.3447)$$

- ***For Y – direction components (pre- collision P_2):***

$$\Delta L_y = \left(L_y * [0.002 + 0.005]\right) + \left(0.330 + [0.330 * 0.002]\right) = \left(L_y * 0.007\right) + (0.3307)$$

- ***For Y – direction components (post- collision P_1):***

$$\Delta L'_y = \left(L'_y * [0.002 + 0.005]\right) + \left(0.344 + [0.344 * 0.002]\right) = \left(L'_y * 0.007\right) + (0.3447)$$

- ***For Y – direction components (post- collision P_2):***

$$\Delta L'_y = \left(L'_y * [0.002 + 0.005]\right) + \left(0.330 + [0.330 * 0.002]\right) = \left(L'_y * 0.007\right) + (0.3307)$$

Calculating the *actual L (for shiny materials – Teflon ball bearings):*

- ***For X – direction components (pre- collision):***

$$\Delta L_{off} = \left(L_{off} * [0.002 + 0.0014]\right) + \left(2.817 + [2.817 * 0.002]\right) = \left(L_{off} * 0.0034\right) + (2.8226)$$

- ***For X – direction components (post- collision P_1):***

$$\Delta L'_x = \left(L'_x * [0.002 + 0.0014]\right) + \left(2.322 + [2.322 * 0.002]\right) = \left(L'_x * 0.0034\right) + (2.3266)$$

- ***For X – direction components (post- collision P_2):***

$$\Delta L'_x = \left(L'_x * [0.002 + 0.0014]\right) + \left(3.312 + [3.312 * 0.002]\right) = \left(L'_x * 0.0034\right) + (3.3186)$$

- ***For Y – direction components (pre- collision P_1):***

$$\Delta L_y = \left(L_y * [0.002]\right) + \left(2.322 + [2.322 * 0.002]\right) = \left(L_y * 0.002\right) + (2.3266)$$

- ***For Y – direction components (pre- collision P_2):***

$$\Delta L_y = \left(L_y * [0.002]\right) + \left(3.312 + [3.312 * 0.002]\right) = \left(L_y * 0.002\right) + (3.3186)$$

- ***For Y – direction components (post- collision P_1):***

$$\Delta L'_y = \left(L'_y * [0.002]\right) + \left(2.322 + [2.322 * 0.002]\right) = \left(L'_y * 0.002\right) + (2.3266)$$

- ***For Y – direction components (post- collision P_2):***

$$\Delta L'_y = \left(L'_y * [0.002]\right) + \left(3.312 + [3.312 * 0.002]\right) = \left(L'_y * 0.002\right) + (3.3186)$$

Table 6-7 presents the total error for the data presented earlier in this chapter in **Table 6-1**, and **Table 6-8** illustrates the error for the relative velocities of the colliding steel balls. As shown in **Table 6-7**, the contributions of errors on the pre- impact relative distance have maximum difference of $\pm 0.70mm$ and $\pm 0.60mm$ for ball 1 and 2 respectively and their corresponding effect on the velocities have maximum errors of $\pm 0.10 \text{ms}^{-1}$ and $\pm 0.09 \text{ ms}^{-1}$ as shown in **Table 6-8**. **Table 6-9** tabulates the velocities and the uncertainties.

	Ball1				Ball2		
No.	*Ln*	*Lx*	*Ly*	Offset	*Ln*	*Lx*	*Ly*
1	0.64	0.39	0.60	0.39	0.54	0.38	0.59
2	0.65	0.39	0.57	0.39	0.55	0.38	0.64
3	0.65	0.39	0.58	0.39	0.55	0.38	0.64
4	0.63	0.39	0.58	0.39	0.54	0.38	0.64
5	0.64	0.39	0.57	0.39	0.53	0.38	0.61
6	0.65	0.39	0.57	0.39	0.54	0.38	0.60
7	0.64	0.39	0.57	0.39	0.54	0.38	0.61
8	0.65	0.39	0.57	0.39	0.54	0.38	0.64
9	0.65	0.39	0.57	0.39	0.54	0.38	0.60
10	0.65	0.39	0.57	0.39	0.55	0.38	0.64

Table 6-7 – Error propagation on relative distances for steel balls ($\pm$ mm)

	Ball1				Ball2		
No.	*Vn*	*Vx*	*Vy*	Offset	*Vn*	*Vx*	*Vy*
1	0.097	0.059	0.089	0.386	0.082	0.057	0.088
2	0.099	0.059	0.084	0.388	0.083	0.057	0.096
3	0.098	0.059	0.085	0.386	0.083	0.057	0.096
4	0.095	0.059	0.085	0.386	0.082	0.057	0.096
5	0.097	0.059	0.084	0.386	0.081	0.057	0.091
6	0.098	0.059	0.084	0.386	0.082	0.057	0.090
7	0.097	0.059	0.084	0.386	0.082	0.057	0.090
8	0.099	0.059	0.085	0.387	0.083	0.057	0.096
9	0.098	0.059	0.084	0.387	0.082	0.057	0.089
10	0.099	0.059	0.085	0.387	0.083	0.057	0.095

Table 6-8 – Error propagation on the relative velocities of steel balls ($\pm$ ms^{-1})

	Ball1			Offset (mm)	Ball2		
No.	*Vn*	*Vx*	*Vy*		*Vn*	*Vx*	*Vy*
1	4.26 ± 0.10	0.03 ± 0.06	3.47 ± 0.09	0.51 ± 0.39	2.72 ± 0.08	0.10 ± 0.06	3.60 ± 0.09
2	4.40 ± 0.10	0.13 ± 0.06	2.96 ± 0.08	1.17 ± 0.39	2.86 ± 0.08	0.18 ± 0.06	4.41 ± 0.10
3	4.37 ± 0.10	0.06 ± 0.06	3.06 ± 0.09	0.65 ± 0.39	2.90 ± 0.08	0.12 ± 0.06	4.43 ± 0.10
4	4.05 ± 0.10	0.09 ± 0.06	3.05 ± 0.09	0.61 ± 0.39	2.76 ± 0.08	0.15 ± 0.06	4.41 ± 0.10
5	4.27 ± 0.10	0.09 ± 0.06	2.91 ± 0.08	0.76 ± 0.39	2.65 ± 0.08	0.07 ± 0.06	3.84 ± 0.09
6	4.35 ± 0.10	0.06 ± 0.06	2.91 ± 0.08	0.58 ± 0.39	2.81 ± 0.08	0.06 ± 0.06	3.76 ± 0.09
7	4.27 ± 0.10	0.06 ± 0.06	2.93 ± 0.08	0.50 ± 0.39	2.71 ± 0.08	0.15 ± 0.06	3.83 ± 0.09
8	4.40 ± 0.10	0.14 ± 0.06	3.03 ± 0.09	0.95 ± 0.39	2.83 ± 0.08	0.17 ± 0.06	4.40 ± 0.10
9	4.29 ± 0.10	0.13 ± 0.06	2.95 ± 0.08	0.84 ± 0.39	2.77 ± 0.08	0.09 ± 0.06	3.64 ± 0.09
10	4.41 ± 0.10	0.10 ± 0.06	2.99 ± 0.09	0.84 ± 0.39	2.84 ± 0.08	0.18 ± 0.06	4.28 ± 0.10

Table 6-9 – Relative velocities and their uncertainties (ms^{-1})

	Ball1				Ball2		
No.	*Vn*	*Vx*	*Vy*	Offset	*Vn*	*Vx*	*Vy*
1	2.28	211.07	2.57	76.19	3.01	59.06	2.45
2	2.24	47.06	2.85	33.17	2.90	31.62	2.17
3	2.25	97.26	2.79	59.52	2.87	47.81	2.17
4	2.36	64.63	2.80	63.60	2.97	37.60	2.17
5	2.28	63.63	2.89	51.04	3.06	77.77	2.36
6	2.25	97.88	2.88	66.77	2.94	89.59	2.39
7	2.28	102.64	2.87	76.92	3.01	39.20	2.36
8	2.24	42.05	2.81	40.91	2.92	33.10	2.17
9	2.27	44.45	2.86	45.97	2.96	62.73	2.44
10	2.24	57.46	2.83	46.04	2.91	31.99	2.21

Table 6-10 – Percentage error contribution for velocities and offset

Table 6-10, tabulates the percentage error contribution on the pre- and post- velocities and offset. It is noted in **Table 6-10,** that the X velocity percentage error components for both particle 1 and 2 are not consistent, whereas the Y velocity components and the offset are consistent. This data is for small offsets, less than 15%, the full data is given in **Appendix F** – Binary impact data, and illustrated in **Figure 6-5**.

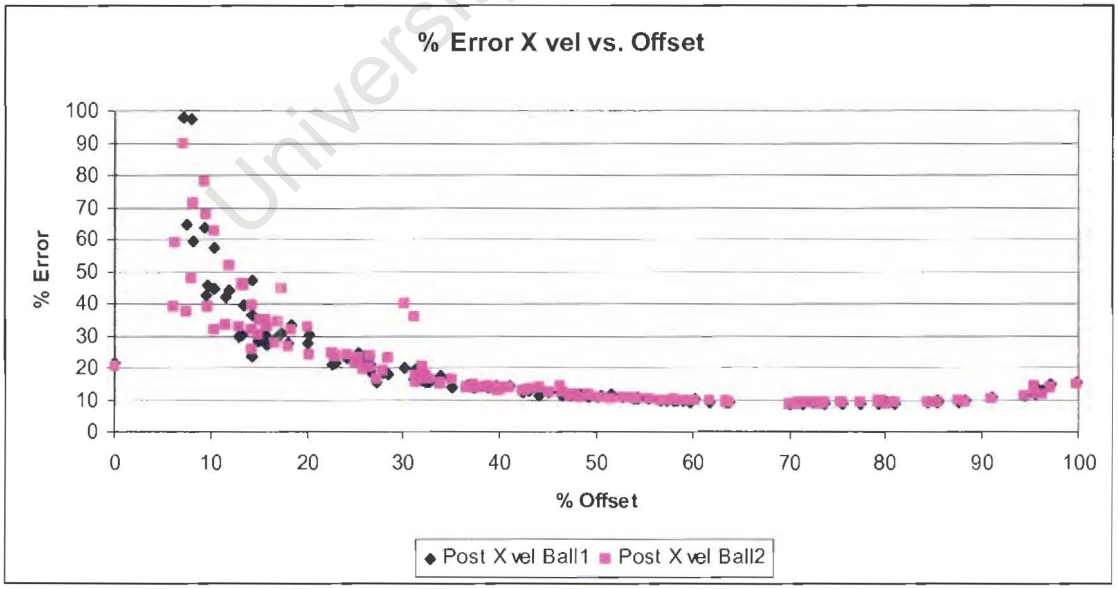

Figure 6-5 - % Propagated error comparison for X velocity component for P_1 and P_2

The percentages propagated X velocity error for both particles follow a non linear trend. This indicates that the measured X velocity percentage error components closer to 0% offset are very sensitive. Therefore it can be concluded that measuring the relative X velocities for direct impacts should be carefully controlled.

Material interaction property errors are now calculated using the contributed measured experimental error. As given in **Equation 6-24** to **Equation 6-28** we calculate the error in pre- and post- velocities about the contact point, and the calculated errors are shown in **Table 6-11**. **Table 6-12** shows the calculated material properties and their uncertainties.

- $\Delta u = \Delta C_1 + \Delta C_2$ **Equation 6-24**

$$\Delta u' = u' \sqrt{\left(\frac{\Delta C_1 + \Delta C_2}{u}\right)^2 + 3\left(\frac{\Delta C_1'}{C_1'}\right)^2 + 3\left(\frac{\Delta C_1}{C_1}\right)^2 + 2\left(\frac{\Delta x_{off}}{D}\right)^2 + \left(\frac{\Delta L_{1y}'}{L_{1y}'}\right)^2 + \left(\frac{\Delta L_{1y}' + \Delta L_{1x}'}{L_1'}\right)^2}$$

Equation 6-25

And their corresponding errors yield errors in the material interaction properties, coefficients of normal and tangential restitution and friction:

- Coefficient of normal restitution:

$$\Delta e = e \sqrt{2\left(\frac{\Delta x_{off}}{D}\right)^2 + 2\left(\frac{\Delta C_1 + \Delta C_2}{u}\right)^2 + 3\left(\frac{\Delta C_1'}{C_1'}\right)^2 + 2\left(\frac{\Delta C_1}{C_1}\right)^2 + 2\left(\frac{\Delta L_{1y}'}{L_{1y}'}\right)^2 + 2\left(\frac{\Delta L_{1y}' + \Delta L_{1x}'}{L_1'}\right)^2}$$

Equation 6-26

- Coefficient of tangential restitution:

$$\Delta \beta = \beta \sqrt{3\left(\frac{\Delta x_{off}}{D}\right)^2 + 2\left(\frac{\Delta C_1 + \Delta C_2}{u}\right)^2 + 3\left(\frac{\Delta C_1'}{C_1'}\right)^2 + 2\left(\frac{\Delta C_1}{C_1}\right)^2 + 2\left(\frac{\Delta L_{1y}'}{L_{1y}'}\right)^2 + 2\left(\frac{\Delta L_{1y}' + \Delta L_{1x}'}{L_1'}\right)^2}$$

Equation 6-27

- Coefficient of friction:

$$\Delta \tan \vartheta = \tan \vartheta \sqrt{3\left(\frac{\Delta C_1^{'}}{C_1^{'}}\right)^2 + 2\left(\frac{\Delta C_1}{C_1}\right)^2 + 2\left(\frac{\Delta L_{1y}^{'}}{L_{1y}^{'}}\right)^2 + 2\left(\frac{\Delta L_{1y}^{'} + \Delta L_{1x}^{'}}{L_1^{'}}\right)^2}$$

Equation 6-28

No.	Psi 1 Ψ_1	Psi 2 Ψ_2	Normal Restitution	Friction	Tangential Restitution
1	±0.004	±0.008	±0.006	±0.003	±0.122
2	±0.010	±0.052	±0.193	±0.007	±0.361
3	±0.005	±0.030	±0.174	±0.004	±0.371
4	±0.005	±0.039	±0.132	±0.002	±0.528
5	±0.006	±0.012	±0.145	±0.003	±0.130
6	±0.005	±0.026	±0.186	±0.004	±0.373
7	±0.004	±0.011	±0.152	±0.002	±0.177
8	±0.008	±0.006	±0.161	±0.002	±0.052
9	±0.007	±0.017	±0.169	±0.001	±0.160
10	±0.007	±0.021	±0.175	±0.004	±0.198

Table 6-11 – Error propagation for the material properties

No.	Ψ_1	Ψ_2	Normal Restitution	Friction	Tangential Restitution
1	0.06±0.004	-0.04±0.01	0.03±0.01	0.027±0.003	0.58±0.12
2	0.14±0.010	-0.24±0.05	0.90±0.19	0.058±0.007	1.64±0.36
3	0.08±0.005	-0.13±0.03	0.79±0.17	0.034±0.004	1.65±0.37
4	0.07±0.005	0.16±0.04	0.56±0.13	0.016±0.002	-2.19±0.53
5	0.09±0.006	-0.06±0.01	0.69±0.15	0.025±0.003	0.61±0.13
6	0.07±0.005	-0.12±0.03	0.87±0.19	0.029±0.004	1.70±0.37
7	0.06±0.004	-0.05±0.01	0.72±0.15	0.019±0.002	0.81±0.18
8	0.12±0.008	0.03±0.01	0.76±0.16	0.014±0.002	-0.24±0.05
9	0.10±0.007	0.07±0.02	0.78±0.17	0.005±0.001	-0.72±0.16
10	0.10±0.004	-0.09±0.02	0.82±0.18	0.031±0.004	0.91±0.20

Table 6-12 – Material properties and their uncertainties

No.	Ψ_1	Ψ_2	Normal Restitution	Friction	Tangential Restitution
1	6.7	21.1	20.6	10.6	21.1
2	6.7	22.1	21.6	11.9	22.1
3	6.7	22.5	22.0	11.6	22.5
4	6.7	24.1	23.6	11.7	24.1
5	6.7	21.3	20.8	12.0	21.3
6	6.7	22.0	21.5	12.0	22.0
7	6.7	21.8	21.2	11.9	21.8
8	6.7	21.7	21.1	11.7	21.7
9	6.7	22.1	21.6	11.9	22.1
10	6.7	21.8	21.3	11.8	21.8

Table 6-13 – %Error propagation for the material properties

As shown in **Table 6-12,** the calculated errors in the ψ_1 and ψ_2, coefficients of normal and tangential restitution and friction values exhibit the reasonable propagation from the measured errors. The percentage error contributions about the mean values are tabulated in **Table 6-13.** As shown in **Table 6-13,** ψ_2, and the restitution values are affected close to 22%, indicating that the these values are affected considerably by small propagations in the error. The ψ_1 and friction values are affected by 7% and 12% respectively. The calculated error propagation data is shown in **Appendix H** – Error propagation data.

For the purpose of DEM comparisons presented in **Chapter 7**, the propagated X velocity percentage error components are averaged, and the percentage error is approximately 20%. For the Y velocity components the maximum percentage error is less than 5%. These average percentages will be added in the DEM comparison sections as the percentage error bars for the various experimental velocity comparisons.

It has been demonstrated that the contribution of various errors in the data can have an influence on the overall acquired raw data. The error calculations presented here are good measures of error contributions which may affect the interpretation of the data. A factor

which may hinder the experimental results is the effect of air drag and contribution of gravity in the calculations. We will test this phenomenon in the following section.

6.2.3 Testing for the effect of air drag and gravity

In this section, we will test the effects of gravity and air drag on the measured data. Because the impact event is not captured on the images, the measured relative velocities from the images are estimated pre- and post- impact. Therefore, the effect of gravity and air drag now has a significant contribution to the velocities.

6.2.3.1 Effect of the air drag – Calculated comparison

For the in-flight impact of two particles, as depicted in **Figure 6-4**, the red ball is the impacting ball and the blue ball is released from the quick release mechanism. Because the impact event is very quick, the illuminating frequency of the strobe does not capture the collision. This is due to the limitation of the overlap of the ball image between the exposure intervals. If the frequency is set high, the images will merge into one path and the individual position will not be distinguished.

To calculate the influence of air drag, we use the conservation of energy to determine the velocity prior to impact. From experimental measurements, the relative heights of ball release nozzles distances are known, therefore we can then calculate the velocity of the impacting ball (released from the centering mechanism) just prior to impact.

Calculating the velocity for each ball position:

- Given that $K.E = \frac{1}{2}mv^2$ and $P.E = mgh$, we can calculate the velocity of each ball position for a given height.

If energy is conserved at the time of impact, that is $K.E = P.E$, due to the fact that for falling objects in freefall, conserve potential energy with respect to initial height, then all that energy is transferred to kinetic when they fall.

- Therefore resolving for velocity at impact, $v = \sqrt{2gh}\ ms^{-1}$, where g is the acceleration due to gravity and h is the height prior to impact.

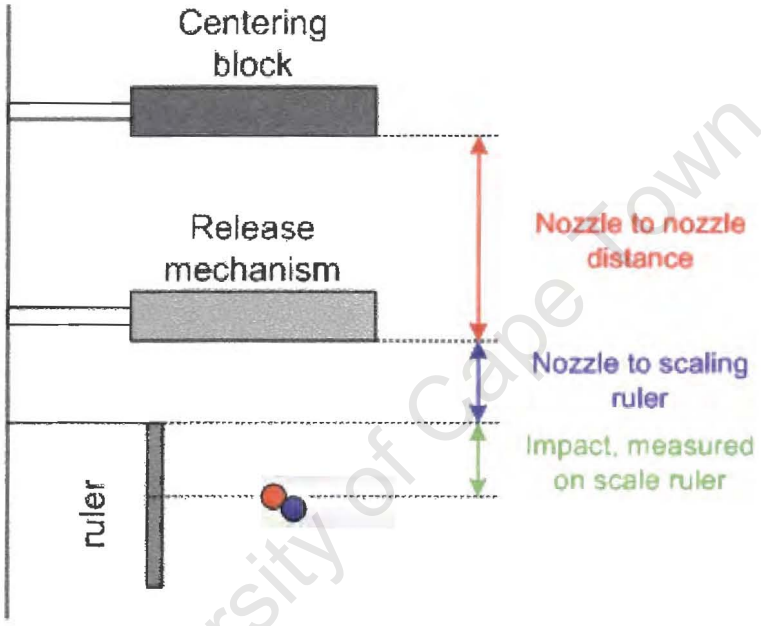

Figure 6-6 – Measuring height to impact

This height is measured from the schematic described in **Figure 6-6**, where the total height h is calculated from: nozzle to nozzle distance, nozzle to top of scaling ruler distance, and finally measured from the image, the height of the pre- impact. Because the impact of the two balls is not captured, we measure ball position prior to impact.

Material	Heights (m)	Calculated velocity (ms^{-1})	Measured velocity (ms^{-1})	ΔVelocity	Error %
Steel	0.968	4.36	4.28	0.08	1.8
	0.488	3.09	3.05	0.04	1.3
	0.427	2.89	2.84	0.05	1.7
Ceramic	0.488	3.09	3.07	0.02	0.6
	0.427	2.89	2.87	0.02	0.7
Teflon	0.832	4.04	3.97	0.07	1.7
	0.705	3.72	3.69	0.03	0.8

Table 6-14 - % Error comparison between measured and calculated velocity for ball1

Comparisons of the calculated velocities with measured velocities from the data for ball 1 are shown in **Table 6-14.** The comparisons show that for the highest height setting, the error is less than 2% for all materials, therefore it can be concluded that calculating velocities from the two ball images and ignoring air drag, contributes little error to the particle velocity at impact. The average error is less than 1.2%.

6.2.3.2 Effect of the air drag – Measured comparison

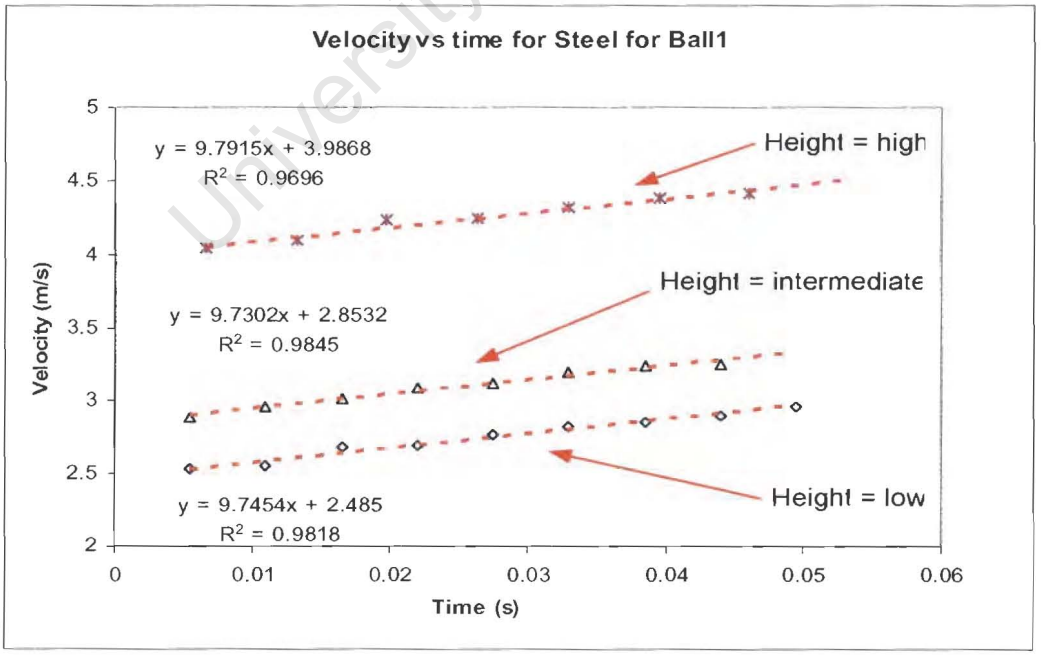

Figure 6-7 – Effect of gravity on Steel

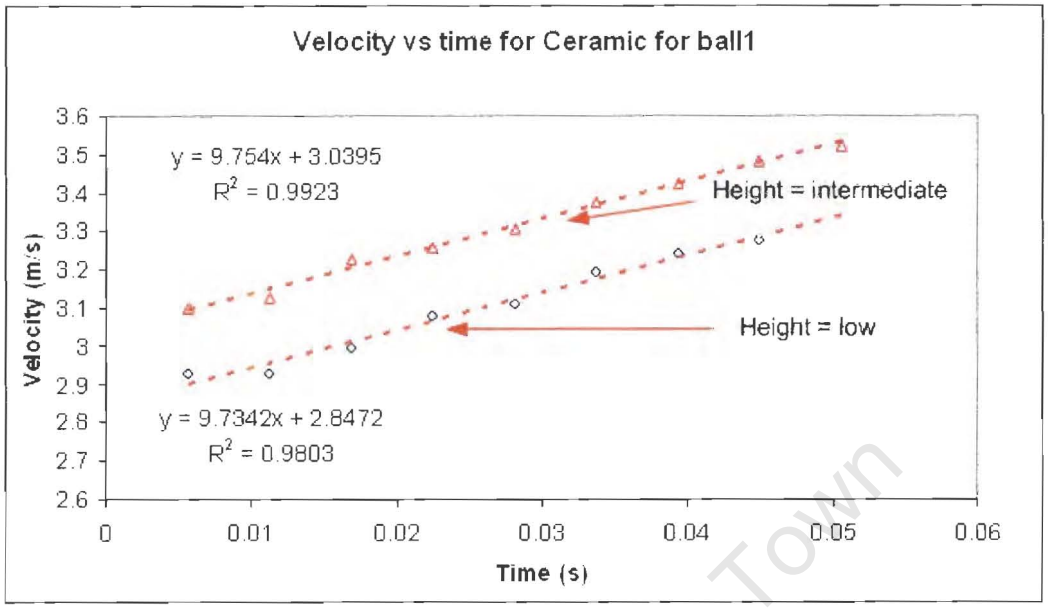

Figure 6-8– Effect of gravity on Ceramic

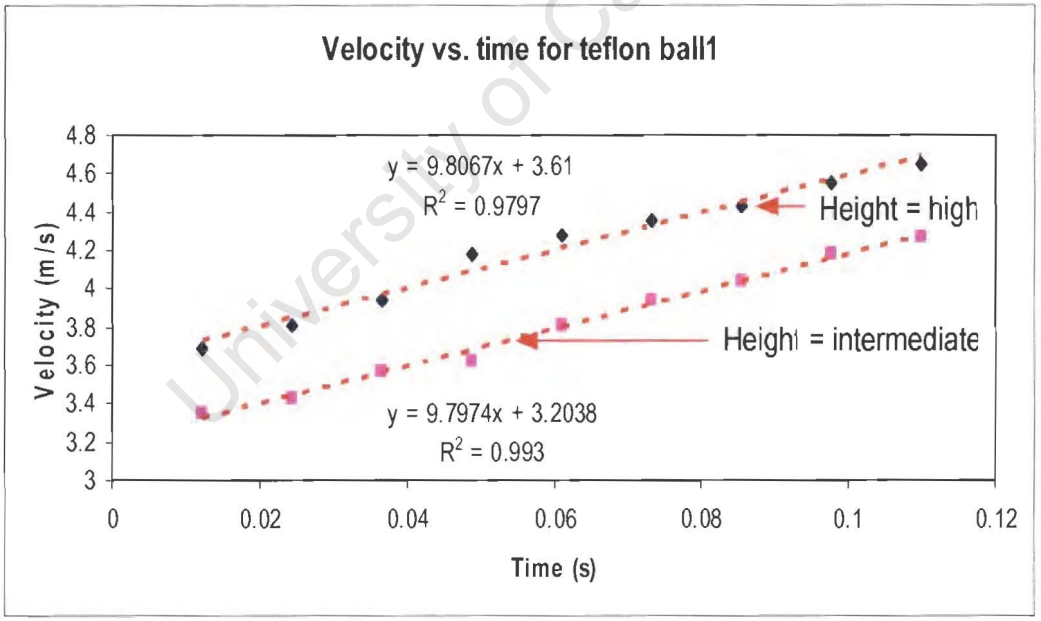

Figure 6-9 – Effect of gravity on Teflon

The effect of gravity and air drag was tested on drop tests for all the materials for the associated drop heights. From the graphs presented in **Figure 6-7, Figure 6-8, Figure 6-9,** the gradients of each line indicates the acceleration of the falling particle, which is

also referred the net effect of gravitational acceleration and drag, g is 9.81m/s^2. The R-squared values are the correlation coefficients of the data points. This determines how well the data fits the trend line. The height designations for the corresponding velocities are shown in **Table 6-15**.

Material	Height (m)	Designation	Measured g (ms^{-2})	% Error
Steel	0.568	High	9.79	0.2
	0.248	Intermediate	9.73	0.8
	0.127	low	9.74	0.7
Ceramic	0.248	Intermediate	9.75	0.6
	0.127	low	9.73	0.8
Teflon	0.632	High	9.80	0.1
	0.505	Intermediate	9.79	0.2
			Average	0.5

Table 6-15 – Error in g due to drag & experimental error

From the illustrations in **Figure 6-7** - **Figure 6-9**, the gradients of the corresponding graphs of the various materials yield the overall acceleration. It is noted that air drag can affect the calculated the gravitational acceleration of the graphs, here it is clearly noticed for the ceramic ball in **Figure 6-8**. From the graphs, the gravitational acceleration is calculated to be slightly less than $g = 9.81\text{m/s}^2$ (approximate value – varies at sea level), indicates that the particles experience drag.

Because the full image of the colliding shiny balls are not captured, the relative positions of the particles are determined by the specular reflections. The effects of specular reflections were mentioned in **Chapter 5** – Experimental Procedure. The corresponding error in the positions of the specular reflections is less than 1% for steel and ceramic respectively; therefore the effect of these offset positions was tested and the calculated acceleration was found to be unchanged.

6.2.4 Summary

Summarising the **Section 6.2**, the methodology of analysing the experimental data shows that it is possible to test key phenomenon such as the effect of gravity and air drag on the particles. The tests show, that the measured average acceleration derived from relative velocities gathered from the images deviated by an average 0.5% from gravity.

The error propagation in the calculated material interaction properties was carefully derived.

6.3 Material interaction results

The material interaction properties of the binary collision of four different materials are obtained. Namely: steel, ceramic, Teflon ball bearing. **Table 6-16** presents the material density and size tested for the range of heights given in **Table 6-15**.

Material	Diameter (mm)	Density (Kg/m^3)
Steel	8.15	7800
Ceramic	6.30	3284
Teflon	19.0	2122

Table 6-16 – Material types

6.3.1 Extracting the properties from the data

Extracting the pertinent material properties from the measured relative velocities is the next step in experimental procedure.

Figure 6-10 below, illustrates the schematic of the least square fit of the non dimensional angles, which is plotted from the Psi 1 and Psi 2. The experimental plots that are presented later are obtained from data such as shown in **Table 6-5**.

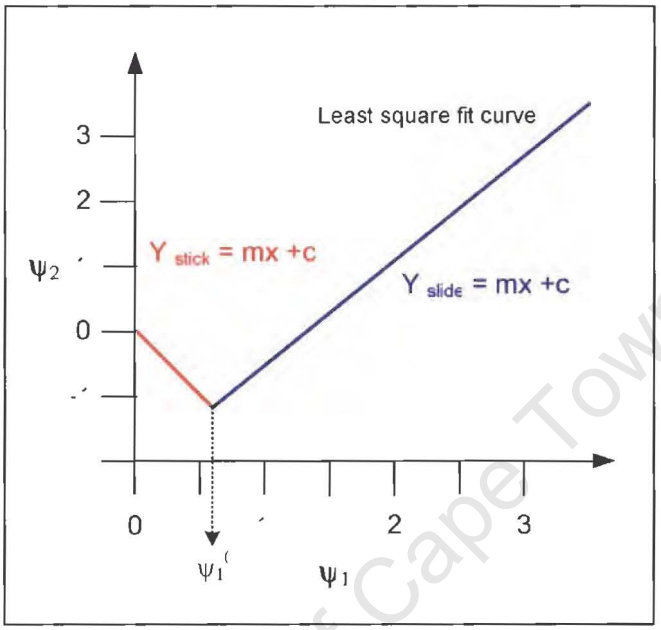

Figure 6-10 – Non dimensional angles of Incidence vs. Reflection

Because the collisions either stick or slide at the contact, it is quite complicated to distinguish the transition. The graph clearly identifies the two regimes of the sticking and slipping conditions delineated using least square fitting. These are indicated by the **red** and **blue** lines respectively in **Figure 6-10**. To identify these regimes, best fits from two regions are derived in order to yield the characteristic trend as observed by Maw *et al* [29] and Foerster *et al* [35]. The abscissa ψ_1^0 at the intersection of the straight lines yields the incidence angle γ_0.

Where,

$$\left|\psi_1^0\right| = \left|\tan \gamma_0\right| \qquad \textbf{Equation 6-29}$$

The sliding region is assumed to be where $|\psi_1| > |\psi_1^0|$ and yields e and μ. Points that lie pre-$|\psi_1|$ are deemed to be the stick region and these produce individual values of e and β_0. In the plot of Ψ_1 vs. Ψ_2, two slopes help distinguish the sticking and sliding regions.

Therefore from the graph, for sticking conditions:

$Y_{stick} = mx + c$ is equated with,

$$\psi_2 = -\beta\psi_1 \qquad \textbf{Equation 6-30}$$

and for sliding:

$Y_{slide} = mx + c$ is equated with,

$$\psi_2 = \psi_1 - \left[\left(\frac{7}{2}(1+e)\mu\right)\mathrm{sgn}(\boldsymbol{u}\cdot\boldsymbol{t})\right] \qquad \textbf{Equation 6-31}$$

From a plot of Ψ_1 vs. Ψ_2, the slope of **Equation 6-30** and the intercept of **Equation 6-31**, yield values for β, e and μ which are obtained from the data.

It is noted, because of the wide scatter observed in the measured data, that it is quite difficult to distinguish or identify the two regions. The observed the scatter in the data is unavoidable, especially for this type of experiment. To select the data which fits in the sliding or sticking regions, the following observation was made:

- Walton [5] described β as the coefficient of rolling restitution (also known as the tangential restitution), this occurs when the collision experiences stick-slip at the contact point.
- Typically, the stick-slip occurs only within the stick region of the Psi graphs.

From the observations made above, if we plot the tangential restitution plots vs. percentage offset as shown in **Figure 6-11**, the plots clearly indicate the transition from stick to slide. The slide region shows considerable stick-slip collisions and the slide regions shows pure slip.

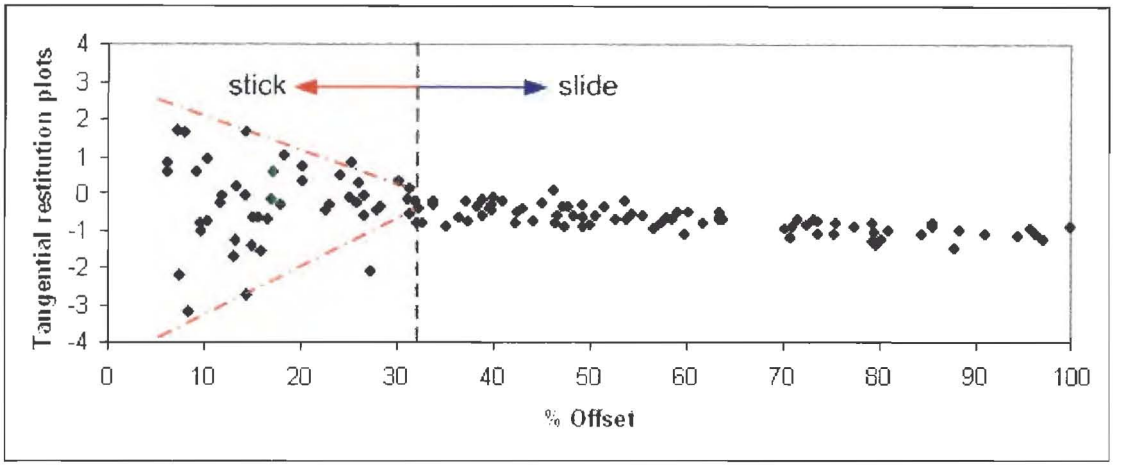

Figure 6-11 – Identifying stick and slide regions

Therefore from the observation made in **Figure 6-11**, it can be concluded that data that lie between 0% – 32% offset are considered to lie in the sticking region. Data that lie beyond 32% are deemed to slide. Note because of the wide scatter at the 32% offset mark, we approximate the data at this point to distinguish sliding and sticking.

In order to extract the pertinent material interaction properties we use the standard t-test distribution on the data. It is noted that the data has wide scatter in the stick and slip regions, a suitable fit of the standard deviation which is close to the mean value is calculated and outliers which do not fit within the standard deviation are omitted.

To visualise the data selection to calculate the mean for the coefficients of normal and tangential restitutions and friction, **Figure 6-12** illustrates the scheme to select the appropriate values from the calculated data. A typical data set looks similar to **Figure 6-12**, where values for the non-dimensional constants Ψ_1 and Ψ_2, coefficient of normal and tangential restitution and friction are calculated for the individual collisions. The legend in the figure illustrates the data which were selected and discarded to determine the mean and standard deviation values of the coefficients.

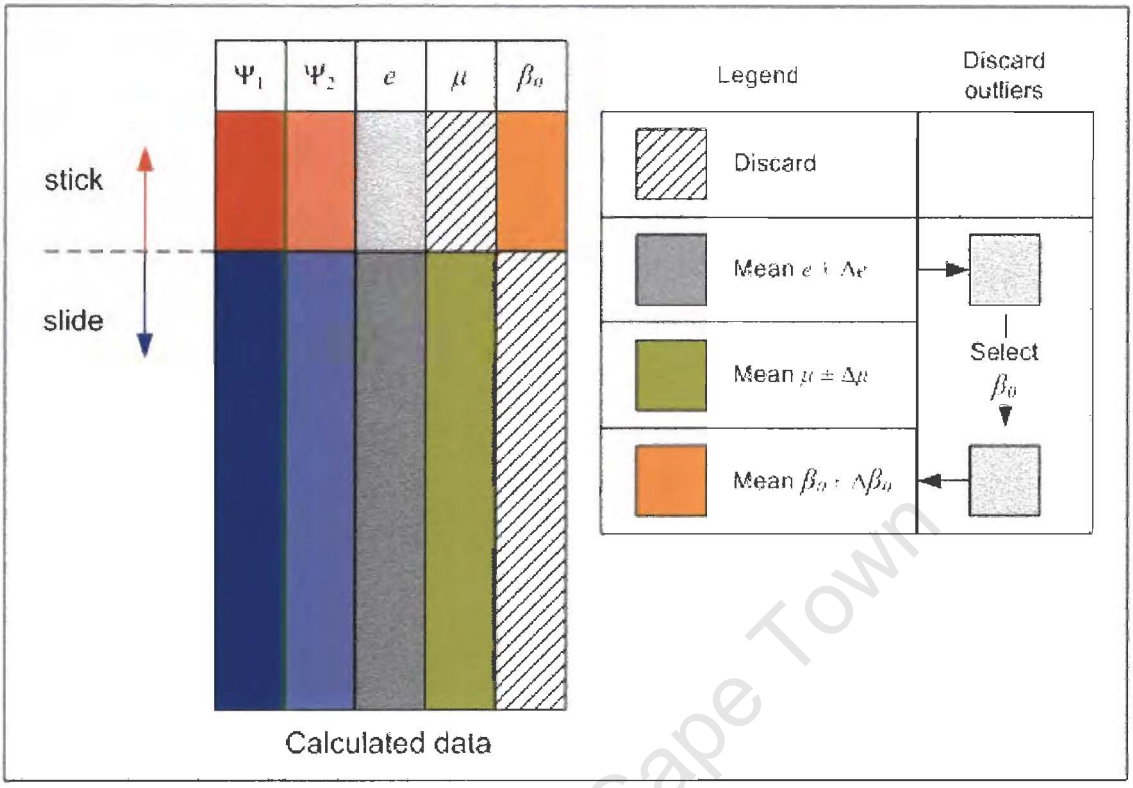

Figure 6-12 – Calculating the mean from the calculated data

The following methodology based on Foerster *et al* [35] was adhered in order to select the appropriate values:

- Friction is only calculated from the sliding region; therefore all the data in the sticking region were discarded. Even though we calculate the friction in the sticking region, this is mainly attributed to stick – slip as postulated by Maw *et al* [29] and Walton [5].

- Normal restitution is estimated from both sticking and sliding regions. The mean and standard deviation is calculated in sliding region. As shown in **Figure 6-13,** outliers in the sticking region that do not lie within the standard deviation derived in the sliding region are discarded. This was done because there is considerably more scatter in the calculated data in the sticking region than in the sliding region. Therefore, it is noted that the sliding region gives a better representation of the mean for *e,* the normal coefficient of restitution.

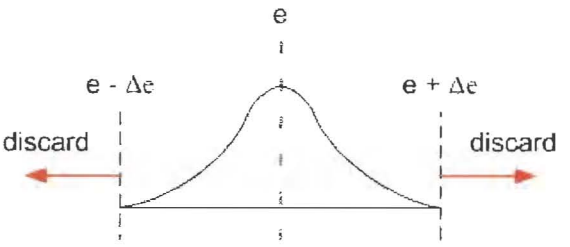

Figure 6-13 – Discarding outliers

- To calculate the coefficient of tangential restitution, data is selected from the sticking region as illustrated in **Figure 6-12.** If we refer to the plot of the tangential restitution vs. percentage offset in **Figure 6-11,** it is clear from the scatter in the graph, that β is poorly defined in the sticking region. To estimate the value of tangential restitution we adapt the assumption made by Foerster *et al* [35] to calculate the three coefficients in the two distinct regions. Because the coefficients of normal restitution, e, are calculated from both the sticking and sliding regions, their values can be used to select the best fit data from the sticking region. By selecting the data points that give e values within the standard deviation range derived from the sticking region, data that gives the best β values can be selected.

For this type of experiment scatter in the data is unavoidable. Selecting data statically will provide a better calculated value of the various material interaction properties. Statistical analysis on the data are conducted in MATLAB, details of the code is described in **Appendix I** – Statistical Analysis of the data.

6.3.2 Visualising the data

Often it is useful to visualise the data; that is to check if the obtained relative velocities and their corresponding offsets lie within acceptable ranges calculated from the measured images. This enables the user to analyse the data in a different perspective. **Figure 6-14** illustrates schematic of the impact plot produced in the MATLAB. The figure describes

the streak of the contact points and their respective unit tangent and normal vectors for the various offset settings.

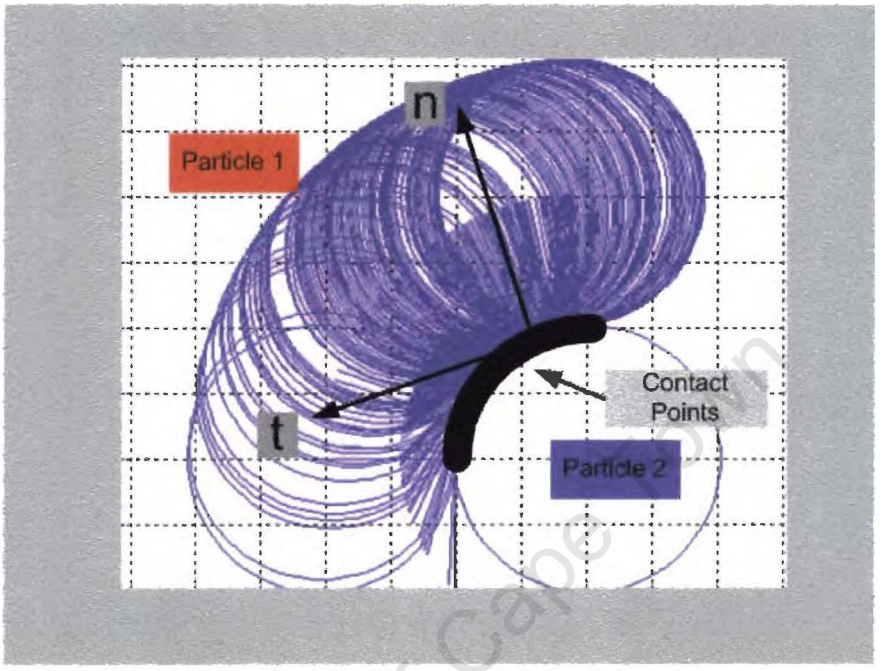

Figure 6-14 – Matlab schematic of the data points for various offsets.

Plots of non dimensional constants of steel, ceramic and Teflon materials are graphed to illustrate the transition from sticking to sliding, **Figure 6-15** to **Figure 6-21**. Initial plots are shown for the raw data. The data to produce these Psi graphs are shown in **Appendix G** – Material interaction property data.

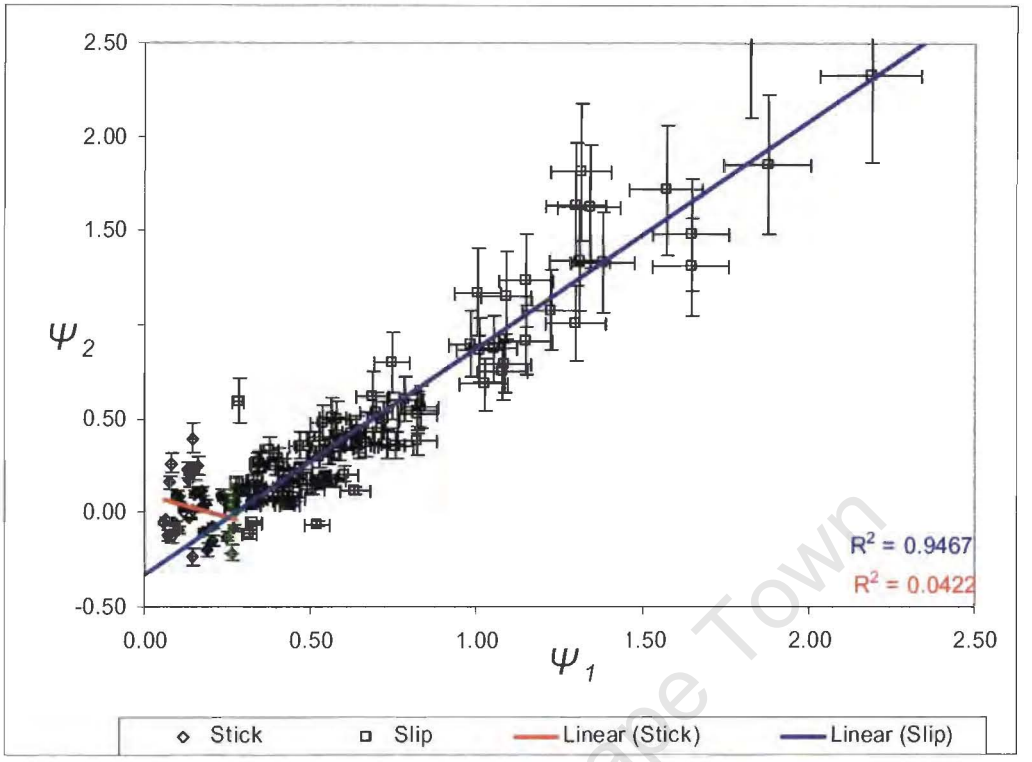

Figure 6-15 – Non dimensional plots for steel balls at height = high setting

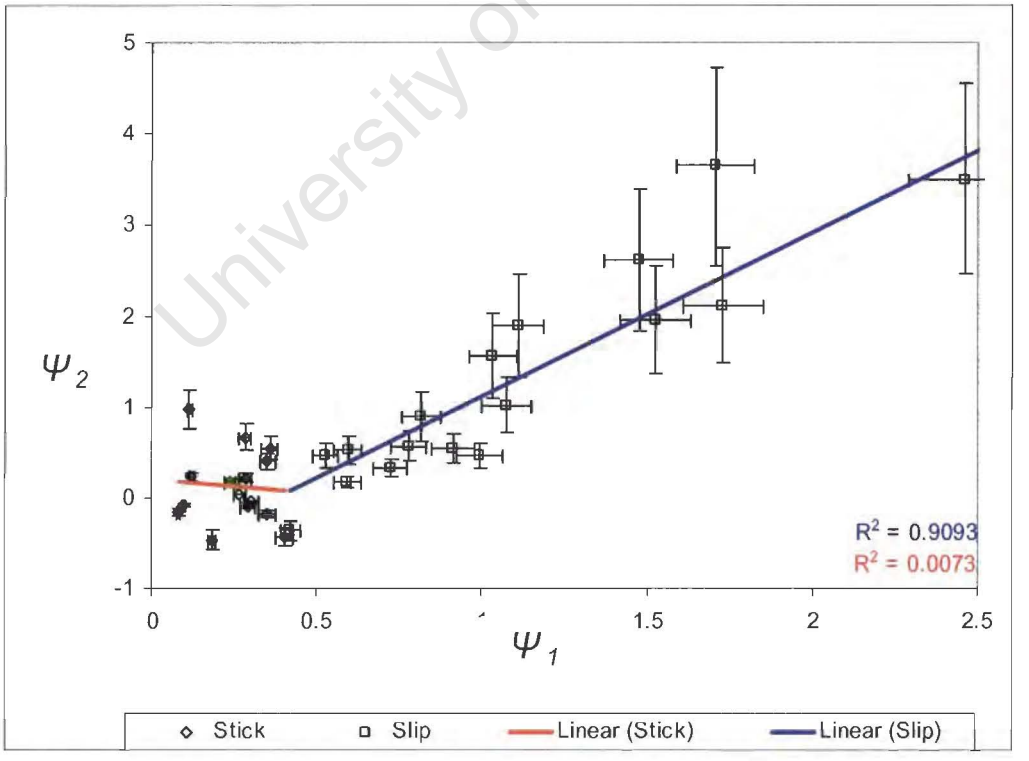

Figure 6-16 - Non dimensional plots for steel balls at height = intermediate setting

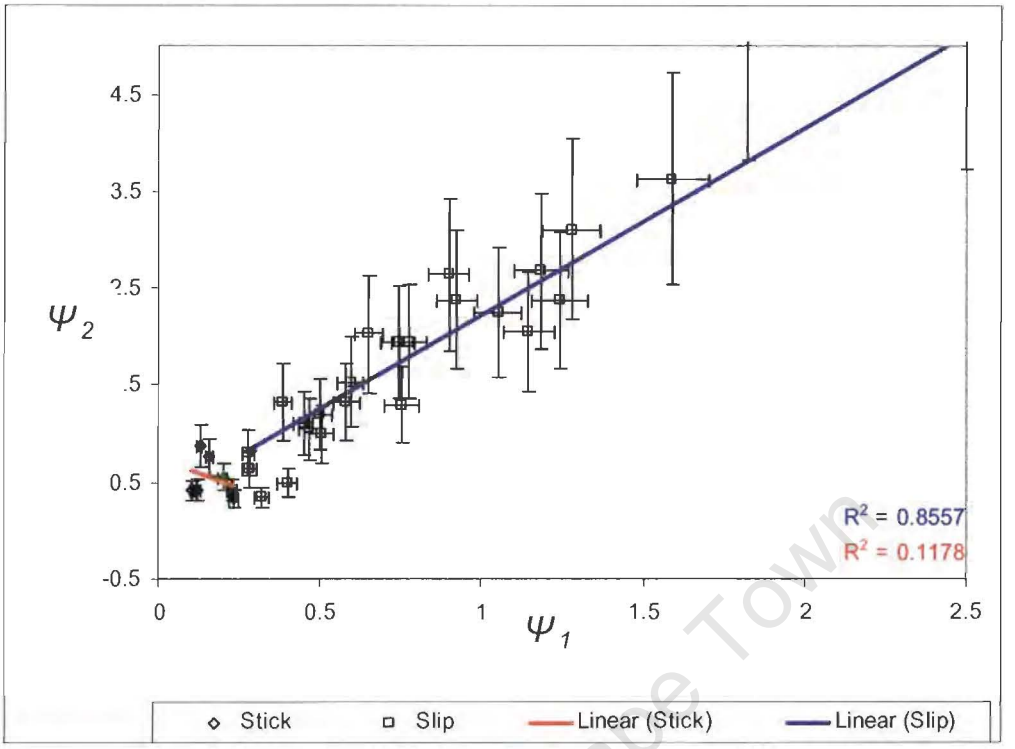

Figure 6-17 - Non dimensional plots for steel balls at height = low setting

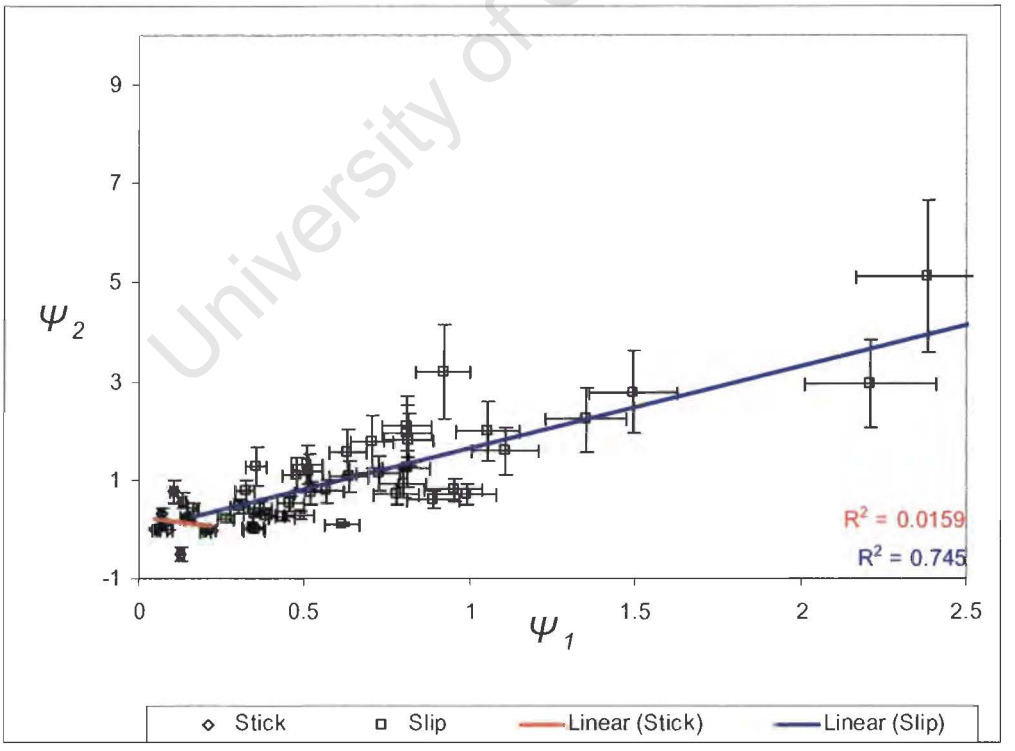

Figure 6-18 - Non dimensional plots for ceramic balls at height = intermediate setting

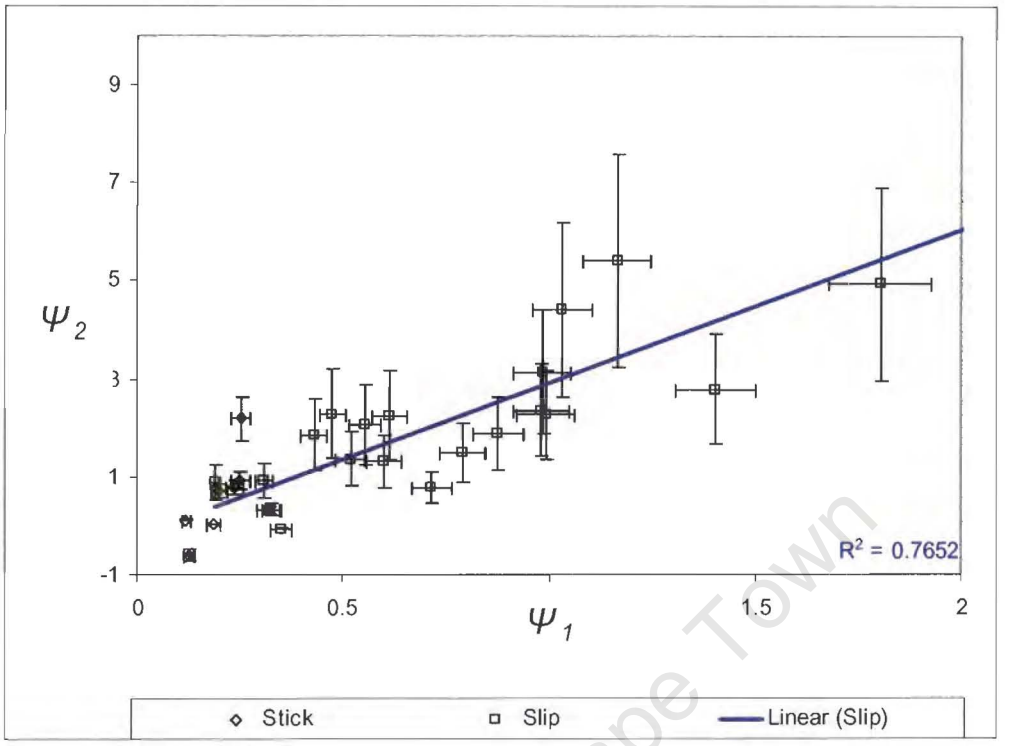

Figure 6-19 - Non dimensional plots for ceramic balls at height = low setting

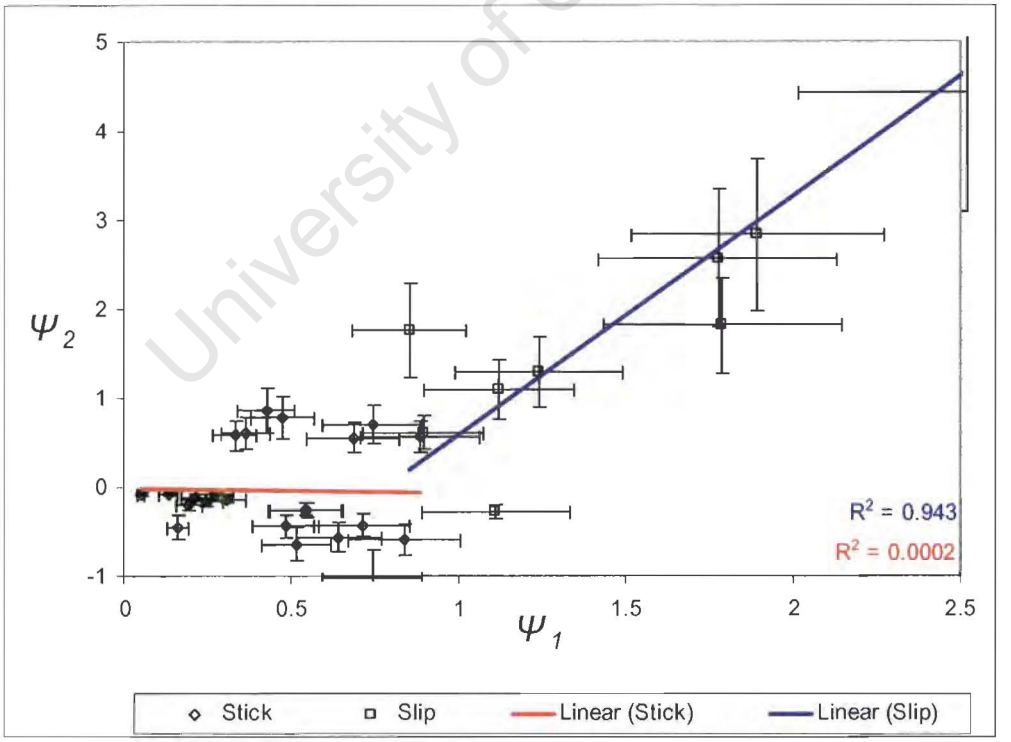

Figure 6-20 - Non dimensional plots for Teflon balls at height = high setting

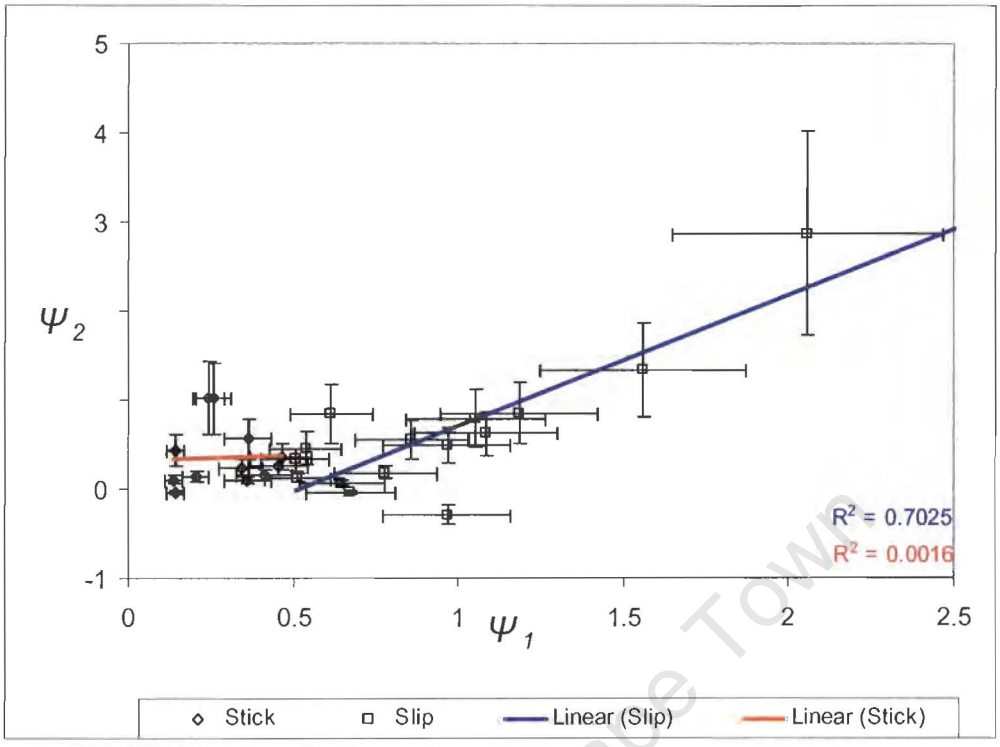

Figure 6-21 - Non dimensional plots for Teflon balls at height = intermediate setting

Error bars in **Figure 6-15** to **Figure 6-21** are derived from the absolute propagated errors in the experiment. **Table 6-17** tabulates the percentage errors for the ψ_1 and ψ_2 values. These errors indicate that the experiment is precise but the measurements are considerably affected by inaccuracies, in particular measuring the relative distances from the photographic images.

Material	ψ_1	ψ_2
Steel high	7%	22%
Steel inter	7%	30%
Steel low	7%	55%
Ceramic inter	9%	30%
Ceramic low	9%	55%
Teflon high	20%	40%
Teflon inter	20%	55%

Table 6-17 – Percentage Error bars

To fit the least square curve as shown in **Figure 6-10** and in **Figure 6-15** to **Figure 6-21** , the standard R-Squared fit from the EXCEL software is employed. R-Squared, is a statistical measure of how successful the fit is in explaining the variation of the data. Put another way, R-square is the square of the correlation between the response values and the predicted response values. It is also called the square of the multiple correlation coefficients and the coefficient of multiple determinations.

Equations for calculating trend lines are given in the "help directory in MATLAB", R-squared is defined as the ratio of the sum of squares of the regression (SSR) and the total sum of squares (SST).

$$R^2 = 1 - \frac{SSE}{SST} = \frac{SSR}{SST}$$

Where, SSR is defined as

$$SSR = \sum \left(\hat{Y}_i - \bar{Y}_i \right)^2$$

$$SSE = \sum \left(Y_i - \hat{Y}_i \right)^2$$

And *SST* is also called the sum of squares about the mean, and is defined as where *SST* = *SSR* + *SSE*.

$$SST = \left(\sum Y_i^2 \right) - \frac{\left(\sum Y_i \right)^2}{n}$$

"*Given these definitions, R-square can take on any value between 0 and 1, with a value closer to 1 indicating a better fit. For example, an* R^2 *value of 0.8234 means that the fit explains 82.34% of the total variation in the data about the average. If you increase the number of fitted coefficients in your model, R-square might increase although the fit may*

not improve. Note that it is possible to get a negative R-square for equations that do not contain a constant term. If R-square is defined as the proportion of variance explained by the fit, and if the fit is actually worse than just fitting a horizontal line, then R-square is negative. In this case, R-square cannot be interpreted as the square of a correlation." – MATLAB ver.6.5 Help

Because the R^2 determines how well the data fits to the plotted curve, we can determine the error for the combined data in sticking and sliding regions. Subsequently, we can determine its effect on the measured material properties from these regions of interaction. **Table 6-18** illustrates the R-squared values for the stick and slide regions.

Material	Height Designation	R^2 stick region	R^2 slide region
Steel	High	0.0421	0.9467
	Intermediate	0.1178	0.8557
	low	0.0204	0.9093
Ceramic	Intermediate	0.0098	0.7450
	low		0.7652
Teflon	High	0.0002	0.9430
	Intermediate	0.0016	0.7025

Table 6-18 - R^2 for stick and slide regions

The stick region R^2 is below 0.1 as seen in **Table 6-18** indicating that the value derived from the fit does not correspond to the experimental data. This is as a result of the wide scatter in this region. The slide region R^2 shows little scatters in the data. To comprehend the scatter in the stick region, we examine **Figure 6-22**.

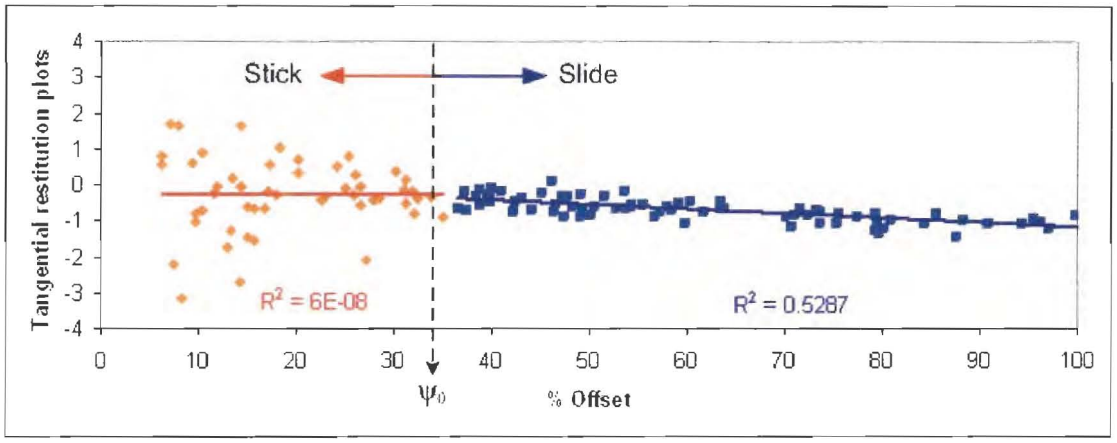

Figure 6-22 – Understanding the Tangential coefficient of restitution

In **Figure 6-22**, plot of % Offset vs. the data obtained for the beta in the calculations for steel at high height setting as an example is illustrated. Upon examining the graph, it is clear that the significant correlation contributed by the R^2 between the predicted and the response values indicates that this region, in particular the β, has a significant error. Referring to Maw *et al* [29] in **Chapter 2** – Evaluation of the contact model, β is defines as the rolling contact at the contact point, where it is continuously either sliding or sticking. In other words, this region is highly unstable, therefore the wide scatter in the sticking region.

The tangential restitution is equated as:

$$\beta = -\frac{(\boldsymbol{n}\times\boldsymbol{u}')}{(\boldsymbol{n}\times\boldsymbol{u})} \qquad \textbf{Equation 6-32}$$

Given that normal $\boldsymbol{n}$ and tangent $\boldsymbol{t}$ vectors are orthogonal to each other, therefore **Equation 6-36** can be rewritten as:

$$\beta = -\frac{(\boldsymbol{t}\cdot\boldsymbol{u}')}{(\boldsymbol{t}\cdot\boldsymbol{u})} \qquad \textbf{Equation 6-33}$$

The tangential restitution is therefore the ratio of pre- and post- velocities in the tangential direction. The wide scatter in the sticking region can be attributed to the post-velocities in the tangential direction. The equations for ψ_1 and ψ_2, are given in **Equation 6-34** and **Equation 6-35.** Data plots of these constants are graphed with respect to the contact offset as shown in **Figure 6-23.**

$$\psi_1 \equiv -\frac{(u \cdot t)}{(u \cdot n)}$$ **Equation 6-34**

$$\psi_2 \equiv -\frac{(u' \cdot t)}{(u \cdot n)}$$ **Equation 6-35**

Therefore the ratio of angle is:

$$\frac{\psi_2}{\psi_1} \equiv \left[-\frac{(u' \cdot t)}{(u \cdot n)}\right] * \left[-\frac{(u \cdot n)}{(u \cdot t)}\right]$$ **Equation 6-36**

$$\frac{\psi_2}{\psi_1} \equiv \frac{(u' \cdot t)}{(u \cdot t)} = (-)\beta$$ **Equation 6-37**

The sign in **Equation 6-30** is in contradiction to **Equation 6-37** found in Foerster *et al* [35] paper. The derived tangential restitution value is not describing its effect in the stick region. Therefore identify this effect the negative sign is reinstated to show the characteristic plot of non dimensional graph showing tow distinct slopes, one for sticking and the other for sliding.

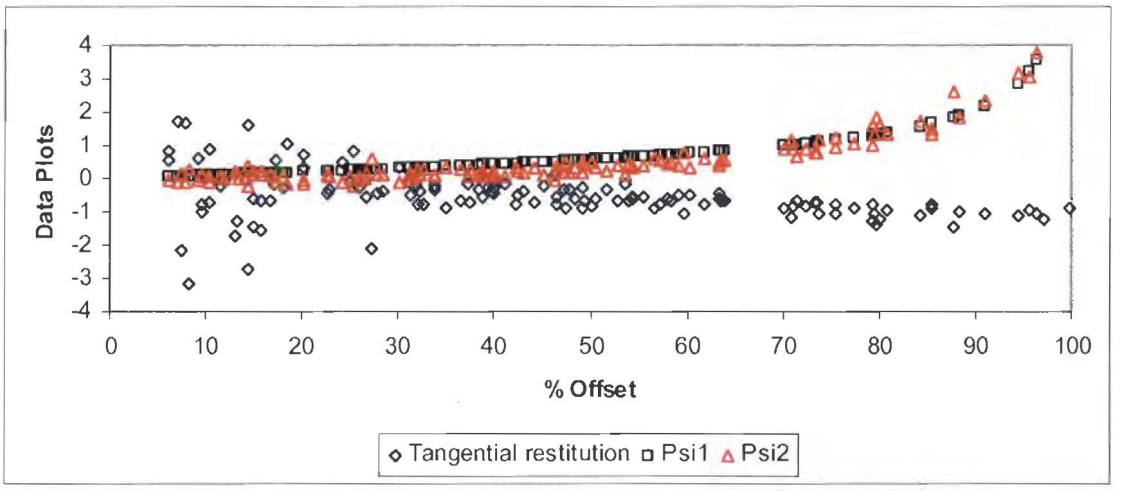

Figure 6-23 – ψ_1 ψ_2 and tangential restitution plots vs. offset

It is assumed that the tangential component in **Equation 6-34** and **Equation 6-35** contributes to the scatter for direct impacts but its effect is masked by the normal component during collision.

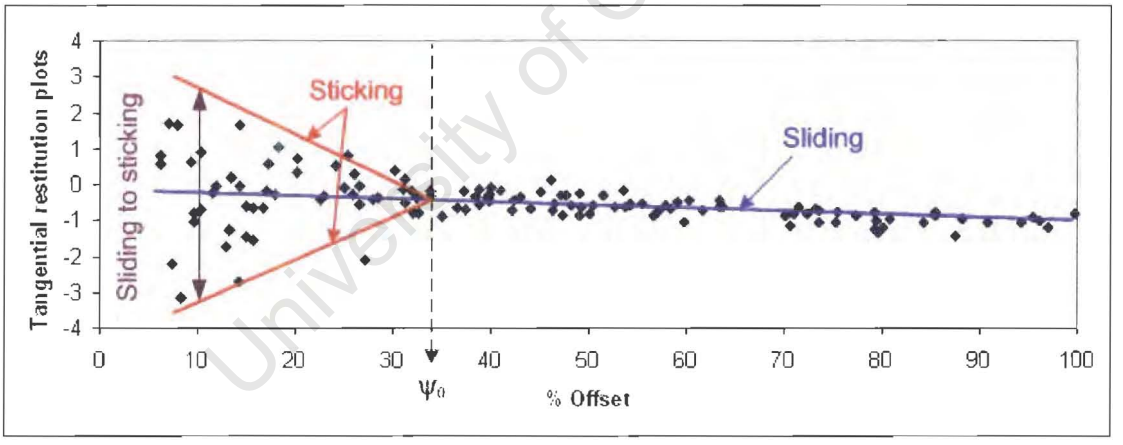

Figure 6-24 – Switching between sticking and sliding

Figure 6-24 shows the unstable region for the steel balls at high height setting. If we assume the blue line indicates the linear fit of the collisions which are in sliding, and the red line indicates the linear boundary for the collisions which are sticking, then the data between the two lines are all the points which are in transition or highly unstable (changing from sliding to sticking).

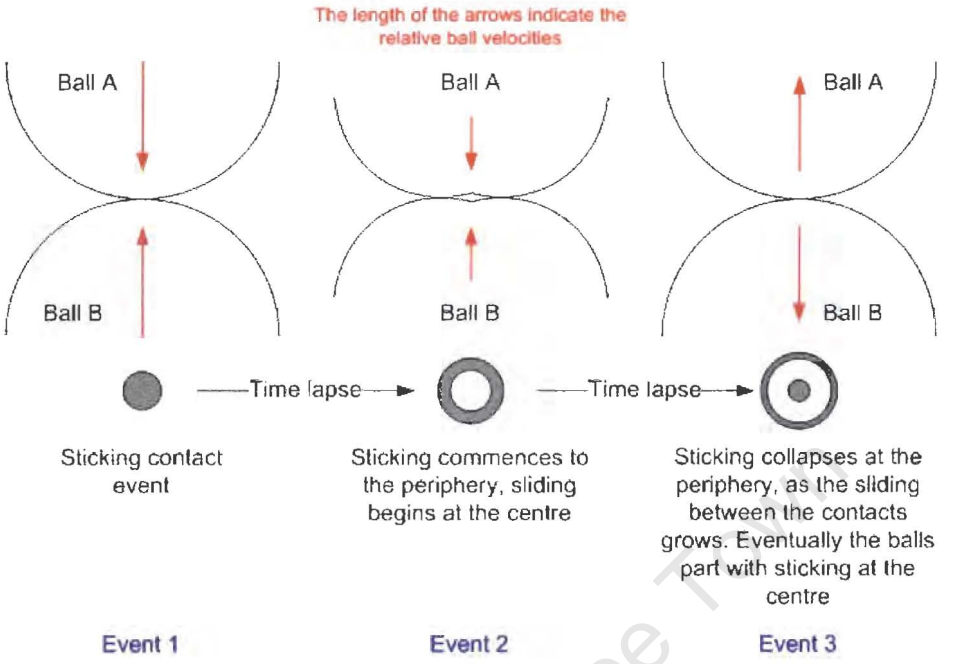

Figure 6-25 – Schematic of the Hertzian theory of contact

Figure 6-25 illustrates the schematic of the Hertzian theory contact. Details of the contact are described in **Chapter 2** – Evolution of the contact model. To understand the instability of the sticking region for the tangential restitution, the Hertzian theory of contact can be used. Based on the theory and referring to **Figure 6-25** the following can be assumed:

- *Event 1*: Beginning of direct contact, sticking occurs between the contacting surfaces. Contact areas are represented by the grey circles.
- *Event 2*: During contact, the deformation caused on both balls, changes the contact area. A periphery of sticking occurs with sliding at the centre.
- *Event 3*: Once the both balls have reached maximum deformation, restitution takes place. This is where the periphery of sticking collapses as the sliding area increases. At the same time sticking occurs at the centre.

The classical approach to impact, states that during collision, the angles of incidence and reflection are equal for impacts with no initial spin. It is noted by Walton [26] that the

stick region is highly erratic; especially the tangential restitution is continually changing between stick and slip. **Figure 6-26** illustrates examples of collision events based on varying slip conditions.

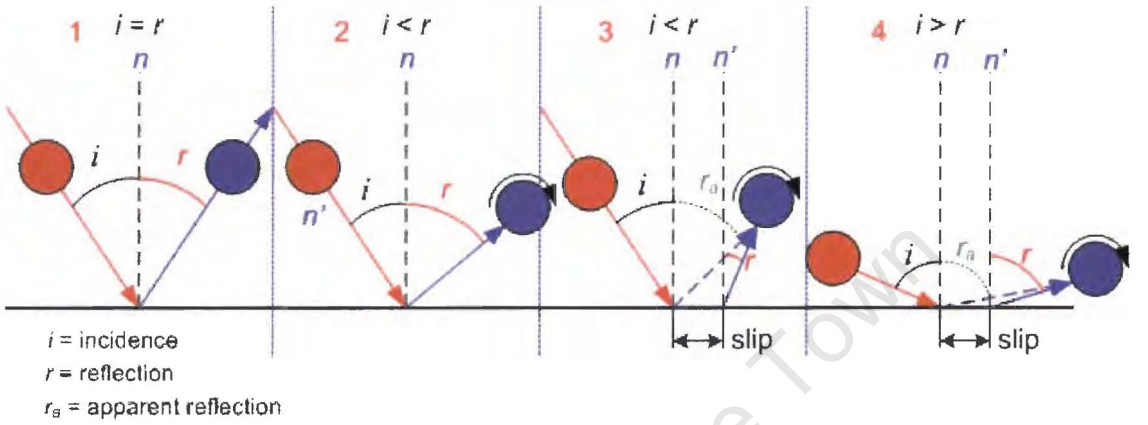

Figure 6-26 – Angles of incidence and reflection orientations

The following scenarios are described to define the various possible types of collisions:

- *Scenario 1*: For a classical impact, the angles incidence and reflection are equal, the normal about the contact point is perpendicular, and there is no post spin after collision.
- *Scenario 2*: For contacts that experience stick during collision, it is assumed that angle of incidence and reflection are not equal and this promotes spin post collision.
- *Scenario 3*: For collisions that experience stick-slip-stick, it is assumed that instantaneous contact is sticking then sliding and sticking and finally depart with spin. For this case, it can be concluded that at initial contact coeffiiecient static friction is promoting stick, and then proceeds to kinetic friction. Because the initial contact angle is small, the colliding ball loses kinetic energy as heat and the kinetic friction is overcome by static friction which causes the ball to depart from the surface with spin.

- *Scenario 4*: For large contact angles, the collision is assumed to be pure sliding. Therefore the contacting surfaces are only governed by the kinetic friction.

This collision history provides high instability in the tangential direction. Kharaz *et al* [31] refer to this as the effect the tangential compliance. Therefore the wide scatter in the sticking region is attributed to the rate of growth of the sticking periphery and collapse, which is an effect of the tangential compliance.

6.3.3 Material Interaction properties

Material interaction properties are presented in **Table 6-19**. Statistical analysis was conduced on the calculated data for all the tested materials using the technique presented in **Section 6.3.2**.

Table 6-20 illustrates the relative velocities about the normal and tangential directions. Maximum and minimum velocities are derived from the data presented for the various materials.

Material	**Height**	e	β_0	μ
Steel	*high*	0.75 ± 0.02	0.58 ± 0.55	0.041 ± 0.003
	intermediate	0.58 ± 0.06	0.43 ± 0.42	0.107 ± 0.015
	low	0.22 ± 0.07	0.71 ± 0.61	0.250 ± 0.024
Ceramic	*intermediate*	0.33 ± 0.10	0.17 ± 0.16	0.101 ± 0.082
	low	0.11 ± 0.06	0.97 ± 0.81	0.256 ± 0.120
Teflon	*high*	0.56 ± 0.02	0.63 ± 0.61	0.184 ± 0.037
	intermediate	0.49 ± 0.02	0.61 ± 0.60	0.105 ± 0.003

Table 6-19 - Material interaction properties for tested materials

Material	Designation	Normal (min)	Normal (max)	Tangent (min)	Tangent (max)
Steel	High	0.077	1.650	0.086	1.567
	intermediate	0.135	0.913	0.041	0.851
	low	0.088	0.477	0.022	0.444
Ceramic	intermediate	0.064	1.245	0.028	1.266
	low	0.138	0.462	0.046	0.379
Teflon	High	0.380	1.995	0.105	2.100
	intermediate	0.208	1.719	0.219	1.681

Table 6-20 – Relative velocities about the normal and tangent (ms^{-1})

Terminology:

- e = coefficient of normal restitution
- β_0 = coefficient of tangential restitution
- μ = friction

The large standard deviation of the tangential restitution is a result of the wide scatter in the region in which the tangential restitution is derived. Comparing the material interaction properties of the various materials for their corresponding impact heights as shown in **Table 6-19;** there is distribution in the measured coefficients. This is noticeable for the changing coefficients of normal restitutions and friction for different impact heights for the steel, ceramic and Teflon.

6.3.4 Material Interaction Comparisons

In this section we will compare visually the measured interaction properties as a function the various heights, this is done because one of the prerequisites of the hypothesis states that material interaction properties could be affected by the changing velocities.

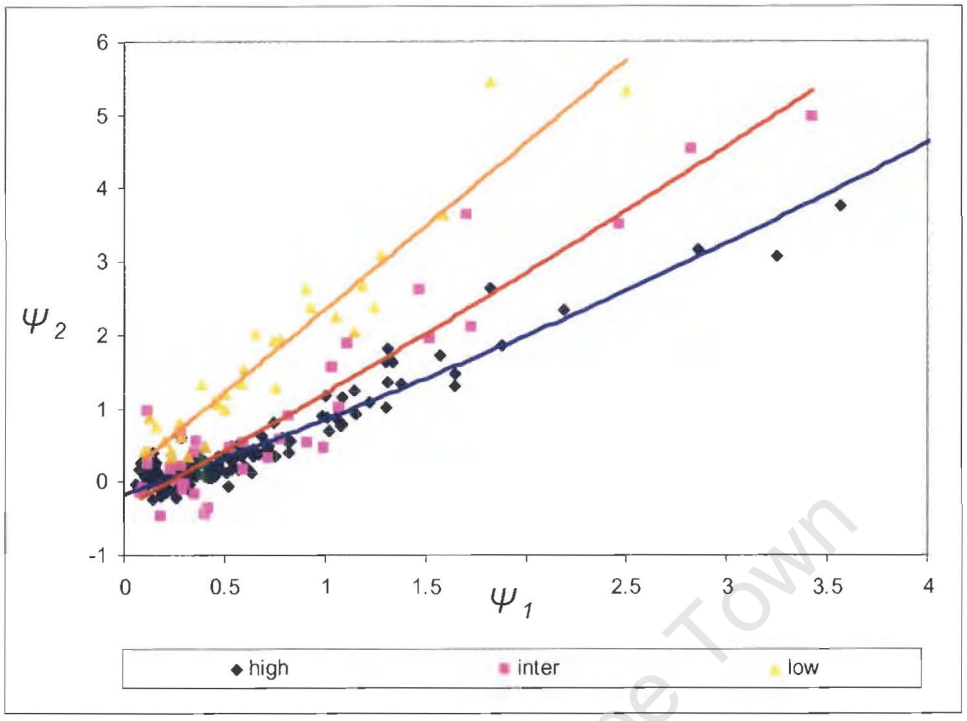

Figure 6-27 – Non dimensional constants compared for Steel ball bearings at various heights

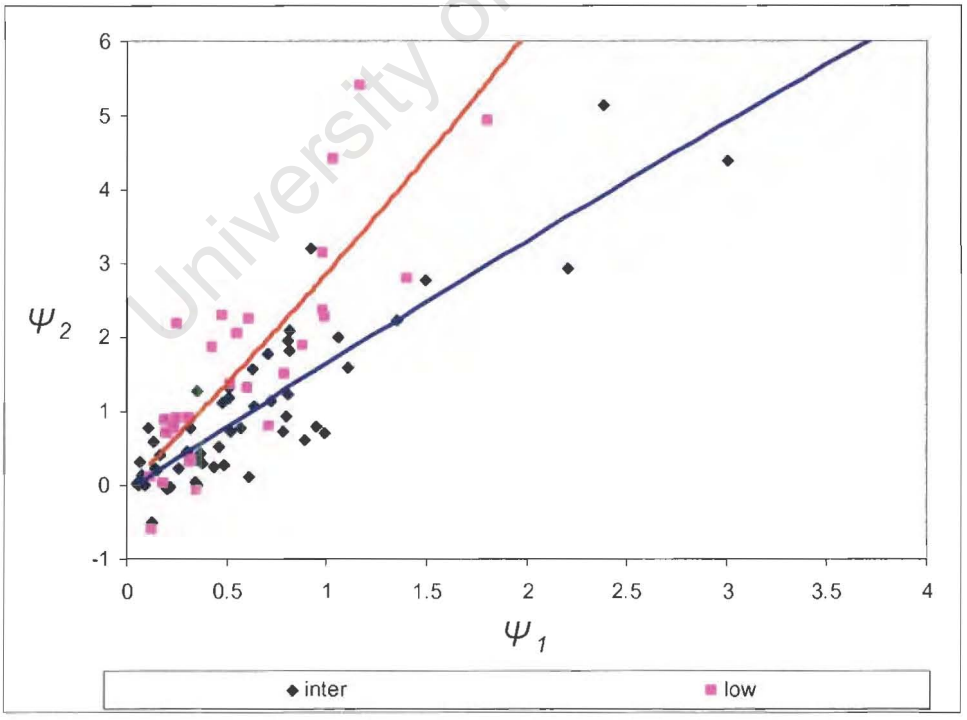

Figure 6-28 – Non dimensional constants compared for Ceramic ball bearings at various heights

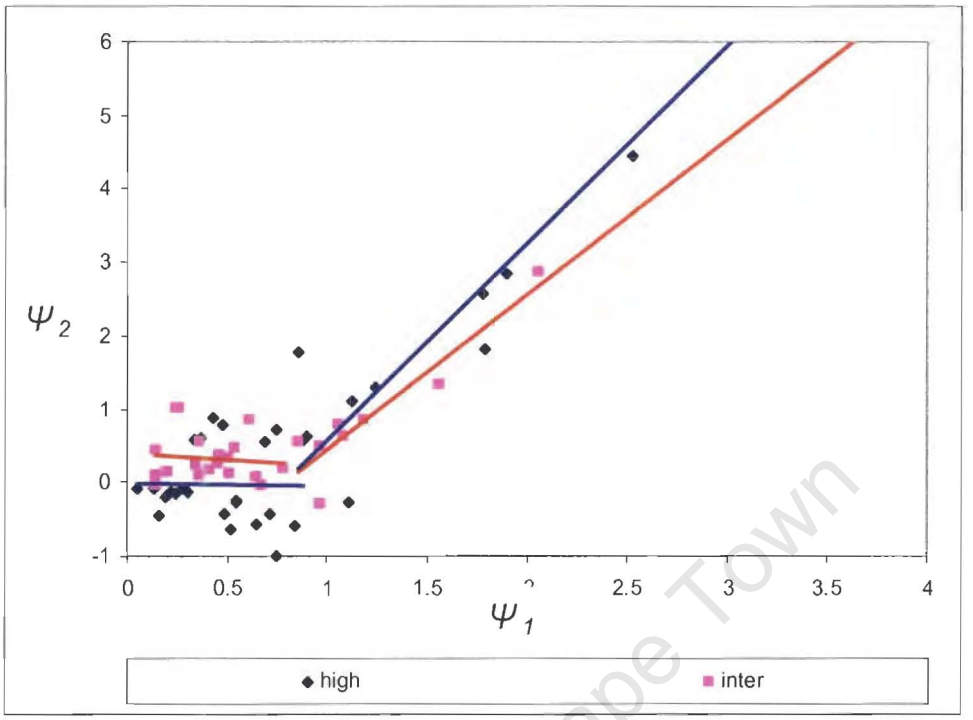

Figure 6-29 - Non dimensional constants compared for Teflon ball bearings at various heights

From the graphs presented in **Figure 6-27** to **Figure 6-29,** the comparisons of the non dimensional constants for the varying heights indicate clear dissimilarity. There is considerable difference for the steel and ceramic ball bearings. Teflon's non dimensional constants seem similar to each other. It can be assumed from the observations that the shiny materials such as the steel and ceramic ball bearings behave differently to materials with a rougher surface such as Teflon. The noticeable differences are in the sliding regions for both steel and ceramic ball. It can be concluded that materials with shiny surfaces may have an increase in friction for increasing velocity, whereas rough the material's friction remains unchanged.

Based on these observations the following assumptions can be drawn for the steel:

- High impact velocities decrease the gradient of the characteristic Psi graph in the sliding region. This indicates that a high impact velocity reduces the contact friction between two surfaces.

- It may be inferred that the coefficient of normal restitution in the sticking region will increase with increasing velocity.

Given these assumptions above, the normal restitution and friction values for the varying heights can be compared as a function offset. These graphs are illustrated in **Figure 6-30** to **Figure 6-35.**

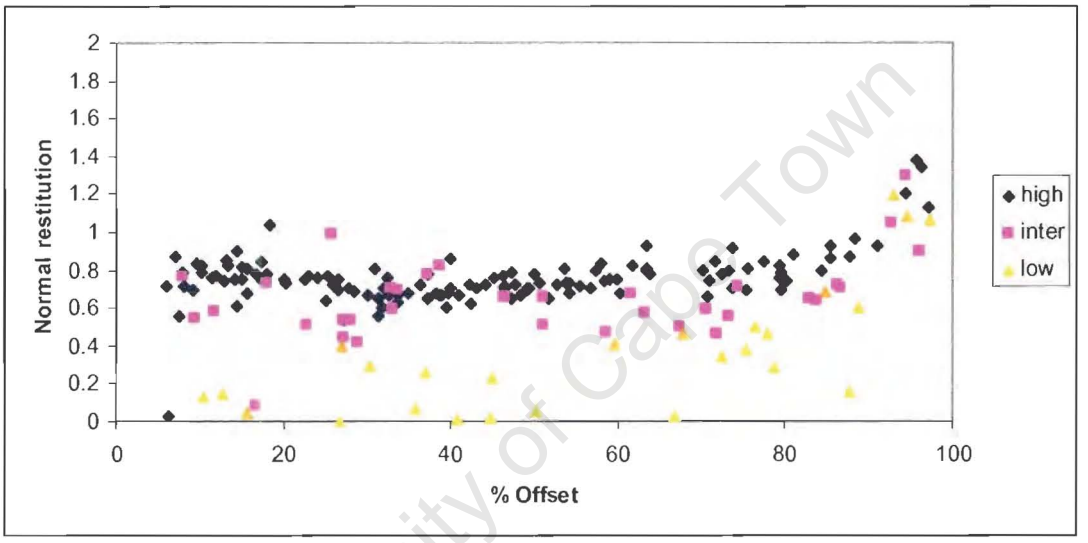

Figure 6-30 – Coefficient of Normal restitution comparison for steel

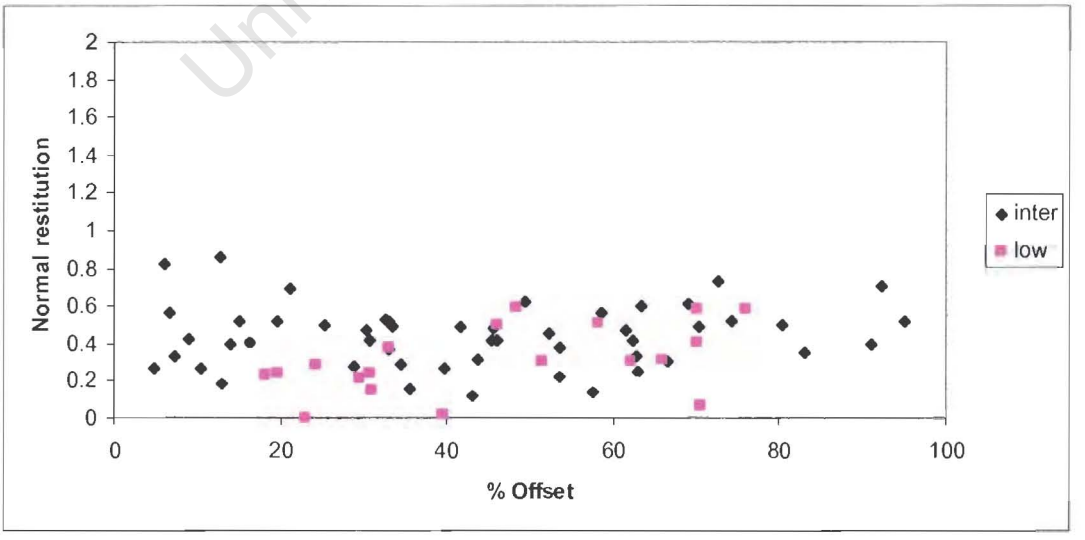

Figure 6-31 – Coefficient of Normal restitution comparison for ceramic

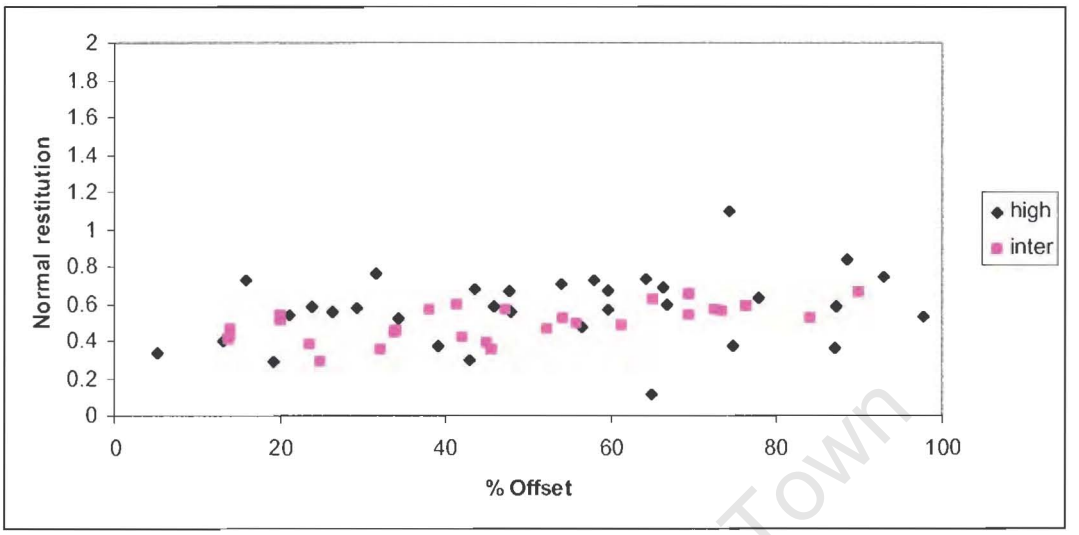

Figure 6-32 – Coefficient of Normal restitution for Teflon

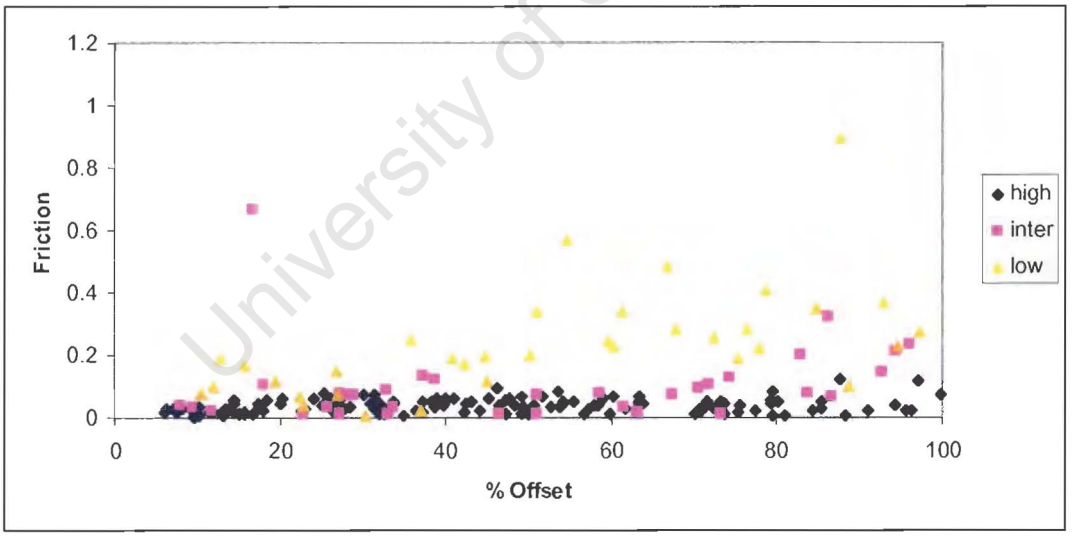

Figure 6-33 – Friction comparisons for Steel

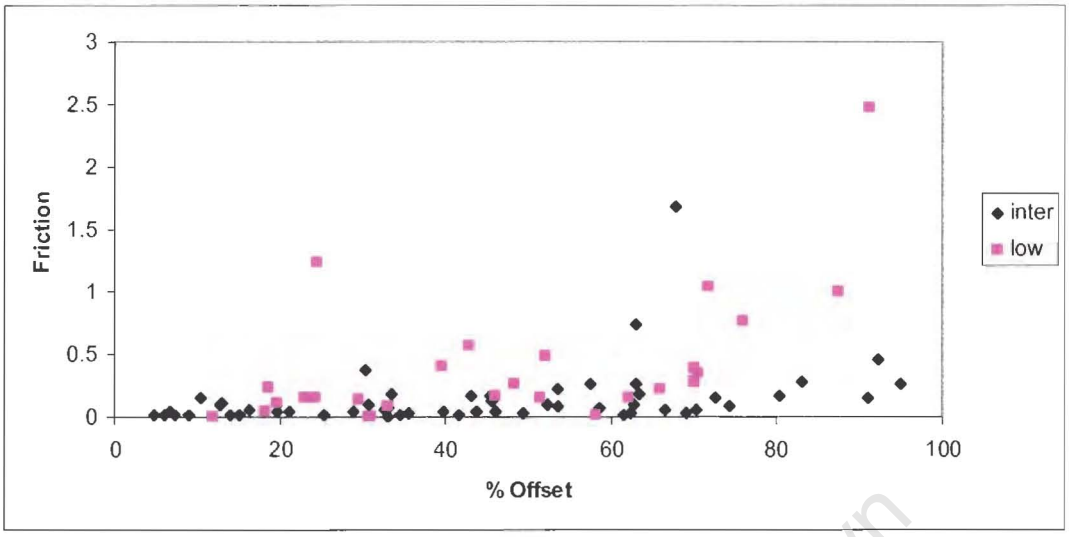

Figure 6-34 – Friction comparison for Ceramic

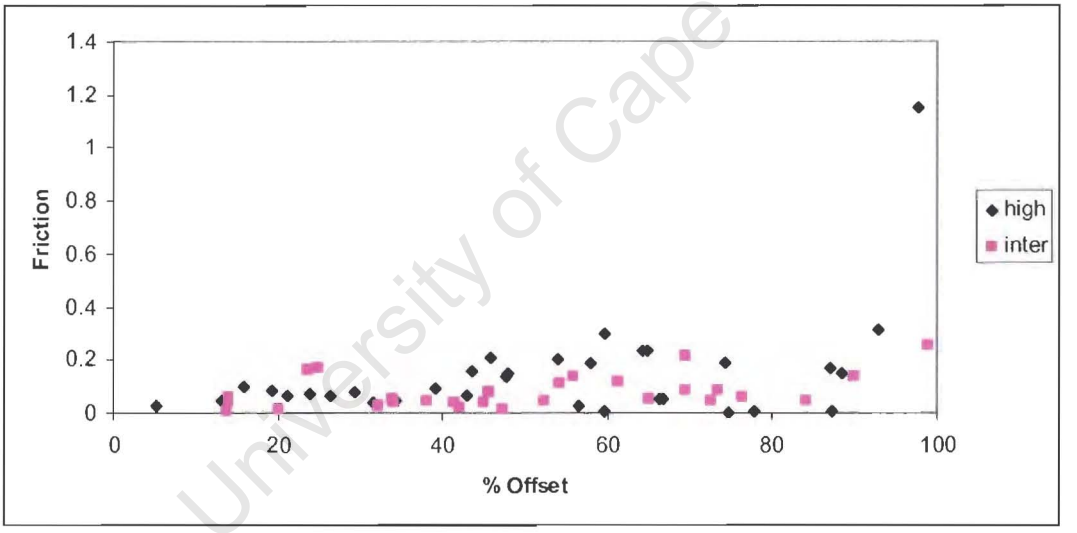

Figure 6-35 – Friction comparisons for Teflon

The plots in **Figure 6-30** to **Figure 6-32** indicate that the steel and ceramic balls behave considerably differently to Teflon. It is observed that the coefficients of restitution of both steel and ceramic decrease with respect to the impact velocity, where the coefficient of restitution for Teflon appears to remain constant.

If we compare the friction vs. offset for the materials in **Figure 6-33** to **Figure 6-35**, the difference is reinforced. The steel and ceramic balls increase in friction for varying impact velocities and the Teflon balls appears to decrease in friction with respect to the impact velocity.

Upon close observations of the friction data and considering observations made of the coefficient of restitution for all materials and comparing the non dimensional graphs for all materials the following conclusions can be drawn:

- A probable explanation for the decreasing normal restitution for the shiny materials, steel and ceramic balls for decreasing impact velocity is that the particles experience a temporary stick at contact and then proceed to part due to momentum.

- The above explanation can also be supported by the fact that friction for shiny materials will be greater at very low impact velocities than at high impact velocities.

- The Teflon materials are generally used as an alternative for bearings in industrial machineries for low speed operations. Therefore, Teflon's friction increases as the impact velocities increase. Because Teflon is made from a hardened polymer compound, rubbing two Teflon samples will induce heat within the material, therefore resulting in stick (i.e. high friction).

Now, that an experiment has been established to measure pertinent material interaction properties, the next stage in the thesis presented here is to test the rest of hypothesis. The hypothesis of thesis states that applying these derived material interaction properties into the Discrete Element Model should improve its reliability. This is tested in the following **Chapter 7** – DEM comparisons and testing.

Chapter 7

DEM Comparisons and Testing

This chapter focuses on testing the models in the Discrete Element Method (DEM) utilising the measured interaction parameters. The tested models include the viscous damping model found in Particle Flow Code, and a range of standard Contact Models

7.1 Approach to Testing DEM

Testing numerical models in DEM must follow a rigorous routine in which simulation is compared with experiment. In order to maintain accurate comparisons, the models in DEM should be repeated with similar conditions to those of the experiment. For the in-flight collision experiment, two particles are subjected to freefall and collide in mid-air to extract the pertinent the pre- and post- relative velocities and their corresponding material interactions properties for varying impact velocities. Referring to the hypothesis of this project:

Applying measured material interaction properties in DEM should improve its predictions.

To test the hypothesis, measured material interaction properties of the tested materials, such as steel, ceramic and Teflon are incorporated into DEM and tested against binary impact data. Applying the interaction properties alone cannot test how well the model can cope with varying conditions. Therefore similar experimental conditions were set up as comparative tests in DEM and the following were compared.

- Post- collision velocities are compared for varying impact velocities (pre-collision velocity)

- Offsets between the two particles are changed to achieve a range of collisions; the collisions range from sticking conditions to complete sliding conditions.

This methodology is illustrated in a flowchart in **Figure 7-1**, where the highlighted yellow boxes indicate the experimental stage and their corresponding components such as particle velocities for both Ball 1 and Ball 2, and measured material interactions for different materials. The red boxes describe the DEM testing phase where a variety of models can be tested. Finally, the green box highlights the comparison stage, where the velocities are compared between DEM and Experimental.

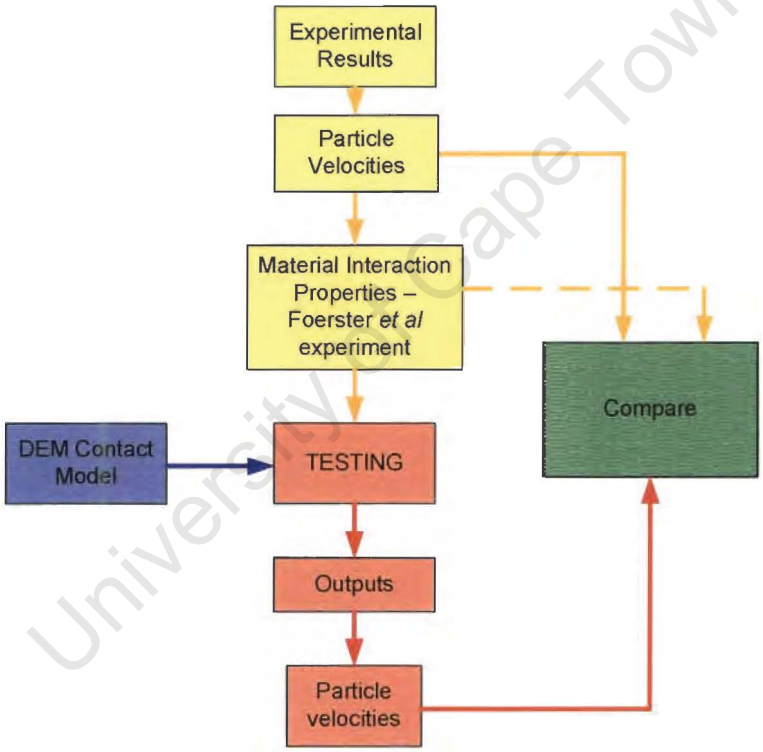

Figure 7-1 – Testing procedure

DEM is tested in two separate packages. Firstly we test the outputs DEM in a commercially available software package called Particle Flow Code (PFC) supplied by Itasca. Secondly, we test the DEM in an in-house model tester encoded in Delphi and developed Dr. R Sarracino of the Mineral Processing Research Unit of UCT.

7.2 Predictions using PFC

For preliminary tests, the values obtained for the material interaction properties were tested in the viscous damping model (VDM) found in the Particle Flow Code (PFC) package distributed by Itasca. **Figure 7-2** below illustrates the schematic of the collision and conditions which are set in PFC. Conditions such as offset, pre-velocities of both particles, initial height and step time of the simulation are inputs, and outputs are post-velocities, position and spin of the particles.

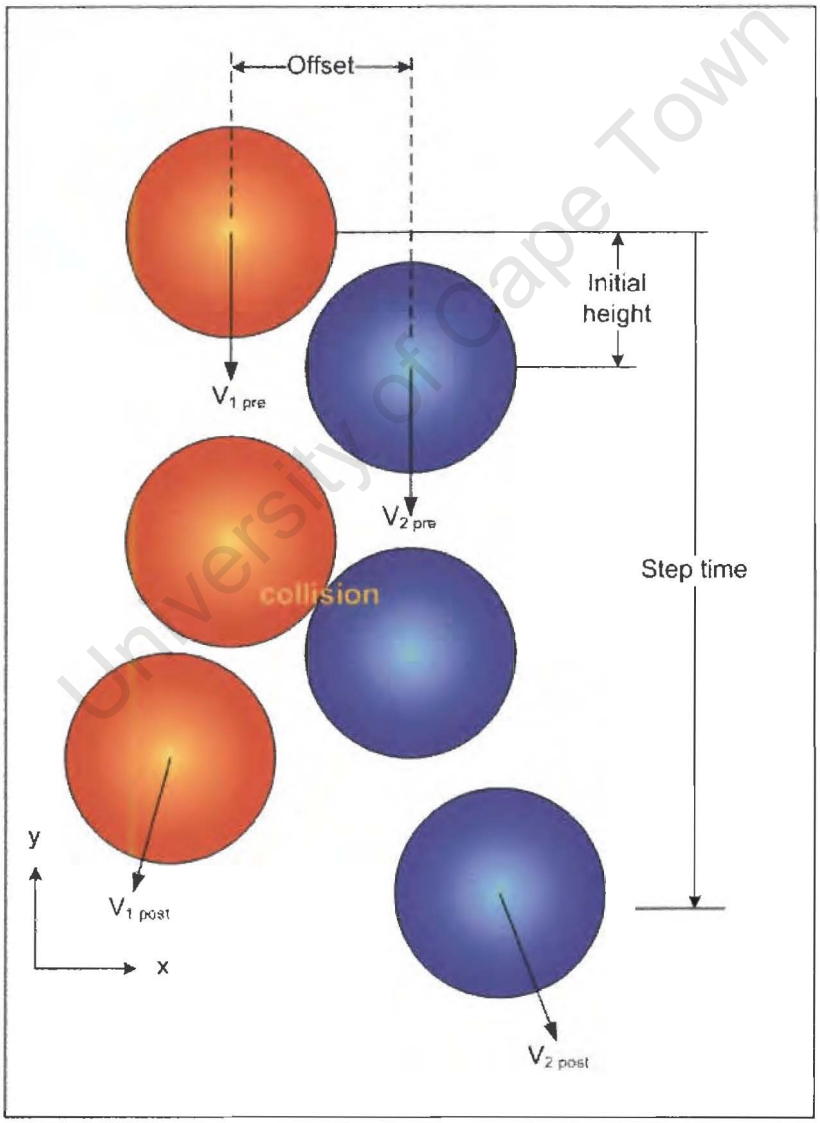

Figure 7-2 – schematic of the PFC experimental setup

```
; simple ball on ball collision
; by Rajiv Chandramohan
; UCT, Mineral Processing Research Unit

new;
set del_dt = 1e-6          ;initial time-step when no contact is detected
set dt max = 1e-6          ;max allowable time-step
set pinterval = 30         ;plot update interval
set plot emf               ;hardcopy plot output is emf
set hist_rep = 10          ;interval at which the history variables are monitored
call fishcall FIS          ;call routine names specific points at which PFC can be
                           interrupted during analysis
;-------------------------

;-------------------------
define initialParamaters
        setv_NormalDamp = 0.3
        setv_ShearDamp = 0.39
        ballDens = 7800
end
initialParamaters
;-------------------------
; generate the ball

ball id = 2 x = 0  y = 0.3 rad = (radius B2)
range name target y(0.2 , .4)
property yv = - (pre- velocity for B2)  xv = 0 range target

ball id = 1 x = - (offset distance) y = 0.301 rad = (radius B1)
range name projectile y(.30, 0.8)
property yv = - (pre- velocity for B1) xv = 0 range projectile

prop density = ballDens kn =12.8e8 ks =12.8e8 fric = 0.031

plot create mainView
plot add wall black
plot add ball yellow
plot ball id on
plot show

history id 1 ball xp id=1
history id 2 ball xp id=2
history id 3 ball yp id=1
history id 4 ball yp id=2
history id 5 ball xv id=1
history id 6 ball xv id=2
history id 7 ball yv id=1
history id 8 ball yv id=2
history id 9 ball sp id=1
history id 10 ball sp id=2

;plot create unbalancedForce
;plot add history 1
;plot add history 2
;plot show

;-------------------------
set grav = 0 -9.81
call ContactDampingModel.dat
;-------------------------
cycle 50000
;solve average=1e-20 maximum=1e-20 clock=10000 cycles=1040000 time= 10000
return
```

Defining the initial material properties

Generate Ball 2 and define property

Generate Ball 1 and define property

Ball property, define friction and stiffness

Generate history of the collision, position, velocity and spin

Set gravity and cycle time

Figure 7-3 – PFC Code for in-flight collision of two particles

A detail of the code written for testing in-flight collision of two particles is presented in **Figure 7-3**. Initial conditions set in the code are given in **Figure 7-3**. The damping parameters are calculated from **Equation 1** which was presented in **Chapter 2** – Discrete Element Method.

$$\alpha_{n,s} = \frac{C_{n,s}}{C_c} \qquad \textbf{Equation 1}$$

α is the fraction of critical damping (α=0 would mean an undamped system and α=1 would mean a critically damped system).

Where

$$C_c = 2m\varpi = 2m\sqrt{\frac{K_{n,s}}{m}} \qquad \textbf{Equation 2}$$

C_c is the critical damping constant, m the reduced mass of the contacting pair, and ϖ the natural frequency of the spring-mass system and $K_{n,s}$ spring stiffness of the material in the normal and tangential direction. Damping can be related to a coefficient of restitution $e_{n,t}$ (normal and tangential) by:

$$C_{n,s} = \frac{-2\ln(e_{n,t})\sqrt{K_{n,s}m}}{\sqrt{\ln^2(e_{n,t}) + \pi^2}} \qquad \textbf{Equation 3}$$

For preliminary tests steel balls were simulated in the PFC. The following damping factors were applied for the various impact velocities. **Table 7-1** below illustrates the material parameters which are entered in the PFC code

Vel.	Initial Velocity B1	Initial Velocity B2	e	β	μ	$K_{n,s}$	Density	α_n	α_s
High	4.31	2.75	0.75	0.58	0.041	3.14e10	7800	0.09	0.17
Inter	3.08	2.28	0.58	0.43	0.107	3.14e10	7800	0.17	0.26
Low	2.95	2.50	0.22	0.71	0.250	3.14e10	7800	0.43	0.11

Table 7-1 – Material input parameters in PFC (steel)

The method of testing is a measure of checking the variables between DEM and Experimental velocities. Here the various post- collisional velocities are compared for varying impact velocity settings; that is for the coefficients of normal and tangential restitutions and friction which were measured for the various height conditions. The combinations presented in **Table 7-2** for the low, intermediate and high drop velocities and the associated material property settings are tested.

Test	Particle	Mat. Prop. (High)	Mat. Prop. (Inter)	Mat. Prop. (Low)	Vel.
1	B1 X - Velocity	X	X	X	High
2	B1 X - Velocity	X	X	X	Inter
3	B1 X - Velocity	X	X	X	Low
4	B2 X - Velocity	X	X	X	High
5	B2 X - Velocity	X	X	X	Inter
6	B2 X - Velocity	X	X	X	Low
7	B1 Y - Velocity	X	X	X	High
8	B1 Y - Velocity	X	X	X	Inter
9	B1 Y - Velocity	X	X	X	Low
10	B2 Y - Velocity	X	X	X	High
11	B2 Y - Velocity	X	X	X	Inter
12	B2 Y - Velocity	X	X	X	Low

Table 7-2 – Test Combinations and comparisons

Comparisons are made between experimental and simulated horizontal (X) and vertical (Y) velocities, immediately after collision, for Steel ball bearings impacting at different offsets. **Figure 7-5** to **Figure 7-16** compare experimental and DEM results using a viscous damping model (VDM) for high, intermediate and low impact velocity settings for each ball. Lines are polynomial fits to the data to show the trends of the compared data.

The simulated DEM outputs are shown as a dotted line and the experimental results with an approximate error bars from **Table 7-3** are shown as a solid line. The derivations of these propagated errors are presented in **Chapter 6** – Error propagation. The offsets of the ball collisions are shown as a percentage, where 0% indicates a direct or sticking impact and 100% indicates a grazing impact. Therefore the impacts range from sticking to sliding.

Material	X Velocity Error	Y Velocity Error
Steel	22%	5%
Ceramic	45%	5%
Teflon	55%	5%

Table 7-3 – Percentage Errors for Velocities

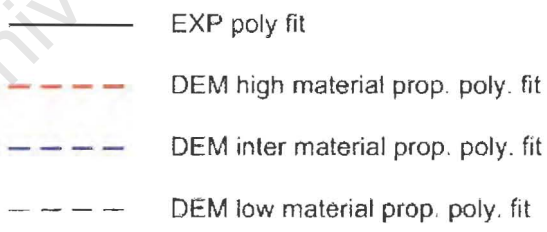

Figure 7-4 – Legend for graphs

Figure 7-4 illustrates the coloured legend used for the graphs. The experimental post-collisional velocities are demarcated with a solid line, and the three material property settings with dashed lines. Note that the high, inter, low material properties is the short hand for the material properties derived from the corresponding relative impact velocities.

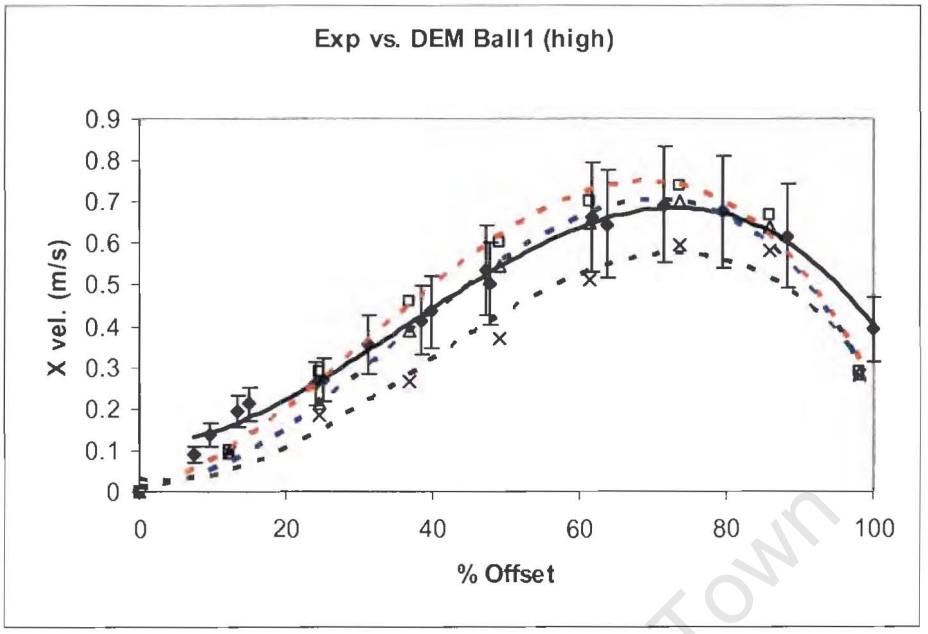

Figure 7-5 – Exp. vs. DEM comparison Test 1

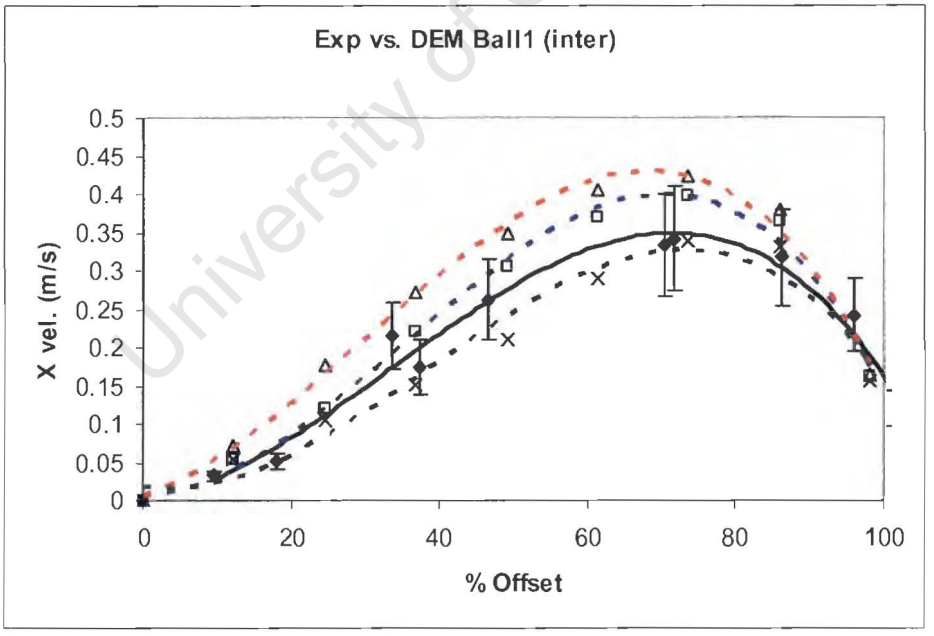

Figure 7-6 – Exp. vs. DEM comparison Test 2

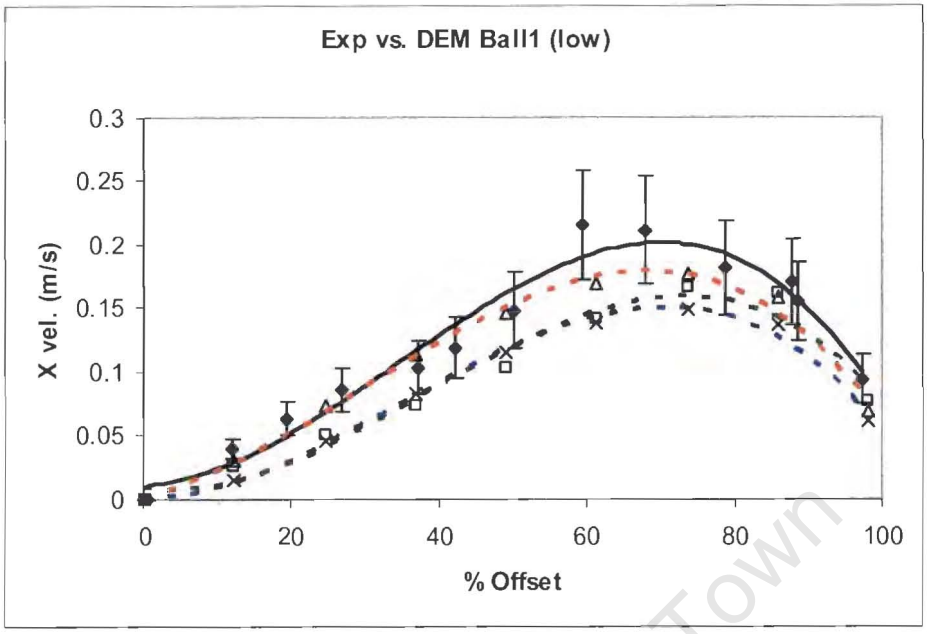

Figure 7-7 – Exp. vs. DEM comparison Test 3

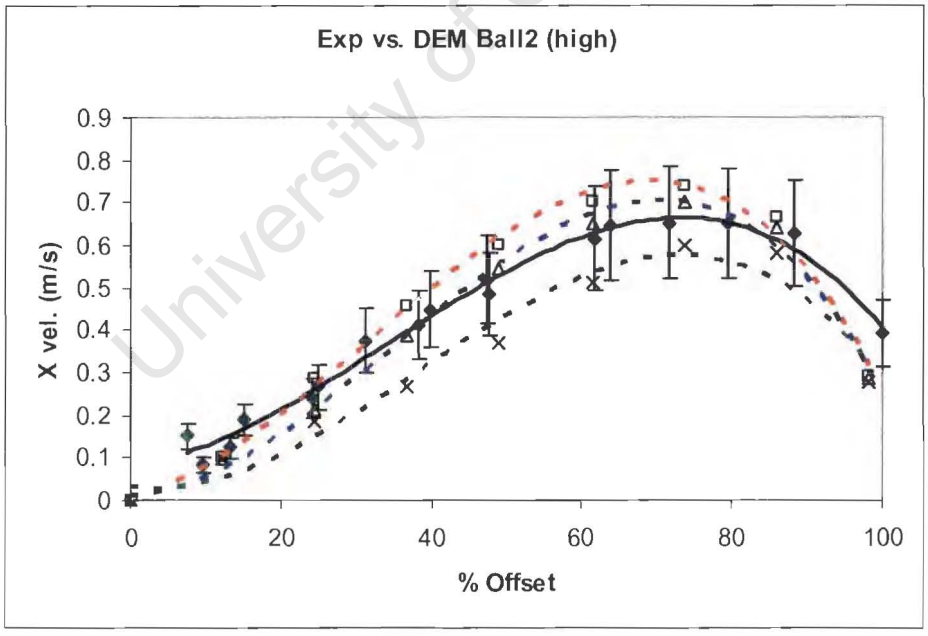

Figure 7-8 – Exp. vs. DEM comparison Test 4

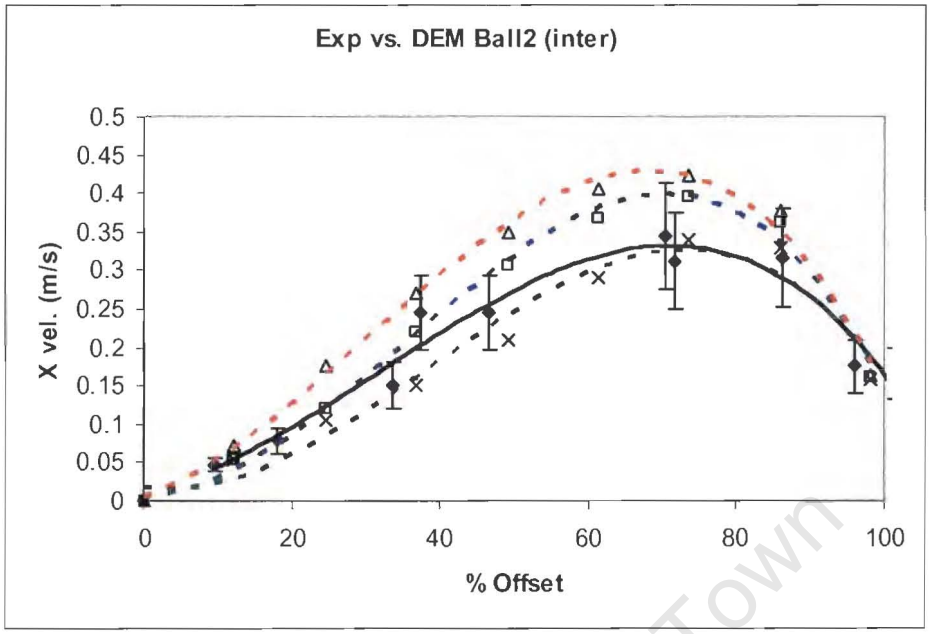

Figure 7-9 – Exp. vs. DEM comparison Test 5

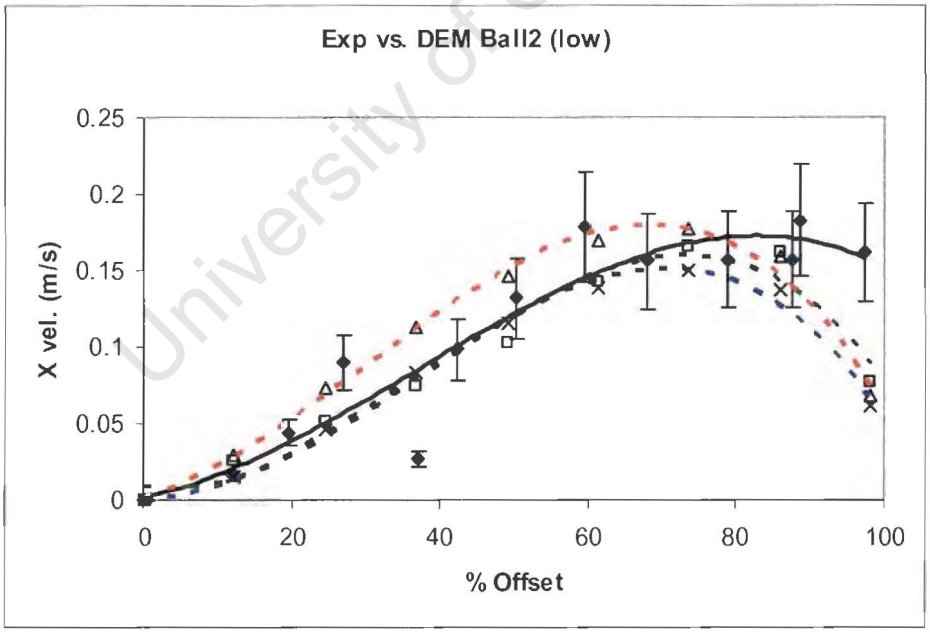

Figure 7-10 – Exp. vs. DEM comparison Test 6

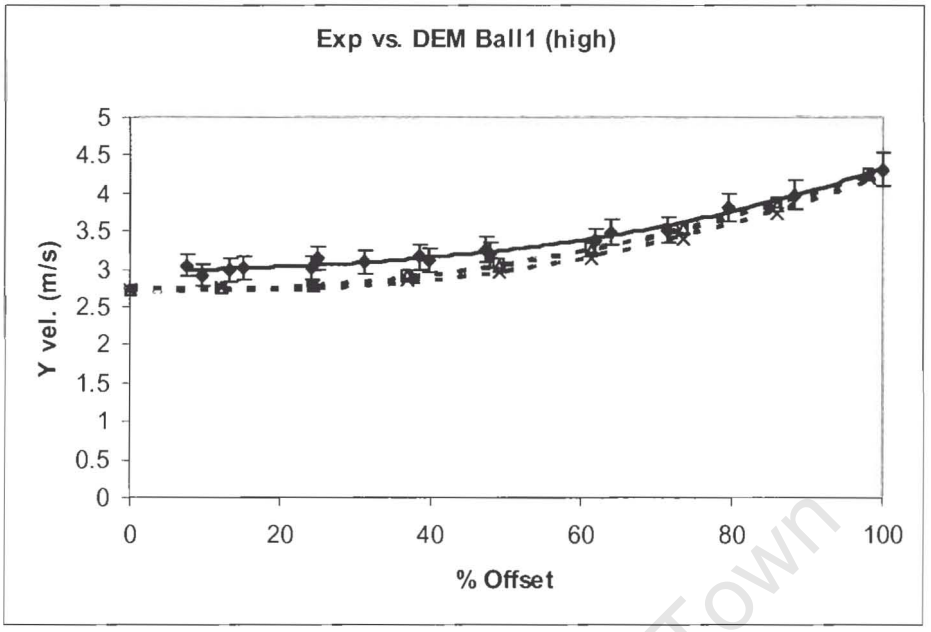

Figure 7-11 – Exp. vs. DEM comparison Test 7

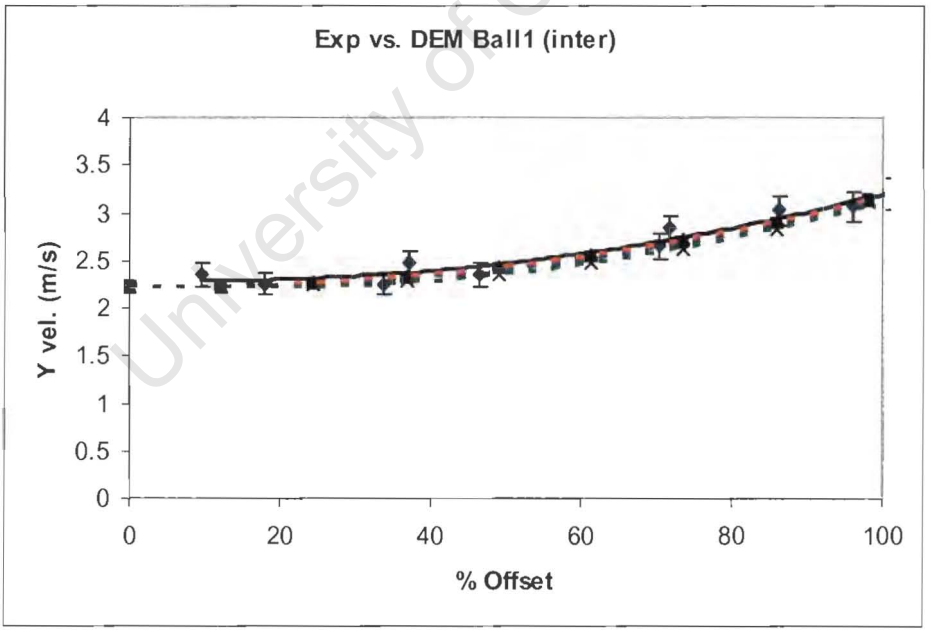

Figure 7-12 – Exp. vs. DEM comparison Test 8

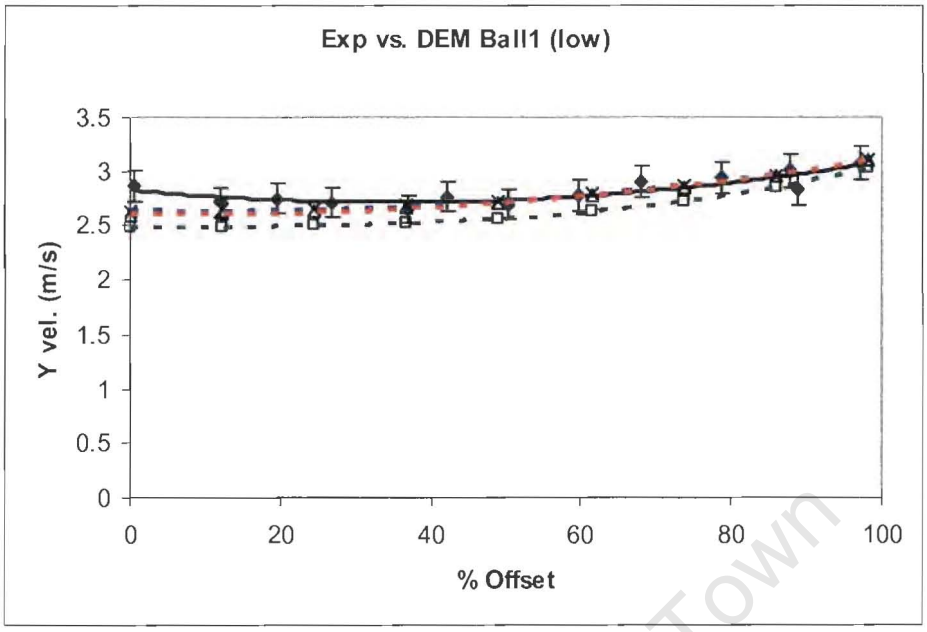

Figure 7-13 – Exp. vs. DEM comparison Test 9

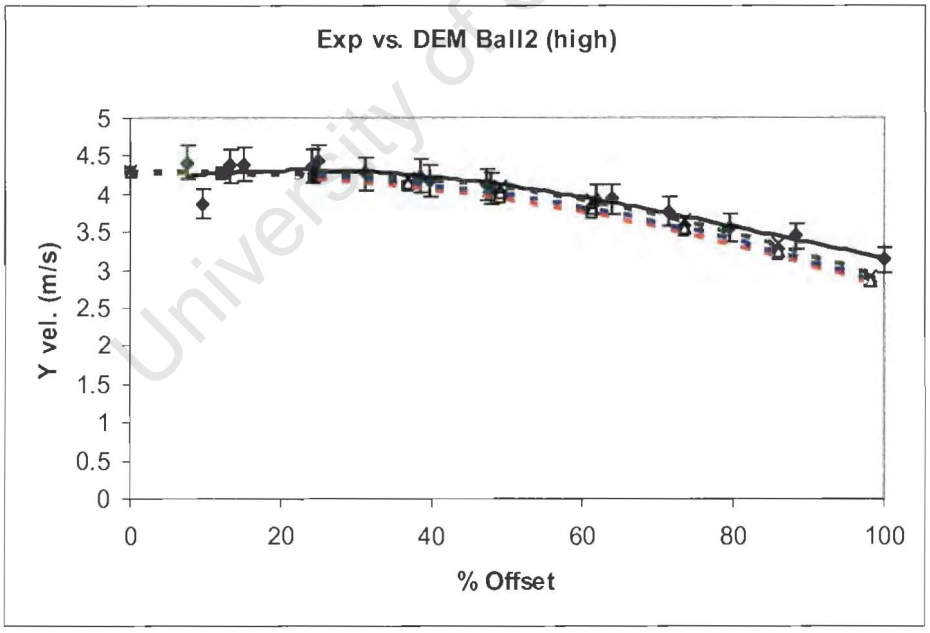

Figure 7-14 – Exp. vs. DEM comparison Test 10

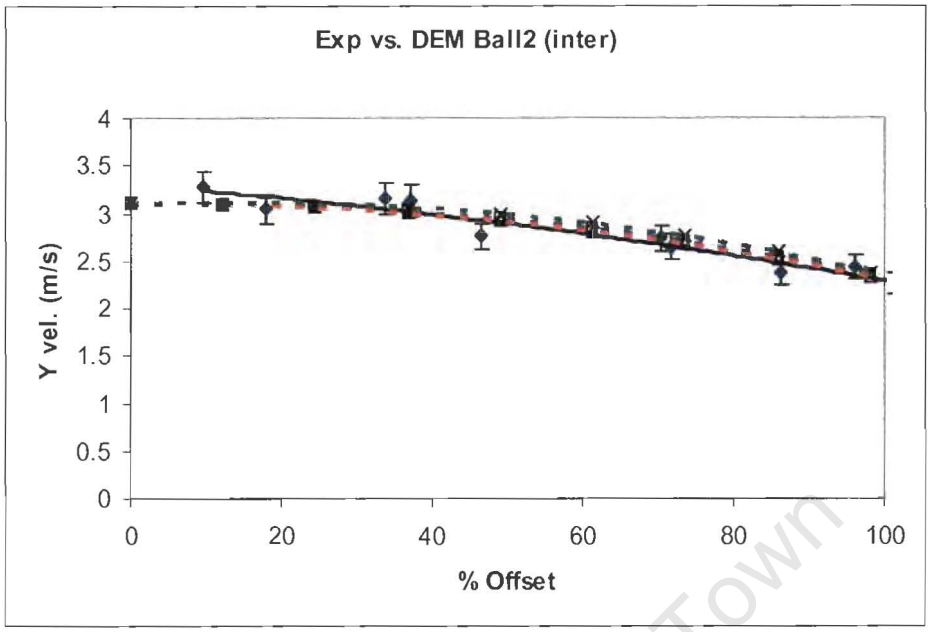

Figure 7-15 – Exp. vs. DEM comparison Test 11

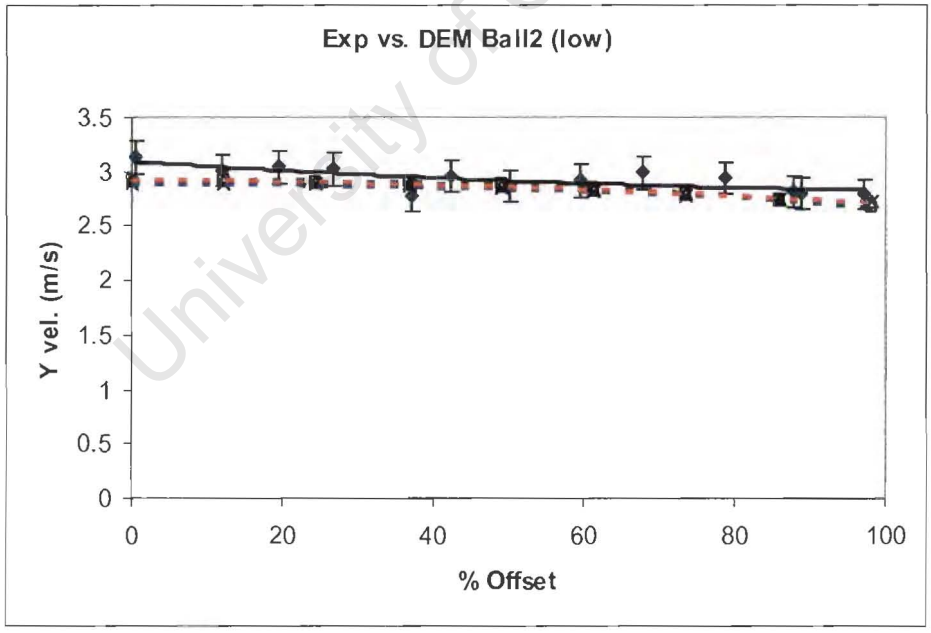

Figure 7-16 – Exp. vs. DEM comparison Test 12

The following observations can be made from DEM vs. Experimental comparison in the tests conducted as illustrated in **Figure 7-5** to **Figure 7-16:**

- The DEM provides a reasonable simulation of the velocities with the Y velocity predictions being better.

- PFC predicts the post velocities in the X direction to be equal for both particles, whereas the experimental data shows a slight variation and is less than the simulated value. This may be related to the slip between the two particles and their energy loss that is not fully accounted for by the simplified contact model.

- It seems in PFC simulation, the intermediate material property works well for high drop velocities, the low material properties works well for intermediate drop velocities and strangely the high material properties works better for low drop velocities.

- It is deduced that a possible reason for the poor predictions is that the DEM simulation fails to accurately model the tangential compliance, which affects the velocities in the X direction.

- For predictions greater than 40% offset settings, the PFC fails to model velocities in this region. It is noted that the sliding region commences in this region (greater than 40%).

- The three material property settings have a substantially larger affect on the predicted velocity in the X direction, than in the Y direction. There is a distribution of velocities for the given material properties in the X direction.

Further comparisons are conducted with the ceramic and Teflon materials and their respective property settings. For ceramic, the material input parameters are presented in **Table 7-4** and their respective predictions in **Figure 7-17** to **Figure 7-24.** For Teflon, the material input parameters are presented in **Table 7-5** and their combination predictions shown in **Figure 7-25** to **Figure 7-32.**

Vel.	Initial Velocity B1	Initial Velocity B2	e	β_0	μ	$K_{n,s}$	Density	α_n	α_s
Inter	3.10	2.33	0.33	0.17	0.101	3.14e10	3284	0.33	0.49
Low	3.00	2.62	0.11	0.97	0.256	3.14e10	3284	0.57	0.01

Table 7-4 – Material input parameters in PFC (ceramic)

Vel.	Initial Velocity B1	Initial Velocity B2	e	β_0	μ	$K_{n,s}$	Density	α_n	α_s
High	4.04	2.04	0.56	0.63	0.184	12.8e8	2122	0.18	0.15
inter	3.75	2.13	0.49	0.61	0.105	12.8e8	2122	0.22	0.16

Table 7-5 – Material input parameters in PFC (teflon)

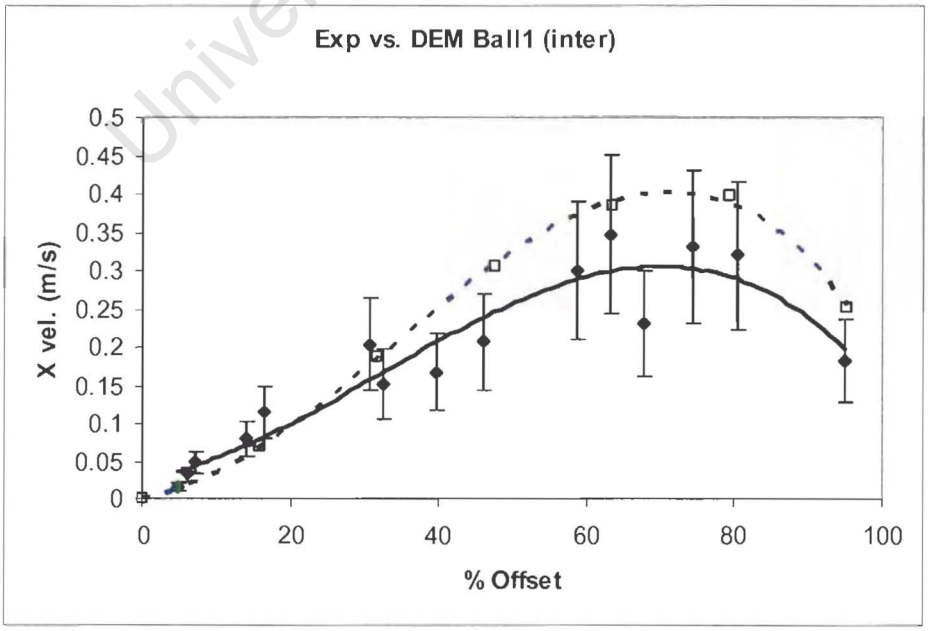

Figure 7-17 – Exp. vs. DEM for Ceramic (intermediate height)

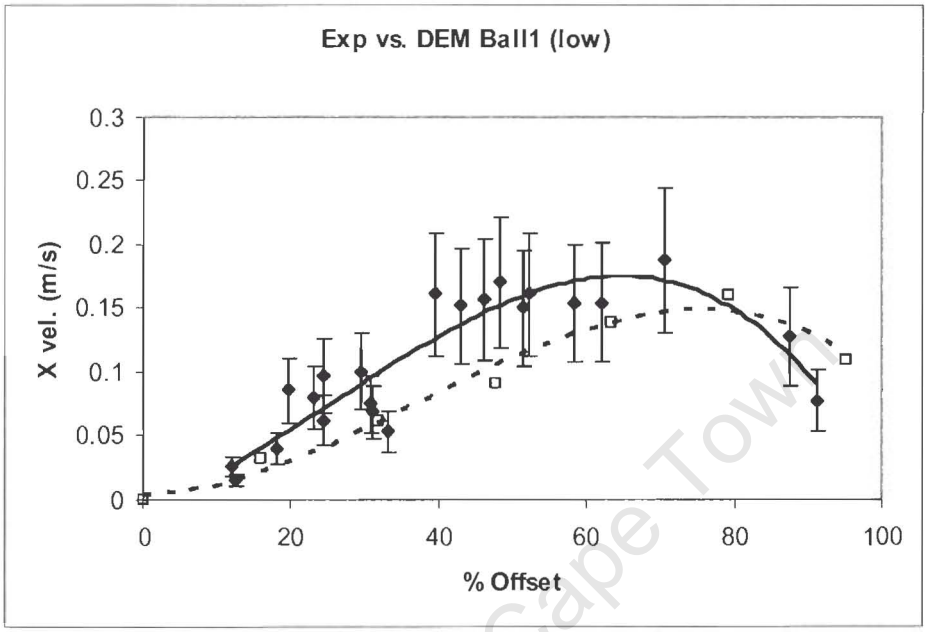

Figure 7-18 – Exp. vs. DEM for Ceramic (low height)

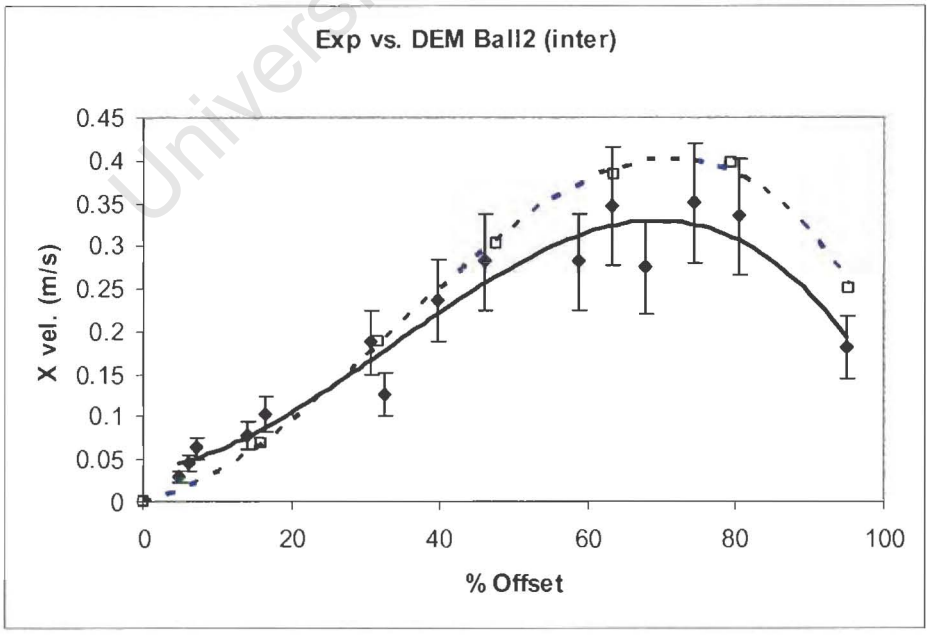

Figure 7-19 – Exp. vs. DEM for Ceramic (intermediate height)

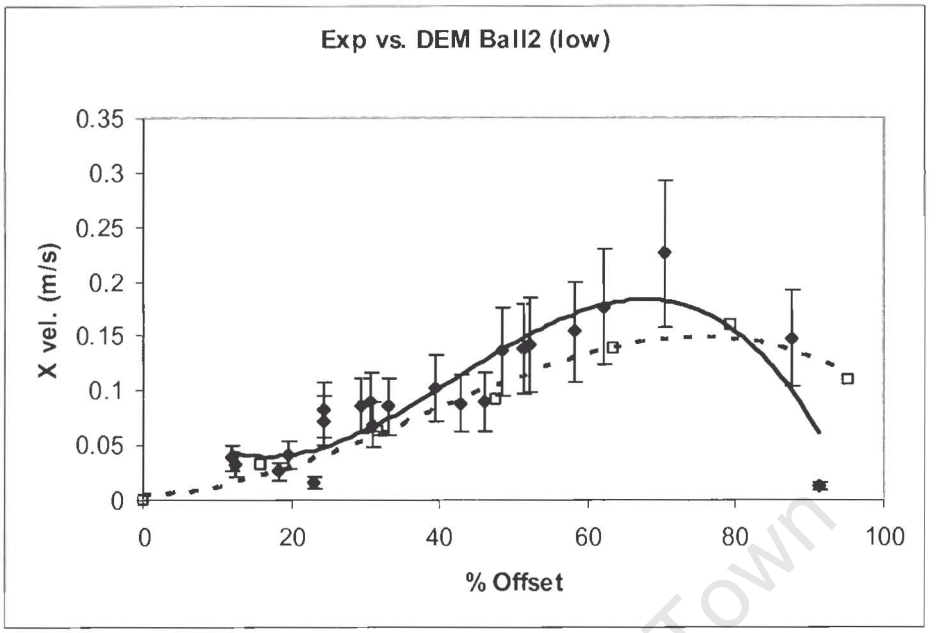

Figure 7-20 – Exp. vs. DEM for Ceramic (low height)

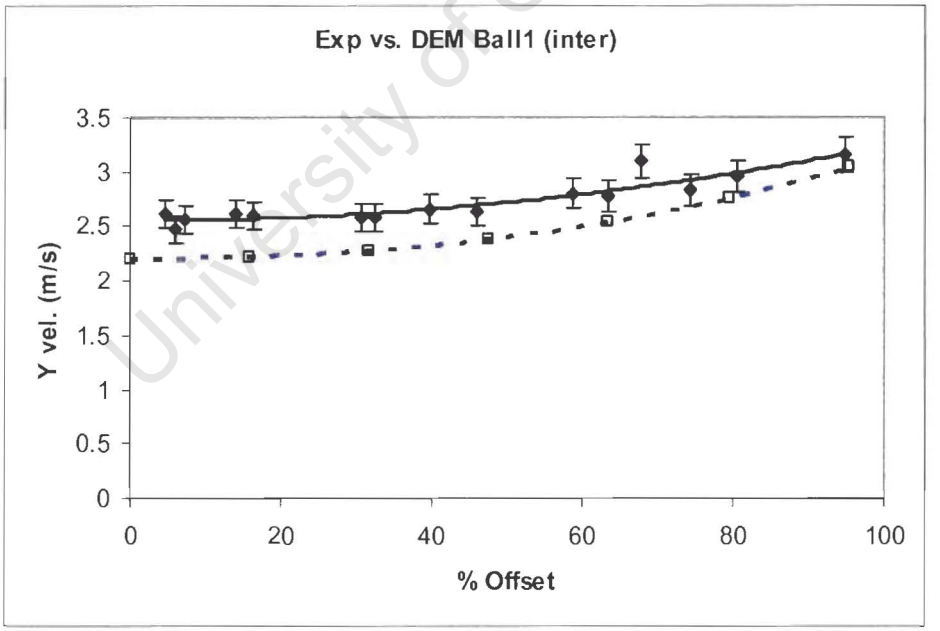

Figure 7-21 – Exp. vs. DEM for Ceramic (intermediate height)

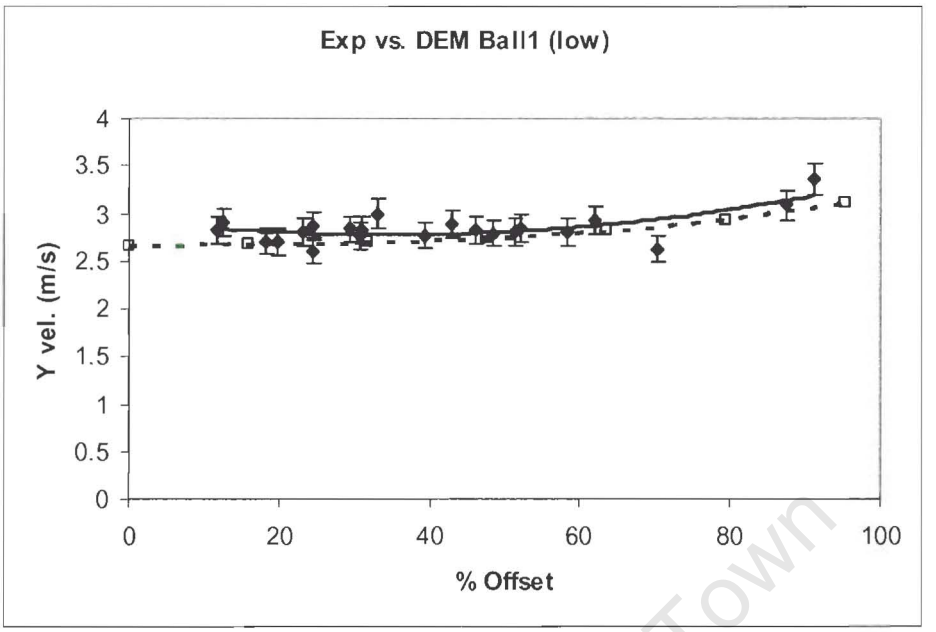

Figure 7-22 – Exp. vs. DEM for Ceramic (low height)

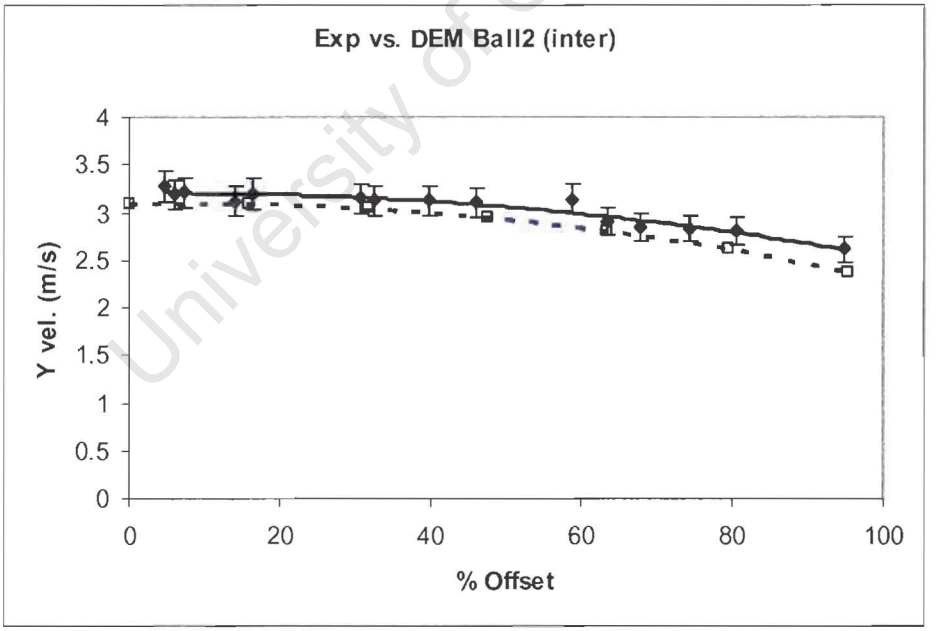

Figure 7-23 – Exp. vs. DEM for Ceramic (intermediate height)

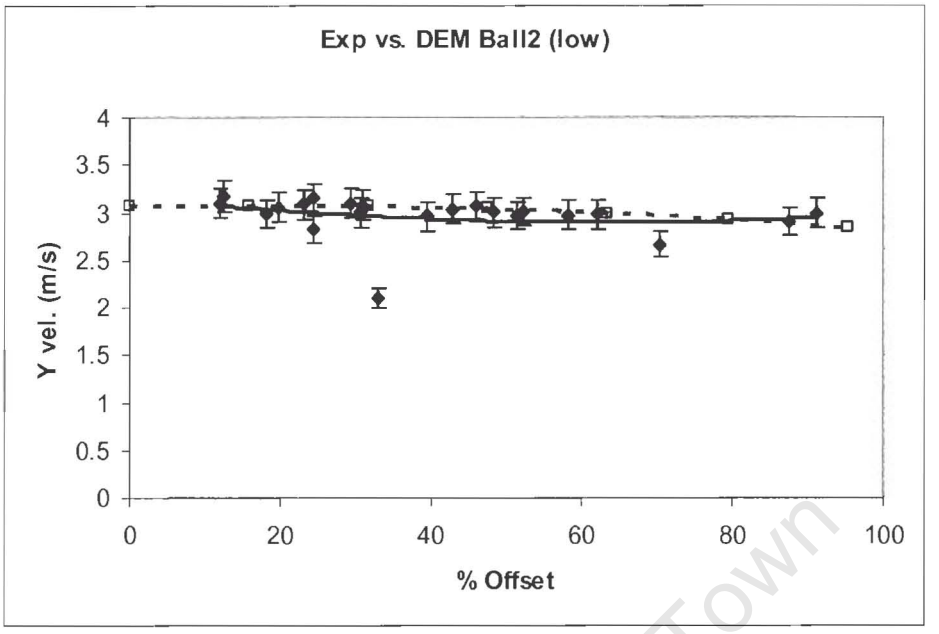

Figure 7-24 – Exp. vs. DEM for Ceramic (low height)

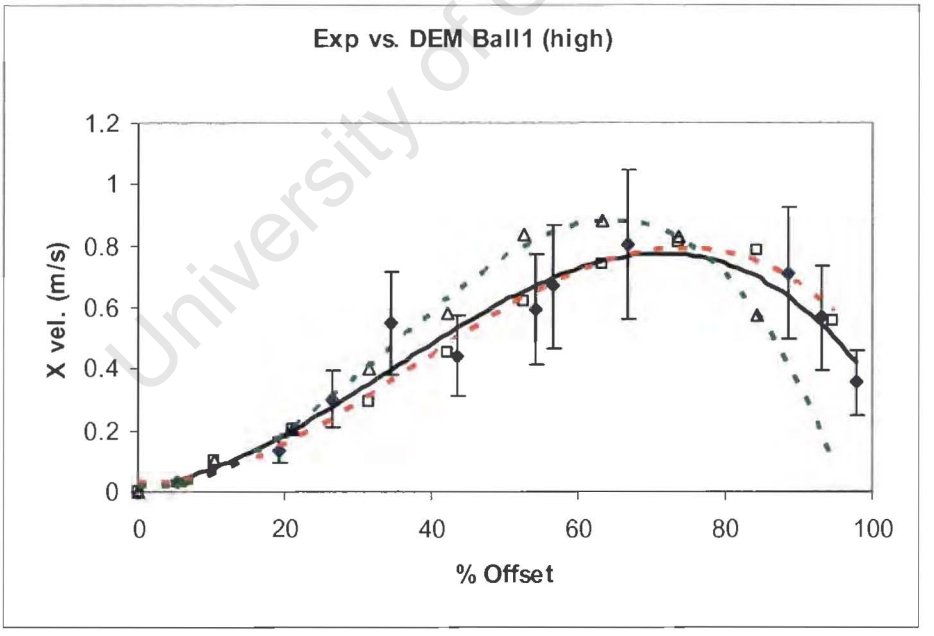

Figure 7-25 – Exp. vs. DEM for Teflon (high height)

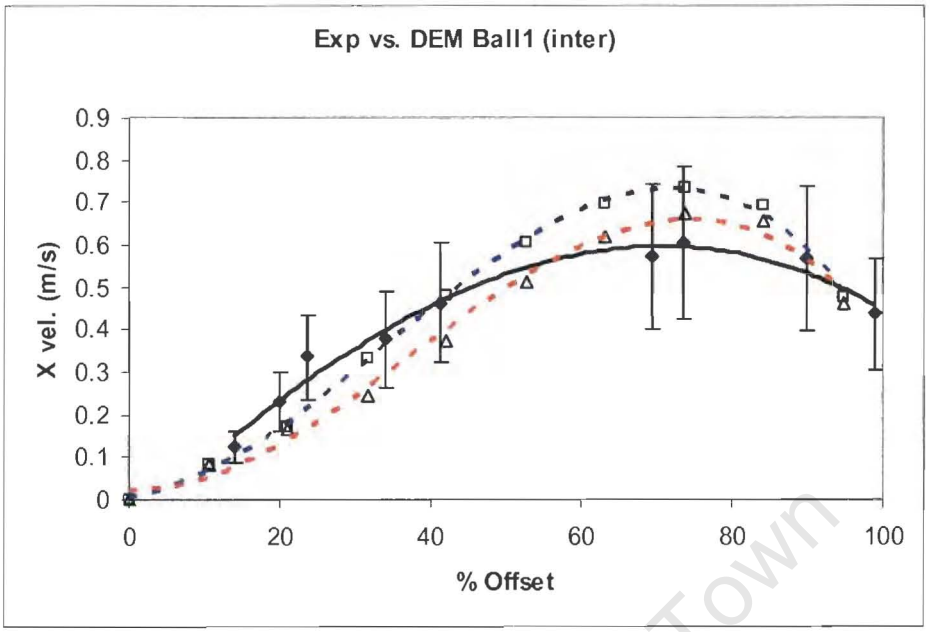

Figure 7-26 – Exp. vs. DEM for Teflon (intermediate height)

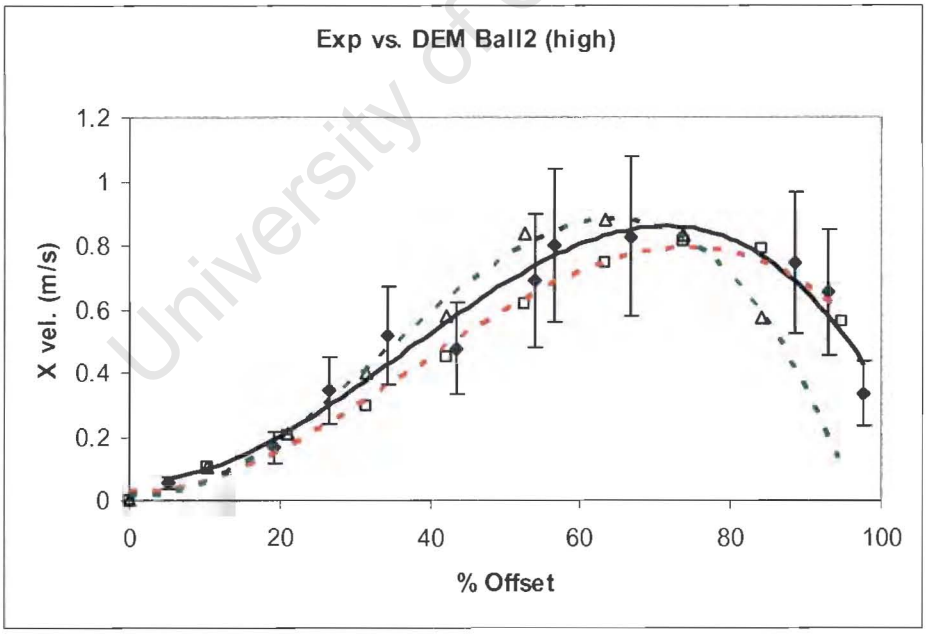

Figure 7-27 – Exp. vs. DEM for Teflon (high height)

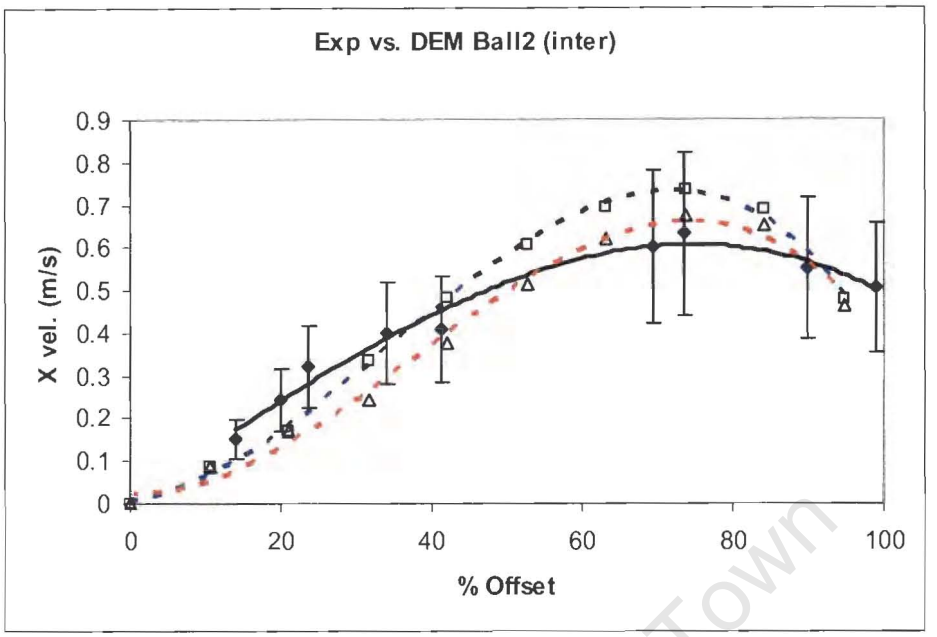

Figure 7-28 – Exp. vs. DEM for Teflon (intermediate height)

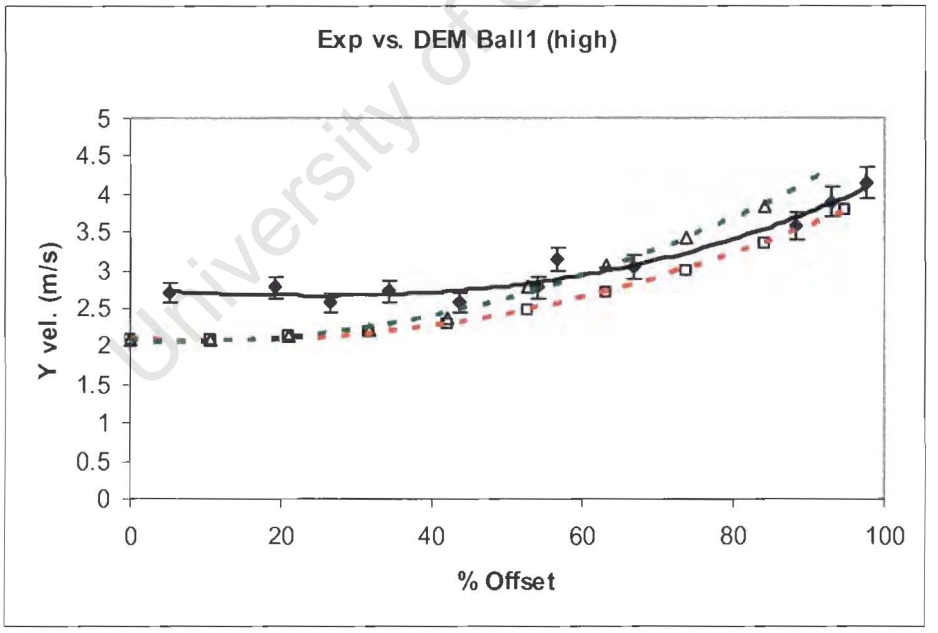

Figure 7-29 – Exp. vs. DEM for Teflon (high height)

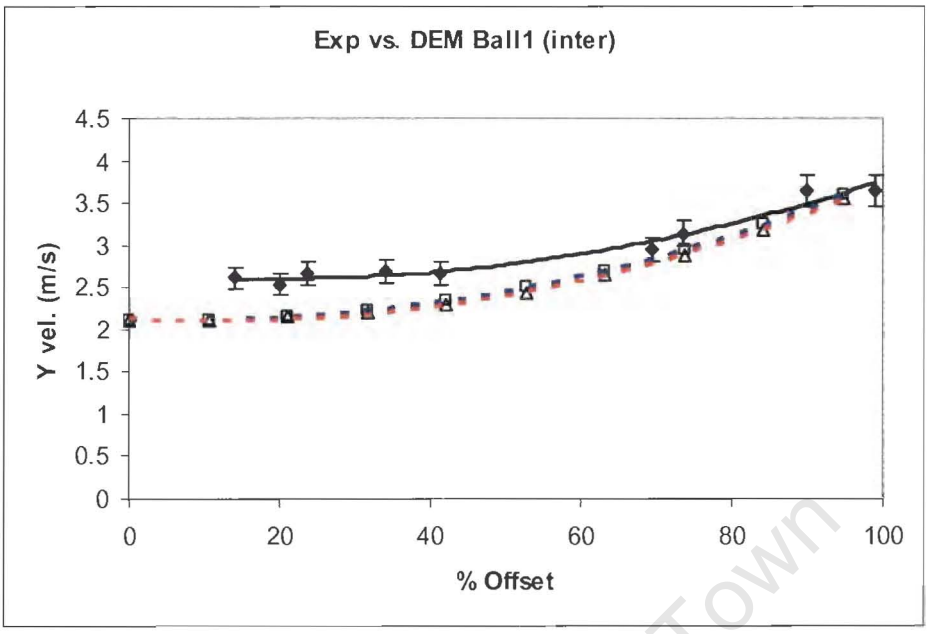

Figure 7-30 – Exp. vs. DEM for Teflon (intermediate height)

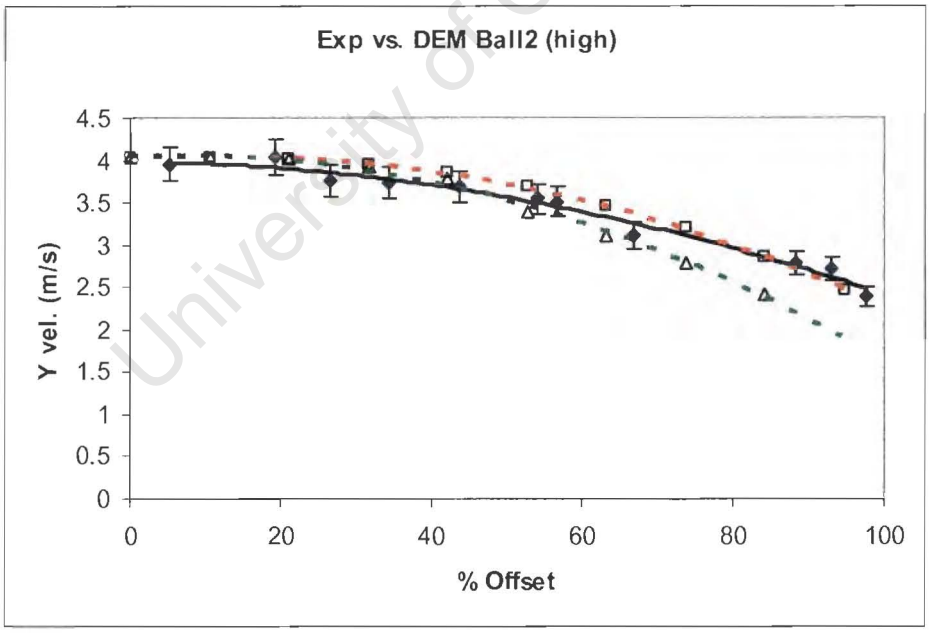

Figure 7-31 – Exp. vs. DEM for Teflon (high height)

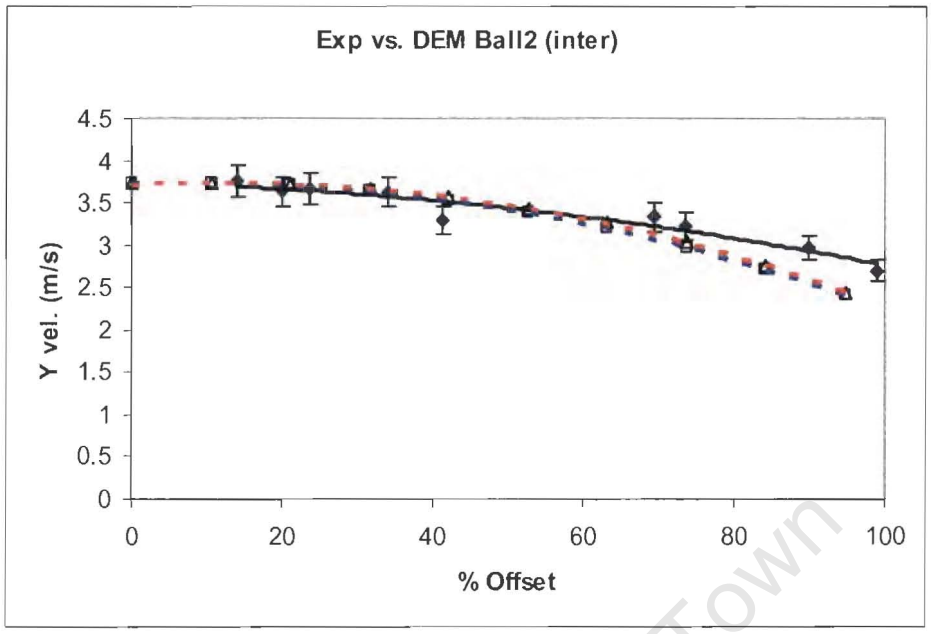

Figure 7-32 – Exp. vs. DEM for Teflon (intermediate height)

As shown in the predictions for the ceramic and Teflon balls in **Figure 7-17** to **Figure 7-32,** it seems the sliding region is not predicted well. Therefore shiny materials with low friction surfaces such as steel and ceramic ball bearings and dull materials with high friction such as Teflon, behave similarly in the viscous damping model in PFC. The tentative conclusion that can be drawn from the mismatch of the experimental data and DEM predictions is that for the spring and dash pot Model, the shear springs and coulomb friction fail to predict the sliding or slipping interactions between particles. It is also possible that these models are not compatible with the analysis from Foerster *et al* [35] assumptions.

To test deduction of sliding collisions which greatly affect the viscous damping model predictions, the spin of the Teflon balls is checked. **Figure 7-33** to **Figure 7-36** illustrates comparisons for experimental spin vs. DEM predictions for the teflon balls with high and intermediate material property settings.

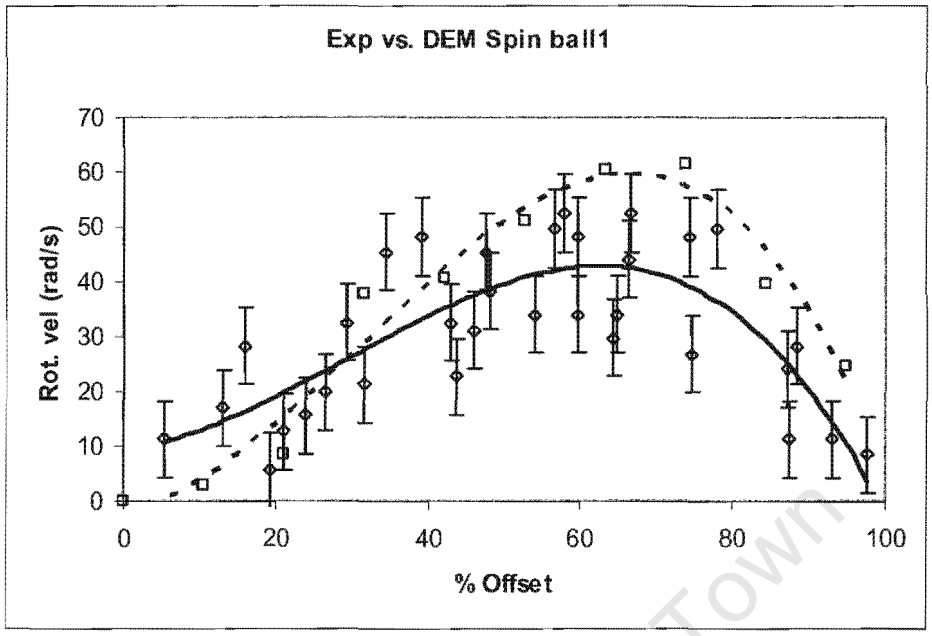

Figure 7-33 – Exp vs. DEM spin for high material property Ball1

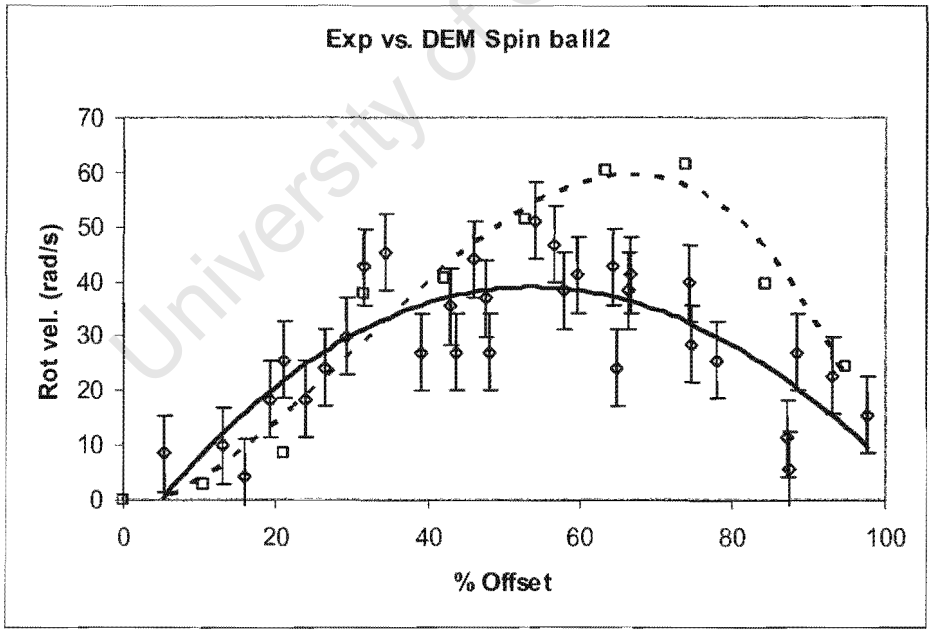

Figure 7-34 – Exp vs. DEM spin for high material property Ball2

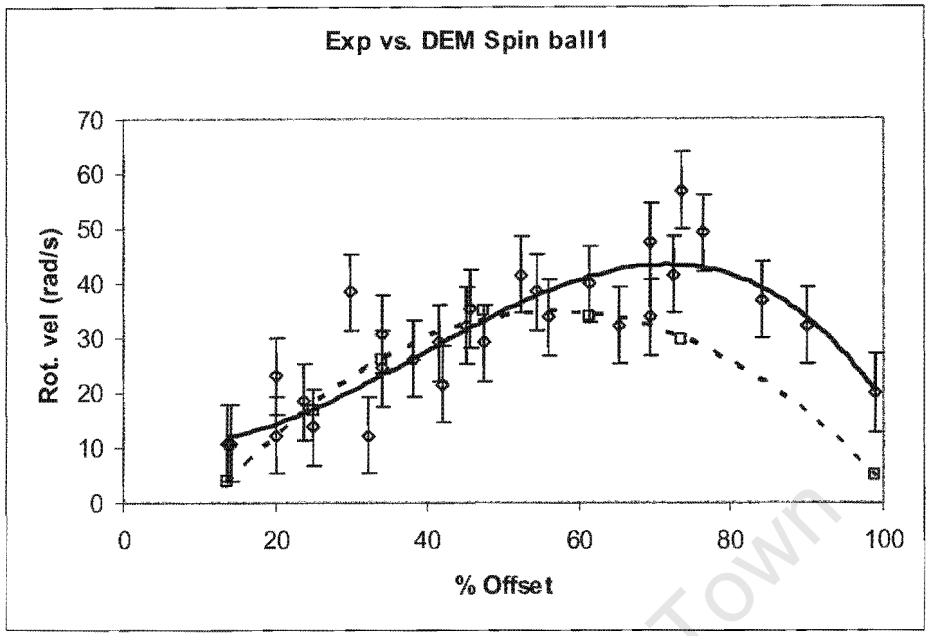

Figure 7-35 – Exp vs. DEM spin for intermediate material property Ball1

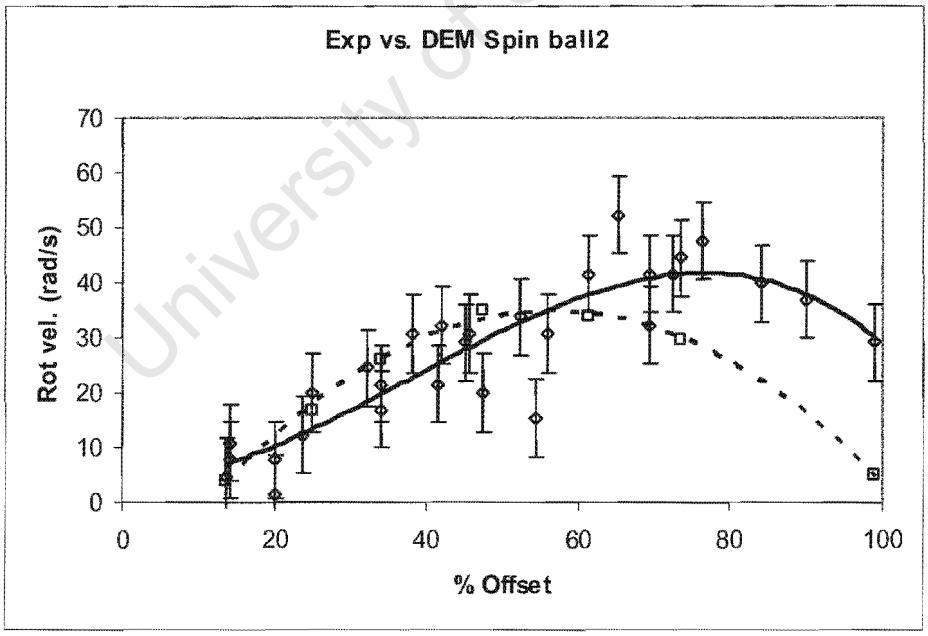

Figure 7-36 – Exp vs. DEM spin for intermediate material property Ball2

Experimental rotational velocities are demarcated with a solid line and the DEM predications are shown as dashed lines. Fixed error bars of ± 7 rad/s were derived from the ± 4 degree deviation in the measured angular rotations. The noticeable differences in the sliding regions, i.e. greater than 60% for both sets of particles, clearly indicate that the model fails to correctly predict this region. For the conditions given, the DEM predictions over predict for high friction, that is for the high material property settings as shown in **Figure 7-33** and **Figure 7-34.** For the low friction settings (intermediate material property setting), the DEM under-predicts the rotational velocities. It is assumed that the introduction of a single friction value in the model appears to have a significant detrimental effect on the accuracy of the predictions. It is deduced from the wide scatter in the experimental data that exceeds the derived error bars, that the Teflon material is a substance that erratically experiences both and stick and slip.

It was shown that the viscous damping model in PFC is considerably affected by the value of tangential compliance. The tangential compliance has the following components: friction and tangential restitution, and these have a substantial effect in the sliding region, due to incorrect dissipation of energy during sliding contact. This results in poor predictions in the sliding region.

7.3 Delphi Interface – R Sarracino

An in-house model tester was developed by Dr R Sarracino (MPRU of UCT) using DELPHI. The model tester allows the user to test a range of contact models written specifically for the two-body collision experiment. An illustration of the front end is shown in **Figure 7-37.**

The Model tester reproduces the in-flight collision of the particles for the various heights using experimentally derived material interaction properties. The software enables the creation of the characteristic Psi graph *a la* Maw *et al* [29] and Foerster *et al* [35] using the defined material interaction properties.

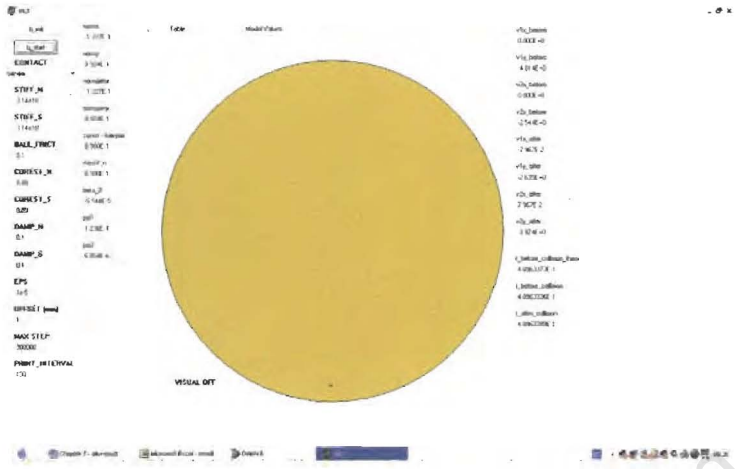

Figure 7-37 – Sarracino Model tester in Delphi

The effect of applying set of material of properties for the given heights is tested. The characteristic Psi graph is produced using the viscous damping model – spring dash pot. For this example the material interaction property of steel is used in the calculations.

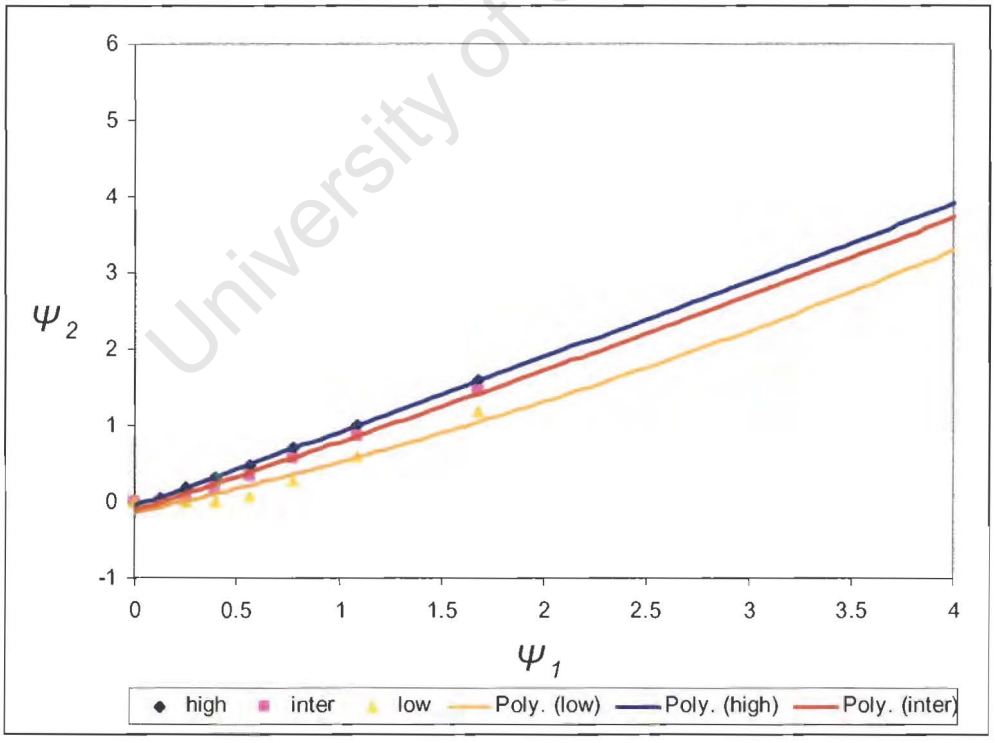

Figure 7-38 – Psi graphs for DEM predictions (steel)

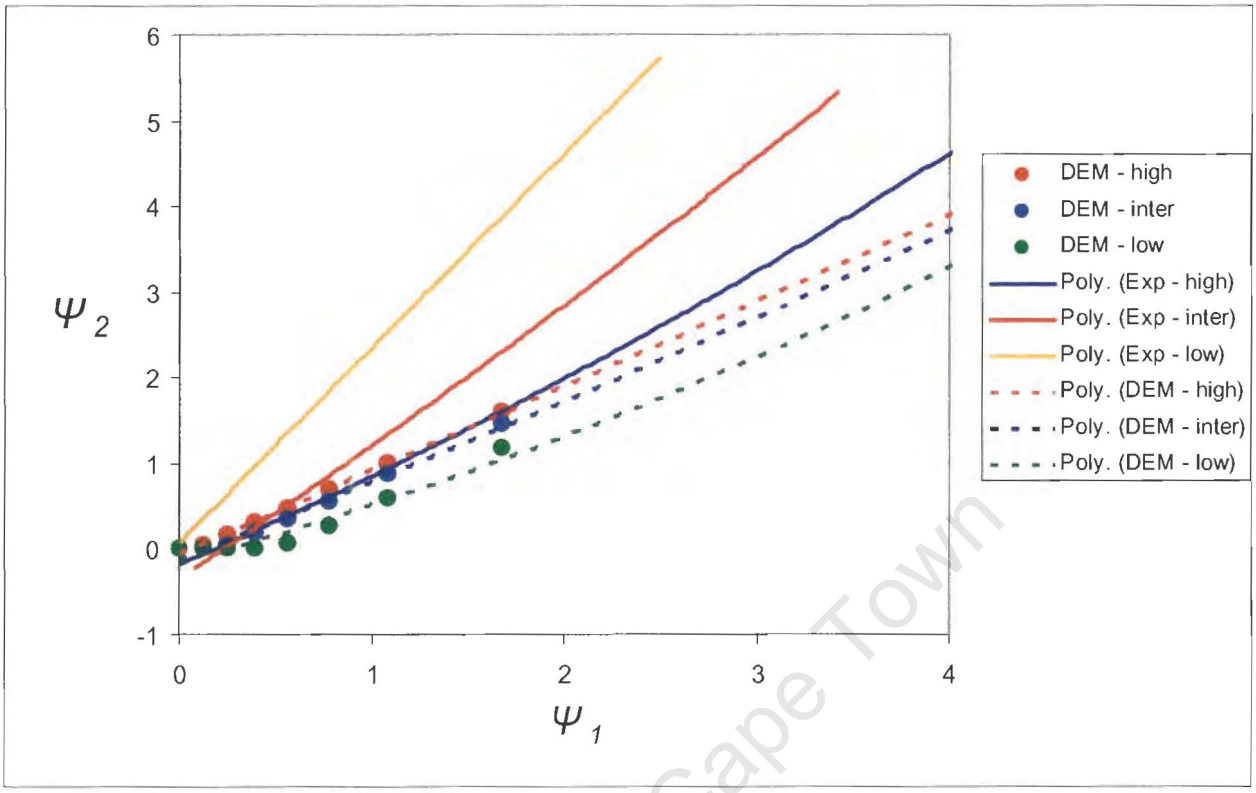

Figure 7-39 – Exp vs. DEM Psi graph for high, inter, low material properties (steel)

Figure 7-38 illustrates the non dimensional plots for the three material property settings in steel. It is noted that for decreasing material property settings, the trend shows that the Psi graphs decrease in gradient where the high material property plot has the steepest gradient. Comparing these predictions with the experimental results for steel as shown in **Figure 7-39,** shows that the predictions are the reverse of the experimental results. In the experimental results, the non dimensional plots increase in gradient in the sliding region for decreasing material property settings. The contrast in the behaviour of the graphs indicates that the viscous damping model fails to simulate the binary impact of particles subjected to free fall collisions.

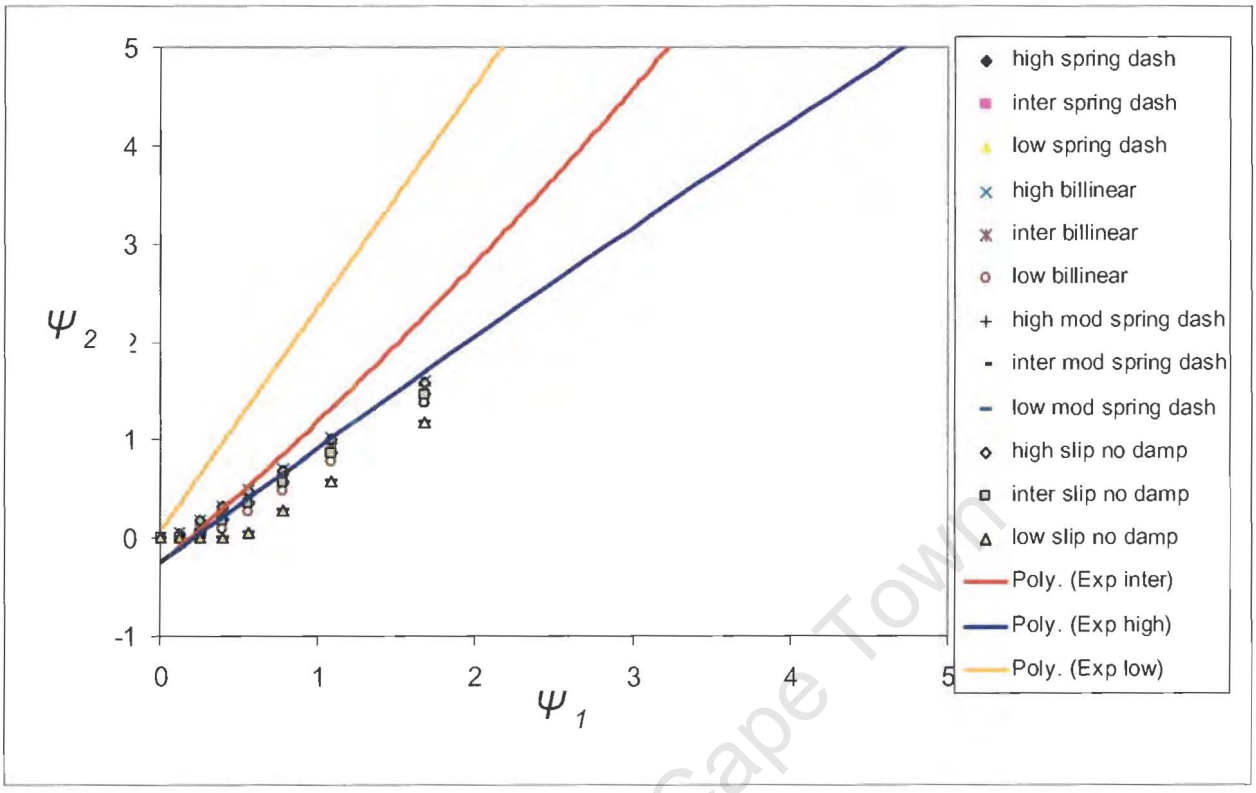

Figure 7-40 – Non dimensional plots for the four DEM models (steel)

Figure 7-40, illustrates the comparisons for four DEM models. They are: viscous damping model or spring dash pot model; a modified spring dash pot model; bilinear model; and a model incorporating slip with no damping in the tangential direction. These modified and new models were written by Dr. R Sarracino. The comparison shown in **Figure 7-40** for steel indicates that the models do not behave similarly to the experimental results, as indicted by comparison with the polynomials of the experimental data, indicating a clear failure of predictions in the sliding region. It is assumed that because of high polished surface of the steel ball bearings, they behave differently to that of rough surface materials. The poor correlation to smooth as oppose to rougher surfaces indicates that the DEM contact models do not adequately describe the slip-stick condition that is deduced to occur for the polished steel surfaces.

Figure 7-41, illustrates the comparison for the Teflon material. The experimental averages are shown as solid lines and the viscous damping model (spring dash pot) is shown as dashed lines.

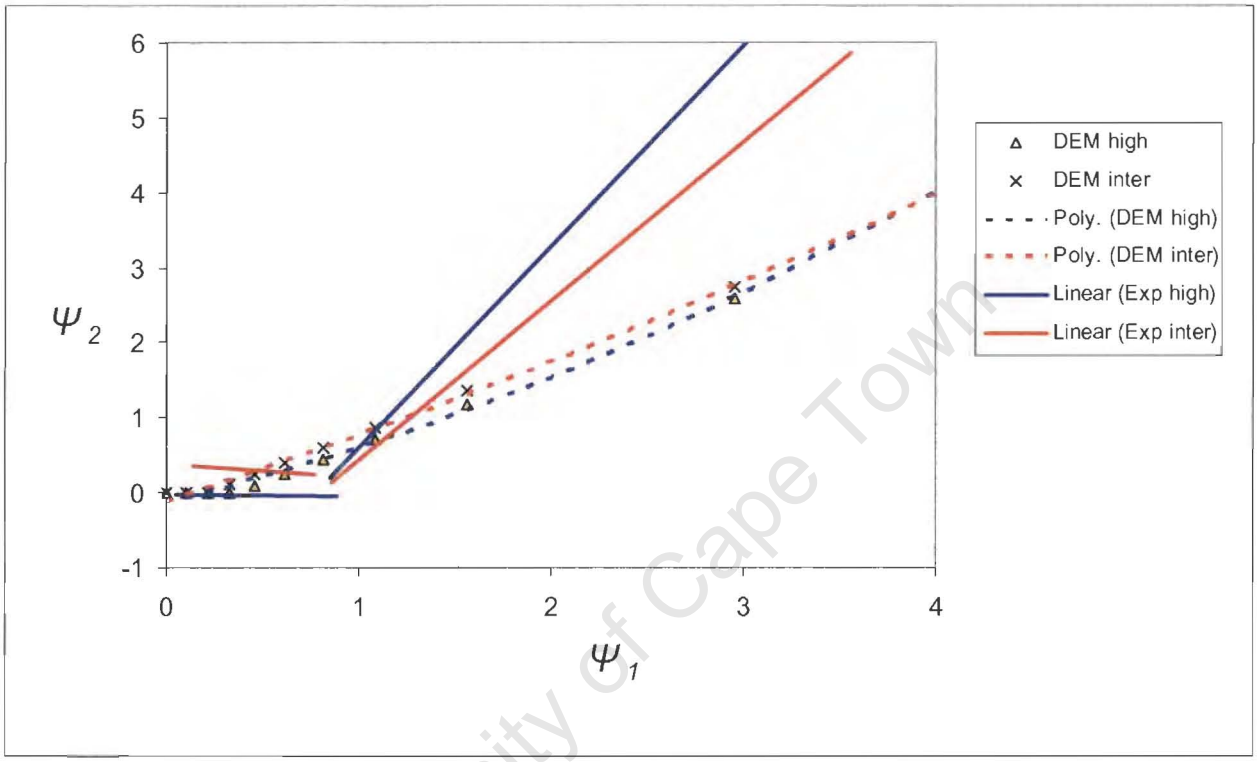

Figure 7-41 – Exp vs. DEM Psi graph for high, inter, low material properties (ceramic)

The comparisons shown in **Figure 7-41,** indicate that again the sliding region is incorrectly predicted. This is a clear indication that the tangential compliance is not modelled well in the sliding region.

Figure 7-42, illustrates the comparisons made for four DEM models for the applied material interaction properties of Teflon. DEM models again fail to predict the region of sliding, in this case for a material with rougher surface properties.

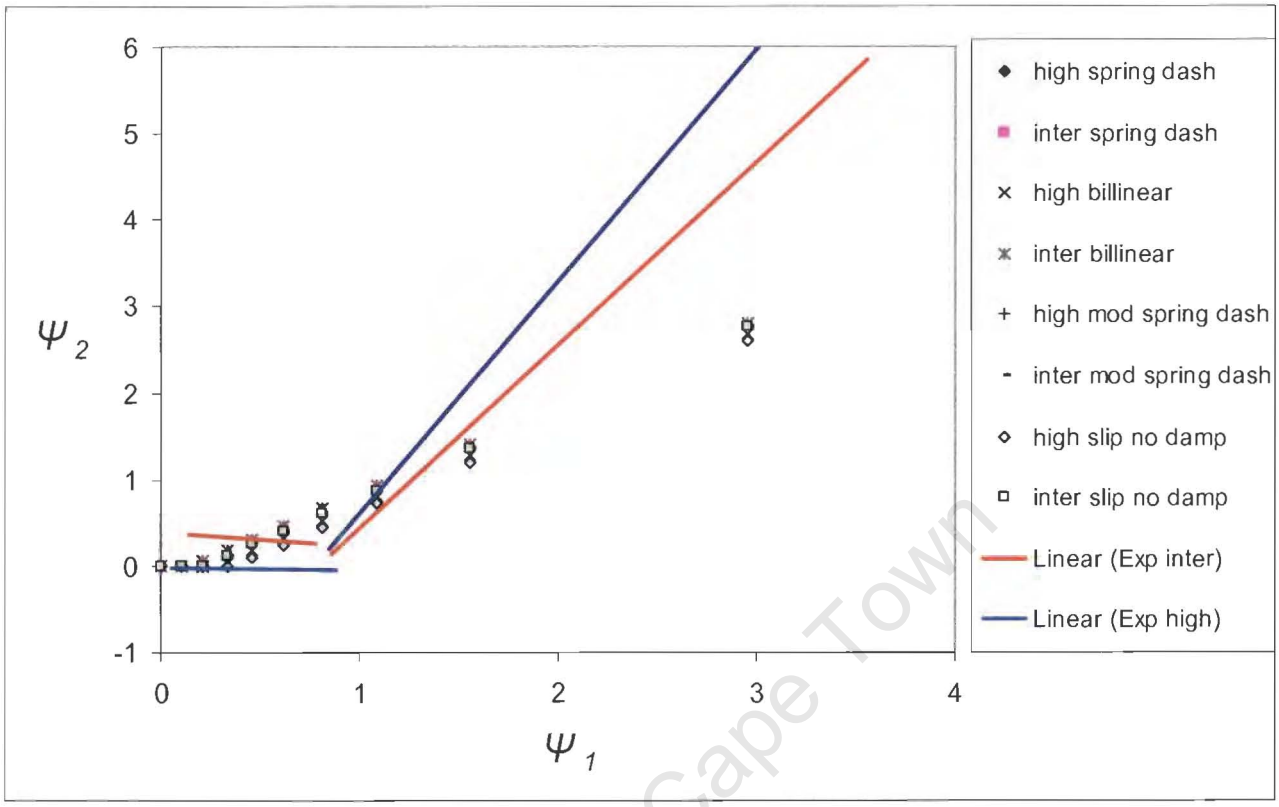

Figure 7-42 – Non dimensional plots for the four DEM models (Teflon)

7.4 Summary

- From the comparisons shown in this chapter, it can be clearly seen that the Models fail to predict experimental results in the sliding region.

- This effect is clearly noticed in the simulations in the PFC for the X velocity. A tentative conclusion that can be drawn from the behaviour is that for the spring-dashpot model the shear springs and coulomb friction fail to predict the sliding or slipping interactions between particles.

- It is possible that these models are not compatible with the analysis from Foerster *et al* [35] assumptions, as shown by the poor predictions given in **Figure 7-5** to **Figure 7-32** and **Figure 7-33** to **Figure 7-36.**

- The comparisons using the Delphi interface show that the predictions fail to plot the characteristic non dimensional graphs used by Foerster *et al* [35] and Maw *et al* [29].

- The anomalies may be due to incorrect derivations arising from the Foerster *et al* [35] relationships that are used to derive the parameters used in the DEM simulations. The relationships contain simplification and assumptions that well may be inaccurate, and this is shown for the tangential restitution in the stick region as this has an uncertainty of almost 100%. Note that there were no "fitted parameters" in the DEM simulations, all input parameters and conditions are fully defined by the Foerster *et al* [35] derivations. Therefore if the calculated parameters are inaccurate then the DEM predictions will be incorrect.

Chapter 8

Conclusions and Recommendations

8.1 Overview

Conclusions and recommendations based on the technique to measure and test pertinent particle interaction properties are presented here. We have shown in the experiment developed to measure these properties, that it is possible to extract them and test them in the Discrete Element Method (DEM) using a suitable methodology. Because DEM is beginning to be a widely accepted numerical technique in the mining industry, rigorous testing of the applied models and its application in the global system (i.e. various mining equipment and machines) should be implemented. Researchers across the world have developed their "favoured model" in DEM to simulate bulk charge motion in mills, but this is purely subjective in that very little testing has been conducted with their models. Until now, in its early stage of development, DEM predictions have been compared with experimental tracking data in mills, Govender [23], Govender *et al* [24].

This project was originally conceived by Dr M S Powell of the Mineral Processing Research Unit. Based on his ideas the following hypothesis was identified earlier in this thesis and their key components concluded:

- *The so called material properties used to derive the parameters used in DEM are not solely properties of the materials but rather material interaction properties that are dependent on the conditions of the impact.*

The material properties used to derive the parameters in DEM were identified as material interaction properties. We have shown this by developing and experiment to measure the in-flight collision of two particles and extract key material interaction properties using

analysis by Foerster *et al* [35]. By varying the drop heights it has been shown that properties such as coefficients of normal and tangential restitution and friction are dependent on the impact velocities.

- *Applying measured material interaction properties in DEM rather than fitting or estimating them, in the contact models that govern the inter-particle contact – force laws,* ***can contribute*** *to the overall reliability and accuracy in predicting the motion of grinding media in rotary mills.*

- *This is because fitting a number of parameters in the simulations does not imply that they are correct. Simulations with new conditions are likely to give incorrect predictions and these parameters therefore don't represent the overall change in conditions.*

The derived material interaction properties were applied as parameters in commercially available software called PFC to model DEM. Tests showed that the reliability of PFC fails to model post-collisional velocities for varying impact velocities with their corresponding material interaction properties. It was determined that the viscous damping model used in PFC is a cause of the inconsistency and it should be addressed before DEM can be used as a tool to accurately predict the overall charge motion in mills.

Because of the poor matching of the DEM and experimental predictions, the full hypothesis could not be successfully tested. However, it is clear that the predictions of DEM can be significantly improved by matching to simple collision experiments prior to conducting full simulations of thousands of colliding particles.

Addressing the thesis objectives and specifications the following conclusions are drawn:

- To establish an experiment that measures the material interaction properties such as coefficient of normal and tangential restitution, and friction.

Based on the work conducted by Foerster *et al* [35] an experiment has been set up to measure the material interaction properties. Refinements were made to the experiment to improve its overall reproducibility and accuracy. Improvements were made to the design, such as varying the drop heights of the impacting ball, testing the general applicability of the experiments by testing a range of materials, and paying careful attention to the alignment of the dropped particles.

- Apply these acquired properties to the various numerical models in DEM that define the contact properties for simulation.

The derived material interaction properties were applied in models such as the viscous damping model used by PFC and a range of modified models developed by Dr R Sarracino using an in-house model tester in Delphi.

- Test the DEM predictions against the experimental data.

The DEM predictions were tested against experimental data by comparing the post-collisional velocities for a range of impact velocities.

8.2 Conclusions and Recommendations

From the Results and Comparisons made between DEM and Experimental, the following observations are made:

8.2.1 Experimental Technique:

Observation: Specular reflections caused by the illuminating strobes on the tested shiny materials make it difficult to pick out the centroid of the spheres in ACAD.

- **Conclusion**: Highly reflective materials such as steel and ceramic ball bearings are not suitable materials to measure material interaction properties.

- **Recommendation**: Coating the particles with a luminescent paint should resolve this issue. But the high surface finish of the tested materials can prevent the luminescent coatings from adhering properly to the surface. An alternative solution is to diffuse the light displayed by the high intensity source (i.e. strobes) using a fluorescent screen. The images captured by the camera will be bright blurred spots of the highly reflective materials. Another solution would be to incorporate radar or an infra red camera instead of an optical camera as illustrated in **Figure 8-1** which captures the images as high density radar images.

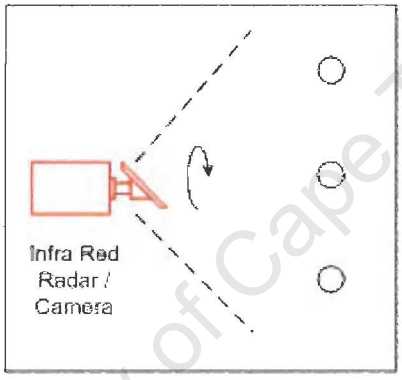

Figure 8-1 – Alternative to optical camera

Observation: The experiments were difficult to reproduce; this was observed on the impact plots on the carbon paper.

- **Conclusion**: Because the colliding contact area is small, aligning the particles precisely is difficult. Scatter is observed on the impact plane. Ideally this impact plane is parallel to the focal plane of the camera. The scatter can be affected by the initial drop height between the particles; as the height is increased the probability of impacting on the same contact point will decrease, plagued by factors such as air-drag. Air-drag has a large contribution to the less dense materials used such as the 5mm plastic and ceramic ball bearings,

and minor difference in surface properties can result in the ball drifting off a vertical path.

- **Recommendation**: The source of the scatter is in the alignment of the particles and the type of material used for the test. Although, a suitable range of materials should be tested and incorporated into DEM, it is recommended that materials that are less dense, i.e. which can be greatly effected by air friction with regards to their size, should be omitted or replaced with larger diameters (larger diameter = denser material). Air-drag will always be a factor contributing to this experiment; therefore it is recommended that reducing the collision drop height (the height between the perpendicular field of view of camera and the quick release mechanism, as illustrated in **Figure 8-2** to a nominal fixed distance and reduce the height between the landing stage and the quick release mechanism so that the angle of rotation of the real impact plane to the desired impact plane will be small thus showing a smaller scatter in the impact points of the balls on the landing surface.

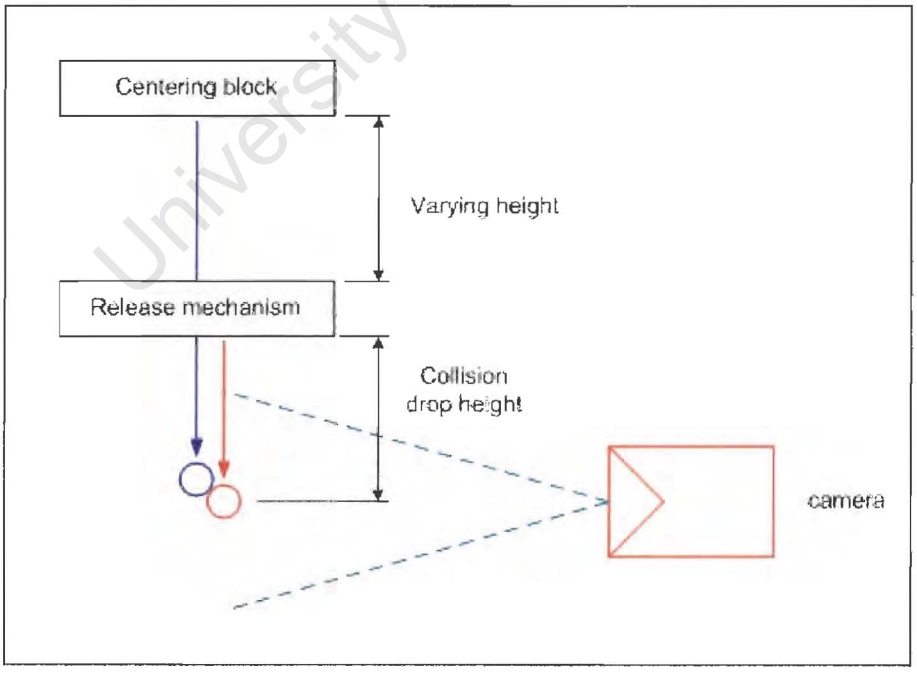

Figure 8-2 – Collision drop height

Observation: It was observed in the imported images in ACAD, the impact between the two particles were significantly harder to determine. This is important in order to determine the pre- and post- relative distances in the image. Also, importing images into ACAD and processing numerous images individually is a complicated and cumbersome task.

- **Conclusion**: Processing of the images is one of the most important stages in the experiment. It is essential that the images are processed in a systematic method in order to prevent operator errors.
- **Recommendation:** It is recommended that an automated image processing technique should be established. The following methodology is suggested for efficient image analysis:

    - Identifying the individual particle images under the strobe illumination is an important stage in the analysis process. The technique used by Govender [23] in his thesis to identify the position of a single coated particle within bulk particles on a series of images is recommended. These images are captured at 50 frames per second; therefore individual images are processed separately using the MATLAB image analysis tool, to determine the exact position of the single coated particle.
    - Once the individual particle images are identified the two colliding particles must be identified: Particle 1 - the particle released from the centering block; and Particle 2 - the particle released from quick release mechanism. To achieve this, the automated toolbox, should scan the individual images vertically as illustrated in **Figure 8-3** to determine the pre-impact particles. Once this has been identified, the toolbox can now determine which are Particle 1 and Particle 2 from calculating the distances between subsequent images. Particle 1 will have a larger relative distance than Particle 2. Useful

information that can be ascertained from this analysis is the offset distance and its error between the Particle 1 and 2.

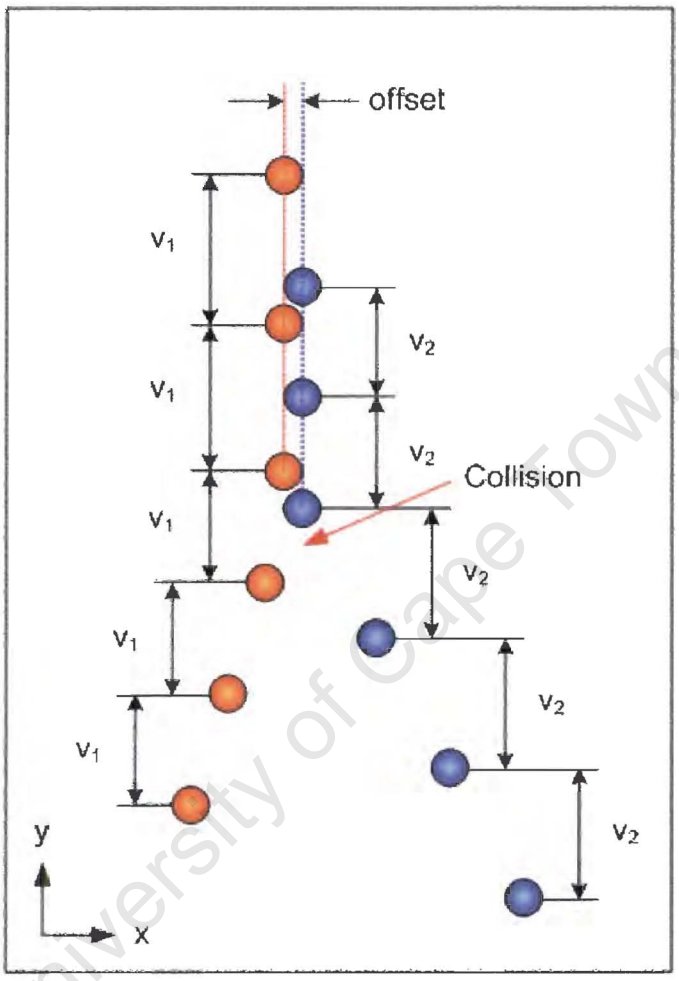

Figure 8-3 – Automated image analysis process

- Once the pre- impact particles have been identified, the toolbox should now determine the post-impact particles. To achieve this, the toolbox should calculate the relative distances / velocities (velocity calculated from the know strobe frequency) for Particle 1 and 2 in the Y component direction as illustrated in **Figure 8-3**. Because the collision of two particles conserves momentum, the velocities for the Particle 1 should decrease

and for Particle 2 should increase post-impact. Since the "collision" of Particle 1 and 2 is not captured in the image, using the change in velocity is an adequate method to determine pre- and post- impact velocities.

- Finally, once all the pertinent information has been measured from the images, the automated toolbox will extract the material interaction properties using the Foerster *et al* [35] and Maw *et al* [29] techniques.

Observation: It was observed that impact time is not measured in the experiment.

- **Conclusion**: Impact time of the two particles is a critical component that cannot be measured using the experimental setup and technique. From the impact one could extract the impulse of the collision or the force of impact over the collision time.

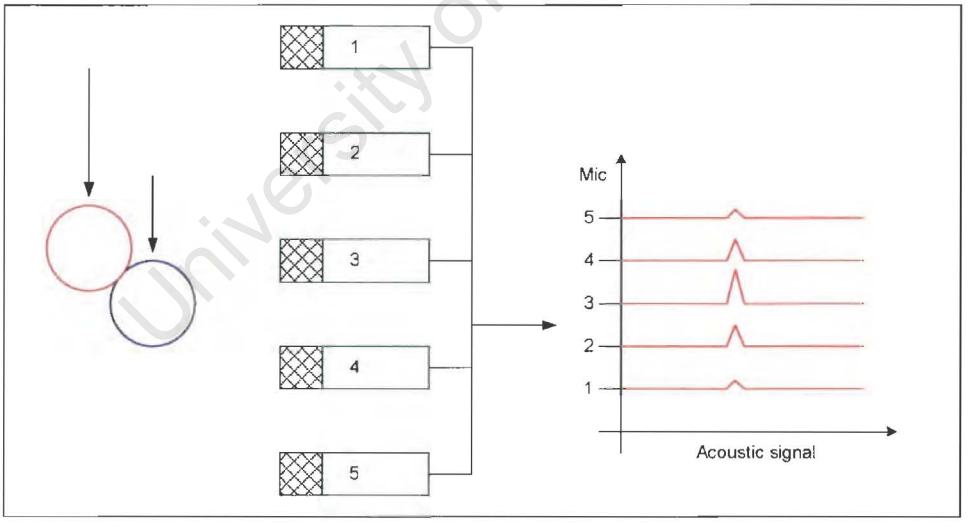

Figure 8-4 – Acoustic microphones to determine the collision

- **Recommendation**: As illustrated in **Figure 8-4** the use of non contact sensors such as acoustic microphones can determine the time of impact. The acoustic peak of the appropriate microphone will provide the information on the

duration of the impact, where this is an unknown factor in the current experimental setup.

Synchronising with the strobe timing could give an accurate time of collision, relating directly to the filmed images.

8.2.2 Experimental Results:

Observation: The results exhibit a scatter in the data, despite extreme care in the setup and measurement.

- **Conclusion**: The sources of scatter result from errors in the image analysis technique and the technique employed to determine the pre- and post- impact velocities. Because the collision of the two in flight particles occur in a small contact area and the collision event is not captured on the photographic images, unknown intrinsic errors such as particles not impacting on the same impact point for each drops could promote to the scatter in the data.
- **Recommendations**: Because the accumulated data has scatter, it is recommended that selective statistical analysis on the data is applied. This involves discarding data points (outliers) which can contribute to the significant overall error of the calculated material properties and estimating their influences on the estimated average calculated valves. Other efforts to reduce the error in results are to employ the automated technique which is described in the experimental setup section above.

  It is assumed that large portion of the scatter in the data is unavoidable and it is an intrinsic property of the binary impact of two materials. It is recommended that a more rigorous calculation routine is developed to reduce the scatter in the calculated data. Because the measured material interaction parameters are used in DEM and the scatter in the data is unavoidable, it is recommended to include a statistical distribution of the scatter per interaction parameter in the numerical models in DEM to give a better prediction for the range of impact velocities.

Observation: Deriving the material interactions properties of the colliding particles using the Non-dimensional constants gives difficulty in assessing the sticking and sliding regions in the graph due to experimental scatter.

- **Conclusion**: This is a significant problem with collisions of two particles in free fall. Previous authors, who conducted similar experiments, stepped away from this type of experiment because of its instabilities.
- **Recommendation**: Because the accumulated data exhibits significant scatter, it is recommend that the data is compared with a static condition. As illustrated on **Figure 8-5** repeating the experiments with impacts on a fixed particle may give a good estimation of the two distinct sticking and sliding regions on the non dimensional graphs.

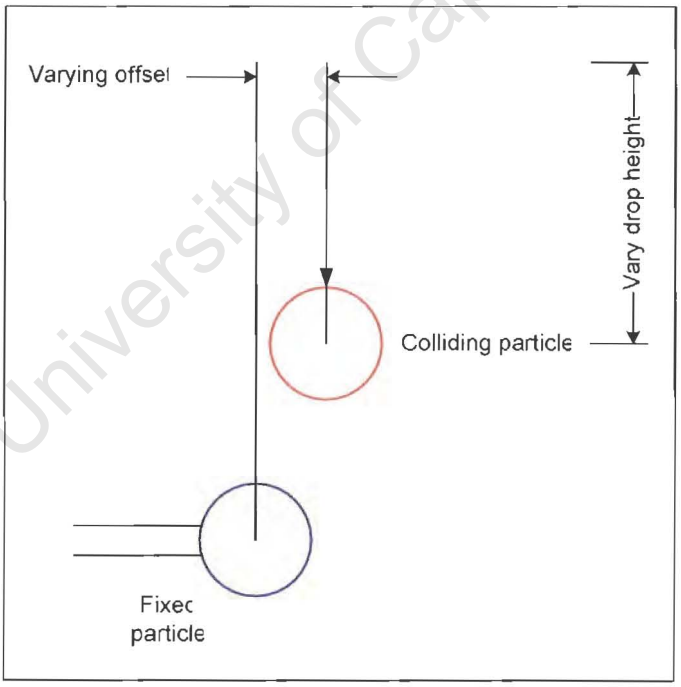

Figure 8-5 – Fixed particle condition

Observation: The technique used to derive the pertinent material interaction properties extracts the coefficients of normal and tangential restitution and one friction value.

- **Conclusion**: Friction is a major contribution in the sliding region; it can be argued that applying one friction in the numerical models will be insufficient to correctly model the sliding behaviour. The limitation is in the mathematical technique employed Foerster *et al* [35] Kharaz *et al* [31] and Maw *et al* [29], they all assume the friction extrapolated from the Non dimensional plots is an average value of static and kinetic friction.
- **Recommendation**: To resolve this issue, it is recommended that the experimental technique utilised to justify Foerster *et al* [35] should be readdressed. It is well known that the kinetic friction is a function of normal and shear force. In Foerster *et al* [35] analysis friction is a component of the Impulse about the normal vector as given in **Equation 8-1**, and angle θ is the angle between the normal n vector and impulse J. The schematic of the collision is illustrated in **Figure 8-6**.

$$\mu = \frac{|n \times J|}{(n \cdot J)} \qquad \textbf{Equation 8-1}$$

Therefore:

$\mu = \tan \vartheta$

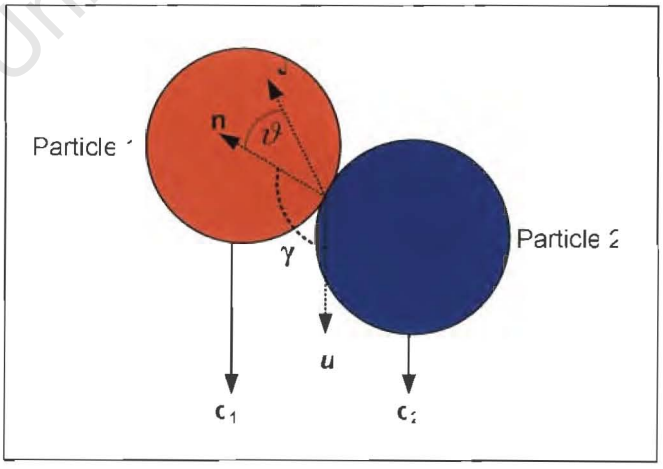

Figure 8-6 – Theta in collision sketch two particles

For a large angle ϑ the coefficient of friction will have a have a large value, and this event can be described as the static friction condition. The Foerster *et al* [35] analysis estimates the maximum static friction. Because the collision event takes place in fraction of a second, the onset of sliding friction is not estimated. Arguably, if this angle ϑ suddenly shifts to a small value, this can be described as kinetic friction where it is a function of the sliding velocity. **Figure 8-7** illustrates difference in static and kinetic friction. A Simple experiment which can measure this frictional behaviour is the classic block on angled slope, where angle ϑ is the angle between the slope and horizontal. But for a dynamic case such as the in-flight collision of two spherical particles, the use of sensitive acoustic microphones such as the setup in **Figure 8-4,** or incorporating a hopkinson bar (a sensitive measuring device which measure the stress waves traversing the bar) in the setup illustrated in **Figure 8-5** where the bar will be attached to fixed particle, can be considered.

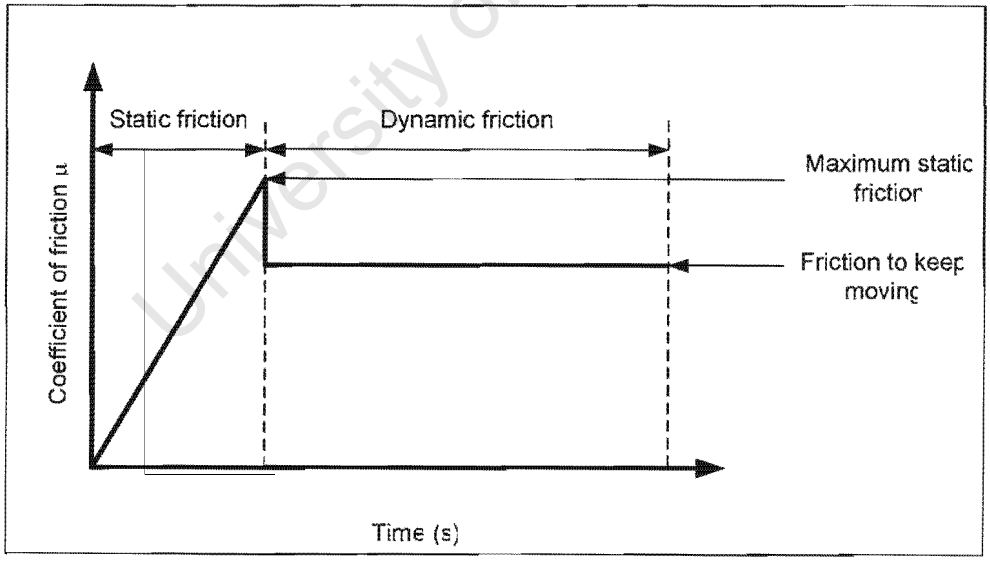

Figure 8-7 – Static and Kinetic friction

It is hypothesised that the signal output from the Hopkinson bar may be of the form illustrated figure in **Figure 8-8.** The red line indicates the magnitude of impulse for time

a, and time *b* represents vibration signal from frictional sliding. Based on the plausible assumption (hypothesis) described earlier, a simple relationship between the vibration signal for time *b* and the onset of dynamic friction can be drawn. Other pertinent information which may arise from this experiment is a test of the assumption of the existence of a slip-stick region during collision. It has been shown in the experimental results for the stick regions, the tangential restitution had significant scatter in the data. In the literature the assumption is presented that the tangential restitution is highly unstable and continuously changing due to the slip-stick phenomenon, and this experiment could possibly test this assumption.

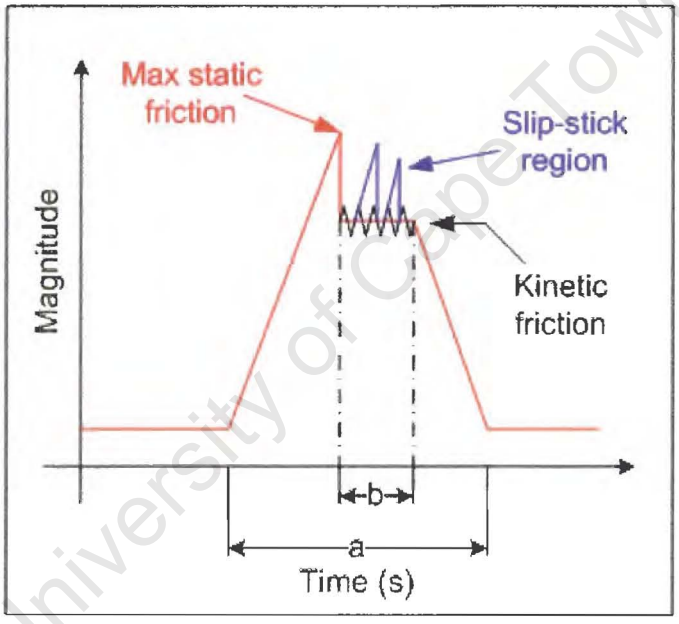

Figure 8-8 – Impact signal on Hopkinson bar

8.2.3 Discrete Element Method vs. Experiment Comparisons

Observation: Comparisons made between the DEM and experimental results of the relative velocities show that the viscous damping model in PFC fails to correctly predict the outcomes of collisions that are in sliding impact (sliding region). Predictions in the

sticking region are good. The application of the various impact parameters for the corresponding impact velocities indicates that the assumption of simple frictional sliding is inadequate in the sliding region.

- **Conclusion**: The effect of tangential compliance on the colliding particles is significant in the post-collision velocities as shown in the above comparisons. The sliding region as postulated by Maw *et al* [29] and Foerster *et al* [35] is governed by the friction and tangential restitution. Particles that exhibit glancing impact or sliding impact are greatly influenced by the friction between the two contacting surfaces, essentially this is the static and dynamic friction. For spherical particles, the influence of rolling friction is also a contributing factor, but this is greatly influenced by the moment of inertia, and thus significantly smaller when compared to dynamic and static friction. The estimated friction from Maw *et al* [29] analysis is an average value which in fact is overestimated for collisions that involve sliding. Typically, static friction is greater than kinetic friction. In the viscous damping model in PFC, the friction is assumed to be one value; i.e. maximum static friction. This however cannot support the particles that are subjected to sliding.

  The application of the viscous damping model was originally designed by Cundall and Strack [2] for the study of soil mechanics. It is possible that the simplifications introduced for slow creeping motion of particles are not appropriate to rapid granular flow.
- **Recommendation**: It is proposed that the introduction of dynamic friction in the simulation model should contribute to better modelling the tangential compliance in the sliding region. Discussions with Djordjevic [38] at the Julius Kruttschnitt Mineral Research Centre indicated that in the PFC DEM code, it is possible to change friction from static to kinetic using a relative velocity rule.

Observation: Foerster *et al* [35] analysis introduces errors in the formulation of the material interaction properties extracted from pre- and post- impact velocities.

- **Conclusion**: It can be concluded that applying the acquired parameters from the experimental results to the DEM models is not necessary as the models can be compared with direct relationships between the pre- and post- impact velocities and modified to fit the data.
- **Recommendation**: It is possible in the numerical models, to make direct comparisons with velocities and change the material interaction properties accordingly. Since, new numerical models are being developed for the simulation of grinding mills, it is sensible to compare direct velocity comparisons because the theory used to extract the pertinent material properties contains assumptions, thus resulting in the introduction of unknown instabilities.

Observation: The DEM model tester developed in Delphi provides a suitable way to test the various numerical models against experimental results.

- **Conclusion**: The DEM model tester developed by Dr. Sarracino is an efficient methodology to test and refine current and new models. This is a well established approach to compare key components in the model.

Conclusion: Now that the experimental technique has been honed and tested, it will be used in an active program to test and possibly refine the DEM contact models for a variety of materials.

- **Recommendation**: The next stage in the development of DEM is incorporating fluid coatings into the simulation. Introduction in the simulation will change the material interaction properties as fluid viscosity is now introduced into the theory. It is possible to reconfigure experimental test rig presented in this thesis for solids coated with interfacial fluids.

8.3 Summary of conclusions and recommendations

- Specular reflection on highly reflective surfaces makes it difficult to determine the overall shape of the colliding particles.

- In-flight collisions of two particles are difficult to reproduce.

- It is recommended that an automated image processing toolbox should be developed to reduce any systematic errors and process numerous images.

- To distinguish the contact time of the collisions, carefully placed acoustic microphones are useful.

- Statistical selective analysis can be used to discard any outliers in the data.

- Despite careful attention to detail in the experiment, small scatter is persistent in the data.

- Scatter in the data is an intrinsic property of collisions of real particles.

- Onset of scatter is unavoidable in the data.

- It is recommended that the analysis of Foerster *et al* [35] should be readdressed.

- It is assessed that the sliding is an effect of the tangential compliance, which is a result of the friction.

- Only one maximum static friction is extracted from the Foerster *et al* [35] analysis.

- Use of sensitive acoustic microphones or Hopkinson bars could determine static and kinetic friction of the colliding materials.

- Comparisons with experimental and DEM models shows that they fail in sliding contact regions.

- Because of the scatter in the interaction properties in the data, it is recommended to apply a distributive function of the scatter in the DEM code.

- The experimental technique to measure and compare material interaction properties in DEM is an active program to test current and new models.

The observations and conclusions with constructive recommendations presented in this chapter will hopefully promote further research into material interaction properties. Ultimately, the use of numerical modelling and simulation will be common practice in the mining industry. Therefore, these models must be sufficiently accurate before they can be accepted as a basis for predicting energy, wear, and breakage.

Chapter 9

Reference:

[1] T J Napier-Munn, S Morrell, R D Morrison, T Kojovic, Mineral Comminution Circuits, Their operation and optimisation, Julius Kruttschnitt Mineral Research Centre (JKMRC), University of Queensland.

[2] P A Cundall and O D L Strack, A discrete numerical model for granular assemblies, Geotechnique 29 (1979) pp 47 - 65

[3] C S Campbell, Rapid granular flows. Annul. Rev. Fluid Mechanics 22 (1990) pp 57 - 92

[4] G C Barker, Computer simulations of granular materials. Mehta A (Ed), Granular Matter: An Interdisciplinary App. Springer-Verlag, NY (1994) pp 35 - 83

[5] O R Walton, Numerical simulation of inelastic frictional particle – particle interaction. Roco, M C (Ed) Particulate Two Phase Flow Chap. 25 (1994) pp 884 - 911

[6] B K Mishra and R K Rajamani, Numerical simulations of charge motion in ball mills. Proceedings, 7th European Conf. on Comminution, Ljubljana (1990) pp 555 -570

[7] T Inoue and K Okaya, Grinding mechanisms of centrifugal mills – batch ball mill simulator. Int. J. Miner. Process. 44 (45) (1996) pp 425 - 435

[8] B K Mishra and R K Rajamani, The discrete element method for the simulation of ball mills. Appl. Math. Model 16 (1992) pp 598 - 604

[9] P W Cleary, Predicting charge motion, power draw, segregation, wear and particle breakage in ball mills using discrete element methods. Miner. Eng. 11 (11) (1998) pp 1061 - 1080

[10] H dong, M H Moys, Measurement of impact behaviour between balls and walls in grinding mills, Minerals Engineering (Article in Press)

[11] Particulate Flow Code 2D, Theory and Background, Itasca Consulting Group, Inc. (1999)

[12] A T McBride and M S Powell, Numerical Simulation of the Milling Process, P9N wrap-up 2002

[13] H A White, Theory of tube mill, J. Chemical and Metallurgical and Mining Society of South Africa. (1905) pp 290 – 305

[14] E W Davis, Fine crushing in ball mills. AMIE Trans. 61 (1919) pp 250 – 296

[15] A M Gow, A B Campbell, W H Coghill, A Laboratory investigation of bal milling. AMIE Trans. Milling methods (1930) pp 51 – 81

[16] A W Fahrenwald, H E Lee, Ball mill studies. AMIE Tech. Pub. 375 (1931)

[17] R E McIvor, Effects of speed and liner configuration on ball mill performance. Mining Engineering (1983) pp 617 – 622

[18] L A Vermeulen and D D Howat, Fluctuations in the slip of grinding charge in rotary mills with smooth liners. Int. J. Mineral Process. 16 (1986) pp 153 – 168

[19] L A Vermeulen and D D Howat, Effects of lifter bars on the motion of the en masse grinding media in milling. Int. J. Mineral Process. 24 (1988) pp 143 – 159

[20] M S Powell and G N Nurick, A Study of charge motion in rotary mills Part 1 – Extension of the theory, Minerals Engineering. 9 (2), (1996) pp 259 – 268

[21] M S Powell and G N Nurick, A Study of charge motion in rotary mills Part 2 – Experimental work, Minerals Engineering. 9 (3), (1996) pp 343 – 350

[22] M S Powell and G N Nurick, A Study of charge motion in rotary mills Part 3 – Analysis of Results, Minerals Engineering. 9 (4), (1996) pp 399 – 418

[23] I Govender, X-ray motion analysis of charge particles in a laboratory mill, PhD Thesis, (2005)

[24] I Govender, A T McBride, and M S Powell, Improved Experimental Tracking Techniques for Validating Discrete Element Method Simulations of Tumbling Mills, Experimental Mechanics. (44), (2004) pp 593 – 607.

[25] Wren, Wallis and Newton, W J Stronge – Impact Mechanics (2000), pp248-265,

[26] O R Walton, Impact Mechanics (2000) pp 6

[27] Goldsmith, W., Impact - The Theory and Physical Behaviour of Colliding Solids, Edward Arnold Ltd, London, 1960.

[28] Hertz, K L Johnson – Contact Mechanics, Cambridge Uni. Press

[29] N Maw, J R Barber, J N Fawcett, - The Role of Elastic Tangential compliance in Oblique Impact, Transactions of the ASME J. of Lubrication Tech. 74/ Vol. 103 (1981)

[30] R D Mindlin – Compliance of Elastic Bodies in Contact, ASME J. of Appl. Mech. Vol. 71 (1949) pp. 259-268

[31] A H Kharaz, D A Gorham, A D Salman – An Experimental study of the elastic rebound of spheres, Powder Tech. 120 (2001) pp 281 - 291

[32] K L Johnson, Proc. Inst. Mech. Eng. 196 (1982) pp 363 - 378

[33] C. Thornton and K. K. Yin, Impact of elastic spheres with and without adhesion, Powder *Technology, 65(1-3), March 1991,153-166*

[34] W J Stronge – Planar Impact of Rough Compliant Bodies, Int. J. Impact Eng. 15 (4) (1990) pp 435 - 450

[35] S F Foerster, M Y Louge, H Chang, K Allia, Measurements of the collision properties of small spheres, Phys. Fluids. 6 (3) (1994) pp 1108 – 1115

[36] Z Ning – PhD Thesis, University of Ashton (1995)

[37] A Lorenz, C Tuozzolo M Y Louge, Measurements of impact of properties of small, nearly spherical particles, Exp. Mech. 37 (3) (1997) pp 292 – 298

[38] Dr Nenad Djordjevic, Julius Kruttschnitt Mineral Research Centre, DEM Research. University of Queensland, Australia

Chapter 10

Appendix A

Drawings of the centering block

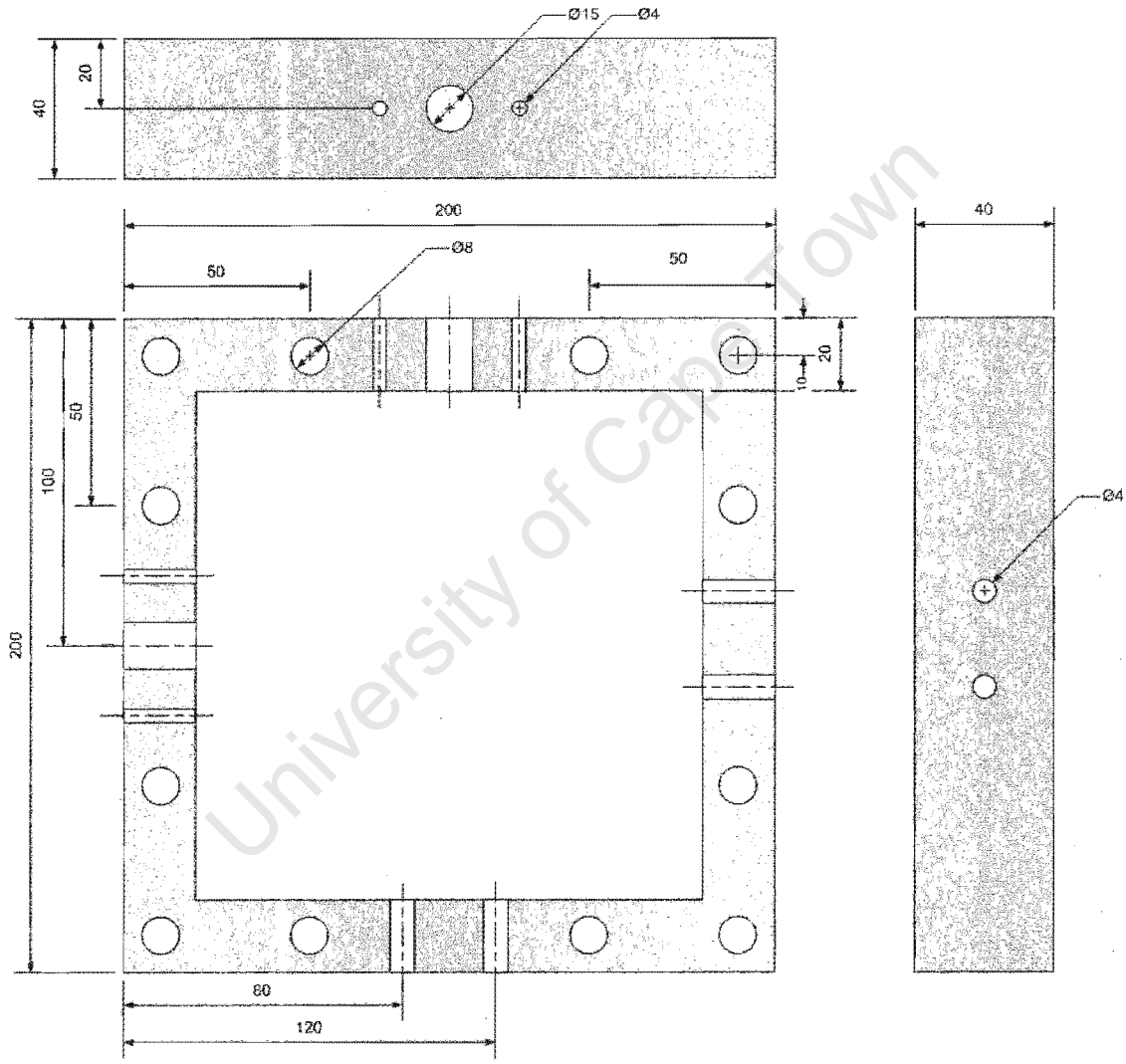

Figure 10-1 – Aluminium centering block

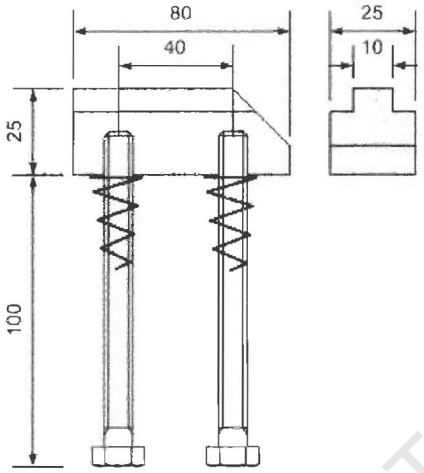

Figure 10-2 – Runner for the nylon block

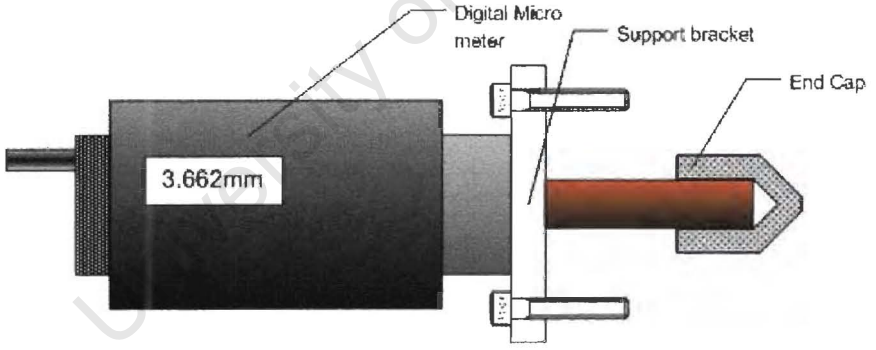

Figure 10-3 – Support bracket for Micrometer

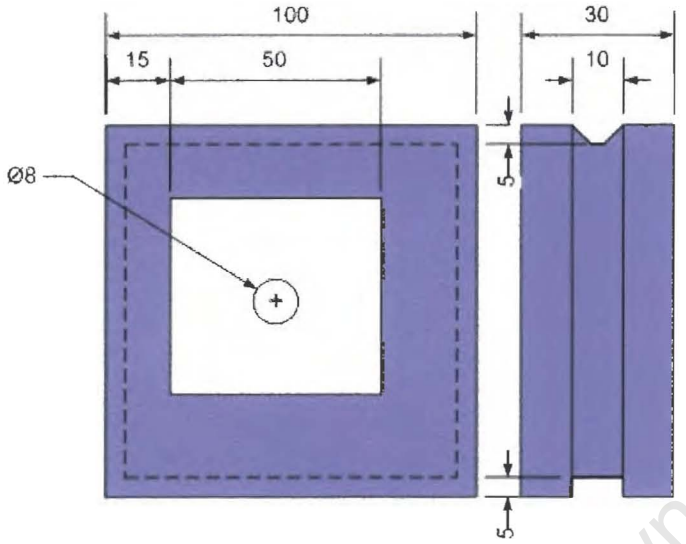

Figure 10-4 – Nylon centering slider

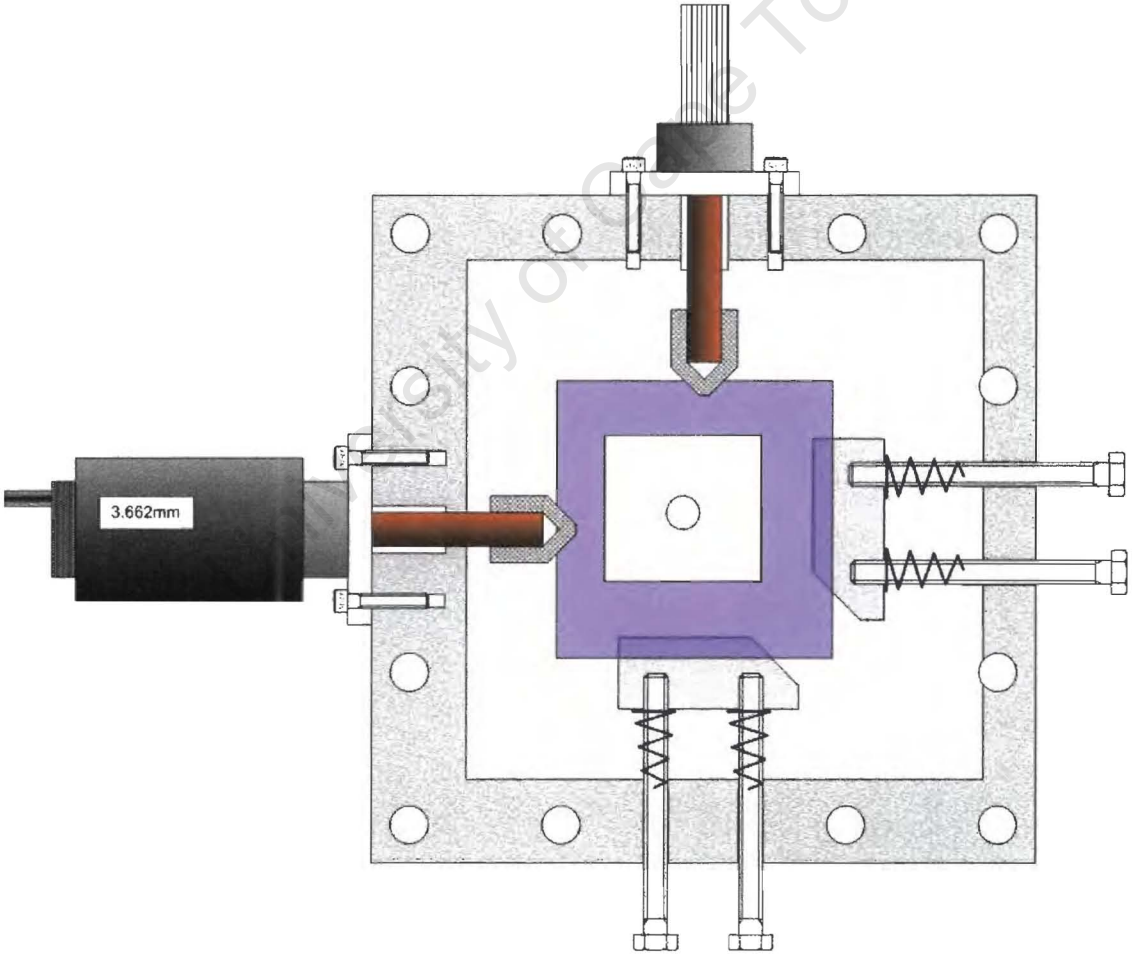

Figure 10-5 – Assembled drawing centering block

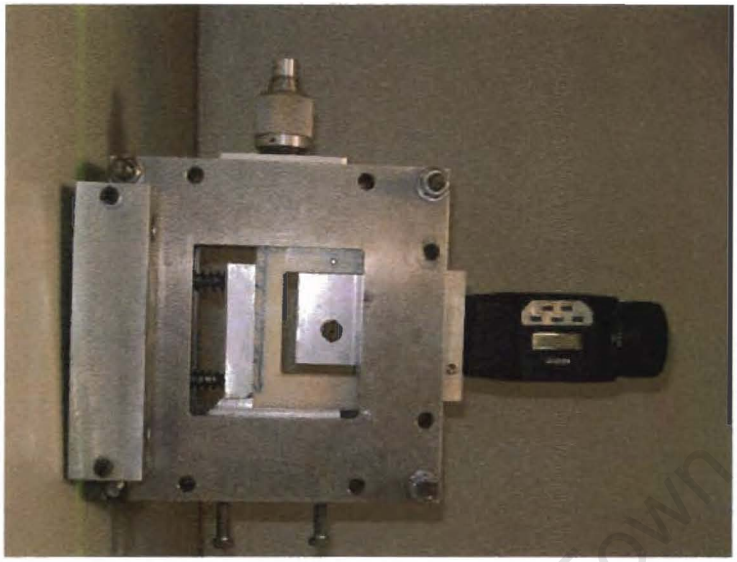

Figure 10-6 – Assembled view centering block (front view)

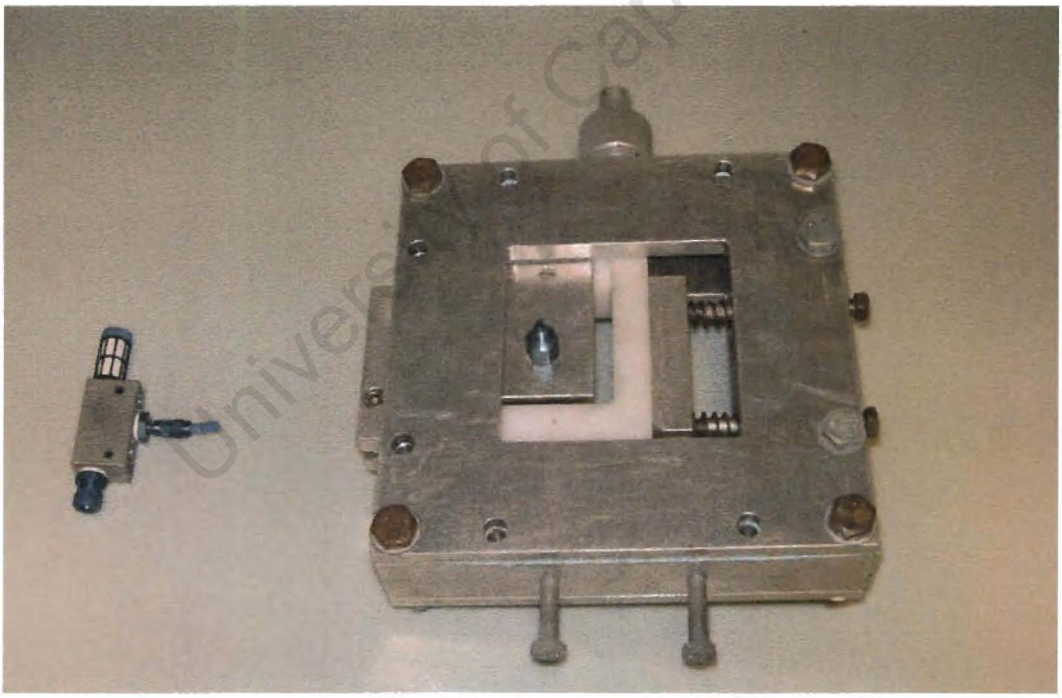

Figure 10-7 – Assembled centering block with vacuum generator

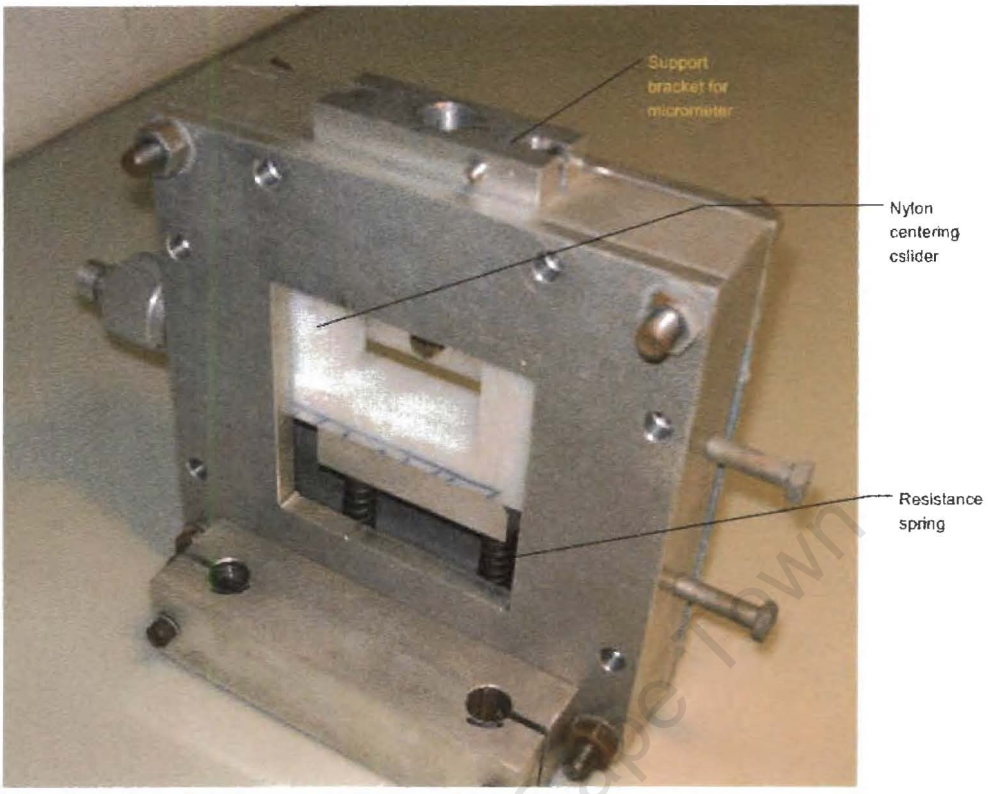

Figure 10-8 – Assembled view centering block (side)

Drawings of the quick release mechanism

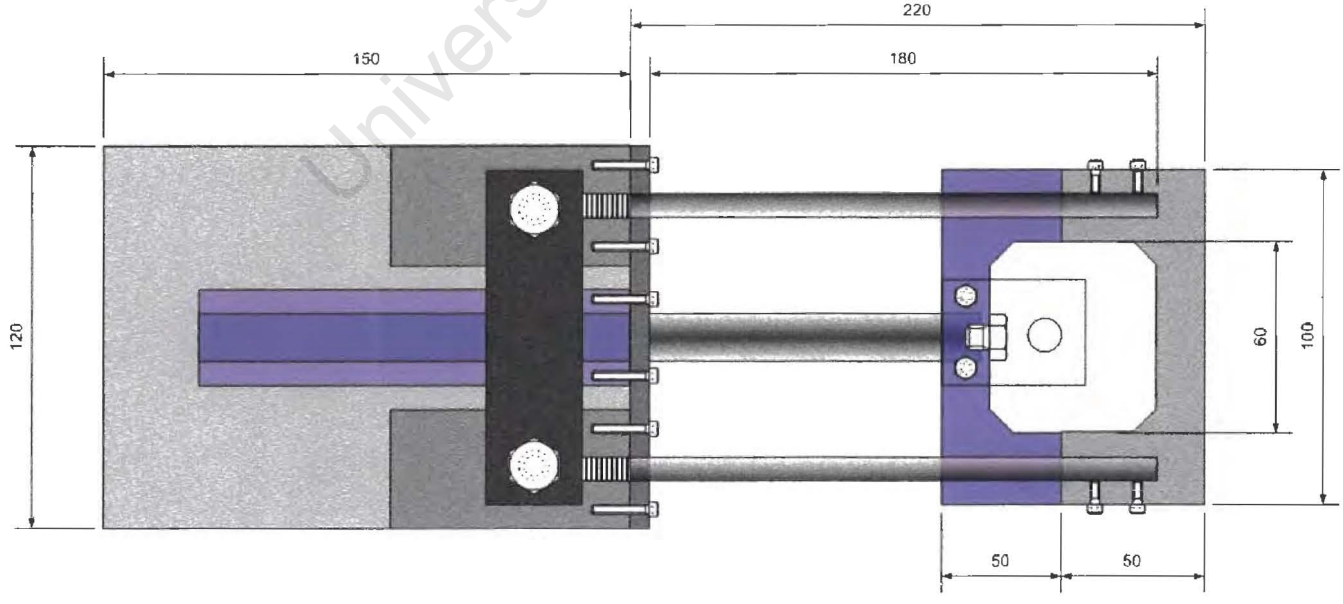

Figure 10-9 – Quick release mechanism

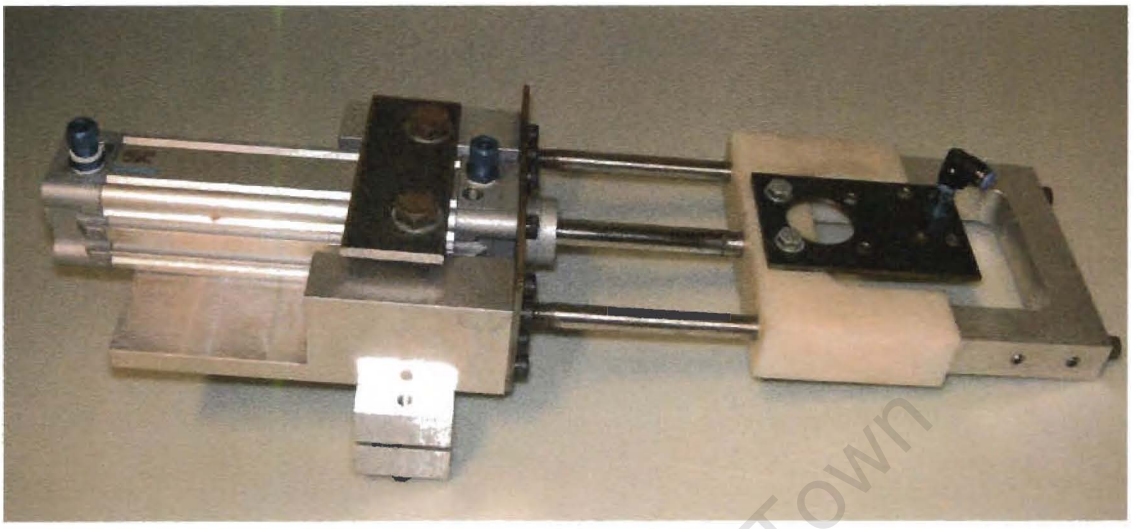

Figure 10-10 – Quick release mechanism assembled view

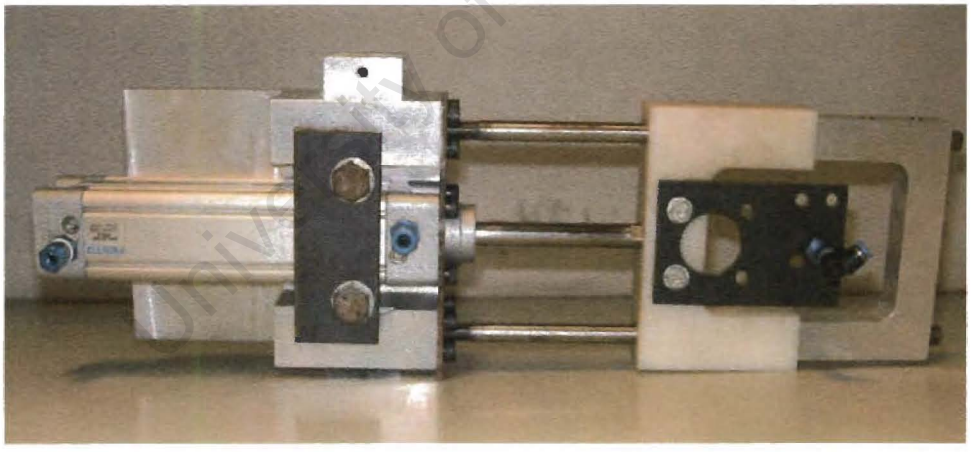

Figure 10-11 – Mechanism arm extended

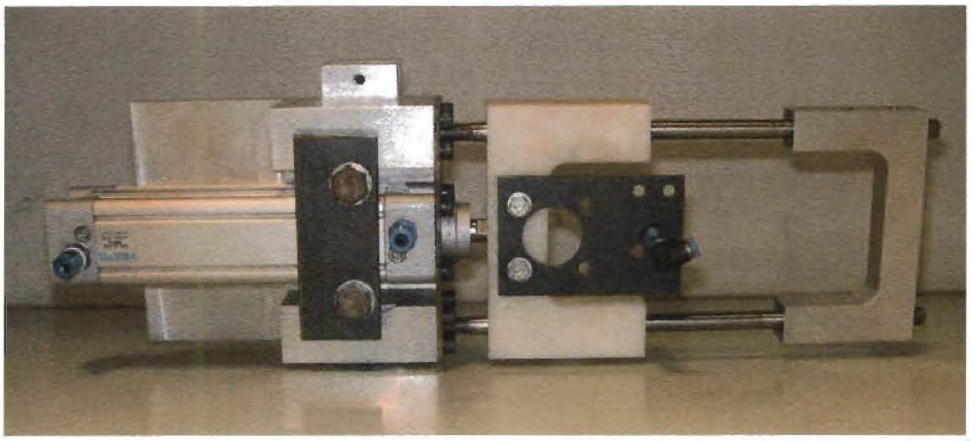

Figure 10-12 – Mechanism arm retracted

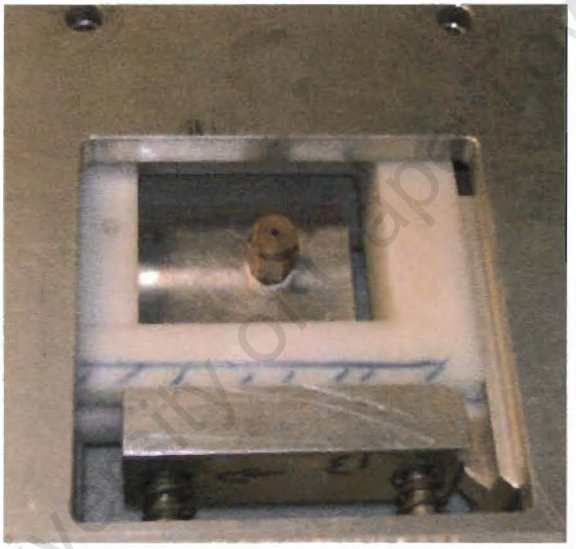

Figure 10-13 – Brass vacuum nozzle (unbeveled)

Drawings of the support structure

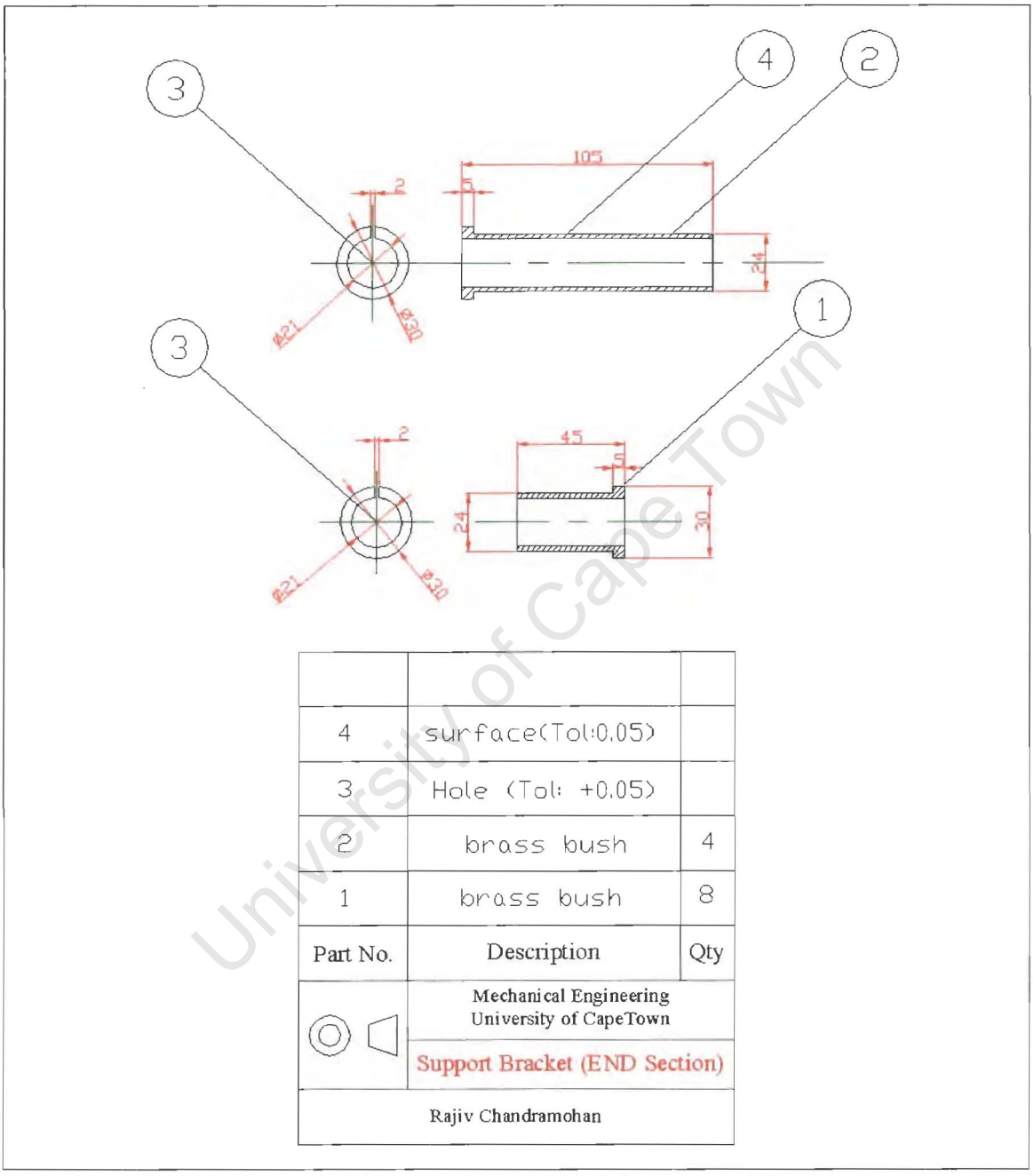

4	surface(Tol:0.05)	
3	Hole (Tol: +0.05)	
2	brass bush	4
1	brass bush	8
Part No.	Description	Qty
	Mechanical Engineering University of CapeTown	
	Support Bracket (END Section)	
	Rajiv Chandramohan	

Figure 10-14 – Brass bushing for the shafts

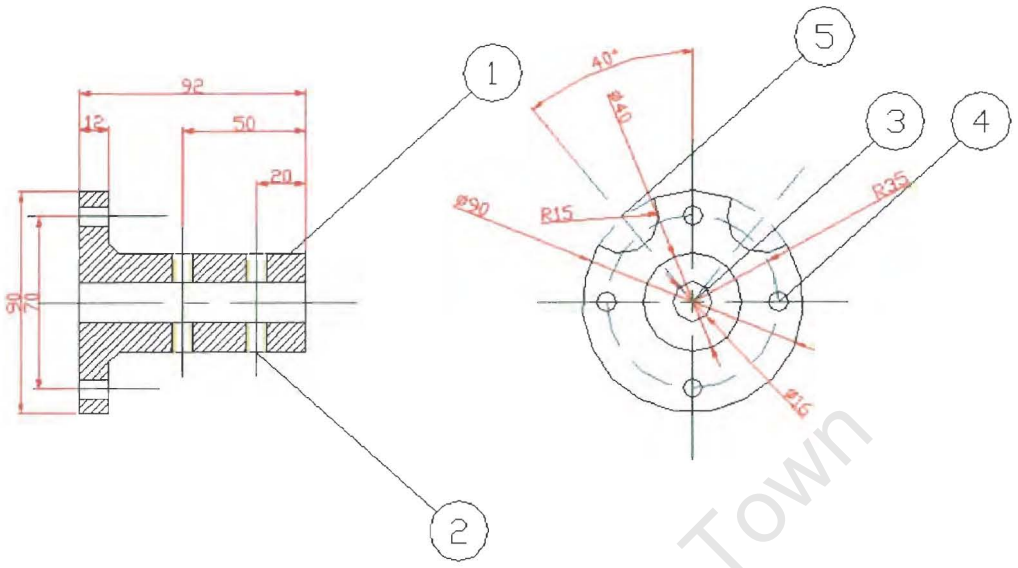

5	cut section R15	2
4	Hole (M8)	4
3	Hole D12 (Tol: +0.05)	1
2	M8 Hole thread grub	4
1	support (mild steel)	4
Part No.	Description	Qty
	Mechanical Engineering University of CapeTown	
	Support extension	
Rajiv Chandramohan		

Figure 10-15 – Support extension

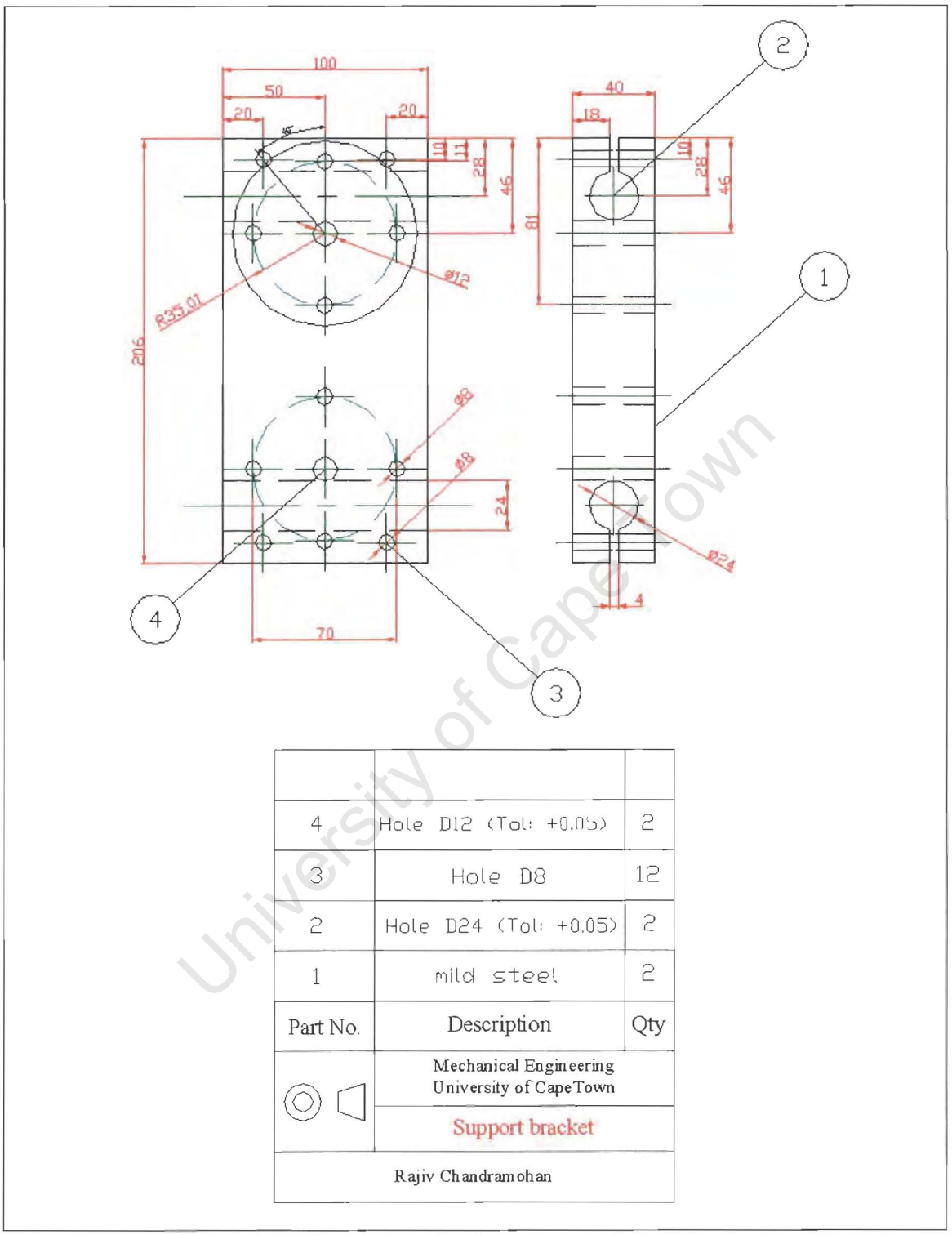

4	Hole D12 (Tol: +0.05)	2
3	Hole D8	12
2	Hole D24 (Tol: +0.05)	2
1	mild steel	2
Part No.	Description	Qty
	Mechanical Engineering University of Cape Town	
	Support bracket	
	Rajiv Chandramohan	

Figure 10-16 – Support bracket

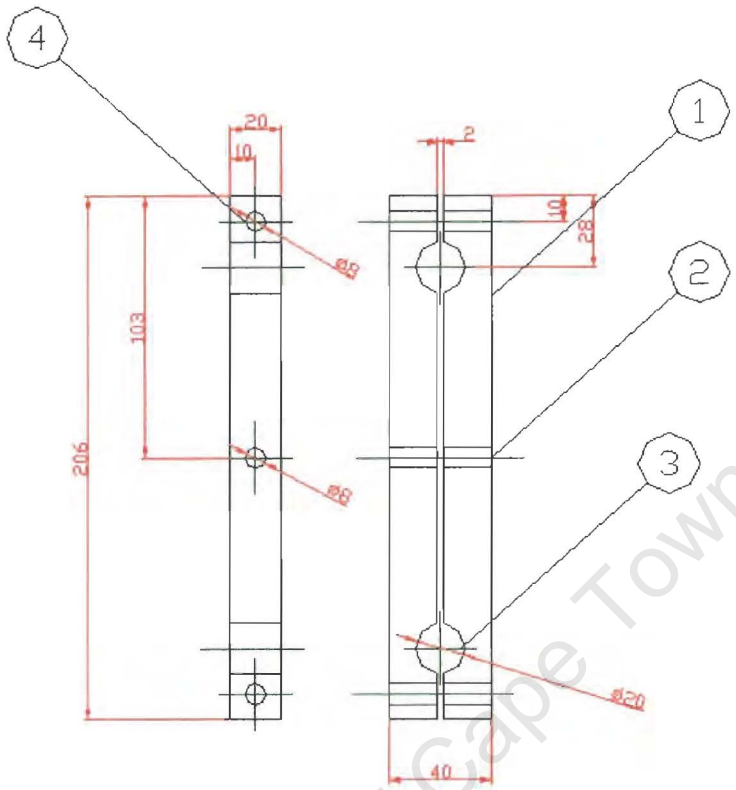

4	Hole (M8)	2
3	Hole (Tol: 0.01)	2
2	Hole (Tol:+0.05)	1
1	aluminium	4
Part No.	Description	Qty
	Mechanical Engineering University of CapeTown	
	mid support bracket	
Rajiv Chandramohan		

Figure 10-17 – Mid support bracket

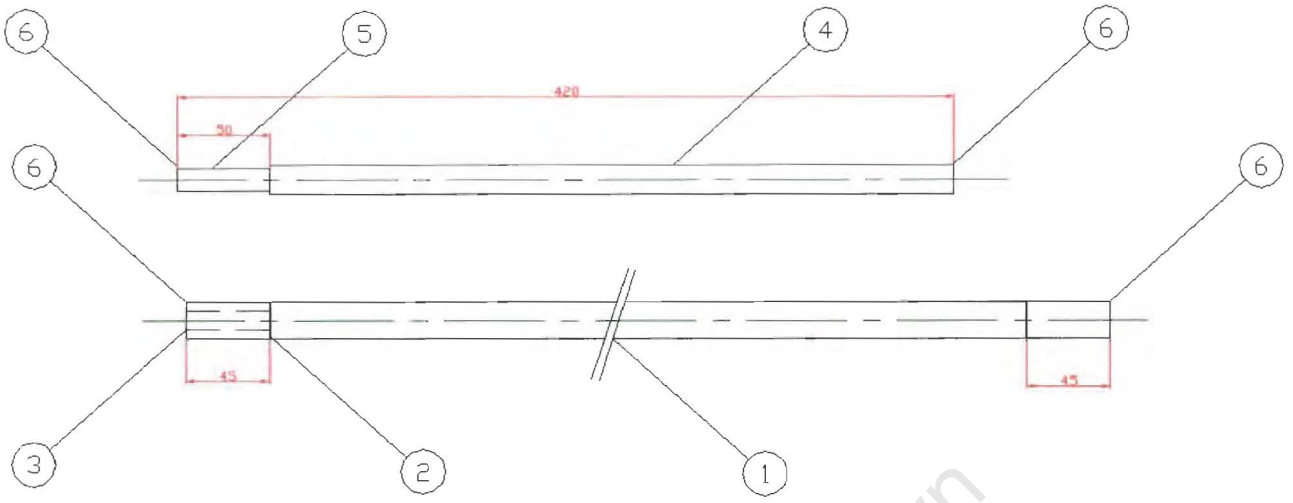

6	chamfer R2	
5	shoulderD12 (Tol-0.05)	1
4	shaft L420, D16	4
3	Hole M10	1
2	circlip groove D18	2
1	shaft L1000, D20	4
Part No.	Description	Qty
	Mechanical Engineering University of CapeTown	
	shafts	
Rajiv Chandramohan		

Figure 10-18 – Shafts

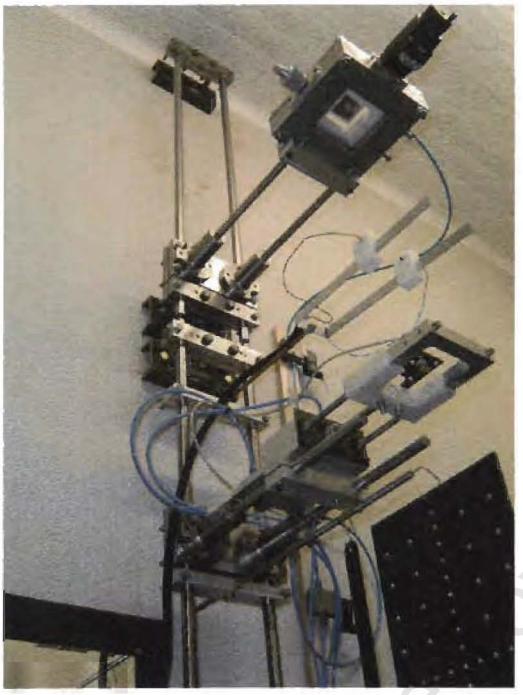

Figure 10-19 – Assembled structure

Figure 10-20 – Camera support (recycled photographic equipment)

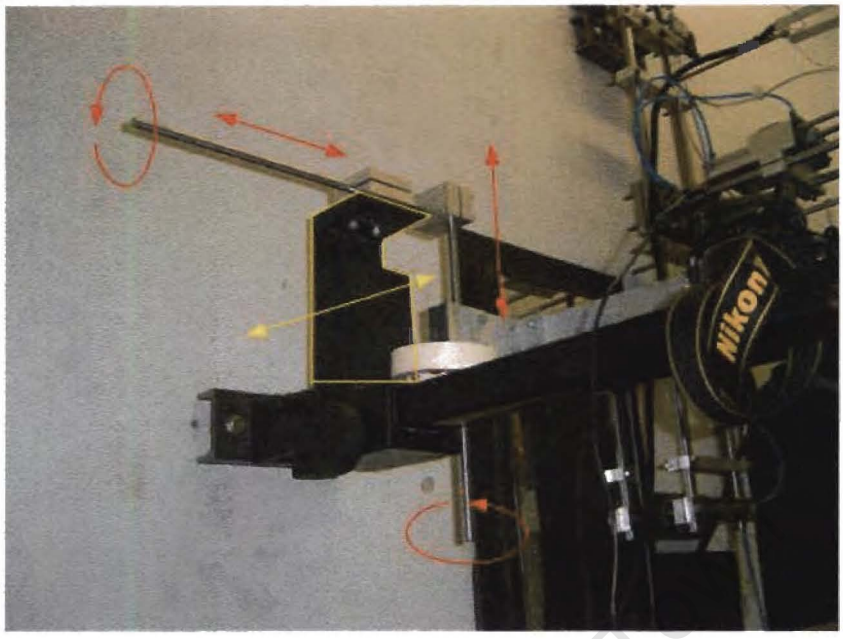

Figure 10-21 – Degree of freedom for the camera support

Equipment details

Micrometer

Figure 10-22 – Mitutoyo digital micrometer

	Description	Range	Accuracy
MITUTOYO	Digimatic Depth Micrometer	0 - 55mm	± 0.001 mm

Digital Strobe

Figure 10-23 – GNS MFS0130 Digital LED Strobe

	Description	Range	Accuracy
Strobe	GNS MFS0130 Digital LED Strobe	300 – 999 Rpm	± 1 Rpm

Relay Board – 24 Volt

Relays are electrically controlled switches. In the type used for this project, a coil pulls in an armature when sufficient coil current flows. **Figure 10-24** below shows the relay board used for controlling the directional control valve to open and close the pneumatic solenoid.

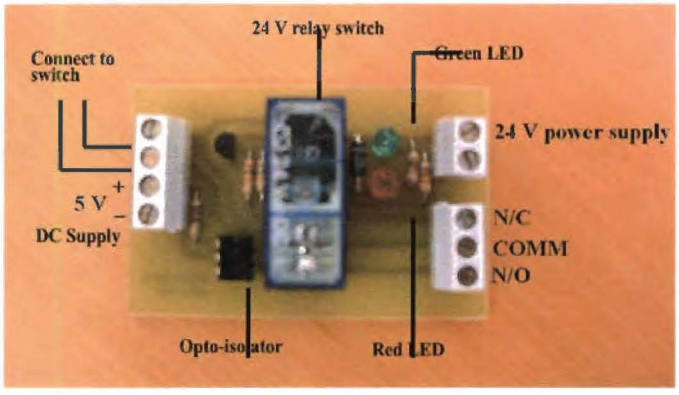

Figure 10-24 – 24 V relay board

The relay is energised by a 24 Volts DC power supply with a maximum current of 30 mA. The opto-isolator (also known as opto-coupler) is an LED emitter combined with a photodetector. The opto-isolator allows signals to be sent between circuits while keeping the circuits completely isolated from one another. This relay board is used to read data into the parallel port of the cell controller and to control the operation of the pneumatic chuck. **Figure 10-25** below shows the circuit diagram of the relay board.

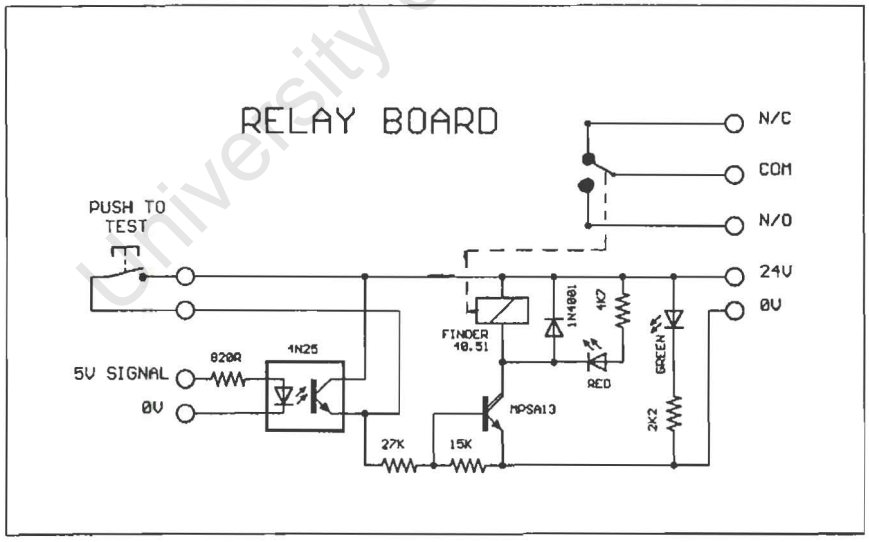

Figure 10-25 – Circuit diagram of relay board

A green LED lights up to indicate the presence of the 24 V supply voltage. The contacts of the relay switch are in the normally closed position (N/C). An input signal of 5 V

(TTL) causes the opto-isolator to start conducting. The latter, in turn, turns on the transistor (MPSA13) and the red LED switches on indicating that the relay has been triggered. The relay contacts now switch position. The 'normally closed' (N/C) becomes open circuit while the 'normally opened' (N/O) closes. Output is between the 'common' (COM) and 'normally opened' (N/O) contacts. This output can now be used to connect to the input lines of the parallel port of a computer and to operate the pneumatic solenoid. As soon as the power is removed, the red LED switches off showing that the contacts have gone back to the 'normally closed' position.

Digital camera

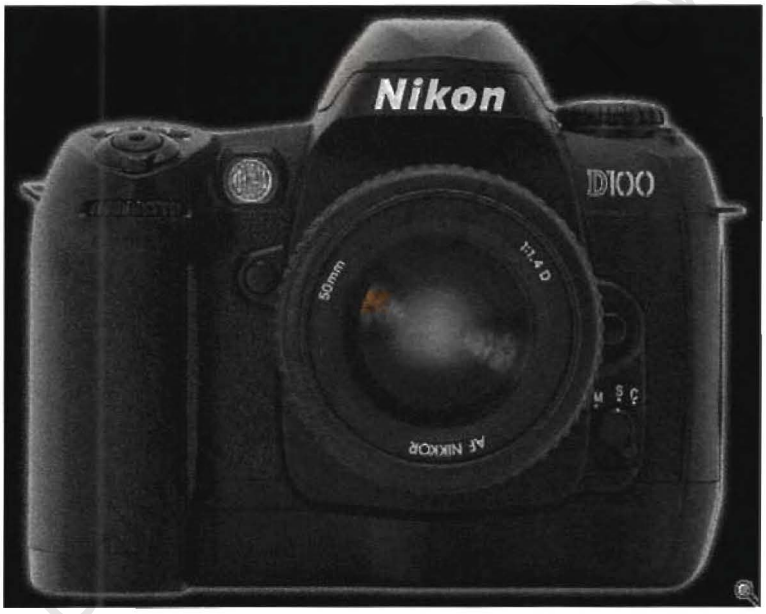

This list, supplied by Nikon Europe

- 6.1 effective Mega Pixels rendering 3,008 x 2,000-pixel images
- Compact and lightweight (weighs approx. 700g/24.7 oz.)
- Low-noise CCD sensor
- 3D Digital Matrix Image Control for precise exposure control, adaptive auto white balance and optimal colour accuracy
- High-performance built-in Speed light with D-TTL flash control

- Three colour modes offered for different workflow environments
- Five-Area Auto focus with Dynamic AF operation
- High-speed image processing provided by new one-chip system LSI
- Top shutter speed of 1/4,000 sec. and flash sync speed up to 1/180 sec.
- Plug-and-play USB 1.1 interface for quick computer connection
- On-Demand Grid Lines can be displayable in viewfinder
- Custom Settings can be selectable in the LCD monitor
- Compatible with Compact Flash™ cards Type I and Type II including 512 MB / 1 GB IBM Micro Drive™
- Nikon View 5.1 software (supplied) enables easy transfer and viewing of images on your computer also includes rudimentary RAW file manipulation and conversion
- Optional Nikon Capture 3 software for excellent image management and remote operation
- Optional Multi Function Battery Pack MB-D100 accepts six 1.5V LR6 (AA-size alkaline) batteries or one or two Li-Ion batteries for extended shooting capability. Features voice memo recording/playback function, vertical shutter release button, Command and Sub Command Dials, AF start button and a 10-pin remote terminal

Pneumatics

Figure 10-26 – Festo Standard Piston

	Description	Range	Pressure
Piston	DNC-32-200-PPV-A	200mm stroke	6 – 12 Bar

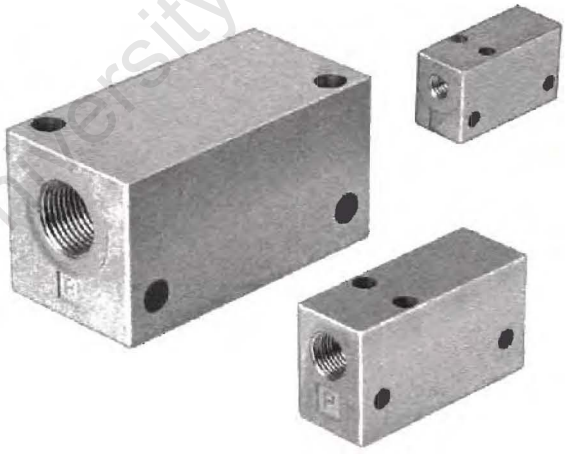

Figure 10-27 – Festo VAD1/8 Vacuum generator

Figure 10-28 – Festo standard 3/2 Valve

	Description	Voltage	Pressure
3/2 Valve	MDH-3/2-24DC	24V DC	8 Bar max

Appendix *B*

Software Code in Qbasic

```
CLS
LET X = 0
PRINT "TEST"
OUT &H378, 0
GOSUB DELAY1
PRINT "DELAY DONE"
OUT &H378, 1
GOSUB DELAY2
PRINT "DELAY DONE"
OUT &H378, 2
GOSUB DELAY3
PRINT "DELAY DONE"
OUT &H378, 4
```

```
GOSUB DELAY1
PRINT "DELAY DONE"
OUT &H378, 0
END

DELAY1:
LET X = 0
10 LET X = X + 1
PRINT X
IF X = 1000 THEN RETURN
GOTO 10

DELAY2:
LET Y = 0
20 LET Y = Y + 1
PRINT Y
IF Y = 100 THEN RETURN
GOTO 20

DELAY3:
LET Z = 0
30 LET Z = Z + 1
PRINT Z
IF Z = 50 THEN RETURN
GOTO 30
```


Press F5 to run and change Y values to control the time release of the second particle

Appendix C

Software code in Matlab

```
% Calculate the coefficient of restitution from drop test experiments
% Assumptions of no spin before
```

```
% Particles are spherical
% ------------------------------------------------------------

% clear all;
% close all;
% clc;

% ------------------------------------------------------------
% Data entry
radius1 = 4.075;
radius2 = 4.075;
density1 = 7800;
density2 = 7800;

mass1 = (4/3)*pi*(radius1^3)*density1
mass2 = (4/3)*pi*(radius2^3)*density2

inertia1 = mass1*((2*radius1)^2)/10
inertia2 = mass2*((2*radius2)^2)/10


For i = 1:132;

Offset = collisions(8,i);


linearVelocity1Pre = [0; collisions(1,i); 0]
linearVelocity2Pre = [0; collisions(2,i); 0]
rotationalVelocity1Pre = [0;0;0]
rotationalVelocity2Pre = [0;0;0]

linearVelocity1Post = [collisions(4,i); collisions(5,i); 0]
linearVelocity2Post = [collisions(6,i); collisions(7,i); 0]
rotationalVelocity1Post = [0;0;0]      % do not need to be measured
rotationalVelocity2Post = [0;0;0]      % do not need to be measured

% ------------------------------------------------------------
```

```
angle2to1 = acos(offset/(radius1 + radius2)) %for angle theta
anglegamma = angle2to1 + (pi/2) % for angle gamma
nX = -1*cos(angle2to1)'
nY = sin(angle2to1)'
n = [nX , nY, 0]
tX = -1*sin(angle2to1)
tY = -1*cos(angle2to1)
t = [tX, tY, 0];
contactPoint = radius1*[nX nY]


%t = (gPre - (dot(gPre,n))*n)/(sqrt((gPre)^2 - (dot(gPre,n))^2))


figure(1)
hold on;
[x,y] = circle(radius1,0,0);
plot(x,y)
text(0,0,'Particle 2')


[x,y] = circle(radius2,-1*offset,sqrt((radius1+radius2)^2-offset^2));
%text(-1*offset,nY*(radius2+radius1),'Particle 1')
plot(x,y)

plot(contactPoint(1),contactPoint(2),'r*')
%text(contactPoint(1),contactPoint(2),'Contact point')

plot([contactPoint(1);contactPoint(1) + nX*radius2] , [contactPoint(2);contactPoint(2) +
nY*radius2])
plot([contactPoint(1);contactPoint(1) + tX*radius2] , [contactPoint(2);contactPoint(2) + tY*radius2])


axis tight;
axis equal;
grid on;
% ------------------------------------------------------------
```

```
% ------------------------------------------------------------
% Main Section

% calc gPre
gPre = (linearVelocity1Pre - linearVelocity2Pre)

% extrapolate linear velocities to determine collisional impulse
impulse1 = mass1 * (linearVelocity1Post - linearVelocity1Pre)
impulse2 = -1 * mass2 * (linearVelocity2Post - linearVelocity2Pre)
impulseMean = (impulse1)% + impulse2) / 2  % danger danger check

deltaImpulsiveSpin = -1*cross(n', impulseMean)

rotationalVelocity1Post = (1/(inertia1/radius1)).*deltaImpulsiveSpin
rotationalVelocity2Post = (1/(inertia2/radius2)).*deltaImpulsiveSpin

rotVel1(i,1) = dot((rotationalVelocity1Post),(rotationalVelocity1Post))
rotVel2(i,1) = dot((rotationalVelocity2Post),(rotationalVelocity2Post))


reducedMass = 1/((1/mass1) + (1/mass2))
gPost = gPre + ((7/(2*reducedMass))*impulseMean) -
((5/(2*reducedMass))*n*dot(impulseMean,n))'

Psi1(i,1) = -1*dot(gPre,t)/dot(gPre,n)
Psi2(i,1) = -1*dot(gPost,t)/dot(gPre,n)
normV = dot(gPre,n)
tanV = dot(gPre,t)

restN(i,1) = -1*(dot(n,gPost))/(dot(n,gPre))
modcross = (cross(n,impulseMean));
magmodcross = sqrt(modcross*modcross');

RelvelnormI(i,1) = abs(dot(gPre,n))
RelveltanI(i,1) = abs(dot(gPre,t))
```

```
friction(i,1) = magmodcross/(dot(n,impulseMean))
beta(i,1) = -1*(cross(n,gPost))/(cross(n,gPre))
symbol(i,1) = sign(dot(gPre,t))

NewPsi2(i,1) = Psi1(i,1) - ((7/2)*(1+restN(i,1))*friction(i,1)*symbol(i,1))
Yint(i,1) = ((7/2)*(1+restN(i,1))*friction(i,1)*symbol(i,1))
NewPsi1(i,1) = Psi2(i,1)/beta(i,1)
Newbeta(i,1) = 1 - ((7/2)*(1+restN(i,1))*friction(i,1)*symbol(i,1))/Psi1(i,1)
Cint(i,1) = ((7/2)*(1+restN(i,1))*friction(i,1)*symbol(i,1))

figure(2)
hold on;
plot([0;gPre(1)],[0,gPre(2)],'r')
plot([0;gPost(1)],[0,gPost(2)],'g')
legend('gPre','gPost')
axis equal
grid on
% ------------------------------------------------------------


end
```

Use the Matlab Excel Link function to import the required data. Name the matrix "collisions".

Appendix D

Software code in PFC

```
;-------------------------
; simple ball on ball collision
; by Rajiv Chandramohan
; UCT, MPRU
```

```
;-------------------------

;-------------------------
new;
set def_dt = 1e-6    ; initial time-step when no contact is detected
set dt max = 1e-6    ; max allowable time-step
set pinterval=30    ;plot update interval
set plot emf        ;hardcopy plot output is emf
set hist_rep=10  ;interval at wich the history variables are monitored
call fishcall.FIS    ;call routine names speicifc points at which PFC can be interrupted
                ;during analysis
;-------------------------

;-------------------------
define initialParamaters
        setv_NormalDamp = 0.3
        setv_ShearDamp = 0.39
        ballDens = 7800
end
initialParamaters
;-------------------------
; generate the wall

;wall id = 1  kn = 1e6 ks = 1e6 fric = 0.067 node (-1.0,0.2) (1.0,0.2)


;-------------------------
; generate the ball
ball id = 2 x = 0  y = 0.30 rad = 0.00315
range name target y(0.2 , .4)
property yv = -2.59835945 xv = 0 range target


ball id = 1 x = -0.004413857 y = 0.31 rad = 0.00315
range name projectile y(.306, 0.8)
property yv = -2.970282857 xv = 0 range projectile
```

```
prop density=ballDens kn=12.8e8 ks=12.8e8 fric=0.031


;---------------------------


;---------------------------
plot create mainView
plot add wall black
plot add ball yellow
plot ball id on
plot show

history id 1 ball xp id=1
history id 2 ball xp id=2
history id 3 ball yp id=1
history id 4 ball yp id=2
history id 5 ball xv id=1
history id 6 ball xv id=2
history id 7 ball yv id=1
history id 8 ball yv id=2
history id 9 ball sp id=1
history id 10 ball sp id=2

;plot create unbalancedForce
;plot add history 1
;plot add history 2
;plot show
;---------------------------


;---------------------------
set grav = 0 -9.81
call ContactDampingModel.dat
;---------------------------
cycle 50000
;solve average=1e-20 maximum=1e-20 clock=10000 cycles=1040000 time= 10000
```

Appendix E

Propagation of Errors

Data Reduction and Error Analysis for the physical sciences; Philip R Bevington, Associate professor of Physics, Case Western Reserve University.

Formulae for error propagation:

Addition & Subtraction:

If Y is the weighted sum of A and B for constants x and z:

$$Y = xA \pm zB$$

Then, $\Delta Y = x|\Delta A| + z|\Delta B|$

Multiplication and Division:

If Y is weighted product of A and B for constant x:

$$Y = \pm xAB$$

Then, $\Delta Y = Y\sqrt{\left(\frac{\Delta A}{A}\right)^2 + \left(\frac{\Delta B}{B}\right)^2}$

Powers:

If Y is obtained by raising the power B to A for constant x:

$$Y = \pm xA^{\pm B}$$

Then, $\Delta Y = Y\sqrt{\left(B\frac{\Delta A}{A}\right)^2}$

Exponentials:

If Y is obtained raising the natural base to power A for constants x and y:

$$Y = \pm xe^{\pm yA}$$

Then, $\Delta Y = Y(y\Delta A)$

Appendix F

Binary Collision Data

Ball1				Ball2		
VPre	VPost(x)	VPost(y)	Offset	VPre	VPost(x)	VPost(y)
4.26	0.03	3.47	0.51	2.72	0.10	3.60
4.40	0.13	2.96	1.17	2.86	0.18	4.41
4.37	0.06	3.06	0.65	2.90	0.12	4.43
4.05	0.09	3.05	0.61	2.76	0.15	4.41
4.27	0.09	2.91	0.76	2.65	0.07	3.84
4.35	0.06	2.91	0.58	2.81	0.06	3.76
4.27	0.06	2.93	0.50	2.71	0.15	3.83
4.40	0.14	3.03	0.95	2.83	0.17	4.40
4.29	0.13	2.95	0.84	2.77	0.09	3.64
4.41	0.10	2.99	0.84	2.84	0.18	4.28
4.39	0.13	3.01	0.78	2.87	0.15	4.41
4.36	0.14	2.92	0.78	2.77	0.08	3.88
3.87	0.10	2.99	0.67	2.83	0.08	4.38
4.37	0.15	3.00	1.09	2.84	0.13	4.40
4.32	0.13	2.99	0.96	2.80	0.11	4.36
4.44	0.19	2.97	1.41	2.82	0.13	4.27
4.38	0.20	3.07	1.28	2.90	0.16	4.39
4.39	0.20	2.99	1.08	2.84	0.12	4.38
4.44	0.19	2.97	1.41	2.82	0.13	4.27
4.38	0.20	3.07	1.28	2.90	0.16	4.39

4.39	0.20	2.99	1.08	2.84	0.12	4.38
4.34	0.18	2.99	1.50	2.98	0.18	4.38
4.38	0.19	3.02	1.23	2.86	0.16	4.39
4.35	0.20	2.99	1.06	2.76	0.17	4.36
4.32	0.21	3.02	1.22	2.80	0.19	4.38
4.35	0.16	3.02	1.16	2.80	0.14	4.41
4.36	0.20	3.02	1.39	2.80	0.17	4.40
4.27	0.22	3.03	1.28	2.75	0.17	4.36
4.33	0.21	3.01	1.47	2.79	0.21	4.33
4.31	0.21	2.97	1.64	2.73	0.17	4.29
4.28	0.21	2.99	1.36	2.79	0.21	4.35
4.36	0.20	3.01	1.65	2.75	0.24	4.36
4.32	0.25	3.02	1.17	2.65	0.22	4.34
4.42	0.26	3.01	1.96	2.75	0.24	4.36
4.32	0.28	2.98	1.87	2.73	0.24	4.31
4.30	0.24	2.97	2.07	2.72	0.25	4.27
4.27	0.28	2.94	1.85	2.67	0.23	4.25
4.29	0.28	3.05	2.17	2.73	0.24	4.32
4.34	0.26	3.08	2.13	2.79	0.28	4.36
4.35	0.30	3.06	2.11	2.77	0.30	4.30
4.33	0.33	3.07	2.27	2.74	0.31	4.28
4.39	0.27	3.14	2.04	2.78	0.27	4.42
4.26	0.32	3.13	2.60	2.71	0.28	4.34
4.29	0.36	2.99	2.53	2.72	0.16	3.75
4.32	0.32	3.08	2.17	2.80	0.29	4.26
4.29	0.31	3.08	2.55	2.60	0.33	4.33
4.26	0.29	3.01	2.46	2.65	0.14	3.39
4.30	0.33	3.04	2.31	2.70	0.25	3.98
4.23	0.38	3.07	2.61	2.72	0.35	4.27
4.33	0.38	3.07	2.64	2.76	0.33	4.27
4.29	0.35	3.10	2.55	2.71	0.38	4.27
4.28	0.39	3.14	2.21	2.65	0.35	4.28
4.22	0.43	3.06	2.85	2.64	0.36	4.21
4.26	0.35	3.12	2.75	2.71	0.38	4.21
4.25	0.35	3.12	2.75	2.74	0.38	4.22
4.26	0.39	3.10	2.66	2.70	0.35	4.27
4.27	0.42	3.11	2.98	2.73	0.42	4.20
4.30	0.41	3.16	3.13	2.73	0.41	4.23
4.24	0.43	3.13	3.16	2.69	0.41	4.20
4.33	0.43	3.06	3.03	2.70	0.39	4.20
4.27	0.43	3.15	3.04	2.71	0.41	4.23
4.32	0.46	3.07	3.26	2.76	0.41	4.19
4.41	0.44	3.16	3.17	2.69	0.41	4.25
4.31	0.44	3.14	3.25	2.71	0.43	4.22
4.26	0.41	3.17	3.23	2.68	0.43	4.28
4.24	0.43	3.12	3.25	2.68	0.45	4.18
4.26	0.50	3.21	3.79	2.71	0.46	4.16
4.33	0.48	3.15	3.77	2.72	0.40	4.12

4.27	0.41	3.16	3.34	2.72	0.41	4.23
4.26	0.45	3.18	3.46	2.67	0.45	4.18
4.27	0.47	3.15	3.51	2.68	0.44	4.17
4.25	0.48	3.13	3.68	2.69	0.47	4.09
4.32	0.52	3.19	3.59	2.71	0.42	3.97
4.27	0.50	3.15	3.45	2.71	0.46	4.10
4.26	0.50	3.19	3.89	2.70	0.48	4.08
4.27	0.52	3.16	3.85	2.71	0.52	4.05
4.29	0.54	3.20	3.78	2.69	0.47	4.17
4.23	0.51	3.23	4.20	2.64	0.57	4.07
4.28	0.54	3.25	4.02	2.71	0.51	4.11
4.27	0.52	3.24	3.94	2.69	0.54	4.07
4.27	0.50	3.23	4.01	2.71	0.53	4.13
4.26	0.53	3.27	4.12	2.75	0.54	4.13
4.28	0.54	3.25	3.86	2.69	0.52	4.13
4.26	0.56	3.24	4.01	2.68	0.50	4.09
4.28	0.56	3.29	4.08	2.80	0.54	4.10
4.31	0.57	3.33	4.42	2.70	0.56	4.07
4.28	0.56	3.21	4.37	2.70	0.55	4.08
4.23	0.61	3.33	4.62	2.68	0.60	4.01
4.25	0.63	3.30	4.67	2.70	0.59	3.93
4.28	0.62	3.34	4.76	2.69	0.59	3.96
4.27	0.59	3.29	4.52	2.67	0.58	4.02
4.27	0.66	3.37	5.03	2.72	0.61	3.93
4.32	0.63	3.35	4.73	2.77	0.58	3.97
4.33	0.61	3.38	4.81	2.74	0.60	3.98
4.32	0.58	3.34	4.39	2.76	0.56	4.05
4.29	0.58	3.29	4.42	2.70	0.56	4.06
4.27	0.57	3.28	4.30	2.71	0.55	4.08
4.29	0.66	3.42	4.87	2.74	0.61	3.92
4.30	0.66	3.43	5.17	2.73	0.60	3.88
4.33	0.58	3.45	4.91	2.76	0.61	4.00
4.34	0.65	3.49	5.20	2.78	0.65	3.94
4.30	0.65	3.42	5.17	2.74	0.65	3.92
4.35	0.64	3.45	5.17	2.86	0.64	3.94
4.32	0.68	3.71	6.00	2.74	0.62	3.64
4.32	0.70	3.61	6.00	2.79	0.65	3.82
4.33	0.68	3.63	5.97	2.74	0.68	3.74
4.34	0.68	3.66	5.90	2.78	0.64	3.81
4.33	0.68	3.62	5.72	2.79	0.67	3.83
4.27	0.69	3.52	5.83	2.68	0.65	3.77
4.28	0.66	3.65	5.77	2.73	0.67	3.72
4.38	0.67	3.81	6.46	2.80	0.65	3.64
4.31	0.67	3.88	6.49	2.77	0.62	3.56
4.34	0.66	3.66	5.79	2.79	0.64	3.83
4.37	0.70	3.72	6.15	2.76	0.65	3.70
4.33	0.67	3.76	6.14	2.76	0.65	3.67
4.28	0.70	3.80	6.46	2.70	0.61	3.63

4.34	0.69	3.75	6.31	2.78	0.65	3.64
4.27	0.66	3.82	6.53	2.74	0.66	3.64
4.32	0.68	3.81	6.47	2.76	0.65	3.56
4.33	0.69	3.83	6.59	2.79	0.64	3.61
4.36	0.64	3.95	6.96	2.78	0.64	3.51
4.31	0.65	4.06	7.14	2.78	0.59	3.45
4.33	0.56	4.09	7.41	2.82	0.57	3.35
4.34	0.64	3.91	6.96	2.80	0.65	3.56
4.33	0.65	3.94	6.87	2.76	0.64	3.48
4.31	0.62	3.98	7.19	2.79	0.63	3.44
4.33	0.47	4.20	7.85	2.78	0.48	3.21
4.37	0.41	4.33	8.18	2.83	0.40	3.18
4.40	0.54	4.23	7.69	2.85	0.52	3.38
4.37	0.52	4.20	7.79	2.82	0.50	3.31
4.38	0.40	4.33	7.91	2.81	0.41	3.17
4.36	0.39	4.32	8.14	2.79	0.39	3.13

Table 10-1 - Steel Ball (high velocity drop)

Ball1				Ball2		
VPre	VPost(x)	VPost(y)	Offset	VPre	VPost(x)	VPost(y)
3.48	0.03	2.95	0.77	2.79	0.05	3.58
2.94	0.02	2.41	0.65	2.34	0.03	3.19
3.08	0.08	3.17	0.92	2.34	0.08	3.34
2.85	0.06	2.45	0.96	2.33	0.10	3.15
2.95	0.05	2.26	1.47	2.14	0.08	3.05
2.45	0.11	2.33	1.37	2.20	0.04	3.04
2.98	0.16	2.27	2.09	2.22	0.15	2.84
2.94	0.14	2.32	2.35	2.01	0.16	2.97
3.12	0.13	2.53	1.86	2.30	0.15	3.21
3.08	0.22	2.53	2.74	2.34	0.15	3.16
3.10	0.21	2.52	2.21	2.22	0.15	3.13
3.08	0.20	2.52	2.70	2.28	0.19	3.12
3.08	0.18	2.41	2.22	2.13	0.18	3.10
3.17	0.17	2.48	3.04	2.31	0.24	3.13
3.38	0.10	2.91	2.28	2.73	0.10	3.31
3.14	0.18	2.41	2.68	2.20	0.18	3.03
3.13	0.19	2.44	3.15	2.28	0.10	2.66
3.16	0.26	2.65	3.79	2.38	0.14	2.75
3.11	0.27	2.56	4.15	2.25	0.06	2.54
3.12	0.27	2.65	4.16	2.28	0.33	3.06
3.13	0.28	2.67	4.77	2.22	0.28	2.93
3.11	0.34	2.84	5.85	2.26	0.21	2.64
3.11	0.33	2.65	5.00	2.25	0.21	2.71
3.10	0.35	2.68	5.15	2.20	0.27	2.77
2.99	0.40	2.71	6.05	2.15	0.21	2.50
3.06	0.33	2.65	5.74	2.14	0.34	2.73
3.01	0.32	2.60	5.49	2.08	0.33	2.73
2.95	0.37	2.80	6.74	2.10	0.21	2.40

3.17	0.33	2.86	5.96	2.32	0.02	2.46
3.08	0.24	3.06	7.82	2.19	0.17	2.43
3.07	0.33	2.89	6.81	2.25	0.33	2.74
3.13	0.32	2.97	7.05	2.29	0.24	2.63
3.10	0.32	3.02	7.03	2.39	0.32	2.66
3.30	0.32	3.25	7.68	2.46	0.25	2.75
3.18	0.31	3.11	7.55	2.37	0.28	2.67
3.07	0.12	3.19	8.26	2.25	0.17	2.55

Table 10-2 – Steel Ball (Intermediate velocity drop)

Ball1				Ball2		
VPre	VPost(x)	VPost(y)	Offset	VPre	VPost(x)	VPost(y)
3.07	0.09	3.07	7.93	2.69	0.16	2.79
3.09	0.17	3.08	7.57	2.70	0.12	2.85
3.05	0.15	3.03	7.71	2.62	0.15	2.79
2.97	0.17	3.01	7.15	2.50	0.16	2.82
2.97	0.21	2.92	6.90	2.50	0.14	2.83
2.90	0.20	2.80	6.35	2.42	0.17	2.80
2.99	0.18	2.94	6.42	2.55	0.16	2.94
3.03	0.19	2.95	6.23	2.63	0.18	2.93
3.05	0.19	2.94	6.14	2.58	0.19	2.91
2.93	0.16	2.83	7.23	2.43	0.18	2.80
2.85	0.18	2.74	5.90	2.42	0.23	2.80
2.93	0.17	2.86	5.44	2.50	0.15	2.89
3.03	0.21	2.90	5.53	2.58	0.16	2.99
2.99	0.14	2.90	4.99	2.57	0.18	3.00
2.98	0.10	2.90	4.91	2.52	0.16	3.03
2.95	0.22	2.78	4.85	2.47	0.18	2.91
2.91	0.13	2.84	4.45	2.47	0.18	2.95
2.91	0.11	2.81	4.16	2.49	0.14	2.96
2.86	0.15	2.70	4.09	2.38	0.13	2.88
2.92	0.13	2.75	3.65	2.46	0.14	2.96
3.01	0.14	2.79	3.67	2.54	0.11	2.97
2.94	0.12	2.77	3.44	2.47	0.10	2.96
2.90	0.13	2.72	3.33	2.43	0.10	2.98
2.91	0.14	2.71	2.91	2.45	0.08	2.97
2.90	0.10	2.65	3.02	2.44	0.03	2.77
2.95	0.09	2.68	2.48	2.49	0.10	2.94
2.99	0.10	2.70	2.21	2.53	0.05	2.97
2.90	0.09	2.71	2.19	2.47	0.09	3.03
2.91	0.05	2.73	1.83	2.44	0.07	2.99
2.91	0.05	2.74	1.87	2.42	0.07	3.02
2.94	0.06	2.75	1.58	2.46	0.04	3.04
2.87	0.07	2.66	1.28	2.45	0.04	3.00
2.91	0.08	2.67	1.03	2.48	0.12	2.99
2.90	0.04	2.72	0.97	2.48	0.02	3.01
2.95	0.04	2.71	0.84	2.53	0.04	3.02
2.79	0.00	2.88	0.04	2.34	0.00	2.43

Table 10-3 – Steel ball (low velocity drop)

Ball1				Ball2		
VPre	VPost(x)	VPost(y)	Offset	VPre	VPost(x)	VPost(y)
3.09	0.03	2.48	0.38	2.42	0.05	3.19
3.71	0.04	2.54	0.80	2.45	0.04	3.22
3.13	0.07	2.54	0.42	2.38	0.01	3.23
3.11	0.05	2.56	0.46	2.27	0.06	3.21
3.06	0.03	2.58	0.57	2.39	0.12	3.23
2.80	0.06	2.55	0.66	2.40	0.09	3.20
2.98	0.01	2.61	0.30	2.40	0.03	3.28
2.79	0.06	2.55	0.82	2.37	0.09	3.20
2.83	0.11	3.94	0.92	2.39	0.07	3.21
3.11	0.08	2.62	0.88	2.39	0.08	3.12
3.12	0.10	2.53	0.95	2.33	0.15	3.17
3.12	0.08	2.58	1.24	2.39	0.11	3.27
3.17	0.12	2.49	1.33	2.34	0.10	3.19
3.12	0.11	2.60	1.03	2.35	0.10	3.20
3.13	0.14	2.58	1.60	2.35	0.14	3.18
3.13	0.14	2.54	9.92	2.33	0.11	3.14
3.03	0.17	2.54	1.82	2.18	0.18	3.01
3.11	0.15	2.58	2.05	2.34	0.13	3.13
3.15	0.19	2.59	2.09	2.33	0.19	3.18
3.13	0.14	2.62	2.08	2.32	0.16	3.10
3.11	0.19	2.62	2.17	2.25	0.20	3.18
3.06	0.20	2.58	1.93	2.29	0.19	3.15
3.10	0.24	2.67	2.11	2.41	0.17	3.10
3.03	0.13	2.66	2.24	2.30	0.25	3.15
3.04	0.17	2.64	2.75	2.30	0.27	3.13
3.09	0.17	2.66	2.50	2.29	0.24	3.13
3.20	0.24	2.68	2.62	2.36	0.18	3.13
3.04	0.25	2.71	2.86	2.39	0.23	3.11
3.04	0.23	2.71	2.87	2.43	0.23	2.99
3.00	0.21	2.64	2.90	2.34	0.28	3.10
3.11	0.24	2.77	2.72	2.29	0.19	3.11
3.12	0.29	2.65	3.11	2.34	0.29	3.03
3.15	0.29	2.77	3.38	2.33	0.31	3.16
3.05	0.23	3.10	4.27	2.21	0.28	2.85
3.06	0.27	2.78	3.37	2.32	0.31	3.10
3.03	0.29	2.78	3.62	2.25	0.32	3.07
3.24	0.24	2.74	3.30	2.35	0.27	3.11
3.16	0.30	2.80	3.69	2.43	0.28	3.14
3.09	0.31	2.77	3.96	2.25	0.31	3.05
3.06	0.17	3.02	3.97	2.31	0.15	2.94
2.95	0.34	2.70	3.96	2.10	0.22	2.84
3.08	0.35	2.78	3.99	2.36	0.35	2.91
3.16	0.29	2.82	3.93	2.36	0.34	3.02
3.13	0.26	2.80	4.19	2.28	0.35	2.89

3.08	0.38	2.82	4.57	2.32	0.33	2.85
3.08	0.33	2.83	4.68	2.27	0.35	2.83
3.16	0.31	2.81	4.43	2.28	0.36	2.91
3.20	0.33	2.77	3.87	2.27	0.33	2.95
3.12	0.33	2.75	4.34	2.27	0.35	2.87
3.13	0.32	2.96	5.07	2.33	0.33	2.80
3.13	0.30	3.03	5.23	2.33	0.35	2.78
3.13	0.27	3.14	5.81	2.37	0.29	2.62
3.16	0.24	3.09	5.74	2.29	0.26	2.62
3.17	0.18	3.15	5.98	2.43	0.18	2.61
3.28	0.00	3.32	6.28	2.49	0.00	2.65

Table 10-4 – Ceramic balls (intermediate velocity drop)

Ball1				Ball2		
VPre	VPost(x)	VPost(y)	Offset	VPre	VPost(x)	VPost(y)
3.23	0.01	3.27	5.13	2.86	0.19	3.14
3.29	0.08	3.36	5.74	2.95	0.01	3.00
3.05	0.13	3.09	5.51	2.62	0.15	2.90
3.14	0.23	3.13	4.78	2.80	1.69	3.01
3.17	0.17	3.18	4.52	2.80	1.71	3.16
3.20	0.20	3.11	4.42	2.84	0.15	3.04
2.72	0.19	2.63	4.44	2.19	0.23	2.66
2.43	0.24	2.29	4.41	1.89	0.24	2.33
3.05	0.15	2.94	4.15	2.69	0.16	2.98
3.07	0.15	2.93	3.91	2.66	0.18	2.98
3.01	0.15	2.80	3.67	2.59	0.15	2.98
2.98	0.15	2.80	3.24	2.57	0.14	2.96
2.96	0.16	2.85	3.29	2.54	0.14	3.01
2.97	0.17	2.79	3.05	2.63	0.14	3.00
3.04	0.16	2.83	2.90	2.65	0.09	3.07
3.00	0.15	2.90	2.71	2.61	0.09	3.04
2.93	0.16	2.77	2.49	2.48	0.10	2.96
3.03	0.07	2.82	1.95	2.63	0.07	3.07
2.93	0.06	2.80	1.17	2.61	0.28	3.10
3.05	0.10	2.84	1.85	2.65	0.09	3.09
3.21	0.05	3.00	2.08	2.88	0.09	2.10
3.00	0.07	2.77	1.93	2.58	0.09	3.01
2.63	0.06	2.60	1.54	2.43	0.08	2.83
3.11	0.10	2.87	1.53	2.71	0.07	3.15
3.00	0.08	2.80	1.45	2.57	0.02	3.09
2.96	0.09	2.70	1.24	2.51	0.04	3.06
3.04	0.03	2.83	0.74	2.58	0.04	3.10
2.98	0.04	2.70	1.14	2.52	0.03	2.98
2.73	0.02	2.91	0.79	3.10	0.03	3.18

Table 10-5 – Ceramic Balls (Low velocity drop)

Ball1				Ball2		
VPre	VPost(x)	VPost(y)	Offset	VPre	VPost(x)	VPost(y)

4.04	0.03	2.71	1.00	2.04	0.06	3.94
3.93	0.12	2.66	2.51	2.04	0.07	3.95
4.04	0.10	2.33	3.01	2.04	0.12	3.97
4.11	0.14	2.78	3.64	2.04	0.17	4.03
4.04	0.22	2.55	4.00	2.04	0.23	3.96
4.04	0.26	2.52	4.55	2.04	0.32	3.76
4.44	0.30	2.57	5.02	2.04	0.35	3.75
4.04	0.32	2.57	5.55	2.04	0.42	3.72
4.04	0.59	2.47	5.98	2.04	0.42	3.75
3.87	0.44	2.58	8.28	2.04	0.48	3.68
4.04	0.39	2.65	8.72	2.04	0.47	3.77
3.99	0.48	2.68	9.12	1.96	0.55	3.74
4.04	0.52	2.66	9.04	2.04	0.55	3.69
4.04	0.55	2.72	6.52	2.04	0.52	3.74
4.23	0.51	2.83	11.33	2.10	0.64	3.65
3.61	0.50	2.72	8.15	1.87	0.65	3.56
4.30	0.59	2.78	10.27	2.07	0.69	3.55
4.02	0.62	2.79	12.21	2.01	0.73	3.48
4.03	0.60	2.92	7.43	2.05	0.74	3.55
4.31	0.67	2.85	11.01	2.07	0.69	3.55
4.16	0.67	3.13	10.75	2.14	0.80	3.51
4.04	0.75	3.02	11.34	2.03	0.75	3.20
4.04	0.75	3.09	12.58	2.14	0.74	3.33
4.04	0.76	3.04	14.12	2.27	0.83	3.32
4.04	0.80	3.04	12.67	1.88	0.83	3.11
4.04	0.78	3.46	12.33	1.80	0.86	3.19
4.04	0.86	3.36	14.79	1.89	0.76	2.94
4.03	0.72	3.38	14.17	1.90	0.83	2.91
3.83	0.71	3.58	16.80	2.10	0.74	2.79
4.06	0.67	3.69	16.58	2.08	0.69	2.78
4.07	0.66	3.83	16.55	2.01	0.68	2.66
3.94	0.57	3.89	17.66	2.25	0.65	2.71
3.88	0.36	4.14	18.57	2.07	0.33	2.39
4.15	0.00	4.11	20.24	2.18	0.00	2.28

Table 10-6 – Teflon Balls (High velocity drop)

Ball1				Ball2		
VPre	VPost(x)	VPost(y)	Offset	VPre	VPost(x)	VPost(y)
3.80	0.13	2.61	2.68	2.12	0.15	3.76
3.74	0.16	2.55	2.60	2.01	0.12	3.46
3.74	0.22	2.63	2.67	2.18	0.20	3.65
3.74	0.23	2.53	3.80	2.11	0.24	3.63
3.86	0.23	2.64	3.81	2.19	0.23	3.28
3.27	0.28	2.64	4.74	2.18	0.26	3.69
3.46	0.33	2.67	4.48	2.19	0.32	3.66
3.82	0.34	2.74	6.13	2.05	0.35	3.70
3.78	0.33	2.69	6.44	2.11	0.36	3.47
3.62	0.38	2.69	6.47	2.15	0.40	3.63

3.70	0.38	2.65	7.24	2.17	0.43	3.53
3.74	0.43	2.76	7.99	2.09	0.35	3.60
3.79	0.46	2.67	7.86	2.12	0.41	3.29
3.73	0.44	2.78	8.56	2.06	0.47	3.53
3.73	0.49	2.79	9.00	2.19	0.40	3.07
3.81	0.42	2.81	8.67	2.02	0.25	2.79
3.77	0.55	2.96	9.95	2.20	0.57	3.42
3.82	0.45	2.90	10.62	2.18	0.41	3.09
3.86	0.51	2.85	10.31	2.11	0.14	2.55
3.77	0.52	2.91	11.66	2.06	0.50	3.49
3.77	0.59	3.00	12.37	2.20	0.51	3.44
3.87	0.57	2.95	13.19	2.09	0.60	3.33
3.84	0.59	3.11	13.19	2.15	0.54	3.32
3.71	0.60	3.08	13.77	2.11	0.60	3.26
3.80	0.60	3.14	13.97	2.11	0.63	3.22
3.74	0.60	3.17	14.52	2.12	0.58	3.13
3.85	0.59	3.43	15.99	2.10	0.59	3.02
3.83	0.57	3.65	17.09	2.20	0.55	2.97
3.82	0.44	3.64	18.80	2.12	0.51	2.70
3.75	0.33	3.88	19.17	2.20	0.34	2.56

Table 10-7 - Teflon Balls (Intermediate velocity drop)

Appendix G

Material interaction property data

Stick region	
Slip region	

ψ_1	ψ_2	e	μ	β
0.06	-0.04	0.03	0.03	0.58
0.14	-0.24	0.90	0.06	1.64
0.08	-0.13	0.79	0.03	1.65
0.07	0.16	0.56	0.02	-2.19
0.09	-0.06	0.69	0.03	0.61
0.07	-0.12	0.87	0.03	1.70
0.06	-0.05	0.72	0.02	0.81
0.12	0.03	0.76	0.01	-0.24
0.10	0.07	0.78	0.00	-0.72
0.10	-0.09	0.82	0.03	0.91
0.10	0.08	0.84	0.00	-0.78
0.10	0.10	0.83	0.00	-1.02
0.08	0.26	0.71	0.03	-3.16
0.13	-0.03	0.82	0.03	0.19
0.12	0.01	0.77	0.02	-0.06

0.18	-0.10	0.85	0.04	0.57
0.16	0.10	0.81	0.01	-0.65
0.13	0.17	0.85	0.01	-1.28
0.18	-0.10	0.85	0.04	0.57
0.16	0.10	0.81	0.01	-0.65
0.13	0.17	0.85	0.01	-1.28
0.19	-0.19	1.03	0.05	1.03
0.15	0.10	0.82	0.01	-0.62
0.13	0.23	0.74	0.02	-1.73
0.15	0.22	0.75	0.01	-1.44
0.14	0.01	0.75	0.02	-0.07
0.17	0.03	0.76	0.02	-0.17
0.16	0.25	0.68	0.02	-1.56
0.18	0.05	0.77	0.02	-0.30
0.21	-0.07	0.75	0.05	0.35
0.17	0.11	0.78	0.01	-0.66
0.21	-0.15	0.73	0.06	0.72
0.14	0.40	0.61	0.04	-2.73
0.25	-0.13	0.76	0.06	0.51
0.24	0.07	0.77	0.03	-0.31
0.26	-0.21	0.77	0.08	0.81
0.23	0.10	0.75	0.02	-0.44
0.28	0.02	0.69	0.04	-0.06
0.27	-0.08	0.71	0.06	0.30
0.27	0.07	0.73	0.03	-0.26
0.29	0.12	0.70	0.03	-0.43
0.26	0.03	0.64	0.04	-0.11
0.34	0.07	0.61	0.05	-0.21
0.33	0.04	0.81	0.04	-0.14
0.28	0.16	0.75	0.02	-0.57
0.33	-0.05	0.56	0.07	0.15
0.32	-0.11	0.67	0.07	0.36
0.30	0.11	0.69	0.03	-0.36
0.34	0.26	0.70	0.01	-0.78
0.34	0.13	0.76	0.03	-0.39
0.33	0.17	0.65	0.03	-0.52
0.28	0.59	0.53	0.06	-2.11
0.37	0.33	0.67	0.01	-0.89
0.36	0.11	0.63	0.04	-0.32
0.36	0.07	0.66	0.05	-0.20
0.35	0.27	0.67	0.01	-0.79
0.39	0.25	0.72	0.02	-0.64
0.42	0.13	0.68	0.05	-0.32
0.42	0.24	0.66	0.03	-0.57
0.40	0.08	0.78	0.05	-0.19
0.40	0.29	0.65	0.02	-0.72
0.44	0.04	0.86	0.06	-0.10
0.42	0.05	0.67	0.06	-0.13

0.44	0.13	0.70	0.05	-0.30
0.43	0.17	0.60	0.05	-0.40
0.43	0.20	0.67	0.04	-0.46
0.53	0.30	0.70	0.04	-0.56
0.52	-0.06	0.77	0.09	0.12
0.45	0.08	0.67	0.06	-0.17
0.47	0.23	0.62	0.04	-0.48
0.48	0.18	0.70	0.05	-0.37
0.51	0.12	0.76	0.06	-0.25
0.49	0.36	0.72	0.02	-0.73
0.47	0.36	0.73	0.02	-0.77
0.54	0.18	0.72	0.06	-0.34
0.54	0.17	0.78	0.06	-0.32
0.52	0.40	0.71	0.02	-0.76
0.60	0.21	0.65	0.07	-0.34
0.57	0.36	0.71	0.03	-0.64
0.55	0.33	0.67	0.04	-0.59
0.57	0.17	0.70	0.07	-0.30
0.59	0.35	0.73	0.04	-0.59
0.54	0.48	0.65	0.01	-0.89
0.56	0.51	0.70	0.01	-0.90
0.58	0.49	0.78	0.01	-0.85
0.65	0.39	0.68	0.04	-0.60
0.63	0.12	0.81	0.08	-0.18
0.69	0.62	0.71	0.01	-0.91
0.70	0.54	0.79	0.03	-0.77
0.72	0.50	0.74	0.04	-0.69
0.67	0.37	0.71	0.05	-0.56
0.78	0.60	0.82	0.03	-0.77
0.71	0.45	0.83	0.04	-0.63
0.73	0.36	0.75	0.06	-0.50
0.64	0.43	0.73	0.03	-0.67
0.65	0.36	0.73	0.05	-0.56
0.62	0.42	0.72	0.03	-0.67
0.75	0.80	0.75	0.01	-1.07
0.82	0.54	0.80	0.04	-0.66
0.76	0.36	0.68	0.07	-0.48
0.83	0.56	0.78	0.04	-0.68
0.82	0.52	0.80	0.05	-0.64
0.82	0.38	0.92	0.06	-0.47
1.09	1.16	0.71	0.01	-1.06
1.09	0.79	0.92	0.04	-0.73
1.08	0.76	0.80	0.05	-0.70
1.05	0.87	0.78	0.03	-0.83
0.98	0.90	0.80	0.01	-0.91
1.02	0.68	0.84	0.05	-0.67
1.00	1.17	0.66	0.03	-1.17
1.30	1.01	0.83	0.05	-0.78

1.31	1.81	0.70	0.08	-1.38
1.01	0.87	0.74	0.02	-0.86
1.15	0.92	0.81	0.04	-0.80
1.15	1.23	0.69	0.01	-1.08
1.30	1.64	0.75	0.06	-1.26
1.22	1.08	0.85	0.02	-0.88
1.34	1.63	0.74	0.05	-1.22
1.31	1.35	0.79	0.01	-1.03
1.38	1.33	0.88	0.01	-0.97
1.65	1.48	0.86	0.03	-0.90
1.82	2.63	0.87	0.12	-1.44
2.19	2.33	0.93	0.02	-1.07
1.65	1.31	0.92	0.05	-0.80
1.57	1.72	0.80	0.02	-1.09
1.88	1.86	0.97	0.00	-0.99
3.56	3.76	1.34	0.02	-1.05
2.34	3.78	0.95	0.12	-0.83
2.86	3.16	1.20	0.04	-1.10
3.25	3.08	1.38	0.02	-0.95
4.04	4.90	1.13	0.12	-1.21
20.42	17.74	9.25	0.07	-0.87

Table 10-8 – Calculated parameters steel (high height)

ψ_1	ψ_2	e	μ	β
0.10	-0.09	0.55	0.03	0.92
0.08	-0.16	0.77	0.04	1.97
0.11	0.98	-1.21	-1.19	-8.61
0.12	0.23	0.58	0.02	-1.92
0.18	-0.46	0.73	0.11	2.53
0.21	0.01	0.09	0.66	-15.80
0.27	0.03	0.99	0.03	-0.13
0.30	-0.05	0.42	0.07	0.15
0.24	0.17	0.51	0.01	-0.73
0.36	0.55	0.69	0.03	-1.54
0.28	0.66	0.44	0.08	-2.35
0.35	0.40	0.59	0.01	-1.15
0.28	0.22	0.53	0.01	-0.77
0.40	-0.44	0.78	0.14	1.10
0.29	-0.10	0.53	0.07	0.35
0.35	-0.18	0.70	0.09	0.50
0.42	-0.36	0.82	0.12	0.87
0.52	0.47	0.66	0.01	-0.90
0.59	0.17	0.65	0.07	-0.29
0.59	0.53	0.51	0.01	-0.89
0.72	0.32	0.47	0.08	-0.45
1.03	1.56	0.46	0.10	-1.51
0.78	0.57	0.68	0.04	-0.73
0.82	0.90	0.57	0.02	-1.11

1.11	1.88	0.71	0.13	-1.70
0.99	0.47	0.60	0.09	-0.47
0.91	0.54	0.50	0.07	-0.59
1.47	2.61	0.65	0.20	-1.77
1.07	1.02	0.56	0.01	-0.95
3.42	4.98	0.90	0.23	-1.46
1.52	1.96	0.64	0.08	-1.29
1.73	2.12	0.70	0.07	-1.23
1.71	3.64	0.72	0.32	-2.14
2.82	4.53	1.29	0.21	-1.61
2.46	3.50	1.05	0.14	-1.42
0.00	0.49	-1.31	1.04	-2.14

Table 10-9 – Calculated parameters steel (intermediate height)

ψ_1	ψ_2	e	μ	β
4.17	6.14	1.06	0.27	-1.47
2.50	5.33	1.20	0.37	-2.13
1.89	5.30	1.08	0.23	-1.57
1.82	5.46	0.16	0.89	-2.99
1.59	3.63	0.68	0.35	-2.29
1.24	2.38	0.46	0.22	-1.91
1.28	3.10	0.29	0.41	-2.43
1.18	2.68	0.50	0.29	-2.26
1.15	2.05	0.38	0.19	-1.79
1.11	2.57	0.60	0.10	-0.71
1.05	2.25	0.34	0.25	-2.14
0.90	2.64	0.03	0.48	-2.94
0.92	2.38	0.46	0.28	-2.57
0.77	1.95	-0.02	0.34	-2.52
0.75	1.29	-0.32	0.23	-1.71
0.74	1.94	0.41	0.24	-2.61
0.65	2.03	-0.31	0.57	-3.12
0.59	1.53	-0.21	0.34	-2.58
0.58	1.32	0.06	0.20	-2.28
0.50	1.20	0.02	0.20	-2.41
0.50	1.00	0.23	0.11	-1.97
0.47	1.06	-0.02	0.17	-2.27
0.45	1.11	0.01	0.19	-2.48
0.38	1.32	0.07	0.25	-3.46
0.40	0.49	0.26	0.02	-1.24
0.32	0.34	0.30	0.01	-1.07
0.28	0.63	0.40	0.07	-2.25
0.28	0.80	0.00	0.15	-2.89
0.23	0.42	-0.19	0.07	-1.84
0.24	0.33	-0.27	0.04	-1.42
0.20	0.56	-0.12	0.12	-2.81
0.16	0.77	0.04	0.17	-4.80

0.13	0.88	0.15	0.19	-6.87
0.12	0.42	-0.12	0.10	-3.53
0.10	0.42	0.13	0.08	-4.00
0.01	0.01	-1.39	-0.01	-2.36

Table 10-10 – Calculated parameters steel (low height)

ψ_1	ψ_2	e	μ	β
0.06	0.01	0.82	0.01	-0.17
0.13	-0.49	0.86	0.09	3.83
0.07	0.32	0.57	0.05	-4.85
0.07	0.14	0.33	0.01	-1.87
0.09	0.00	0.43	0.02	0.04
0.11	0.77	0.27	0.15	-7.28
0.05	0.01	0.27	0.01	-0.29
0.13	0.58	0.18	0.11	-4.41
0.15		0.34	-0.25	-30.67
0.14	0.23	0.39	0.02	-1.63
0.15	0.21	0.52	0.01	-1.39
0.20	-0.05	0.51	0.05	0.26
0.22	-0.02	0.70	0.04	0.09
0.17	0.42	0.41	0.05	-2.53
0.26	0.22	0.50	0.01	-0.83
0.28	0.34	0.47	0.38	15.05
0.30	0.46	0.28	0.04	-1.54
0.34	0.05	0.53	0.06	-0.13
0.35	0.33	0.52	0.00	-0.94
0.35	0.00	0.37	0.07	0.00
0.37	0.43	0.29	0.01	-1.17
0.32	0.77	0.42	0.09	-2.40
0.36	1.28	0.49	0.18	-3.59
0.38	0.30	0.16	0.02	-0.78
0.49	0.28	0.31	0.04	-0.58
0.43	0.26	0.27	0.04	-0.60
0.46	0.52	0.49	0.01	-1.14
0.51	1.32	0.42	0.16	-2.59
0.51	1.18	0.48	0.13	-2.31
0.52	0.73	0.42	0.04	-1.41
0.48	1.11	0.12	0.16	-2.33
0.57	0.76	0.62	0.03	-1.34
0.63	1.06	0.38	0.09	-1.67
0.92	3.21	-0.61	1.68	-3.49
0.63	1.57	0.23	0.22	-2.48
0.70	1.77	0.14	0.27	-2.52
0.61	0.11	0.46	0.10	-0.18
0.72	1.14	0.57	0.08	-1.57
0.81	1.24	0.34	0.09	-1.53
0.81	2.08	-0.50	0.73	-2.57

0.81	1.95	0.25	0.26	-2.41
0.82	1.81	0.60	0.18	-2.22
0.80	0.92	0.42	0.02	-1.15
0.89	0.61	0.31	0.06	-0.68
1.05	1.99	0.73	0.15	-1.89
1.11	1.59	0.52	0.09	-1.43
0.99	0.71	0.49	0.05	-0.72
0.78	0.72	0.47	0.01	-0.93
0.95	0.80	0.61	0.03	-0.84
1.35	2.23	0.50	0.17	-1.64
1.49	2.78	0.35	0.27	-1.86
2.38	5.13	0.70	0.46	-2.15
2.21	2.94	0.40	0.15	-1.33
3.01	4.38	0.52	0.26	-1.46

Table 10-11 – Calculated parameters ceramic (intermediate height)

ψ_1	ψ_2	e	μ	β
1.40	2.79	-1.13	-3.16	-1.98
2.22	7.27	-0.42	2.47	-3.27
1.80	4.94	-0.10	1.00	-2.74
1.17	5.42	0.59	0.77	-4.65
1.03	4.41	-0.07	1.04	-4.28
0.98	3.14	0.58	0.39	-3.19
0.99	2.27	0.06	0.34	-2.29
0.98	2.36	0.40	0.28	-2.41
0.88	1.89	0.31	0.22	-2.15
0.79	1.49	0.30	0.15	-1.89
0.72	0.79	0.51	0.01	-1.10
0.60	1.31	0.31	0.16	-2.19
0.61	2.25	-0.03	0.48	-3.68
0.55	2.05	0.60	0.27	-3.71
0.52	1.36	0.50	0.16	-2.62
0.48	2.29	-0.09	0.57	-4.81
0.43	1.86	0.02	0.40	-4.34
0.33	0.33	0.15	0.00	-1.03
0.19	0.89	-0.15	0.24	-4.71
0.31	0.92	0.22	0.14	-2.98
0.35	-0.07	0.38	0.09	0.19
0.32	0.31	0.24	0.00	-0.96
0.25	2.19	-0.55	1.24	-8.68
0.25	0.92	0.29	0.15	-3.66
0.24	0.78	0.00	0.15	-3.28
0.20	0.71	0.24	0.12	-3.53
0.12	0.12	-0.05	0.00	-0.99
0.18	0.03	0.23	0.04	-0.14
0.13	-0.60	-0.05	-0.22	4.72

Table 10-12 – Calculated parameters ceramic (low height)

ψ_1	ψ_2	e	μ	β
0.05	-0.08	0.34	0.03	1.57
0.13	-0.08	0.40	0.04	0.57
0.16	-0.45	0.73	0.10	2.79
0.20	-0.19	0.29	0.09	1.00
0.22	-0.12	0.54	0.06	0.57
0.25	-0.16	0.58	0.07	0.66
0.27	-0.08	0.56	0.06	0.28
0.31	-0.14	0.57	0.08	0.47
0.33	0.58	0.77	0.04	-1.75
0.48	-0.44	0.67	0.16	0.91
0.52	-0.64	0.59	0.21	1.24
0.55	-0.26	0.56	0.15	0.48
0.54	-0.25	0.67	0.13	0.46
0.37	0.61	0.52	0.05	-1.66
0.74	-1.01	0.67	0.30	1.36
0.48	0.78	0.30	0.07	-1.65
0.64	-0.56	0.71	0.20	0.87
0.84	-0.59	0.74	0.23	0.70
0.43	0.87	0.38	0.09	-2.04
0.71	-0.43	0.73	0.19	0.60
0.69	0.55	0.47	0.03	-0.80
0.74	0.71	0.57	0.01	-0.96
0.88	0.57	0.69	0.05	-0.65
1.11	-0.28	1.10	0.19	0.25
0.89	0.62	0.59	0.05	-0.69
0.85	1.76	0.11	0.23	-2.07
1.24	1.29	0.63	0.01	-1.04
1.12	1.11	0.37	0.00	-0.99
1.89	2.84	0.84	0.15	-1.50
1.79	1.82	0.58	0.01	-1.02
1.77	2.58	0.36	0.17	-1.45
2.52	4.44	0.74	0.31	-1.76
4.64	10.83	0.53	1.15	-2.34

Table 10-13 – Calculated parameters Teflon (high height)

ψ_1	ψ_2	e	μ	β
0.14	-0.04	0.43	0.04	0.26
0.14	0.11	0.41	0.01	-0.77
0.14	0.43	0.47	0.06	-3.04
0.20	0.14	0.54	0.01	-0.68
0.20	0.13	0.52	0.01	-0.65
0.26	1.01	0.29	0.17	-3.93
0.24	1.02	0.38	0.16	-4.21

0.34	0.23	0.35	0.02	-0.68
0.36	0.09	0.45	0.05	-0.25
0.36	0.56	0.45	0.04	-1.55
0.41	0.16	0.57	0.05	-0.38
0.46	0.36	0.42	0.02	-0.78
0.45	0.25	0.59	0.04	-0.56
0.50	0.33	0.39	0.04	-0.65
0.54	0.46	0.56	0.01	-0.85
0.51	0.13	0.35	0.08	-0.25
0.62	0.84	0.47	0.04	-1.37
0.67	-0.04	0.50	0.14	0.06
0.65	0.06	0.52	0.11	-0.10
0.78	0.19	0.48	0.11	-0.24
0.86	0.55	0.62	0.05	-0.64
0.97	-0.29	0.66	0.22	0.30
0.97	0.50	0.54	0.09	-0.51
1.05	0.79	0.57	0.05	-0.75
1.08	0.62	0.56	0.09	-0.57
1.18	0.85	0.59	0.06	-0.72
1.56	1.33	0.52	0.04	-0.85
2.06	2.87	0.66	0.14	-1.39
6.80	3.55	2.71	0.25	-0.52

Table 10-14 – Calculated parameters Teflon (intermediate height)

Appendix H

Error propagation data

$\pm\psi_1$	$\pm\psi_2$	$\pm e$	$\pm\mu$	$\pm\beta$
0.004	0.008	0.006	0.003	0.122
0.010	0.052	0.193	0.007	0.361
0.005	0.030	0.174	0.004	0.371
0.005	0.039	0.132	0.002	0.528
0.006	0.012	0.145	0.003	0.130
0.005	0.026	0.186	0.004	0.373
0.004	0.011	0.152	0.002	0.177
0.008	0.006	0.161	0.002	0.052
0.007	0.017	0.169	0.001	0.160
0.007	0.021	0.175	0.004	0.198
0.006	0.017	0.182	0.000	0.173
0.006	0.021	0.175	0.000	0.220
0.006	0.073	0.196	0.004	0.886
0.009	0.006	0.177	0.003	0.043
0.008	0.002	0.165	0.002	0.014
0.012	0.021	0.177	0.005	0.122
0.011	0.023	0.176	0.001	0.145

0.009	0.037	0.182	0.001	0.281
0.012	0.021	0.177	0.005	0.122
0.011	0.023	0.176	0.001	0.145
0.009	0.037	0.182	0.001	0.281
0.013	0.046	0.241	0.006	0.245
0.010	0.021	0.177	0.001	0.138
0.009	0.049	0.156	0.002	0.373
0.010	0.048	0.162	0.001	0.318
0.010	0.002	0.160	0.003	0.014
0.012	0.006	0.161	0.003	0.036
0.011	0.055	0.145	0.002	0.342
0.012	0.012	0.166	0.002	0.066
0.014	0.016	0.159	0.005	0.076
0.011	0.025	0.171	0.001	0.149
0.014	0.032	0.152	0.007	0.154
0.010	0.083	0.124	0.005	0.571
0.017	0.026	0.155	0.007	0.107
0.016	0.016	0.162	0.003	0.068
0.018	0.046	0.162	0.009	0.174
0.016	0.022	0.157	0.003	0.094
0.019	0.004	0.147	0.005	0.013
0.018	0.017	0.150	0.007	0.065
0.018	0.015	0.152	0.004	0.056
0.020	0.027	0.147	0.003	0.091
0.018	0.006	0.132	0.005	0.023
0.023	0.015	0.127	0.005	0.045
0.022	0.010	0.171	0.005	0.030
0.019	0.035	0.160	0.002	0.126
0.022	0.010	0.112	0.008	0.031
0.022	0.024	0.138	0.009	0.076
0.020	0.023	0.143	0.004	0.077
0.023	0.058	0.150	0.001	0.171
0.023	0.028	0.160	0.004	0.083
0.022	0.037	0.135	0.003	0.111
0.019	0.124	0.109	0.007	0.441
0.026	0.072	0.140	0.001	0.192
0.024	0.025	0.133	0.005	0.069
0.024	0.015	0.142	0.006	0.043
0.024	0.059	0.141	0.001	0.169
0.027	0.055	0.153	0.003	0.139
0.028	0.028	0.141	0.005	0.069
0.029	0.051	0.140	0.004	0.122
0.027	0.016	0.160	0.006	0.041
0.028	0.062	0.136	0.002	0.155
0.030	0.009	0.181	0.007	0.021
0.029	0.011	0.133	0.007	0.026
0.030	0.028	0.146	0.006	0.065
0.030	0.037	0.125	0.005	0.085

0.030	0.043	0.141	0.005	0.100
0.036	0.064	0.147	0.004	0.121
0.036	0.013	0.159	0.011	0.024
0.031	0.017	0.141	0.007	0.037
0.032	0.048	0.129	0.005	0.102
0.033	0.037	0.145	0.006	0.079
0.035	0.027	0.158	0.007	0.053
0.034	0.075	0.147	0.002	0.153
0.032	0.077	0.152	0.002	0.165
0.037	0.039	0.151	0.007	0.073
0.037	0.037	0.164	0.007	0.069
0.036	0.084	0.146	0.002	0.161
0.042	0.044	0.134	0.008	0.072
0.039	0.078	0.147	0.004	0.137
0.038	0.069	0.138	0.004	0.125
0.039	0.037	0.146	0.007	0.065
0.040	0.075	0.155	0.004	0.129
0.037	0.101	0.133	0.001	0.187
0.039	0.107	0.144	0.001	0.190
0.040	0.109	0.168	0.002	0.188
0.045	0.082	0.138	0.005	0.127
0.044	0.025	0.168	0.009	0.039
0.048	0.133	0.146	0.001	0.193
0.048	0.114	0.164	0.003	0.163
0.050	0.105	0.152	0.004	0.145
0.046	0.079	0.145	0.005	0.118
0.055	0.129	0.171	0.003	0.164
0.049	0.096	0.173	0.004	0.134
0.051	0.077	0.154	0.006	0.105
0.044	0.092	0.153	0.004	0.144
0.045	0.076	0.149	0.005	0.117
0.043	0.089	0.150	0.004	0.143
0.052	0.170	0.155	0.001	0.228
0.057	0.115	0.163	0.005	0.140
0.052	0.076	0.140	0.007	0.100
0.058	0.120	0.161	0.004	0.145
0.057	0.111	0.166	0.005	0.135
0.057	0.085	0.197	0.007	0.103
0.076	0.241	0.143	0.001	0.221
0.076	0.169	0.190	0.004	0.156
0.075	0.158	0.161	0.005	0.146
0.074	0.184	0.159	0.003	0.175
0.069	0.191	0.165	0.001	0.194
0.072	0.143	0.171	0.005	0.140
0.070	0.248	0.135	0.003	0.247
0.091	0.210	0.167	0.004	0.162
0.093	0.382	0.143	0.008	0.291
0.071	0.183	0.152	0.002	0.182

0.081	0.190	0.162	0.004	0.165
0.081	0.258	0.140	0.001	0.225
0.092	0.339	0.152	0.005	0.261
0.086	0.227	0.173	0.002	0.186
0.094	0.344	0.151	0.005	0.257
0.092	0.282	0.160	0.001	0.216
0.097	0.281	0.181	0.001	0.204
0.116	0.307	0.172	0.002	0.186
0.129	0.552	0.178	0.012	0.303
0.155	0.495	0.192	0.002	0.227
0.116	0.276	0.189	0.005	0.168
0.111	0.358	0.161	0.002	0.228
0.133	0.394	0.199	0.000	0.210
0.254	0.783	0.271	0.002	0.220
0.000	0.173	-0.193	0.011	0.173
0.203	0.660	0.243	0.004	0.231
0.231	0.642	0.279	0.002	0.198
0.288	1.012	0.226	0.011	0.251
1.458	3.664	1.853	0.007	0.179

Table 10-15 – Calculated error Steel (high height)

$\pm\psi_1$	$\pm\psi_2$	$\pm e$	$\pm\mu$	$\pm\beta$
0.006	0.038	0.238	0.005	0.404
0.005	0.077	0.374	0.006	0.961
0.008	0.388	0.477	-0.161	3.424
0.008	0.126	0.322	0.003	1.064
0.012	0.176	0.275	0.019	0.963
0.011	2.953	0.093	0.115	17.321
0.018	0.014	0.399	0.006	0.051
0.020	0.016	0.140	0.012	0.051
0.016	0.064	0.189	0.002	0.271
0.024	0.226	0.281	0.005	0.633
0.019	0.235	0.156	0.012	0.833
0.024	0.155	0.224	0.002	0.442
0.019	0.074	0.178	0.002	0.260
0.027	0.161	0.283	0.022	0.402
0.020	0.047	0.244	0.010	0.161
0.024	0.060	0.238	0.015	0.172
0.029	0.134	0.299	0.020	0.319
0.036	0.183	0.254	0.001	0.349
0.041	0.062	0.235	0.012	0.104
0.041	0.193	0.186	0.002	0.326
0.050	0.111	0.160	0.012	0.153
0.072	0.562	0.165	0.015	0.545
0.054	0.206	0.243	0.006	0.264
0.057	0.313	0.196	0.002	0.384
0.078	0.686	0.257	0.020	0.618

0.069	0.159	0.200	0.014	0.160
0.064	0.184	0.168	0.011	0.202
0.104	0.935	0.229	0.030	0.634
0.075	0.369	0.200	0.001	0.344
0.244	1.719	0.307	0.033	0.502
0.108	0.720	0.234	0.011	0.473
0.122	0.767	0.253	0.009	0.444
0.121	1.517	0.299	0.045	0.889
0.201	1.656	0.468	0.028	0.587
0.175	1.303	0.387	0.020	0.529
0.000	0.179	0.480	0.141	0.790

Table 10-16 – Calculated error Steel (intermediate height)

$\pm\psi_1$	$\pm\psi_2$	$\pm e$	$\pm\mu$	$\pm\beta$
0.297	4.444	0.766	0.037	1.066
0.177	3.794	0.851	0.049	1.519
0.208	2.979	0.698	0.031	1.019
0.129	3.212	0.095	0.123	1.761
0.112	2.152	0.402	0.049	1.354
0.087	1.368	0.264	0.032	1.103
0.090	1.932	0.178	0.056	1.511
0.083	1.820	0.337	0.040	1.538
0.081	1.219	0.225	0.026	1.064
0.136	0.755	0.329	0.014	0.392
0.074	1.427	0.217	0.037	1.357
0.063	1.657	0.018	0.069	1.845
0.065	1.481	0.286	0.040	1.602
0.054	1.281	0.012	0.048	1.653
0.052	0.767	0.190	0.032	1.017
0.051	1.111	0.233	0.035	1.500
0.045	1.268	0.192	0.081	1.948
0.041	0.997	0.139	0.049	1.676
0.040	0.757	0.033	0.030	1.304
0.034	0.720	0.013	0.029	1.439
0.035	0.582	0.133	0.017	1.155
0.032	0.627	0.012	0.025	1.346
0.031	0.649	0.006	0.028	1.450
0.026	0.793	0.040	0.037	2.072
0.027	0.299	0.157	0.003	0.749
0.022	0.208	0.178	0.001	0.650
0.019	0.383	0.241	0.011	1.361
0.019	0.507	0.001	0.022	1.818
0.016	0.243	0.108	0.010	1.058
0.016	0.187	0.152	0.006	0.796
0.013	0.319	0.071	0.017	1.611
0.011	0.501	0.029	0.025	3.149
0.009	0.550	0.092	0.028	4.302

0.008	0.276	0.076	0.014	2.308
0.007	0.273	0.087	0.012	2.621

Table 10-17 – Calculated error Steel (low height)

$\pm\psi_1$	$\pm\psi_2$	$\pm e$	$\pm\mu$	$\pm\beta$
0.005	0.004	0.307	0.001	0.065
0.010	0.121	0.208	0.013	0.948
0.005	0.111	0.193	0.006	1.668
0.006	0.043	0.102	0.002	0.589
0.007	0.001	0.158	0.002	0.014
0.008	0.450	0.155	0.020	4.272
0.004	0.006	0.113	0.001	0.120
0.010	0.323	0.101	0.015	2.453
0.012	2.434	3.215	0.033	16.476
0.011	0.081	0.137	0.002	0.574
0.012	0.070	0.170	0.001	0.459
0.016	0.019	0.178	0.006	0.092
0.017	0.006	0.221	0.005	0.028
0.013	0.141	0.136	0.007	0.854
0.022	0.073	0.164	0.001	0.279
0.000	1.049	0.153	0.051	4.934
0.025	0.145	0.085	0.005	0.481
0.029	0.015	0.175	0.007	0.045
0.030	0.107	0.165	0.001	0.304
0.029	0.000	0.119	0.010	0.001
0.031	0.134	0.087	0.002	0.366
0.027	0.262	0.139	0.012	0.812
0.030	0.467	0.177	0.023	1.316
0.032	0.103	0.054	0.003	0.272
0.042	0.098	0.107	0.006	0.201
0.037	0.086	0.087	0.005	0.199
0.039	0.165	0.153	0.002	0.360
0.044	0.509	0.160	0.021	0.999
0.044	0.478	0.193	0.017	0.936
0.045	0.277	0.157	0.006	0.535
0.041	0.355	0.038	0.021	0.743
0.050	0.256	0.205	0.005	0.451
0.056	0.341	0.119	0.011	0.538
0.085	1.005	0.187	0.198	1.092
0.056	0.547	0.077	0.028	0.865
0.063	0.589	0.046	0.034	0.839
0.054	0.035	0.137	0.013	0.056
0.065	0.401	0.196	0.010	0.555
0.074	0.391	0.104	0.012	0.484
0.074	0.710	0.169	0.087	0.876
0.074	0.610	0.077	0.034	0.754
0.075	0.644	0.211	0.023	0.788

0.073	0.302	0.134	0.003	0.378
0.082	0.191	0.094	0.008	0.214
0.099	0.679	0.244	0.020	0.644
0.104	0.516	0.164	0.011	0.466
0.092	0.219	0.146	0.007	0.221
0.071	0.215	0.138	0.001	0.276
0.088	0.253	0.187	0.003	0.266
0.129	0.736	0.162	0.020	0.544
0.144	0.912	0.113	0.033	0.611
0.234	1.755	0.235	0.054	0.736
0.217	0.917	0.121	0.018	0.415
0.297	1.543	0.179	0.030	0.513

Table 10-18 – Calculated error Ceramic (intermediate height)

$\pm\psi_1$	$\pm\psi_2$	$\pm e$	$\pm\mu$	$\pm\beta$
0.134	1.813	0.728	0.351	1.291
0.218	5.177	0.295	0.269	2.332
0.175	2.721	0.056	0.117	1.509
0.110	3.719	0.401	0.094	3.191
0.096	2.883	0.045	0.126	2.797
0.091	2.083	0.385	0.045	2.118
0.092	1.032	0.028	0.046	1.040
0.091	1.040	0.176	0.042	1.059
0.081	1.230	0.204	0.027	1.403
0.072	0.872	0.175	0.019	1.102
0.065	0.444	0.285	0.002	0.620
0.053	0.752	0.175	0.020	1.255
0.054	1.274	0.017	0.060	2.084
0.048	1.417	0.410	0.034	2.564
0.045	0.820	0.298	0.020	1.581
0.041	1.377	0.055	0.070	2.895
0.037	0.980	0.009	0.051	2.283
0.027	0.196	0.087	0.000	0.602
0.015	0.647	0.111	0.030	3.420
0.026	0.541	0.126	0.018	1.758
0.029	0.047	0.277	0.010	0.135
0.027	0.175	0.133	0.000	0.543
0.021	2.469	0.624	0.165	9.794
0.021	0.546	0.172	0.018	2.175
0.019	0.428	0.001	0.019	1.808
0.016	0.372	0.124	0.015	1.854
0.009	0.061	0.026	0.000	0.510
0.015	0.013	0.120	0.005	0.070
0.010	0.382	0.030	0.026	3.017

Table 10-19 – Calculated error Ceramic (low height)

$\pm\psi_1$	$\pm\psi_2$	$\pm e$	$\pm\mu$	$\pm\beta$
0.011	0.048	0.187	0.011	0.906
0.028	0.045	0.228	0.017	0.337
0.034	0.276	0.435	0.045	1.722
0.041	0.110	0.158	0.033	0.562
0.045	0.073	0.307	0.026	0.339
0.052	0.097	0.335	0.031	0.394
0.058	0.043	0.299	0.026	0.158
0.065	0.084	0.327	0.033	0.275
0.070	0.345	0.440	0.017	1.039
0.103	0.266	0.397	0.063	0.550
0.110	0.372	0.330	0.082	0.719
0.116	0.152	0.310	0.058	0.278
0.115	0.143	0.375	0.053	0.265
0.077	0.347	0.289	0.017	0.950
0.158	0.561	0.359	0.111	0.755
0.101	0.477	0.178	0.026	1.005
0.137	0.307	0.374	0.076	0.479
0.179	0.335	0.406	0.088	0.399
0.090	0.487	0.203	0.033	1.145
0.151	0.231	0.379	0.069	0.324
0.146	0.300	0.246	0.009	0.437
0.158	0.394	0.303	0.002	0.530
0.188	0.322	0.373	0.018	0.364
0.237	0.161	0.616	0.066	0.145
0.191	0.332	0.306	0.017	0.372
0.182	0.900	0.055	0.074	1.056
0.265	0.677	0.316	0.003	0.547
0.239	0.582	0.186	0.001	0.520
0.406	1.612	0.458	0.047	0.851
0.383	0.968	0.298	0.002	0.541
0.380	1.340	0.181	0.051	0.755
0.541	2.519	0.405	0.095	0.999
0.997	5.936	0.281	0.344	1.279

Table 10-20 – Calculated error Teflon (high height)

$\pm\psi_1$	$\pm\psi_2$	$\pm e$	$\pm\mu$	$\pm\beta$
0.030	0.025	0.282	0.016	0.176
0.029	0.071	0.265	0.003	0.515
0.030	0.299	0.317	0.025	2.100
0.043	0.095	0.362	0.005	0.466
0.043	0.090	0.337	0.006	0.438
0.054	0.856	0.243	0.073	3.322
0.051	0.783	0.286	0.069	3.223
0.072	0.150	0.219	0.010	0.440
0.076	0.061	0.290	0.023	0.169

0.077	0.398	0.313	0.017	1.097
0.087	0.110	0.387	0.020	0.266
0.098	0.240	0.272	0.008	0.517
0.096	0.169	0.385	0.015	0.371
0.107	0.215	0.252	0.015	0.426
0.114	0.313	0.376	0.006	0.582
0.109	0.082	0.221	0.034	0.159
0.131	0.558	0.300	0.017	0.907
0.143	0.026	0.317	0.055	0.039
0.137	0.042	0.329	0.045	0.064
0.166	0.119	0.301	0.045	0.153
0.183	0.363	0.400	0.021	0.423
0.206	0.179	0.399	0.085	0.186
0.206	0.313	0.330	0.033	0.325
0.225	0.516	0.362	0.018	0.491
0.232	0.391	0.341	0.032	0.361
0.253	0.546	0.368	0.023	0.461
0.334	0.808	0.309	0.015	0.519
0.441	1.780	0.398	0.047	0.865
1.462	2.173	1.607	0.086	0.319
0.000	0.434	-0.719	0.134	1.010

Table 10-21 – Calculated error Teflon (intermediate height)

Appendix I

Statistical analysis code in MATLAB

A

```
clear all
clc

% load interactionProperties.mat
%   load psivalues.mat

 load contactParams2.mat
% ========================================================
% normal restitution using stick and slip regions
e = [esl;est];
 me = mean(e);
 se = std(e);
```

```
ediff = e - me;
ediff = abs(ediff);
[rw,col] = find(ediff < se/4);

e_new = e(rw,1);

me_new = mean(e_new);
se_new = std(e_new);

% ========================================================
% tangential restitution (b)

% removing clear outliers upfront. These are typically values that are
% unphysical

bb = abs(bst);

[rw,col] = find(bb < 1);

bb = bb(rw,1);

mb = mean(bb);
sb = std(bb);

% remove outliers

bdiff = bb - mb;
bdiff = abs(bdiff);
[rw,col] = find(bdiff < sb);

b_new = bb(rw,1);

mb_new = mean(b_new);
sb_new = std(b_new);

% ========================================================
```

```
%friction

 mf = mean(fsl);
 sf = std(fsl);

 fdiff = fsl - mf;
 fdiff = abs(fdiff);
 [rw,col] = find(fdiff < sf/4);

 f_new = fsl(rw,1);

 mf_new = mean(f_new);
 sf_new = std(f_new);

 sl1_new = sl1(rw,1);
sl2_new = sl2(rw,1);

 [m,c,U,E] = strLineFit(sl1_new,sl2_new);

 x1 = 0 : max(sl1_new)/100 : max(sl1_new);
 y1 = m.*x1 + c;

 % ==========================================

 % get stick values used in final fit

 ee = [est];
 mee = mean(ee);
 see = std(ee);

 eediff = ee - mee;
 eediff = abs(eediff);
 [rw,col] = find(eediff < see/4);

st1_new = st1(rw,1);
st2_new = st2(rw,1);
```

```
[m,c,U,E] = strLineFit(st1_new,st2_new);

x2 = min(st1_new) : (max(st1_new)-min(st1_new))/100 : max(st1_new);
y2 = m.*x2 + c;


plot(st1_new,st2_new,'r*','LineWidth',3)
hold on
plot(x2,y2,'r')

plot(sl1_new,sl2_new,'k*','LineWidth',3)

plot(x1,y1,'k')

xlabel('\psi_1','FontSize',20)
ylabel('\psi_2','FontSize',20)

end
```